Rotating Rayleigh-Bénard Convection

Thesis by

Janet D. Scheel

In Partial Fulfillment of the Requirements

for the Degree of

Doctor of Philosophy

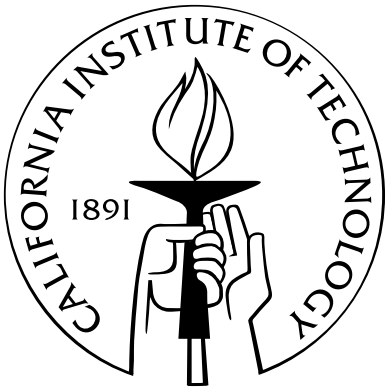

California Institute of Technology

Pasadena, California

2007

(Defended August 14, 2006)

Acknowledgements

First of all I would like to thank my advisor, Professor Michael Cross, for his generous support and guidance. I have greatly benefitted from his incredible insight and intuition. I also want to thank him for providing support for the many useful conferences I attended over the years. Since our group at Caltech is so small, it was essential to make contact with the larger pattern formation community. I would especially like to thank my collaborators: Professor Henry Greenside, Professor Guenter Ahlers, and Dr. Nathan Becker. I have learned so much from them. I am also grateful to Dr. Keng-Hwee Chiam, Professor Mark Paul, Dr. Anand Jayaraman, Professor Werner Pesch, Dr. Carina Kamaga, and Dr. Kapil Krishan. I would also like to thank Dr. Paul Fischer, the author of the numerical code used in the thesis. I benefitted from spending one summer as a Givens Associate working with him at Argonne National Laboratory. I would also like to thank the members of my thesis committee, Professors Ken Libbrecht, Dan Meiron, Mory Gharib, and Gil Refael.

On a more personal note, I would like to thank my office mates, Oleg Kogan and Keng-Hwee Chiam, for their support and lively discussions, and my good friend Loly Ekmekjian for always being there for me. I wish to thank my mentor Lisa Taneyhill for her support and guidance. I am grateful to my family for their encouragement. Last, but not least, I would like to thank my husband, Dr. Mark Scheel. I would not have been able to complete this thesis without his unparalleled support, friendship, and understanding.

This work was supported by the Engineering Research Program of the Office of Basic Energy Sciences at the Department of Energy, Grants DE-FG03-98ER14891 and DE-FG02-98ER14892.

The numerical code was run on the following supercomputing sites: the National Computational Science Alliance under DMR040001, which utilized the NCSA Xeon Linux Supercluster; the IBM "Blue Gene" system at the San Diego Supercomputing Center; the National Energy Research Scientific Computing Center, which is supported by the Office of Science of the U.S. Department of Energy under Contract No. DE-AC03-76SF00098; the Center for Computational Sciences at Oak Ridge National Laboratory, which is supported by the Office of Science of the Department of Energy under Contract DE-AC05-00OR22725; "Jazz," a 350-node computing cluster operated by the Mathematics and Computer Science Division at Argonne National Laboratory as part of its Laboratory Computing Resource Center; the North Carolina Supercomputing Center; and the Caltech Center for Advanced Computing Research.

Abstract

Rotating Rayleigh-Bénard convection (rRBC) is studied as a paradigmatic example of pattern formation and spatiotemporal chaos. For large enough rotation rates, this system undergoes a supercritical bifurcation from the uniform state to a state known as domain chaos.

In domain chaos, domains of straight parallel rolls change their orientation and size discretely. This roll switching causes an overall counterclockwise precession of the pattern. An additional mechanism of precession, glide-induced precession, is introduced here, by deriving the rRBC amplitude equation to higher order. New terms due to the rotation cause rolls to precess whenever there is an amplitude gradient in the direction parallel to the rolls. Hence, dislocations which are stationary in a nonrotating system will glide in a rotating frame, causing the overall precession.

Theory that includes the Coriolis force but ignores the centrifugal force predicted scaling laws near the transition to domain chaos. However, experimenters found different scaling laws. The scaling laws are studied here by direct numerical simulations (DNS) for the exact parameters as experiments. When only the Coriolis force is included, the DNS scaling laws agree with theory. When the centrifugal force is also included, the DNS scaling laws agree better with experiment; hence the centrifugal force cannot be neglected from theory.

The coefficients of the amplitude equation for the Complex Ginzburg-Landau equation (CGLE) are found for DNS of traveling waves. They agree well with experimental results. The CGLE is chaotic for certain values of the coefficients. However, for the parameters in the DNS, those chaotic regimes were not realized.

Leading order Lyapunov exponents (LLE) and eigenvectors are computed for both

rotating and nonrotating convection. For certain parameters, these systems are found to have positive LLEs; hence they are truly chaotic. For time-dependent systems, the leading eigenvector is characterized by localized bursts of activity which are associated with dynamical events. The short-time dynamics of the LLE is correlated with these dynamical events. However, contributions to the LLE are due to non-periodic events only.

Lagrangian particle tracking methods are employed for rRBC. These systems exhibit chaotic advection in that initially localized particle trajectories explore the available phase space.

Contents

List of Figures

List of Tables

Chapter 1

Introduction

1.1 Pattern Formation

Pattern formation involves the study of systems that are far from equilibrium. These systems are driven from equilibrium by some mechanism such as a temperature difference, an electropotential difference, or a chemical reaction. For every driving force, there are dissipative mechanisms like viscosity which act to restore the system to equilibrium. The balance between driving and dissipation causes these systems to form patterns, such as stripes, squares, hexagons, and spirals. One of the best examples of a pattern-forming system is Rayleigh-Bénard convection [13], in which a fluid-filled cell is subjected to a temperature difference leading to a buoyancy-driven instability (to be described in detail in Section 1.3). Some examples of patterns seen in Rayleigh-Bénard systems are shown in Figure 1.1. There are many variants on Rayleigh-Bénard convection such as electroconvection [66] (where the fluid is liquid crystal and there is a time-varying potential applied across the cell), binary fluids [65, 102] (where two different fluids are in the cell), and Bénard-Marangoni convection [111] (where there is no top plate so surface tension acts as an additional driving force). Other systems which exhibit patterns are Taylor-Couette flow [36] (flow between concentric rotating cylinders), Faraday waves [21] (seen in a vertically shaken fluid cell), and reaction-diffusion systems [103] (oscillatory chemical reactions).

The goal of pattern formation is to determine if diverse pattern phenomena can be understood using reduced equations [31] that are based on the underlying symmetries.

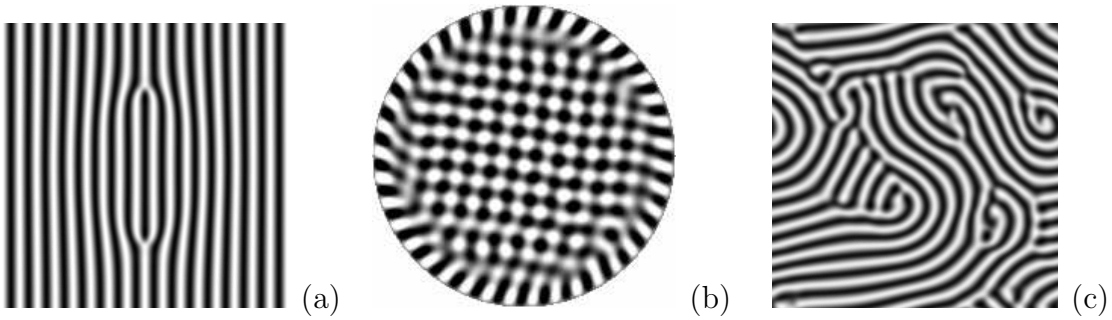

Figure 1.1: Various patterns seen in numerical simulations of Rayleigh-Bénard convection. (a) Stripes (broken by two dislocations), $\Gamma = 20, \sigma = 0.98, \Omega = 0, R = 2400(\epsilon = 0.49), t = 10$, periodic lateral boundary conditions; (b) Squares (in the interior of the cell), $\Gamma = 5, \sigma = 6.4, \Omega = 274, R = 33657(\epsilon = 0.019), t = 33$, conducting lateral thermal boundaries; (c) Spiral Defect Chaos, $\Gamma = 20, \sigma = 0.78, \Omega = 5, R = 2400(\epsilon = 0.34), t = 83$, periodic lateral boundary conditions. See Section 2.1 for definitions of the parameters.

These equations will therefore have a form common to many different physical systems. Examples of underlying symmetries are: discrete translational symmetry in one direction for stripe states and discrete translational symmetry in two dimensions for square states. An example of a reduced equation is the Ginzburg-Landau equation, which describes systems with translational invariance, such as a stripe state. These equations are called reduced equations because they reduce the degrees of freedom of a system by removing those variables which are fast and modeling the evolution of the slow variables. Since the fast variables adiabatically follow the evolution of the slow variables, the slow variables are all that is needed to model the entire system. The stripe pattern in Figure 1.1a is a good example of this. The fast variables describe the stripe pattern at wavenumber k, and the slow variables describe the amplitude and phase modulation which gives rise to the dislocations. This theoretical framework has been enormously successful in predicting the linear stability of uniform periodic states as a control parameter is varied. The theory has also been successful in describing coherent structures, such as dislocations and domain walls. In this thesis we will derive and analyze the reduced equations which describe rotating Rayleigh-Bénard convection.

The subject of nonequilibrium pattern formation has applications to a variety of

problems. Some examples include understanding the motion of flame fronts produced in combustion [41], using morphogenesis to explain the biological development of patterns in nature [115], describing the growth of dendritic tips [63], and explaining the aggregation of slime molds [47].

1.2 Spatiotemporal Chaos

Spatiotemporal chaos refers to a system that shows disorder in both space and time. Examples are given in Figure 1.1c and in Figure 5.1. Many pattern forming systems can exhibit spatiotemporal chaotic states, and the study of such systems has made important contributions to chaos and bifurcation theory [64]. For example, rotating a Rayleigh-Bénard convection cell breaks the reflection symmetry, which gives rise to a bifurcation to a chaotic state known as domain chaos as a control parameter is varied. Since most reduced equations in pattern formation contain a nonlinear term, they can be chaotic for certain parameters. One example is the Complex Ginzburg-Landau equation, which will be discussed in Chapter 3.

However, spatiotemporal chaotic states remain poorly understood. Researchers do not know how to predict the parameter values for which spatiotemporal chaos occurs, the way a spatiotemporal chaotic state changes as some parameter is varied, or the values of physically significant quantities such as transport coefficients of matter and energy. In most cases the description of the chaos has been somewhat anecdotal. Even the definition of spatiotemporal chaos is not completely rigorous.

In this thesis we will investigate states exhibiting spatiotemporal chaos in rotating and non-rotating Rayleigh-Bénard convection by computing leading-order Lyapunov exponents and eigenvectors. Lyapunov exponents are a measure of the exponential divergence of nearby trajectories, and the Lyapunov eigenvector is the vector field associated with the difference between the two trajectories. A system with N dimensions will have N Lyapunov exponents, and the system is chaotic if any of these exponents are positive.

Egolf et al. computed the Lyapunov spectral density (number of positive Lya-

punov exponents, roughly speaking) for large aspect ratio Rayleigh-Bénard systems which exhibit Spiral Defect Chaos (SDC). SDC is characterized by a disordered collection of rotating spirals which nucleate and annihilate randomly [24, 22]. An example of an SDC state is given in Figure 1.1c. They demonstrated that the Lyapunov spectral density was extensive in that it scaled with system size. However, they used periodic boundary conditions. Lyapunov exponents have never been computed for realistic boundary conditions or for any other Rayleigh-Bénard convection system. If the extensive scaling of the Lyapunov spectral density were true in general, this would provide a rigorous definition of spatiotemporal chaos and a fundamental length scale for such systems [108]. By developing a Lyapunov solver which computes the leading Lyapunov exponent and eigenvector for realistic boundary conditions (2.23, 2.24, 2.25), we have made the first step in computing the full spectrum of positive Lyapunov exponents and hence the Lyapunov spectral density for our systems.

We will also study transport by tracking fluid particles to better understand the chaos in these systems. Hassan Aref [4] noted that the appropriate phase space of canonically conjugate variables for a two-dimensional fluid is its real space. We will analyze particle trajectories for large aspect ratio, three-dimensional rotating Rayleigh-Bénard convection to study mixing and to investigate three-dimensional generalizations of Aref's ideas.

In addition to being important for theoretical considerations, spatiotemporal chaos can be applied to a variety of problems such as weather forecasting [86] and controlling the chaotic ventricular fibrillation in a human heart [119].

1.3 Definition of Rayleigh-Bénard Convection

Rayleigh-Bénard convection is one of the most productive systems for studying pattern formation, based on its accessibility to experimenters and its ability to be modeled theoretically [31, 13, 74, 17].

In Rayleigh-Beńard convection, a fluid cell is bounded by horizontal parallel plates kept at a constant temperature difference ΔT, as shown in Figure 1.2. This leads to a

buoyancy-driven instability as ΔT increases past a critical value. A control parameter can characterize this transition. This control parameter ϵ measures the strength of the driving above the onset of convection and is linear in the temperature difference.

In non-rotating Rayleigh-Bénard convection, the conducting state bifurcates to a convection state consisting of straight, parallel rolls as shown in Figure 1.3 (by moving up the vertical axis at $\Omega = 0$). The parameter regime where parallel rolls are stable is well-modeled theoretically near threshold by an amplitude equation, the reduced equation which describes Rayleigh-Bénard convection [30]. Then, if the aspect ratio (ratio of radius to depth) is large, or if ϵ is increased further, this state can bifurcate to a state exhibiting SDC.

It is particularly interesting to study *rotating* Rayleigh-Bénard convection, where the entire cell rotates rigidly about a vertical axis, as described in Figure 1.2. For large enough rotation rates, a chaotic state known as domain chaos has been found to exist [70, 113]. Examples of domain chaos states are shown in Figures 5.1, 5.4, 6.1, 6.3, 6.4, 6.5, 7.20, and 7.21. This state consists of domains of parallel rolls, each of whose particular location and size vary chaotically. Domain chaos is one of the few experimentally known spatiotemporal chaotic states that bifurcates supercritically from a time-independent, spatially uniform state (here the motionless conducting state of the fluid), as shown by the thick dashed arrow in Figure 1.3. A supercritical bifurcation is particularly useful to study since the new state evolves continuously out of the old state.

A perturbation expansion of the equations which model rotating Rayleigh-Bénard convection (by including the Coriolis force) [70, 69] predicted this supercritical bifurcation from a conducting state to an unstable convection state. In the original work by Küppers and Lortz [70], the convection state consisted of straight parallel rolls which were unstable to rolls at a different, distinct orientation. This is known as the Küppers-Lortz instability. Busse and Heikes [19] proved that the time between roll switches should increase as the perturbation which causes the instability decays.

However, in experimental systems, one typically sees a more constant switching frequency. Busse and Heikes suggested that thermal or other extrinsic noise would

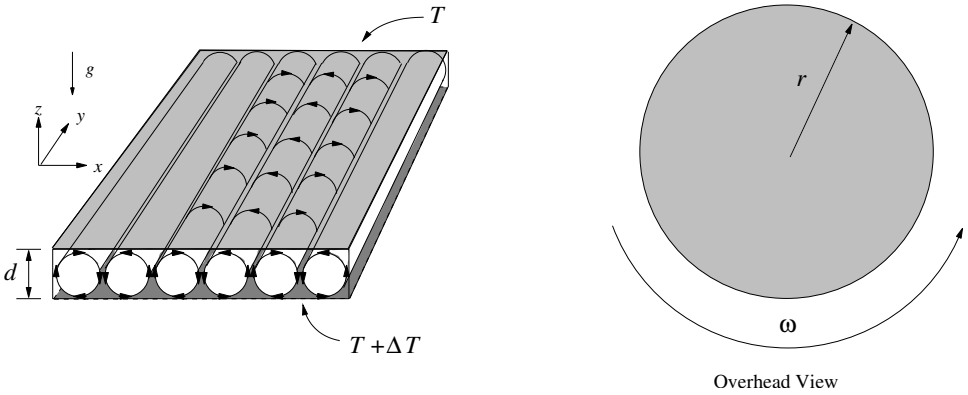

Figure 1.2: Schematic for rotating Rayleigh-Bénard convection. Parallel plates separated by a distance d are kept at a constant temperature difference ΔT, where the bottom plate is kept at a higher temperature than the top plate. Due to the orientation of gravity g, for high enough ΔT, conduction gives way to convection in the form of parallel rolls as shown. In rotating Rayleigh-Bénard convection, the entire cell rotates rigidly about a vertical axis with rotation rate ω.

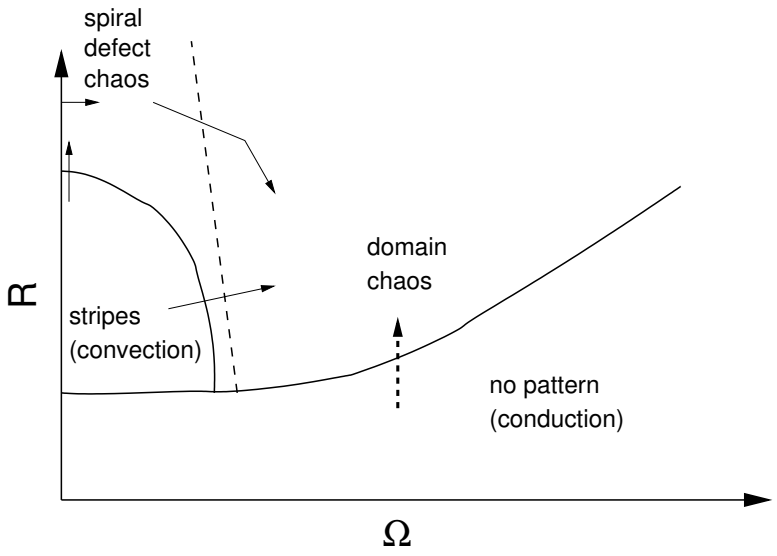

Figure 1.3: A schematic of a stability diagram for rotating Rayleigh-Bénard convection. Stability regimes for various values of Rayleigh number, R, and dimensionless rotation rate, Ω, are plotted (see Section 2.1 for definitions of the parameters). The arrows indicate bifurcations to different states.

cause the roll switches to occur at a relatively constant rate. Laveder et al. [71] demonstrated that a noise floor would also have a significant effect on the scaling laws for correlation lengths. However, Oh and Ahlers showed [84] that the experimental noise in Rayleigh-Bénard convection systems is very small. It is practically insignificant in the parameter range investigated by the experiments of Hu et al. [57]. Cross and Tu [113] showed that in realistic systems the chaotic fluctuations from a complex spatial structure are important, leading to roll switches occurring at a relatively constant rate.

This led to theoretical modeling of rotating Rayleigh-Bénard convection via three coupled Ginzburg-Landau equations [113, 33, 64], which confirmed the presence of a supercritical bifurcation. The patterns switched at a constant rate and looked similar to those seen in experiments. The theory uses periodic boundary conditions and assumes that the dynamics is dominated by domain wall motion. When one set of rolls is replaced by another, the region containing the new, growing set of rolls spreads by the motion of a front, i.e., the boundary between the two different regions of roll orientation. Except for the special case of a front perpendicular to the rolls, the velocity of propagation of the front scales as $\epsilon^{1/2}$ [12], and the pertinent length scale varies as $\epsilon^{-1/2}$. This leads to the time scale for perturbations to grow, which scales as ϵ^{-1}. These scaling predictions are some of the first quantitative, theoretical predictions for a spatiotemporal chaotic state.

Extensive experiments were done on cylindrical rotating Rayleigh-Bénard cells for aspect ratios 20 and 40 [121, 57, 58, 59]. The scaling laws for characteristic lengths and times were found to differ from the theoretical predictions. Experimenters measured the scaling exponent for lengths to be -0.2 and times to be -0.6, if they assumed that the length and time quantities diverged at onset [57]. However, the data could also be fit by assuming no divergence at onset.

We will use numerical simulations with exactly the same parameters and boundary conditions as the experiments. We find that our numerical results agree quite well with the theoretical scaling results when we only include the Coriolis force to model the rotaiton. However, the theory includes only the Coriolis force and neglects the

centrifugal force. Recent experiments by Becker and Ahlers [9] have shown that the centrifugal force cannot be neglected. When we include the centrifugal force as well as the Coriolis force in our simulations, we find we get better agreement with the experimental results.

In addition to roll switching, we also find that dislocation defects are present in our numerical simulations. These defects glide perpendicular to the rolls and also cause the rolls to precess. We will call this glide-induced precession. To investigate this new mechanism for precession, we derive the amplitude equation for rotating Rayleigh-Bénard convection for higher order terms than the computations by Küppers and Lortz. We will show that the higher order terms will cause rolls to precess whenever there is a gradient in the amplitude in the direction parallel to the rolls. This gives rise to the precession phenomenon observed in the simulations, including that of glide-induced precession. We will prove that glide-induced precession has a scaling exponent of 3/4, closer to that of the experiments. We make the conclusion that the centrifugal force causes a large scale flow to develop, which in turn encourages the production of defects which causes glide-induced precession to have a more dominant effect on the scaling.

1.4 Summary of thesis

This thesis is organized as follows:

In Chapter 2 we derive the basic equations which describe Rayleigh-Bénard convection and explain our computational methodology. We also provide an introduction to amplitude equations, which will be the main theoretical focus in this thesis. We then discuss our methods of computing Lyapunov exponents, which are used to characterize chaotic states. Finally, we discuss our methods of tracking particles to study transport. We then analyze traveling waves in Chapter 3 to demonstrate the utility of amplitude equations in a simpler system. Traveling waves are wall-localized modes which occur when a Rayleigh-Bénard convection system is rotated at a very high rotation rate. We show that such wall modes are well-described by an ampli-

tude equation known as the complex Ginzburg-Landau equation. In Chapter 4 we derive the amplitude equation to higher order for rotating Rayleigh-Bénard convection, with the rotation described by the Coriolis force. Our analysis includes the non-trivial contributions due to the mean flow. We then discuss the implications of the new terms that arise from the Coriolis force, such as wall-induced precession and the gliding motion of defects, and make a comparison to numerical results. In Chapter 5 we study the transition to domain chaos by determining the scaling laws for time and length quantities as the control parameter ϵ is varied. We compare our numerical results with previous theoretical and experimental results. We find that the numerical results which only include the Coriolis force agree with the theoretical model (which also only includes the Coriolis force). However, we find we get much better agreement with the experimental results when we include the centrifugal force as well, which we discuss in Chapter 6. Finally, in Chapter 7 we compute leading order Lyapunov exponents for both rotating and non-rotating Rayleigh-Bénard convection systems and demonstrate that these systems are indeed chaotic in the sense of having a positive Lyapunov exponent. We also examine the leading order Lyapunov eigenvector and note that it is characterized by localized bursts of activity when the system is time-dependent. We investigate the correlations between such bursts in the eigenvector and dynamical events such as dislocation creation/annihilation and roll compression. In Chapter 8 we discuss our preliminary results on particle tracking. We provide concluding remarks in Chapter 9.

Chapter 2

Background

2.1 Boussinesq Equations

The Boussinesq Equations consist of the Navier-Stokes equation, the heat equation, and mass conservation. In order to correctly model the system in Figure 1.2, we include the gravitational force ($-g\hat{z}$), the Coriolis force ($-2\,\omega\,\hat{z}\times\mathbf{u}$), and the centrifugal force ($\omega^2\mathbf{r}$) in the momentum equation. Here the equations are first written in dimensional form:

$$\begin{aligned}(\partial_t+\mathbf{u}\cdot\nabla)\,\mathbf{u} &= -\frac{\nabla P}{\rho}+\nu\nabla^2\mathbf{u}-g\hat{z}-2\,\omega\,\hat{z}\times\mathbf{u}+\omega^2\mathbf{r},\\ (\partial_t+\mathbf{u}\cdot\nabla)\,T &= \kappa\nabla^2 T,\quad \text{and}\\ \nabla\cdot\mathbf{u} &= 0,\end{aligned}\tag{2.1}$$

where $\mathbf{u}\equiv(u,v,w)$ is the velocity field, T is the temperature field, and P is the pressure. In addition, ν is the kinematic viscosity, κ is thermal diffusivity, ω is the rotation rate, g is the gravitational constant, and ρ is the fluid density.

We also assume the only temperature dependence is in the density:

$$\rho=\bar{\rho}[1-\alpha(T-\bar{T})],\tag{2.2}$$

where α is the thermal expansion coefficient, and $\bar{\rho},\bar{T}$ are the reference densities and

temperatures, respectively. Hence we can expand the pressure term:

$$-\frac{\nabla P}{\rho} \simeq -\frac{\nabla P}{\bar{\rho}}[1+\alpha(T-\bar{T})]. \tag{2.3}$$

Next, since the pressure is determined from a gradient, we can absorb part of the gravitational force and the centrifugal force into the pressure. We will redefine

$$P' = P + \bar{\rho} g z \hat{z} - \frac{\bar{\rho}}{2}\omega^2(x^2\hat{x} + y^2\hat{y}); \tag{2.4}$$

then

$$-\frac{\nabla P}{\bar{\rho}}\left[1+\alpha(T-\bar{T})\right] = \left(-\frac{\nabla P'}{\bar{\rho}} + g\hat{z} - \omega^2\left(x\hat{x}+y\hat{y}\right)\right)\left[1+\alpha(T-\bar{T})\right]. \tag{2.5}$$

If we substitute (2.5) into (2.1), the terms not proportional to the temperature will be absorbed into the redefined pressure. However, the other terms will not and we obtain

$$\begin{aligned}
\left(\partial_t + \mathbf{u}\cdot\nabla\right)\mathbf{u} &= -\frac{\nabla P'}{\bar{\rho}} + \nu\nabla^2\mathbf{u} + g\alpha(T-\bar{T})\hat{z} - 2\,\omega\,\hat{z}\times\mathbf{u} - \omega^2\alpha(T-\bar{T})\mathbf{r}, \\
\left(\partial_t + \mathbf{u}\cdot\nabla\right)T &= \kappa\nabla^2 T, \quad \text{and} \\
\nabla\cdot\mathbf{u} &= 0,
\end{aligned} \tag{2.6}$$

where we have assumed the term $\nabla P'\alpha(T-\bar{T})/\bar{\rho}$ is small.

Now let us nondimensionalize everything:

$$\begin{aligned}
t' &= \frac{t}{\tau_v}, \quad \omega' = \omega\tau_\nu, \quad \tau_v = \frac{d^2}{\kappa}, \\
l' &= \frac{l}{d}, \quad \text{where } d = \text{cell height}, \\
u' &= u\left(\frac{d}{\kappa}\right), \\
T' &= \frac{T}{\Delta T}, \quad \Delta T = T_{\text{bot}} - T_{\text{top}}, \quad \text{and} \\
\frac{P''}{\bar{\rho}'} &= \frac{P'}{\bar{\rho}}\left(\frac{d^3}{\kappa^2}\right).
\end{aligned} \tag{2.7}$$

Hence, (2.6) becomes

$$\begin{aligned}
(\partial_{t'} + \mathbf{u}' \cdot \nabla)\,\mathbf{u}' &= -\frac{\nabla P''}{\bar{\rho}'} + \frac{\nu}{\kappa}\nabla^2\mathbf{u}' + \frac{d^3\Delta T g\alpha}{\kappa^2}(T' - \bar{T}')\hat{z} - 2\omega'\hat{z}\times\mathbf{u}' - \omega'^2\Delta T\alpha(T' - \bar{T}')\mathbf{r}, \\
(\partial_{t'} + \mathbf{u}' \cdot \nabla)\,T' &= \nabla^2 T', \quad \text{and} \\
\nabla \cdot \mathbf{u}' &= 0. \qquad (2.8)
\end{aligned}$$

Now, if we define

$$\begin{aligned}
\sigma &= \frac{\nu}{\kappa}, \qquad (2.9) \\
R &= \frac{d^3\Delta T g\alpha}{\nu\kappa}, \qquad (2.10) \\
\Omega &= \frac{\omega'}{\sigma} = \frac{\omega d^2}{\nu}, \quad \text{and} \qquad (2.11) \\
P &= \frac{P''}{\sigma\bar{\rho}'}, \qquad (2.12)
\end{aligned}$$

and drop all the primes, then we obtain

$$\begin{aligned}
\sigma^{-1}\,(\partial_t + \mathbf{u} \cdot \nabla)\,\mathbf{u} &= -\nabla P + \nabla^2\mathbf{u} + R(T - \bar{T})\hat{z} + 2\Omega\mathbf{u}\times\hat{z} - \sigma\Omega^2\Delta T\alpha(T - \bar{T})\mathbf{r}, \\
(\partial_t + \mathbf{u} \cdot \nabla)\,T &= \nabla^2 T, \quad \text{and} \\
\nabla \cdot \mathbf{u} &= 0. \qquad (2.13)
\end{aligned}$$

As a result, our Coriolis term is

$$2\Omega\mathbf{u}\times\hat{z}, \qquad (2.14)$$

and our centrifugal term is

$$-\sigma\Delta T\alpha\Omega^2(T - \bar{T})\mathbf{r} = -\beta\sigma\Omega^2\frac{R}{R_c}(T - \bar{T})\mathbf{r}, \qquad (2.15)$$

where $\beta = \alpha\Delta T_c$, and ΔT_c (and corresponding critical Rayleigh number R_c) is the temperature difference at which conduction gives way to convection. The Coriolis term will be used throughout this thesis to model rotating Rayleigh-Bénard convection, and the centrifugal term will be important in Chapter 6.

We can also write the Boussinesq equations in terms of $\theta = R\left[(T - \bar{T}) - T_o(z)\right]$,

the temperature deviation from the linear conduction profile $T_o(z)$:

$$\begin{aligned}
\sigma^{-1}\left(\partial_t + \mathbf{u}\cdot\nabla\right)\mathbf{u} &= -\nabla P + \nabla^2\mathbf{u} + \theta\hat{z} + 2\Omega\mathbf{u}\times\hat{z} - \frac{\beta\sigma\Omega^2}{R_c}\theta\mathbf{r}, && (2.16)\\
\left(\partial_t + \mathbf{u}\cdot\nabla\right)\theta &= \nabla^2\theta + Rw, \quad \text{and} && (2.17)\\
\nabla\cdot\mathbf{u} &= 0, && (2.18)
\end{aligned}$$

where w is the z-component of the velocity vector $\mathbf{u}$.

The aspect ratio Γ is defined as the ratio of radius to depth for cylindrical regions and as the ratio of width to depth for square/periodic regions:

$$\begin{aligned}
\Gamma &= \frac{\text{radius}}{\text{depth}} \quad \text{for cylindrical regions, and}\\
\Gamma &= \frac{\text{width}}{\text{depth}} \quad \text{for square regions.} && (2.19)
\end{aligned}$$

To review, our important parameters are

$$\begin{aligned}
\sigma &= \frac{\nu}{\kappa},\\
R &= \frac{d^3\Delta T g\alpha}{\nu\kappa}, \quad \text{and}\\
\beta &= \alpha\Delta T_c, && (2.20)
\end{aligned}$$

where ν is the kinematic viscosity, κ is thermal diffusivity, Ω is the dimensionless rotation rate, g is the gravitational constant, ρ is the fluid density, α is the thermal expansion coefficient, and ΔT is the temperature difference between the top and bottom plates. The quantities R_c and ΔT_c are the critical Rayleigh number and temperature difference at which conduction gives way to convection. The control parameter ϵ is defined as

$$\epsilon = \frac{R - R_c}{R_c}. \tag{2.21}$$

The vertical diffusion time τ_ν has already been defined in (2.7) as the fundamental

unit of time in these systems, but another important time scale is the horizontal diffusion time τ_h:

$$\begin{aligned} \tau_\nu &= \frac{d^2}{\kappa} \qquad \text{for a vertical diffusion time, and} \\ \tau_h &= \Gamma^2 \tau_\nu \qquad \text{for a horizontal diffusion time.} \end{aligned} \tag{2.22}$$

The horizontal diffusion time is approximately the time it takes for heat to diffuse across the horizontal length of the cell, and typically simulations should be run for at least this long to allow for transients to fully relax.

Along the top and bottom plates we use realistic no-slip velocity boundary conditions and constant values for the temperature boundary conditions:

$$\mathbf{u} = 0, \quad \theta = 0 \quad \text{at } z = 0, 1. \tag{2.23}$$

For realistic boundary conditions on the sidewalls, we use no-slip velocity boundary conditions and conducting or insulating thermal boundaries:

Conducting boundaries

$$\mathbf{u} = 0, \ \theta = 0 \text{ at } r = \Gamma, \tag{2.24}$$

Insulating boundaries

$$\mathbf{u} = 0, \ \frac{\partial \theta}{\partial r} = 0 \text{ at } r = \Gamma. \tag{2.25}$$

We will also use periodic (for square regions only, of course) boundary conditions on the sidewalls:

Periodic boundaries

$$\begin{aligned} \mathbf{u}(x + \Gamma, y) = \mathbf{u}(x, y), \ \theta(x + \Gamma, y) = \theta(x, y), \quad \text{and} \\ \mathbf{u}(x, y + \Gamma) = \mathbf{u}(x, y), \ \theta(x, y + \Gamma) = \theta(x, y). \end{aligned} \tag{2.26}$$

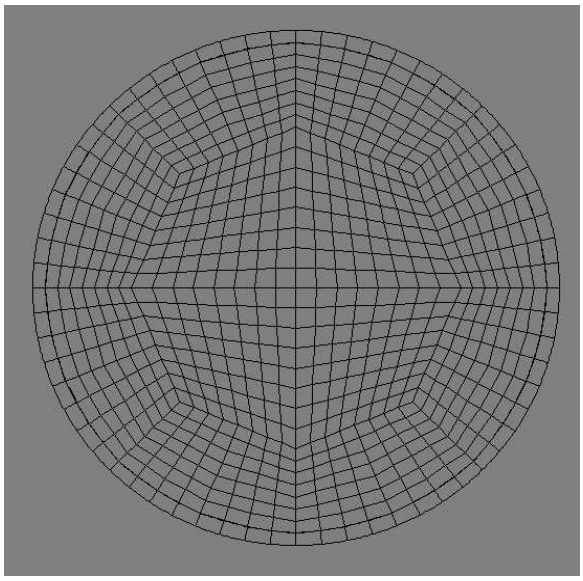

Figure 2.1: Example mesh of 768 elements for an aspect ratio Γ of 20.

2.2 Computational Methodology

To solve the Boussinesq equations with rotation, we use nek5000 [42, 35], a highly efficient parallel, spectral element code developed by Paul Fischer to solve the Navier-Stokes equation. The code nek5000 has already been used to analyze many aspects of Rayleigh-Bénard convection [88, 87, 89, 90, 24, 23, 100, 99, 60, 97, 9, 98].

The spatial discretization is based upon the spectral element method: the computational domain is divided into elements, and in each element the solution is represented as a high order polynomial (usually N=11-13). We use Lagrangian interpolants based upon Gauss-Lobatto-Legendre (GLL) quadrature points. This approach is appropriate for parallelization, because communication between elements is much less than for a single domain. Also, the spatial decomposition of the domain into elements enables one to easily change the geometry of the situation without code modification. The high-order spatial discretization is exponentially convergent, and hence reduces the number of spatial degrees of freedom for a given level of accuracy. An example cylindrical mesh is shown in Figure 2.1 for an aspect ratio Γ of 20. We found the best resolution was about one element per roll; hence we need 768 elements for a Γ of 20.

Nek5000 employs a second (or third) order operator split formulation in time,

in which the nonlinear (convective) and driving (buoyancy, Coriolis, and centrifugal) terms are treated explicitly. The remaining linear, symmetric Stokes problem is solved implicitly. This system is also split, decoupling the viscous and pressure steps into independent symmetric positive definite subproblems which are solved either by Jacobi (viscous) or overlapping Schwartz (pressure) preconditioned conjugate gradient iteration. The fast parallel coarse grid solver [114] as well as the preconditioners for the intermediate elliptic steps [43] readily scale to thousands of processors. The operator splitting method allows large time steps to be taken (and in particular convective CFL numbers [94] in excess of unity), which is essential in order to investigate the long-term dynamical behavior of these systems.

We demonstrate the parallel speed-up of nek5000 in Figure 2.2. We have simulated rotating Rayleigh-Bénard convection (Coriolis force only) on the linux supercluster "Jazz" at the Laboratory Computing Resource Center at Argonne National Laboratory. We ran the simulations for one vertical diffusion time τ_ν (2.22) and tested both $\Gamma = 20$ and $\Gamma = 40$. The parameters used for both cases were $R = 2400$ $(\epsilon = 0.068), \sigma = 0.78$, and $\Omega = 17.6$, conducting lateral boundary conditions, 11 grid points per element per spatial dimension. For the $\Gamma = 20$ case, 192 elements and a time step of 0.005 were used. For the $\Gamma = 40$ case, 768 elements and a time step of 0.005 were used.[1] We see excellent parallel speedup in either case. Note that the $\Gamma = 40$ case takes about a factor of 7.5 longer on average to run.

We also performed convergence tests every time we altered the code. We show some representative tests in Figures 2.3 and 2.4. Convergence tests are essential for ensuring that the code is correctly representing the situation to be simulated [15]. If the solution changes dramatically as the time step is decreased and/or the number of elements are increased, then the simulation was not correctly resolved. These convergence tests also give us a sense of the accuracy of our simulations.

We will use a quantity known as the Nusselt number to determine our errors. The Nusselt number is defined as the ratio of the total heat transported across the cell

[1]Note that with these resolutions the cells are slightly under-resolved. The results presented in this thesis have all been run with a factor of four more elements than those used to demonstrate the parallel speed-up.

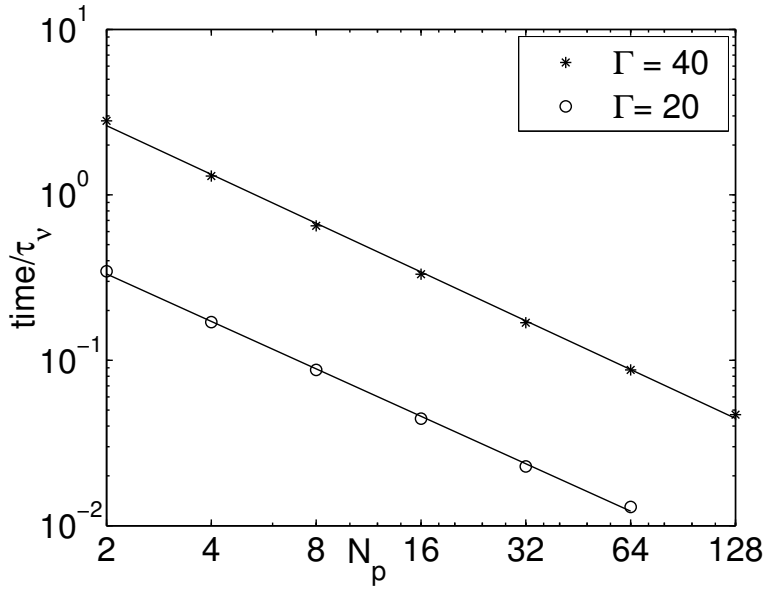

Figure 2.2: Parallel speedup for nek5000. We plot the time to run out to one vertical diffusion time τ_ν versus the number of processors N_p. The parameters are $R = 2400$ $(\epsilon = 0.068), \sigma = 0.78, \Omega = 17.6$, and conducting lateral boundary conditions.

in the z-direction divided by the heat transported via conduction only. Hence, if the Nusselt number is one, there is only conduction, and if the Nusselt number is greater than one, there is convection as well. To allow for a simpler comparison, the reduced Nusselt number $\mathcal{N}$ is studied:

$$\mathcal{N} = \frac{\text{Total heat transported}}{\text{Heat transported via conduction}} \; - \; 1. \tag{2.27}$$

In all cases we ran the simulations until the reduced Nusselt number converged to a stable value. Since $\mathcal{N}$ is computed from the state variables (see 2.50), it should also be convergent with respect to temporal and spatial resolution, just as the state variables. We prefer using $\mathcal{N}$ to the state variables since these systems can be chaotic, so the evolution of the specific state variable trajectories may change with resolution. However, $\mathcal{N}$, as an average quantity, will remain relatively constant.

The error, Δ Nusselt, is computed by finding the reduced Nusselt number for each spatial resolution N, which is the number of GLL points in one dimension per element. The entire number of GLL points per element is N^3. Then we assume the

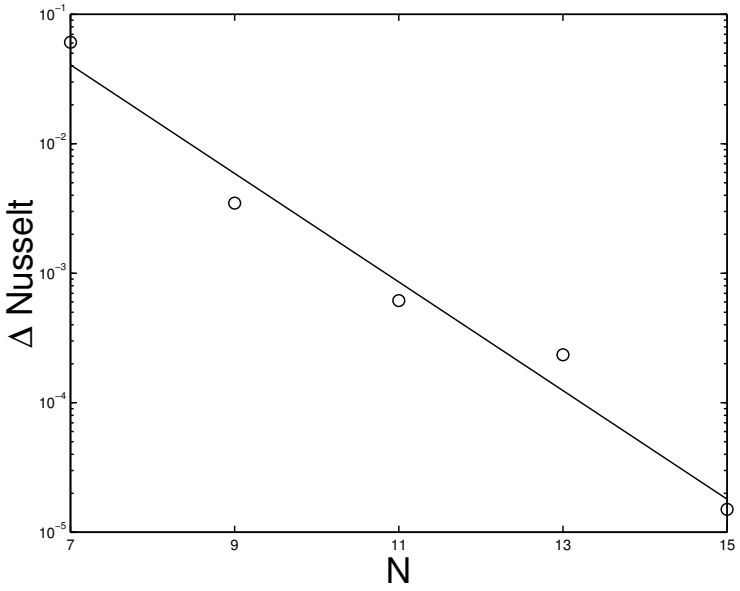

Figure 2.3: Error in Nusselt number, Δ Nusselt, versus number of grid points N. This semilog plot shows that convergence is exponential in N. The geometry is for a cylinder with no-slip velocity boundary conditions on all sides, conducting thermal boundary conditions on the plates, and insulating thermal boundary conditions on the sidewalls. The parameters used were:$R = 2000$, $\Omega = 0$, $\sigma = 0.78$, $\Gamma = 2.08$, 48 elements, and a dt of 0.001. The slope of the best fit line is -0.97.

highest spatial resolution is the most accurate. That would correspond to $N = 17$ for Figure 2.3. Hence,

$$\Delta\text{Nusselt} = \left(\frac{\mathcal{N}_N - \mathcal{N}_{17}}{\mathcal{N}_{17}}\right), \tag{2.28}$$

where $\mathcal{N}_N$ is the reduced Nusselt number for a resolution N.

Since our code is spectral in the spatial domain, we expect exponential convergence as the spatial resolution N is increased. We find this to be true in Figure 2.3, where we have plotted the error in the reduced Nusselt number, Δ Nusselt (2.28), versus our spatial resolution per element, N.

We have also investigated convergence in the time domain. Since we use an explicit time stepping routine, namely a second- or third-order Adams-Bashforth routine, we expect our convergence to be the same as the order of our time stepping algorithm. In Figure 2.4 we used the second-order Adams-Bashforth routine, so we expect our

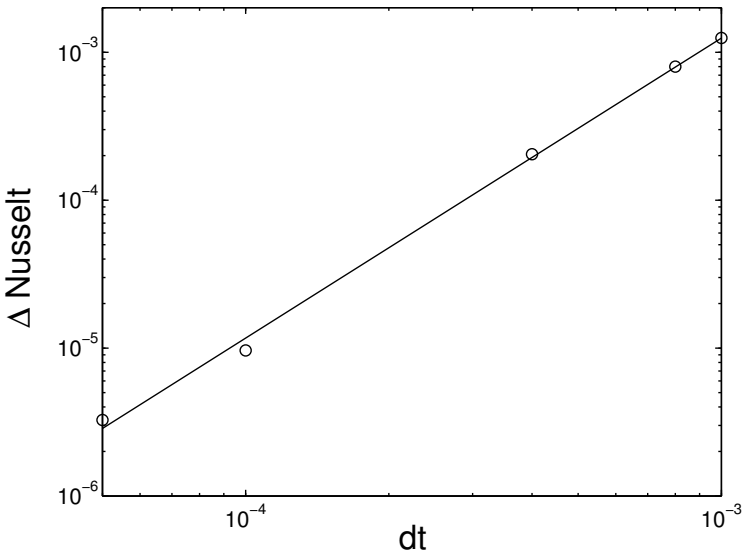

Figure 2.4: Error in Nusselt number, Δ Nusselt, versus time step dt. This log-log plot shows convergence is second order in dt as expected. The geometry is for an annulus with no-slip velocity boundary conditions on all sides, conducting thermal boundary conditions on the plates and insulating thermal boundary conditions on the sidewalls. The parameters used were:$R = 6100$, $\Omega = 70$, $\sigma = 6.4$, $r_{\text{inner}} = 1$, $r_{\text{outer}} = 2$, eight elements, and a dt of 0.0001. The number of grid points N is 11. The slope of the best fit line is 2.03.

errors to fall off as dt^2, where dt is our time step. We see this to be true in Figure 2.4. Here we have defined our error similarly to (2.28):

$$\Delta\text{Nusselt} = \left(\frac{\mathcal{N}_{dt} - \mathcal{N}_{0.00001}}{\mathcal{N}_{0.00001}}\right), \tag{2.29}$$

where $\mathcal{N}_{dt}$ is the reduced Nusselt number for a time resolution of dt, and $\mathcal{N}_{0.00001}$ is the reduced Nusselt number for our finest time step, $dt = 0.00001$.

2.3 Perturbation Methodology

2.3.1 Introduction

As stated in Section 1.1, one of the goals of studying pattern formation is to derive reduced equations which contain the features common to a number of different systems, all of which have the same underlying symmetry properties. Such equations reduce the degrees of freedom of a system by removing those variables which are fast and modeling the evolution of the slow variables. These reduced equations are known as amplitude equations when used to describe Rayleigh-Bénard convection, since the fast variables' solutions can be described by sinusoidal functions, and the slow variables are the amplitude modulation of these functions.

These amplitude equations can then be used to predict and describe bifurcations due to symmetry breaking [31, 74]. Since we want to study bifurcations, amplitude equations are derived near the threshold of such a transition. Hence, they are an expansion in the control parameter ϵ introduced in (2.21). We will use multiple scales perturbation theory [81] for this expansion to separate the system into its fast and slow modes. Then, by eliminating secular terms by imposing solvability conditions [80] we integrate over the fast modes and retain an equation which only involves the slow modes.

We will demonstrate with the Swift-Hohenberg equation with rotation [33] a model equation. Model equations are an intermediate step, since they are equations which, like amplitude equations, describe a number of systems with the same underlying symmetry properties. Unlike amplitude equations, however, they can contain both the fast and the slow variables. These model equations are easier to solve than the full equations describing a particular system (such as the Boussinesq equations (2.13)). Model equations reduce to the same amplitude equation as the systems they model. By analogy to phase transitions, where model equations are also used, we typically call the dependent variable the order parameter.

The Swift-Hohenberg equation with rotation is

$$\partial_t \psi \;=\; \epsilon\psi - (\nabla^2 + q_0^2)^2\psi - g_1\psi^3 + g_2\hat{z}\cdot\nabla\times\left[(\nabla\psi)^2\nabla\psi\right] + g_3\nabla\cdot\left[(\nabla\psi)^2\nabla\psi\right]. \tag{2.30}$$

The order parameter is ψ, q_0 is the wave number of the rolls, g_1 and g_3 are coefficients of the nonlinear terms, and g_2 is the coefficient of the term due to the Coriolis force, which is proportional to the rotation rate.

Using the method of multiple scales, we will separate out fast (x, z) and slow (X, Y, T, T') scales in the following manner:

$$\partial_x \to \partial_x + \epsilon^{\frac{1}{2}}\partial_X, \quad \partial_y \to \epsilon^{\frac{1}{4}}\partial_Y, \quad \text{and} \quad \partial_t \to \epsilon\partial_T + \epsilon^{\frac{5}{4}}\partial_{T'}. \tag{2.31}$$

The fast spatial variables are defined as those that vary on the order of a typical wavelength for the system, which is the same magnitude as the depth of the system. The slow parameters describe, then, the temporal and spatial modulation of these fast variables, and it is this modulation which leads to interesting dynamics. Note we have defined different scalings for each of the slow variables. This is motivated by the dependence of the growth rate on wave vector perturbations in the x and y directions. Via symmetry arguments (translation for x and rotation for y) one sees that the scaling in (2.31) is the most natural phenomenologically.

We will also expand our order parameter ψ in the small parameter ϵ:

$$\psi = \epsilon^{\frac{1}{2}}\psi_0 + \epsilon^{\frac{3}{4}}\psi_1 + \epsilon\psi_2 + \epsilon^{\frac{5}{4}}\psi_3 + \epsilon^{\frac{3}{2}}\psi_4 + \epsilon^{\frac{7}{4}}\psi_5 + \ldots \tag{2.32}$$

We will assume $\psi = Ae^{iq_0x}$, where the amplitude A describes the overall modulation of the roll structure and hence only depends on the slow variables X, Y, T, T'. The amplitude A will also be expanded in ϵ as

$$A = \epsilon^{\frac{1}{2}}A_0 + \epsilon^{\frac{3}{4}}A_1 + \epsilon A_2 + \epsilon^{\frac{5}{4}}A_3 + \epsilon^{\frac{3}{2}}A_4 + \epsilon^{\frac{7}{4}}A_5 + \ldots \tag{2.33}$$

Substituting (2.32) and (2.31) into (2.30) and equating like powers of ϵ yields

$$\epsilon^{\frac{1}{2}}: \quad \left(\partial_x^2 + q_0^2\right)^2 \psi_0 = 0, \tag{2.34}$$

$$\epsilon^{\frac{3}{4}}: \quad \left(\partial_x^2 + q_0^2\right)^2 \psi_1 = 0, \tag{2.35}$$

$$\epsilon: \quad \left(\partial_x^2 + q_0^2\right)^2 \psi_2 + 2\left(\partial_Y^2 + 2\partial_x\partial_X\right)\left(\partial_x^2 + q_0^2\right)\psi_0 = 0, \tag{2.36}$$

$$\epsilon^{\frac{5}{4}}: \quad \left(\partial_x^2 + q_0^2\right)^2 \psi_3 + 2\left(\partial_Y^2 + 2\partial_x\partial_X\right)\left(\partial_x^2 + q_0^2\right)\psi_1 = 0, \tag{2.37}$$

$$\begin{aligned}\epsilon^{\frac{3}{2}}: \quad & \left(\partial_x^2 + q_0^2\right)^2 \psi_4 + 2\left(\partial_Y^2 + 2\partial_x\partial_X\right)\left(\partial_x^2 + q_0^2\right)\psi_2 \\ & + \Big[\partial_T - 1 + 2\partial_X^2\left(\partial_x^2 + q_0^2\right) + \left(2\partial_x\partial_X + \partial_Y^2\right)^2 \\ & + g_1\psi_0^2 - 3g_3(\partial_x\psi_0)^2\partial_x^2\Big]\psi_0 = 0, \quad \text{and}\end{aligned} \tag{2.38}$$

$$\begin{aligned}\epsilon^{\frac{7}{4}}: \quad & \left(\partial_x^2 + q_0^2\right)^2 \psi_5 + 2\left(\partial_Y^2 + 2\partial_x\partial_X\right)\left(\partial_x^2 + q_0^2\right)\psi_3 + \\ & \Big[\partial_T - 1 + 2\partial_X^2\left(\partial_x^2 + q_0^2\right) + \left(2\partial_x\partial_X + \partial_Y^2\right)^2 + 3g_1\psi_0^2\Big]\psi_1 + \partial_{T'}\psi_0 \\ & -2g_2\Big[(\partial_x\psi_0)(\partial_x^2\psi_0)(\partial_Y\psi_0) - (\partial_x\psi_0)^2(\partial_x\partial_Y\psi_0)\Big] \\ & -3g_3\Big[(\partial_x^2\psi_1)(\partial_x\psi_0)^2 + 2(\partial_x\psi_1)(\partial_x\psi_0)(\partial_x^2\psi_0)\Big] = 0.\end{aligned} \tag{2.39}$$

If we define

$$\begin{aligned}\psi_0 &= A_0(X,Y,T)e^{iq_0x} + A_0^*(X,Y,T)e^{-iq_0x}, \\ \psi_1 &= A_1(X,Y,T)e^{iq_0x} + A_1^*(X,Y,T)e^{-iq_0x}, \\ \psi_2 &= A_2(X,Y,T)e^{iq_0x} + A_2^*(X,Y,T)e^{-iq_0x}, \quad \text{and} \\ \psi_3 &= A_3(X,Y,T)e^{iq_0x} + A_3^*(X,Y,T)e^{-iq_0x},\end{aligned} \tag{2.40}$$

then (2.34-2.37) are satisfied. Now we will need to set the coefficients of the secular terms to zero. Secular terms are solutions to (2.34) and are of the form $e^{\pm iq_0x}$, as in (2.40). These secular terms can arise in the driving parts at each order above the lowest one. The driving parts are those parts in the ϵ expansion that are not of the lowest order form (i.e., $(\partial_x^2 + q_0^2)^2$). Because of the nonlinearity in our equations, these secular terms act as resonant driving terms at higher order and lead to non-periodic solutions which grow with time. As a result, we impose a solvability condition,

to require that the driving part of our higher order equations does not drive an eigenvector of the harmonic part with zero eigenvalue. We discuss the mathematics behind solvability conditions in Appendix 4.C. For the cases we simply set the driving terms to zero after substituting in (2.40). We find that (2.38) and (2.39) result in the only nontrivial equations. We obtain

$$\left[-\partial_T + 1 - \left(2iq_0\partial_X + \partial_Y^2\right)^2 - 3\left(q_0^4 g_3 + g_1\right)|A_0|^2\right] A_0 = 0 \tag{2.41}$$

and

$$\begin{aligned}\partial_{T'} A_0 = &\left[-\partial_T + 1 - (2iq_0\partial_X + \partial_Y^2)^2 - 6(g_1 + q_0^4 g_3)|A_0|^2\right] A_1 \\ &-3(g_1 + q_0^4 g_3)(A_0^2)(A_1)^* - 4iq_0^3 g_2(|A_0|^2\partial_Y A_0 + A_0^2\partial_Y A_0^*).\end{aligned} \tag{2.42}$$

If we now make the following scalings:

$$\begin{aligned} g_0 &= 3\left(q_0^4 g_3 + g_1\right), \\ \xi_0^2 &= 4q_0^2, \\ \tilde{A}_0 &= \sqrt{g_0}A_0, \quad \tilde{A}_1 = \sqrt{g_0}A_1, \\ \partial_{\tilde{X}} &= \xi_0\partial_X, \quad \partial_{\tilde{Y}} = \left(\frac{\xi_0}{q_0}\right)^{1/2}\partial_Y, \quad \text{and} \\ \tilde{g}_{\text{cor}} &= 4q_3^3 g_2\left(\frac{q_0}{g_0^2\xi_0}\right)^{1/2}, \end{aligned} \tag{2.43}$$

we then obtain our amplitude equations (where we set $\tilde{T} = T, \tilde{T}' = T$ just to have a consistent set of notation):

$$\partial_{\tilde{T}}\tilde{A}_0 = \tilde{A}_0 + (\partial_{\tilde{X}} - (i/2)\partial_{\tilde{Y}}^2)^2\tilde{A}_0 - |\tilde{A}_0|^2\tilde{A}_0 \tag{2.44}$$

and

$$-\partial_{\tilde{T}}\tilde{A}_1 + \tilde{A}_1 + (\partial_{\tilde{X}} - \tfrac{i}{2}\partial_{\tilde{Y}}^2)^2\tilde{A}_1 - 2|\tilde{A}_0|^2\tilde{A}_1 - \tilde{A}_0^2\tilde{A}_1^* = \partial_{\tilde{T}'}\tilde{A}_0 + i\tilde{g}_{\mathrm{cor}}\tilde{A}_0\partial_{\tilde{Y}}(|\tilde{A}_0|^2). \tag{2.45}$$

These agree with (4.13) and (4.14).

We will reserve comment on (2.45) until Section 4.3, since this equation contains our new rotation terms on the right-hand side. Equation (2.44) highlights many of the features of the systems we seek to describe with amplitude equations: (a) the growth of a perturbative state from the spatially uniform state, (b) the effect of modes with wave vectors near the critical wave vector, and (c) the saturation of this growth by nonlinearity.

We can demonstrate these features by assuming our amplitude $\tilde{A}_0$ has the following dependence:

$$\tilde{A}_0(\tilde{X}, \tilde{T}) = \sum_{\tilde{k}} a_{\tilde{k}} e^{\gamma_{\tilde{k}}\tilde{T} + i\tilde{k}\tilde{X}}. \tag{2.46}$$

The variable $a_{\tilde{k}}$ represents the amplitude of each mode, $\gamma_{\tilde{k}}$ is the growth rate, and $\tilde{k}$ represents the difference in the wave number for that particular mode as referenced to the critical value q_0, i.e., $\tilde{k} = C(q - q_0)$, where q is the absolute wave number of the mode and C is some constant. When (2.46) is substituted into (2.44) and only the linear terms are kept, we obtain a growth rate for each individual mode:

$$\gamma_{\tilde{k}} = 1 - \tilde{k}^2. \tag{2.47}$$

When converted to unscaled variables using (2.43) and the ϵ dependence is added back in, this becomes

$$\gamma_k = \epsilon - (\xi_0 k)^2 . \tag{2.48}$$

Hence, one obtains the maximum growth rate for $k = 0$, the critical wave number, and a range of stable modes for $\epsilon > 0$. An example is plotted in Figure 2.5. Any

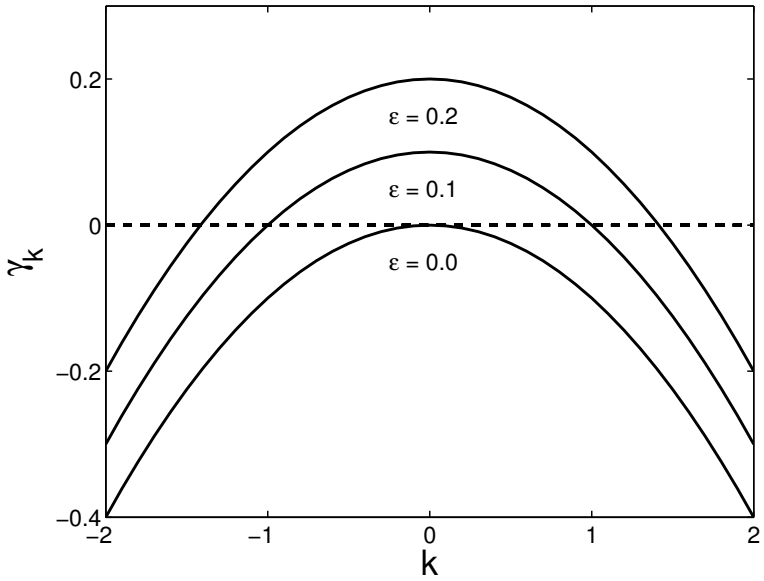

Figure 2.5: Growth rate γ_k as a function of k as given by (2.48) for a ξ_0 of 0.32.

wave number with a positive growth rate is a stable solution at that particular ϵ. If we assume only one mode, k, then we can simply add in the nonlinearity from (2.44) to obtain (in the scaled variables)

$$\gamma_k a_k = \left(1 - k^2\right) a_k - a_k^3, \tag{2.49}$$

and hence the growth rate will become zero when $a_k = \sqrt{1 - k^2}$. The real situation with a number of modes is much more complicated, but this simple case demonstrates how the nonlinearity saturates mode growth.

2.3.2 Code Verification

We can use the amplitude equation (2.44) for code verification by comparing amplitudes and Nusselt numbers computed by the code with those predicted by the amplitude equation (of course very near threshold).

We will use a simulation of a Rayleigh-Bénard convection cell with mixed boundaries, rigid (2.24) in the y direction and periodic (2.26) in the x direction. We have selected 64 elements, a dx of 0.06, and a dt of 0.005. We run the simulations with a

Prandtl number of 0.93. We will use one simulation with rotation[2] $\Omega = 17.6$ and aspect ratio 10.5896×10, and one without rotation $\Omega = 0$ and aspect ratio 10.0692×10. In both cases we choose the aspect ratio so that an integral number of rolls fits in the x direction at the critical wave number for that Ω ($q_0 = 3.56$ and 3.12, respectively).

For our numerical simulations, we compute the Nusselt number by finding the heat transported out of the cell:

$$\mathcal{N}_{\text{num}} = \frac{\int \nabla T \cdot \mathbf{dA}}{\int \hat{n} \cdot \mathbf{dA}} - 1, \tag{2.50}$$

where $\mathbf{dA}$ is an area element of the top surface whose normal is parallel to the direction of heat transport $\hat{n}$. For the nonrotating case, we wait until the rolls relax to a steady-state solution. Then we compute the Nusselt number and find the maximum amplitude achieved in the cell. For the rotating case, we find the amplitude by demodulating the mid-plane temperature data (removing the fast wave vector). We select the amplitude in the center of the cell. Since this value changes in time, we take the largest amplitude and the corresponding Nusselt number achieved in the center of the cell early on, before effects such as roll rotation become important.

For theoretical comparison, we find the amplitude by solving the amplitude equation (2.44) (or equivalently (4.13)), assuming that there is no variation in the amplitude in the slow $\tilde{X}$-direction, and only in the slow $\tilde{Y}$-direction. Then we convert to unscaled variables by using (4.28) and (4.225). We must use the coefficients corresponding to the specific parameters in our simulations (Table 4.1 for the rotating case and Section 4.A.7.1 for the non-rotating case). We compute the Nusselt number from the solved amplitude a_0 by

$$\mathcal{N}_{\text{amp}} = \frac{\int a_0^2 \, dy}{\int dy}. \tag{2.51}$$

We plot the results for the nonrotating case in Figure 2.6a for amplitude and Figure 2.6b for Nusselt number, and we plot the the corresponding results for the

[2]This is the same case as that used in Section 4.3.1

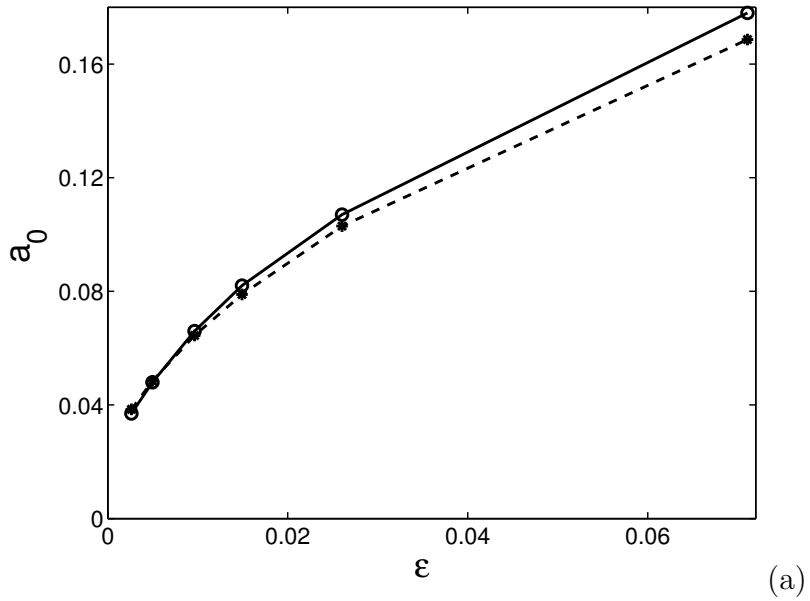

(a)

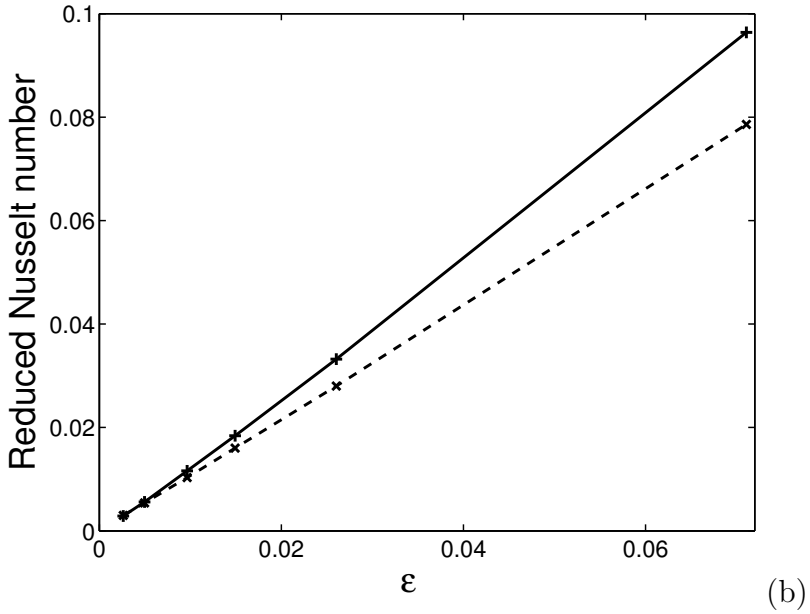

(b)

Figure 2.6: Comparison of (a) Amplitude a_0 versus ϵ and (b) Reduced Nusselt number versus ϵ for the following parameters: $\Gamma = 10.0692 \times 10$, $\sigma = 0.93$, and $\Omega = 0$, partially conducting boundaries. Legend: solid line = results from amplitude equation, dotted line = results from numerical simulations. Note that the lines are just a guide to the eye.

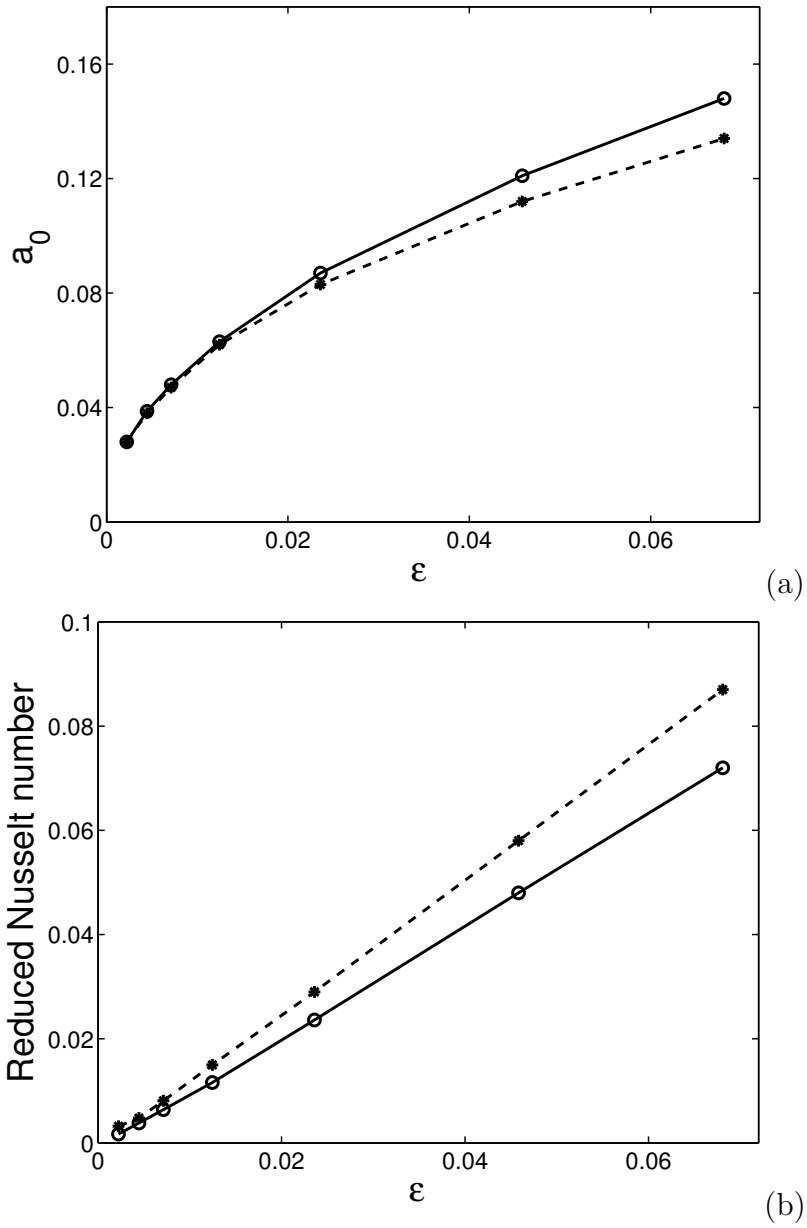

Figure 2.7: Comparison of (a) Amplitude a_0 versus ϵ and (b) Reduced Nusselt number versus ϵ for the following parameters: $\Gamma = 10.5896 \times 10$, $\sigma = 0.93$, and $\Omega = 17.6$, partially conducting boundaries. Legend: solid line = results from amplitude equation, dotted line = results from numerical simulations. Note that the lines are just a guide to the eye.

rotating case in Figure 2.7a and Figure 2.7b. We see that the amplitudes are in good agreement for small ϵ, but not for larger ϵ. The Nusselt number agreement is worse than the amplitude agreement, which is expected since the Nusselt number is proportional to the square of the amplitude. For the Nusselt number plot, as $\epsilon \to 0$, the slope seems to agree well. We compare the amplitude profiles for the rotating case in Figures 4.5 and 4.7.

2.4 Computation of Lyapunov Exponents

Spatiotemporal chaos in Rayleigh-Bénard convection was discovered by Ahlers and Beringer [2], Maurer and Libchaber [75], and Gollub and Benson [46]. In 1978, Ahlers and Behringer reported that as the control parameter ϵ (defined in (2.21)) was increased, they found a transition to aperiodic time dependence in heat transport measurements of cylindrical Rayleigh-Bénard convection cells for a variety of aspect ratios. They also noted that as the aspect ratio Γ (defined in (2.19)) was increased, the critical value of R for this transition decreased. Maurer and Libchaber studied rectangular convection cells and discovered frequency-locking followed by a period doubling cascade to chaos as ϵ was increased. They also observed hysteresis in these systems. Gollub and Benson performed visualizations on rectangular convection cells and found many of the signatures of chaos, including period-doubling bifurcations, entrainment, and intermittency. These three works provided strong evidence that Rayleigh-Bénard convection systems were chaotic for certain parameters. However, the Lyapunov exponents for experimentally realistic systems have never been computed. We will show that these systems are indeed chaotic in the sense of having a positive Lyapunov exponent [98]. We also investigate the associated Lyapunov eigenvector. We describe our computational methods here and will report our results in Chapter 7.

The leading order Lyapunov exponent is defined as the measure of the exponential stretching of the nearby trajectories $\mathbf{y}(t)$ and $\mathbf{y}(t) + \delta\mathbf{y}(t)$. We define $\mathbf{y}(t) = [\mathbf{u}, \theta]$ as the four $\times N$ dimensional array describing the state of the N fluid elements as a

function of time and $\delta\mathbf{y}(t) = [\delta\mathbf{u}(t), \delta\theta(t)]$ as the corresponding perturbation field. The pressure P can be determined from $\mathbf{y}$, and the perturbation pressure δP can be determined from $\delta\mathbf{y}$. If two states of the fluid differed initially by the small amount $\delta\mathbf{y}(0)$, then we can track the evolution of the perturbation by the linearized equations

$$\frac{d\delta\mathbf{y}}{dt} = \mathbf{J}(\mathbf{y}(t))\delta\mathbf{y}, \tag{2.52}$$

where $\mathbf{J}$ is the Jacobian of the system. If we define the full field evolution equations (2.16)-(2.18) as $d\mathbf{y}(t)/dt = \mathbf{F}(\mathbf{y})$, then $\mathbf{J} = \delta\mathbf{F}/\delta\mathbf{y}$. In our case, the specific equations are (for Coriolis force only)

$$\begin{aligned}
\sigma^{-1}\left[\left(\partial_t + \mathbf{u}\cdot\nabla\right)\delta\mathbf{u} + (\delta\mathbf{u}\cdot\nabla)\mathbf{u}\right] &= -\nabla\delta P + \nabla^2\delta\mathbf{u} + \delta\theta\hat{z} + 2\Omega\delta\mathbf{u}\times\hat{z}, && (2.53)\\
\left(\partial_t + \mathbf{u}\cdot\nabla\right)\delta\theta + (\delta\mathbf{u}\cdot\nabla)\theta &= \nabla^2\delta\theta + R\delta w, \quad \text{and} && (2.54)\\
\nabla\cdot\delta\mathbf{u} &= 0. && (2.55)
\end{aligned}$$

The leading Lyapunov exponent λ_1 is then defined as [120, 44, 37, 38, 50]

$$\lambda_1 = \lim_{t\to\infty}\frac{1}{t}\ln\left(\frac{\|\delta\mathbf{y}(t)\|}{\|\delta\mathbf{y}(0)\|}\right), \tag{2.56}$$

where the normalization is defined over the interior volume V as

$$\|\delta\mathbf{y}(t)\| = \sqrt{\frac{1}{V}\int_V \left[R_c\delta\mathbf{u}(t)^2 + \sigma\delta\theta(t)^2\right]\, dV}. \tag{2.57}$$

We have chosen the above normalization to be consistent with the inner product used by Cross [30] in his analytical work, although the result for λ_1 should be independent of the choice of normalization since (2.56) is a ratio of lengths at different times.

Likewise, the instantaneous leading Lyapunov exponent is defined as [39, 60]

$$\lambda_1^{\text{inst}} = \frac{d}{dt}\ln\left(\frac{\|\delta\mathbf{y}(t)\|}{\|\delta\mathbf{y}(0)\|}\right). \tag{2.58}$$

The above quantity is useful for studying how λ_1 varies over short time intervals.

If the system is truly chaotic, the perturbation $\delta\mathbf{y}$ will grow exponentially fast; hence it must be renormalized after a certain amount of time Δt to avoid overflow errors. If we call that normalization $\|\delta\mathbf{y}(\Delta t)\|$, then the evolution of the perturbation field can be rewritten as [85]

$$\delta\mathbf{y}(t) = \left(\prod_{j=1}^{k} \|\delta\mathbf{y}(j\Delta t)\| \right) \delta\mathbf{y}(0) \tag{2.59}$$

for $t = k\Delta t$. By inserting (2.59) into (2.56) and (2.58) we find

$$\lambda_1 = \lim_{t\to\infty} \frac{1}{t} \sum_{j=1}^{k} \ln \|\delta\mathbf{y}(j\Delta t)\| \quad \text{and} \tag{2.60}$$

$$\lambda_1^{\text{inst}} = \frac{d}{dt} \sum_{j=1}^{k(t)} \ln \|\delta\mathbf{y}(j\Delta t)\|. \tag{2.61}$$

Hence, the running sum of the logarithm of the normalization gives us a means of finding both λ_1 and λ_1^{inst}. In practice we computed the quantity we define as S_λ:

$$S_\lambda = \ln \left(\frac{\|\delta\mathbf{y}(t)\|}{\|\delta\mathbf{y}(0)\|} \right) \quad \text{and}$$

$$S_\lambda = \sum_{j=1}^{k} \ln \|\delta\mathbf{y}(j\Delta t)\|. \tag{2.62}$$

The slope of S_λ versus time gives an approximate value for λ_1 and the derivative of S_λ versus time is λ_1^{inst}. We find this quantity to be more fundamental and useful than either λ_1^{inst} or λ_1.

We find λ_1 and λ_1^{inst} by numerically integrating the full fields (2.16)-(2.18) concurrently with the perturbation fields (2.53)-(2.55). We start the initial conditions for the full fields as small, random values, and for the perturbation field as random values as well. Then we compute S_λ from (2.62). Typically we choose Δt to be twenty time steps. Also, we have computed the derivative in (2.61) by using a first order finite difference method.

The Lyapunov eigenvector is the quantity $\delta\mathbf{y}(t)$ just after being normalized by $\|\delta\mathbf{y}(\Delta t)\|$. We plot this field after being scaled to have unit norm, so we can compare

the structure of the eigenvector, and not its absolute size.

2.5 Lagrangian Particle Tracking

We also have developed numerical techniques to compute particle trajectories, inspired by Hassan Aref's [4] concept of chaotic advection. By considering the stream function ψ (4.65) of a two-dimensional fluid as a Hamiltonian equation, Aref showed that the x and y positions of the particles are canonically conjugate variables:

$$\dot{x} = -\frac{\partial \psi}{\partial y} \quad \text{and} \quad \dot{y} = \frac{\partial \psi}{\partial x}. \tag{2.63}$$

Hence, the appropriate phase space of canonically conjugate variables for a two-dimensional fluid is its real space. We will analyze particle trajectories for large aspect ratio, three-dimensional rotating Rayleigh-Bénard convection to investigate three-dimensional generalizations of this mapping onto Hamiltonian and Lagrangian systems.

We also investigate rotating Rayleigh-Bénard convection as a physical application of the blinking roll model of chaotic advection presented by Mullowney et al. [79]. In the blinking roll model of chaotic advection, a three-dimensional model state consisting of parallel rolls is replaced aperiodically by a set of rolls at an orthogonal orientation. Particles have been shown to mix well (i.e., explore the entire available real space) in such a blinking roll state. We report our results in Chapter 8.

We track individual particles by computing

$$\frac{d\mathbf{x}}{dt} = \mathbf{v}(x, y, z, t), \tag{2.64}$$

making sure to update the velocity at each time step by interpolation. Because of the type of interpolants used (Gauss-Lobatto-Legendre), this interpolation is nontrivial for a cylindrical mesh such as the one shown in Figure 2.1. As a result, we perform our particle tracking for periodic geometries only.

Chapter 3

Traveling waves in rotating Rayleigh-Bénard convection: Analysis of modes and mean flow

3.1 Introduction

For certain choices of the parameters in rotating convection, traveling wave wall modes have been found experimentally [121, 83, 72, 5] and studied theoretically [68, 28, 45, 53, 55, 91]. Theoretically this system has been well-modeled near threshold by an amplitude equation known as the Complex Ginzburg-Landau equation (CGLE). However, the nonlinear theories have assumed either free slip boundary conditions and semi-infinite geometries [68, 55, 53], or no-slip boundary conditions with periodic boundary conditions [28]. A recent theoretical analysis [91] has used realistic no-slip boundary conditions but still neglects curvature effects. Here [100] we use numerical simulations with no-slip boundary conditions and finite annular geometries, with the same parameters that experimenters have used [72]. We compute the coefficients of the CGLE and compare with previous experimental and theoretical results. Mean flows are also computed and found to be more significant as the Prandtl number decreases (from $\sigma = 6.4$ to $\sigma = 1$). In addition, the mean flow around the outer radius of the annulus appears to be correlated with the mean flow around the inner radius.

We are interested in computing the coefficients for the CGLE, because for certain

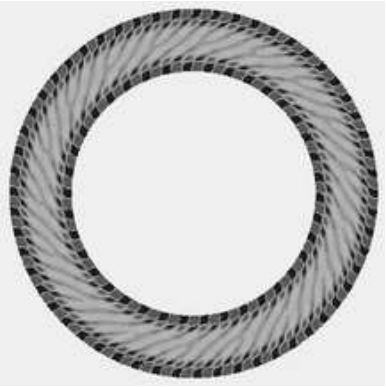

(a)

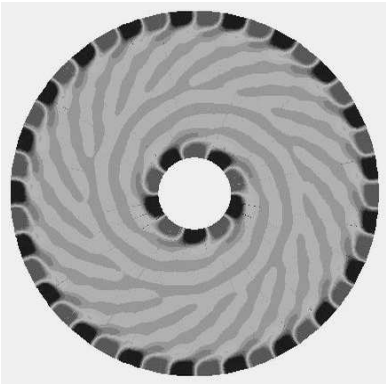

(b)

Figure 3.1: Snapshot of temperature T at the midplane for traveling wave wall modes with the following parameters: $\sigma = 6.4$ and either (a) inner radius = 10, outer radius = 15, $\epsilon = 0.017$, $\Omega = 70$, and $t = 37$ or (b) inner radius = 1, outer radius = 5, $\epsilon = 0.13$, $\Omega = 274$, and $t = 3$. The lightest grey in the center of the annular region denotes the conduction value ($T = 0.5$), and darker grey scale deviations give the values above and below this, which range from $T = 0.49$ to 0.51 for (a), and 0.45 to 0.55 for (b). Note that the inner and outer waves are counterpropagating.

values of the coefficients, the CGLE exhibits spatiotemporal chaos [53]. We would like to determine which, if any, parameters for the traveling wave wall modes of rotating Rayleigh-Bénard convection would cause the system to bifurcate to a chaotic regime as had been predicted by van Hecke [52].

We have performed our numerical simulations of the Boussinesq equations using the parallel, spectral element code described in Section 2.2. We used our usual boundary conditions for the top and bottom plates (2.23) and insulating boundaries (2.25) along the sidewalls.

As the Rayleigh number is increased, for large enough rotation rates, the conduction profile gives way to a traveling wave state localized along the walls. See Figure 3.1 for examples. In the rotating frame, the inner and outer waves are counterpropagating, and the outer wave moves in the opposite direction of the rotation. As the Rayleigh number is increased even higher, this wall mode transitions to a bulk mode. In the case of zero rotation rate, patterns seen were similar to the results from simulations done by Sensoy and Greenside [104].

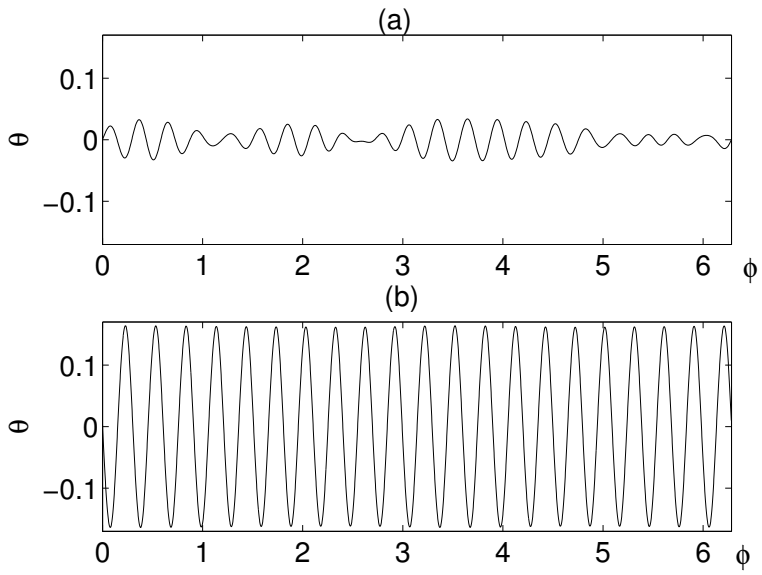

Figure 3.2: Temperature deviations θ as a function of angle ϕ at fixed outer radius for (a) t = 0.8 and (b) t =3.44. The following parameters were used: inner radius = 1, outer radius = 5, $\sigma = 6.4$, $\epsilon = 0.13$, and $\Omega = 274$.

3.2 Complex Ginzburg-Landau Equation

The wall mode is useful to study because, for a large enough separation between inner and outer wall, the waves are mostly decoupled. Therefore, the outer wave (or inner) can be treated essentially as having only one spatial dimension. For all our cases, we analyzed the outer wave unless otherwise specified.[1] See Figure 3.2 for examples of temperature versus angle data at fixed outer radius.

Near threshold, we can model this system with an amplitude equation [68]. We set the temperature deviation $\theta = T - T_o$ (where $T_o(z)$ is the linear conduction profile) to be equal to

$$\theta(\phi, r, z, t) = A(\phi, t) \exp\left(i\left[q_c r_o \phi - \omega_c t\right]\right) \chi(r, z), \tag{3.1}$$

where q_c is the critical wavenumber (i.e., the wavenumber at the onset of convection),

[1]Since the traveling waves have a decay length of the order of the depth of the fluid d, the inner and outer waves are decoupled for the annular geometries used. Runs were made with conducting temperature boundary conditions on the inner wall instead of insulating (which suppresses wall modes), and outer wave results were unchanged.

ω_c is the critical precession frequency, and r_o is the outer radius. The function $\chi(r,z)$ represents the decay into the bulk, which is obtained from a linear stability analysis. Note that we have used the convention that the wave number $q = \text{mode number}/r_o$, since the decay length into the bulk is rather short, i.e., on the order of the depth. We then expect the complex amplitude A to be described by the CGLE [116, 117, 3]:

$$\tau_o \left(\partial_t + s\,\partial_x\right) A = \epsilon \left(1 + i\,c_o\right) A + \xi_o^2 \left(1 + i\,c_1\right) \partial_{xx} A - g \left(1 + i\,c_3\right) |A|^2 A, \tag{3.2}$$

where ∂_x represents partial differentiation with respect to $x \equiv r_o\phi$ and ϵ is defined in (2.21). The coefficients τ_o, and ξ_o are the characteristic time and length scales, respectively. The coefficient s is the group velocity, g gives the normalization of the amplitude, and c_o is a constant that can be removed by transforming to a phase rotating frame. Since all the other coefficients can be scaled or transformed away, c_1 and c_3 essentially determine the behavior of the CGLE [52]. If $c_1 = c_3$ or c_1 and c_3 are small, the equation is in the relaxational limit, where the CGLE reduces to the real Ginzburg-Landau equation and steady patterns are seen. If $c_1\,c_3 + 1 < 0$, the Newell criterion is reached, and solutions to the CGLE enter a spatiotemporal chaotic regime.

3.2.1 Method of Determining the Coefficients

The temperature deviations $\theta(\phi)$ for a fixed radius r_o, depth z, and time t as shown in Figure 3.2 can be spatially demodulated by Fourier analysis. By choosing random initial conditions, one can cause a rather large number of modes to be present. The amplitude of each individual mode as a function of time is shown in Figure 3.3 for a representative case. At early times ($t \lesssim 0.75$), one can see the growth (decay) of stable (unstable) modes. After some time has elapsed ($t \approx 1.5$), the nonlinearities cause this growth to saturate.

We can take advantage of these individual modes to determine the CGLE coefficients. In Figure 3.4 we show the growth rates as a function of wave number for fixed ϵ, which were determined by taking the slopes of each of the mode curves in the linear

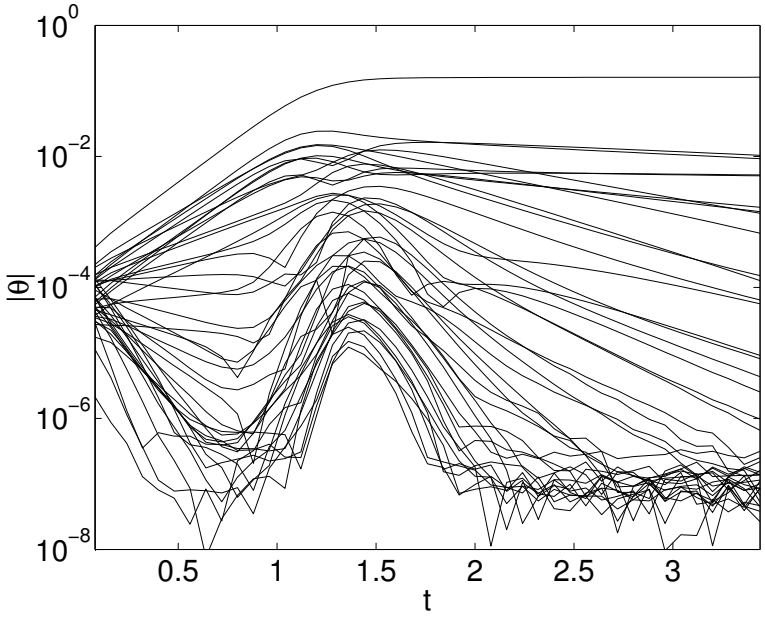

Figure 3.3: Amplitudes $|\theta|$ of individual modes (obtained by Fourier analysis) versus time. Only the modes that have significant amplitudes are plotted, which range from $r_o q = 2$ to 40 ($r_o q_c = 21$ here). The parameters are as in Figure 3.2. The largest amplitude mode corresponds to a mode number of 21.

regime. Only modes with significant growth rates or small decay rates are shown in Figure 3.4. By finding the roots of each of these curves, one can find the borders of the marginal stability diagram. This is shown in Figure 3.5. For wave numbers inside the dashed line, the uniform state will be unstable to wall modes.

In Figure 3.4 the curves squish together as $q \to 0$. This result is expected from the linearized, normal mode analysis of the Boussinesq equations [74]. The growth rate approaches a constant value as q approaches zero, independent of ϵ.

Likewise, the precession frequencies of each of the individual modes can be found from the rate of change of phase with respect to time (the phase is also obtained from Fourier demodulation of $\theta(\phi)$). Some representative cases are shown in Figure 3.6. The negative sign on the precession frequency indicates that it is retrograde.

We now assume that the complex amplitude can be written as the sum of individual modes [67]:

$$A(\phi, t) = \sum_k a_k e^{\gamma_k t + i(k r_o \phi - \omega_k t)}. \tag{3.3}$$

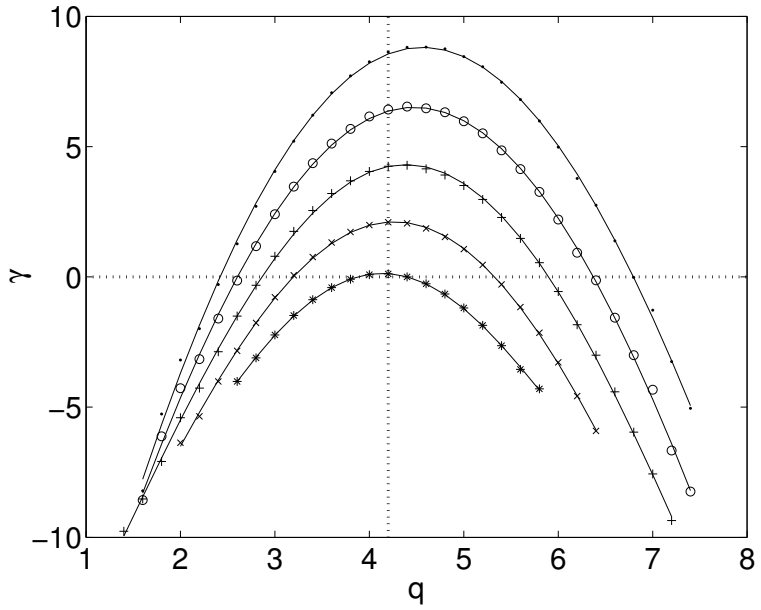

Figure 3.4: Growth rates γ as a function of wave number q for the parameters as in Figure 3.2. The markers correspond to the following values of ϵ: "$*$" = 0.003, "x" = 0.05, "+" = 0.10, "o" = 0.15, and "$\cdot$" = 0.21. The vertical dotted line is at $q = q_c = 4.2$ (i.e., $r_o q_c = 21$).

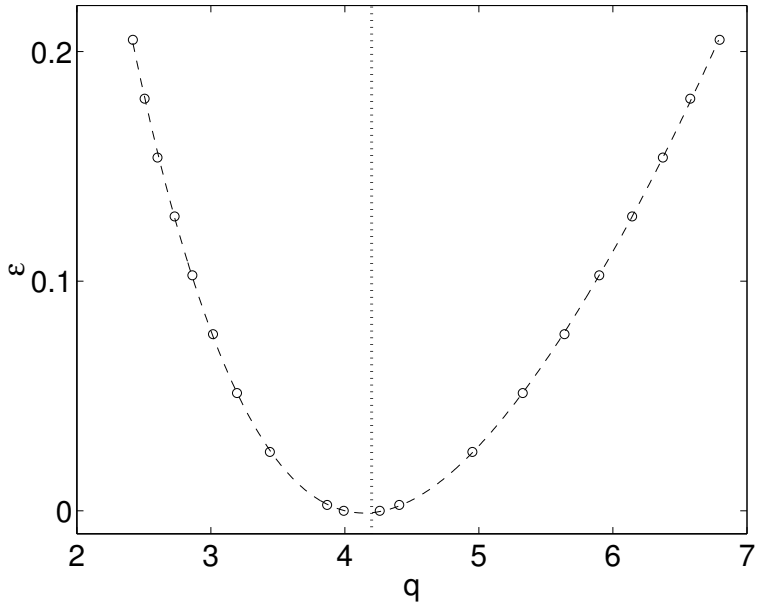

Figure 3.5: Marginal stability diagram for the parameters as in Figure 3.2. Data points were computed by finding the roots of the growth curves shown in Figure 3.4. The dashed curve is a fourth-order polynomial fit. The vertical dotted line is at $q = q_c = 4.2$.

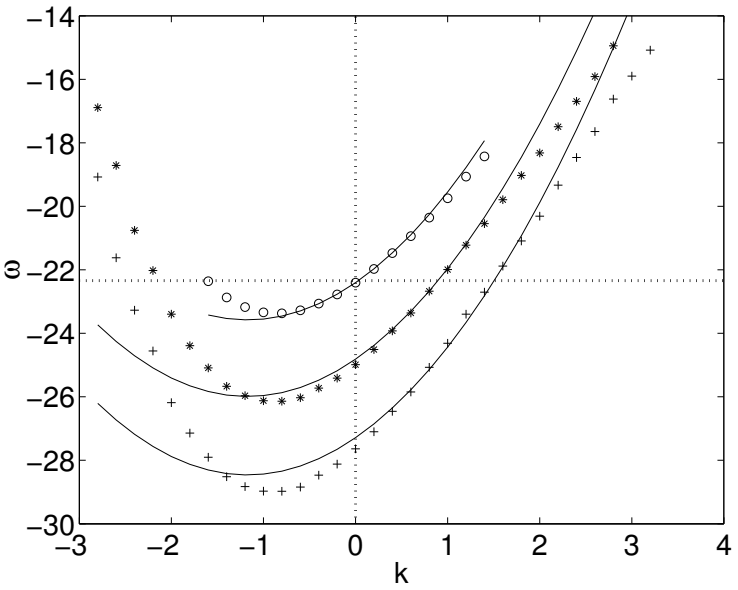

Figure 3.6: Precession frequency ω as a function of reduced wave number $k = q - q_c$, where q_c is the critical wave number (4.2 for this particular set of parameters—see Figure 3.2). The markers correspond to ϵ's: "o" $= 0.003$, "$*$" $= 0.10$, and "+" $= 0.21$. The curves shown are the fits to (3.5), where the values of the CGLE coefficients are given in Table 3.1.

The variable a_k represents the amplitude of each mode, γ_k is the growth rate, and k and ω_k represent the difference in the wave number and precession frequency for that particular mode as referenced to the critical values (q_c, ω_c). If these are substituted into (3.2) and linearized, one obtains for each individual mode (by equating real and imaginary parts)

$$\gamma_k = \tau_o^{-1}\left(\epsilon - \xi_o^2\, k^2\right) \quad \text{and} \tag{3.4}$$

$$\omega_k = s\, k + \tau_o^{-1}\left(-\epsilon\, c_o + \xi_o^2\, c_1\, k^2\right). \tag{3.5}$$

If we drop the subscripts and instead think of γ and ω as functions of k as well as ϵ, then we can compute all of the linear coefficients of the CGLE by taking various partial derivatives:

$$\frac{1}{\tau_o} = \left.\frac{\partial\gamma}{\partial\epsilon}\right|_{\epsilon=k=0}, \tag{3.6}$$

$$\xi_o^2 = -\frac{\tau_o}{2}\left.\frac{\partial^2\gamma}{\partial k^2}\right|_{\epsilon=k=0}, \tag{3.7}$$

$$s = \left.\frac{\partial\omega}{\partial k}\right|_{\epsilon=k=0}, \tag{3.8}$$

$$c_o = -\tau_o\left.\frac{\partial\omega}{\partial\epsilon}\right|_{\epsilon=k=0}, \quad \text{and} \tag{3.9}$$

$$c_1 = \frac{\tau_o}{2\xi_o^2}\left.\frac{\partial^2\omega}{\partial k^2}\right|_{\epsilon=k=0}. \tag{3.10}$$

Since we can calculate $\gamma(\epsilon, k)$ and $\omega(\epsilon, k)$ from (fourth-order) polynomial fits to the data (see Figure 3.4 and Figure 3.6), we can compute each of these coefficients.[2]

The nonlinear coefficients g, c_3 can be found by using initial conditions so that only a single mode (k_s) is excited. If the nonlinear terms are retained, the single mode versions of (3.4) and (3.5) are

$$\gamma = \tau_o^{-1}\left(\epsilon - \xi_o k_s^2 - g\,|a|^2\right) \quad \text{and} \tag{3.11}$$

$$\omega = s\,k_s + \tau_o^{-1}\left(-\epsilon\,c_o + \xi_o\,c_1\,k_s^2 + g\,c_3\,|a|^2\right). \tag{3.12}$$

If we are far enough into the nonlinear regime, we can set the growth rate to zero and determine g:

$$g = \left.\frac{\epsilon}{|a^2|}\right|_{\gamma=k_s=0}. \tag{3.13}$$

Likewise, if we eliminate g, we obtain

$$c_o - c_3 = -\tau_o\left.\frac{\partial\omega}{\partial\epsilon}\right|_{\gamma=\epsilon=k_s=0}. \tag{3.14}$$

[2]The characteristic length scale ξ_o can also be found from the marginal stability diagram, by noting that the boundaries of the stability diagram were found from setting the growth rate in equation (3.4) to zero: $\xi_o^2 = \frac{1}{2}\left.\frac{\partial^2\epsilon}{\partial k^2}\right|_{\gamma=k=0}$.

We use the normalization convention described in the Section 3.4. By combining (3.13) and (3.17), we can eliminate the amplitude and solve for g by simply looking at how the Nusselt number $\mathcal{N}$ scales with ϵ:

$$\mathcal{N} - 1 = \frac{c}{g}\epsilon. \tag{3.15}$$

The results are shown in Table 3.1 [3]. Agreement (except[4] for the value of g) with the theory that uses no-slip velocity boundary conditions [91] is very good, whereas there is understandably some disagreement with the theory that employed free-slip velocity boundary conditions [68]. We find only partial agreement with experimental results. However, the coefficients are all extremely sensitive to the fit, as can been seen in Figure 3.6. Representative data for precession frequency are plotted along with a fit to the linearized CGLE (3.5), with the values of the coefficients given in Table 3.1. The fits are good only very close to threshold (small ϵ and small k). Higher-order corrections to the CGLE would improve the fits, as was appropriately explored in [72].

3.3 Mean Flow

Here we explore the role mean flow plays in rotating convection. Theoretically, one expects mean flow to be important for multiply-connected domains like an annulus [91, 92]. Mean flow in non-rotating convection arises from large-scale variations in local wave number and amplitude, which cause non-local pressure gradients [82, 34]. For rotating convection, the traveling wave propagation will also drive a mean flow [107].

We calculated the total mean flow for our system by performing an average of the

[3]Since we have a finite system and have defined qr_o = mode number, a change in r_o (say of order 1/2 the penetration depth) would cause a 10% change in q_c, ξ_o, and s. All other coefficients would be unaffected.

[4]We cannot explain this discrepancy. Our reduced Nusselt numbers for a given ϵ are about half as big as the data quoted by Liu and Ecke [72] on page 4093. Our Nusselt number versus ϵ calculations do agree to within 4% of Behringer and Ahler's results [11] for a nonrotating cell of aspect ratio 4.72 near threshold.

Table 3.1: CGLE coefficients for the system parameters given in Figure 3.4. Comparisons are made with experiment (LE = Liu and Ecke [72]) and theory (KC = Kuo and Cross [68], and P = Plaut (Table I from [91])). Also note we found $c_0 = 0.60, c_1 = 0.44$, and $c_3 = 0.12$.

	Present Work	LE	KC	P
R_c	19500	20850	19500	19660
q_c	4.2	4.65	4.00	4.22
ω_c	-22.3	-22.0	-24.0	-22.4
τ_o	0.025	.03	0.026	0.025
ξ_o	0.22	0.179	0.24	0.21
s	2.0	2.65	2.22	1.91
g	1.63	0.74	1.11	0.53
$\tau_o^{-1}(c_o - c_1)$	6.4	4.2	14.4	6.40
$\tau_o^{-1}(c_o - c_3)$	19.3	20.4	19.2	19.7

horizontal velocity $\mathbf{u}_\perp = (u_r, u_\phi)$ over the depth and the radius:

$$\langle \mathbf{u}(\phi, t) \rangle_{r,z} = \int_{r_{\text{in}}}^{r_{\text{out}}} dr \int_0^1 dz \, \mathbf{u}_\perp(r, \phi, z, t). \tag{3.16}$$

Often it is useful to separate the mean flow for the inner and outer waves by performing the radial average only to the radius half-way between the inner and outer radii. Because the traveling waves decay exponentially into the bulk, these half-averaged mean flows are a good measure of the inner and outer mean flows. For our traveling wave trials (when the inner and outer waves are decoupled), the mean flow is observed to be in the same direction as the phase velocity of the waves, so the outer mean flow is retrograde, and the inner flow is in the same direction as the rotation.

Results for various geometries and parameters are shown in Table 3.2. Mean flow is present in all cases, but it becomes more significant for smaller Prandtl number. Also, the ϕ-component of total mean flow (3.16) is non-zero but decreases as the aspect ratio increases. This result indicates that the total tangential mean flow is due to the fractional difference in radii between the inner and outer waves, and the total tangential mean flow should become zero as the aspect ratio goes to infinity.

Table 3.2: Tangential mean flow results. The fluctuating components in the ϕ direction (see Figure 3.7) have been averaged over for inner and outer mean flows. The velocities are scaled by α as defined in (3.19). The root mean square convection velocity u_{rms} is given in the last column. In all cases, traveling waves were stable, and random initial conditions were used.

$r_{\text{in}}, r_{\text{out}}$	R	Ω	σ	t	$\alpha\langle u_\phi\rangle_{z,r,\phi}$ inner half	$\alpha\langle u_\phi\rangle_{z,r,\phi}$ outer half	$\alpha\langle u_\phi\rangle_{z,r}$ total	u_{rms}
1,5	23500	274	6.40	3.0	0.334	-0.448	-0.114	2.774
1,5	23500	274	1.00	3.0	0.650	-0.918	-0.268	3.194
10,15	23500	274	6.40	3.0	0.423	-0.438	-0.015	2.702
10,15	23500	274	1.00	3.0	0.820	-0.875	-0.055	3.026
10,15	6500	70	6.40	12.0	0.205	-0.220	-0.015	2.340

The last line of Table 3.2 corresponds to an ϵ of 0.08 and is included for comparison with Plaut's theoretical calculations shown in Figure 5 of [91]. The parameters used in [91] are: $\Omega = 100, \sigma = 6.3, \epsilon = 0.1$, and $r_{\text{out}} - r_{\text{in}} = 3$. If we radially average the azimuthal component of the large-scale mean flow data over the outer half of the geometrical domain used in [91], we obtain a value of approximately -0.4. This agrees to within 5% of our value for the outer half mean flow if we take into account the scaling discrepancy in g from Table 3.1 and, hence, α in equation (3.19).

The outer and inner wave tangential mean flows have small fluctuating components in the angular coordinate, as seen in Figure 3.7. These components are equal and opposite, as they must be to satisfy incompressibility. Thus, the tangential component of the *total* mean flow $\langle u_\phi\rangle_{r,z}$ is independent of the angular coordinate ϕ. The presence of these fluctuations indicates that the outer and inner mean flows are correlated. The fluctuations are not seen when only a single mode is present (obtained by starting with initial conditions resembling the desired mode). Defects and large-scale wave number variations are thought to be a reason for the mean flow correlations.

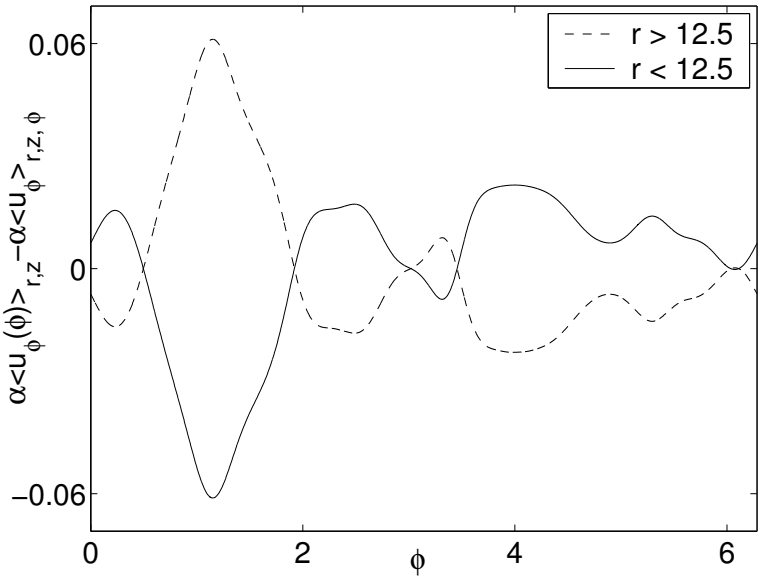

Figure 3.7: Tangential mean flow averaged over the outer (or inner) half of the annulus, where the average over the angular coordinate ϕ has been subtracted for ease of comparison (see Table 3.2 for these averages). Data is for inner radius = 10, outer radius = 15, $\sigma = 1.0$, $R = 23500$, $\Omega = 274$, and $t = 3$.

3.4 Scaling

The magnitude of the amplitude $|A|$ depends on the choice of normalization for the linear mode $\chi(r, z)$. Typically, the scaling of the amplitude is defined so that the Nusselt number $\mathcal{N}$ is proportional to the amplitude squared $|A|^2$:

$$\mathcal{N} - 1 = |A|^2 c. \tag{3.17}$$

The Nusselt number is the ratio of the total heat flux to the heat flux in the conduction regime. For the nonrotating case, since the convection extends over the whole cell, c is chosen to be unity. In the case of traveling waves, the convention has been to use a scale factor c corresponding to the ratio of the area occupied by the waves to the total area of the cell [72], so we define our proportionality constant c to be

$$c = \left(\frac{(2r_{\text{out}} - 1) + (2r_{\text{in}} + 1)}{r_{\text{out}}^2 - r_{\text{in}}^2} \right), \tag{3.18}$$

where we have estimated the penetration of the wave in the radial direction to be 1 (in depth units). As a result, we can define a scaling constant:

$$\alpha = \sqrt{\left.\frac{\mathcal{N}-1}{c|A|^2}\right|_{t\to\infty}}. \tag{3.19}$$

3.5 Conclusions

Traveling wave wall states were observed in numerical simulations of the Boussinesq equations with rotation for experimentally realistic geometries and boundaries. The CGLE coefficients were computed and agree (except for the value of g) with experiment and theory. So far the coefficients found have been close to the relaxational limit (c_1, c_3 small), where coherent patterns are expected. We searched extensively in the parameter range where van Hecke and van Saarloos suggest chaotic dynamics exist [53], that is where $c_1 c_3 < -1$, but we were unable to achieve this criterion for our coefficients. It was suggested by Plaut [91] that van Hecke's calculations did not incorporate the mean flow correctly.

Mean flow was also calculated and seen to be significant for a rotating annulus which supports Plaut's conclusions. Mean flow correlations were observed, which provide a long-range coupling between inner and outer waves that otherwise would be exponentially small.

The mean flow correlations may be useful in understanding the interesting square patterns observed by Sánchez-Álvarez et al. [96] for large rotation rates ($170 < \Omega < 274$) and $0.7 < \sigma < 6.4$ in the region where domain chaos is expected to coexist with traveling waves. An example of such a pattern is shown in Figure 1.1b. The authors suggest that the interaction of the wall mode with the bulk is responsible for the square patterns and that this is not a new instability in the bulk for those parameters.

Chapter 4

The Amplitude Equation for Rotating Rayleigh-Bénard Convection

4.1 Introduction

Dislocations which are stationary in a non-rotating Rayleigh-Bénard convection system will glide in a rotating system. The results from our simulations clearly demonstrate this, as shown in Figures 5.13 and 5.14. These results were not predicted by the amplitude equation at the order derived by Küppers and Lortz. As a result we have derived the amplitude equation for rotating Rayleigh-Bénard convection from the full equations (2.16, 2.17, 2.18) with realistic boundary conditions (2.23) up to higher order [97]. For a specific set of parameters, we will use the new higher order terms in the amplitude equation to compute dislocation glide as well as mean flow and wall induced precession (another phenomenon the new terms predict), and compare to our numerical results. We find we get good agreement very near threshold.

We will only include the Coriolis term (2.14) and neglect the centrifugal term (2.15). We will address the centrifugal term in Chapter 6. See Section 2.3 for an introduction to our perturbation methodology and how it is used to derive amplitude equations. Deriving the amplitude equation to higher order for rotating Rayleigh-Bénard convection for no-slip boundary conditions is very involved. As a result, we have included the details in Appendix 4.A. This appendix is only suggested for

those wishing to duplicate our calculations. The other appendices are suggested even for the general reader. For example, Appendix 4.B explains our method of treating mean flow, Appendix 4.C discusses solvability conditions, Appendices 4.D and 4.E discuss useful relations derived from invariances, and Appendix 4.F discusses our normalization condition. Also note that the numerical simulations used in this chapter for comparison to our amplitude equation results are discussed in more detail in Chapter 5.

4.2 Multiple Scales Analysis

We can write[1] (2.16, 2.17, 2.18) in a more transparent form, if we assume the operator notation

$$LV = N, \tag{4.1}$$

where

$$V = \begin{bmatrix} u \\ v \\ w \\ \theta \\ P \end{bmatrix}, \tag{4.2}$$

$$L = \begin{bmatrix} \nabla^2 & 2\Omega & 0 & 0 & -\partial_x \\ -2\Omega & \nabla^2 & 0 & 0 & -\partial_y \\ 0 & 0 & \nabla^2 & 1 & -\partial_z \\ 0 & 0 & R & \nabla^2 & 0 \\ \partial_x & \partial_y & \partial_z & 0 & 0 \end{bmatrix}, \tag{4.3}$$

[1]To be consistent with the literature, we choose the formulation of the Boussinesq equations which includes the temperature deviation θ instead of the temperature T.

and

$$N = \begin{bmatrix} \sigma^{-1}\left(\partial_t + \mathbf{u}\cdot\nabla\right)) \\ \sigma^{-1}\left(\partial_t + \mathbf{u}\cdot\nabla\right)) \\ \sigma^{-1}\left(\partial_t + \mathbf{u}\cdot\nabla\right)) \\ \left(\partial_t + \mathbf{u}\cdot\nabla\right)) \\ 0 \end{bmatrix}. \tag{4.4}$$

In this manner L is not self-adjoint, but it is somewhat easy to find the adjoint (see Appendix 4.C).

We will separate out fast (x, z) and slow (X, Y, T, T') scales by the following replacements as was done in (2.31):

$$\partial_x \to \partial_x + \epsilon^{\frac{1}{2}}\partial_X, \quad \partial_y \to \epsilon^{\frac{1}{4}}\partial_Y, \quad \text{and} \quad \partial_t \to \epsilon\partial_T + \epsilon^{\frac{5}{4}}\partial_{T'}, \tag{4.5}$$

where our control parameter ϵ is defined in equation (2.21). Hence, $R = R_c + \epsilon R_c$ in (4.3).

The Coriolis term (2.14) will result in terms of multiples of $\epsilon^{1/4}$, which motivates our expansion of V in the small parameter ϵ as follows:

$$V = \epsilon^{\frac{1}{2}}V_0 + \epsilon^{\frac{3}{4}}V_1 + \epsilon V_2 + \epsilon^{\frac{5}{4}}V_3 + \epsilon^{\frac{3}{2}}V_4 + \epsilon^{\frac{7}{4}}V_5 + \ldots \tag{4.6}$$

We will not perform the usual reduction of (2.16, 2.17, 2.18) to a potential formulation [28, 101], since this requires the mean flow to be incorporated in a non-trivial way. We will use the potential formulation for our linear stability analysis as discussed in Appendix 4.A.2.

We will assume the following form for the solution V_0:

$$\begin{aligned} V_0 &= \beta\bar{A}_0(X, Y, T, T')e^{ikx}\bar{\mathcal{V}}(z) + cc \quad \text{and} \\ &= A_0(X, Y, T, T')e^{ikx}\bar{\mathcal{V}}(z) + cc, \end{aligned} \tag{4.7}$$

where

$$A_0 = \beta \bar{A}_0, \qquad \beta = \frac{1}{\sqrt{2}}, \tag{4.8}$$

and

$$\bar{\mathcal{V}}(z) = \begin{bmatrix} \bar{U}(z) \\ \bar{V}(z) \\ \bar{W}(z) \\ \bar{\Theta}(z) \\ \bar{P}(z) \end{bmatrix}. \tag{4.9}$$

The bar indicates that the z solutions have been minimized for marginal stability (see Section 4.A.2). The variable k is the critical wavenumber of the rolls and A_0 is the amplitude of the rolls, which is a function of X, Y, T, and T' only. We have redefined our amplitude in (4.8) to simplify our calculations.

The details of our ϵ expansion are given in Appendix 4.A, Appendix 4.B explains our method of treating mean flow, Appendix 4.C discusses solvability conditions, Appendices 4.D and 4.E discuss useful relations derived from invariances, and Appendix 4.F discusses our normalization condition.

To summarize our results: at order $\epsilon^{3/2}$, our multiple scales expansion and solvability condition lead to the same form of amplitude equation as that for $\Omega = 0$ [30]:

$$-\tau_0 \partial_T A_0' + A_0' + \xi_0^2 (\partial_X - \frac{i}{2k} \partial_Y^2)^2 A_0' - g_0' |A_0'|^2 A_0' = 0, \tag{4.10}$$

where the coefficients τ_0, ξ_0, g_0' are found as a function of σ and Ω. The lateral boundary conditions are arbitrary at this point. Equation (4.10) is the same as (4.150). Our normalization convention is discussed in Appendix 4.F and the primes indicate the normalized quantities.

At order $\epsilon^{7/4}$, our multiple scales expansion leads to the following amplitude equa-

tion:

$$-\tau_0 \partial_T A_1' + A_1' + \xi_0^2 (\partial_X - \tfrac{i}{2k}\partial_Y^2)^2 A_1' - 2g_0' |A_0'|^2 A_1' - g_0' A_0'^2 A_1'^* \\ = \tau_0 \partial_{T'} A_0' + i g_{\rm cor}' A_0' \partial_Y (|A_0'|^2), \tag{4.11}$$

where the right-hand side contains the new terms resulting from the Coriolis force. The coefficient $g_{\rm cor}'$ depends on the rotation Ω and is proportional to Ω if Ω is small. Equation (4.11) is the same as (4.177). The consequences of these new terms are explored in Section 4.3.

We find (4.11) agrees with the stress-free calculations of Cox and Matthews [29] when we convert to our scaling convention (4.5). They expanded both X and Y in multiples of $\epsilon^{\frac{1}{4}}$. We also find we obtain the same equation if we perform the same multiple scales expansion on the Swift-Hohenberg equation with rotation (as in (2.45), but ignoring the tildes and primes).

We can compute the coefficients of (4.10) and (4.11) for any σ and Ω. Various representative values are plotted in Figures 4.1-4.4. The τ_0 (see Figure 4.1) and ξ_0 (see Figure 4.2) curves for $\sigma = 10.0$ agree with the results of Clune and Knobloch [28]. As another check, the coefficient g_0' (see Figure 4.3) goes subcritical (sign becomes negative) for $\sigma = 0.2$ at $\Omega_{\rm sc} = 11.6$, which is in good agreement with the results of Bajaj et al. [5] of $\Omega_{\rm sc} \simeq 12$. The curves shown in Figure 4.4 are our new results, and just like g_0', the coefficient $g_{\rm cor}'$ shows much more radical behavior as a function of Ω for lower Prandtl number.

4.3 Implications of the new rotation terms

If one makes appropriate scaling (similar to (2.43)),

$$\tilde{A}_0 = (g_0')^{1/2} A_0', \qquad \partial_{\tilde{X}} = (\xi_0)\, \partial_X, \qquad \partial_{\tilde{Y}} = \left(\tfrac{\xi_0}{k}\right)^{1/2} \partial_Y, \qquad \partial_{\tilde{T}} = (\tau_0)\, \partial_T,$$

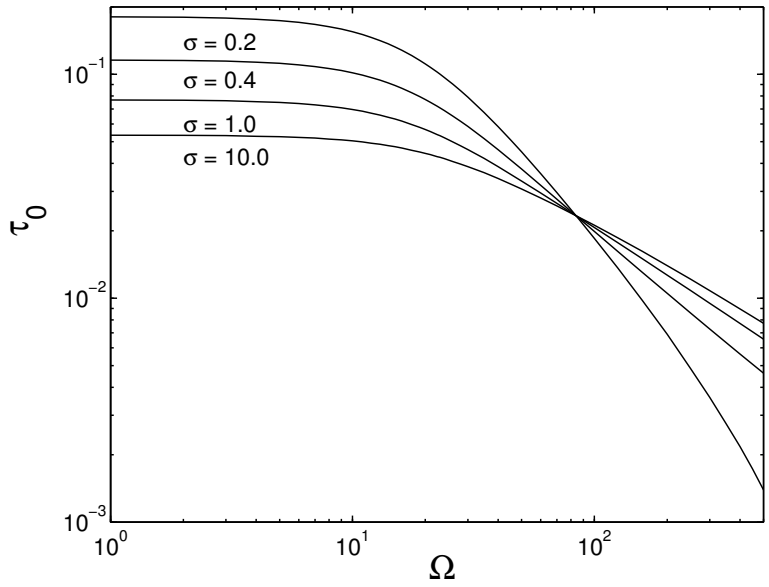

Figure 4.1: The computed coefficient τ_0 versus Ω for $\sigma = 0.2$, 0.4, 1.0, 10.0.

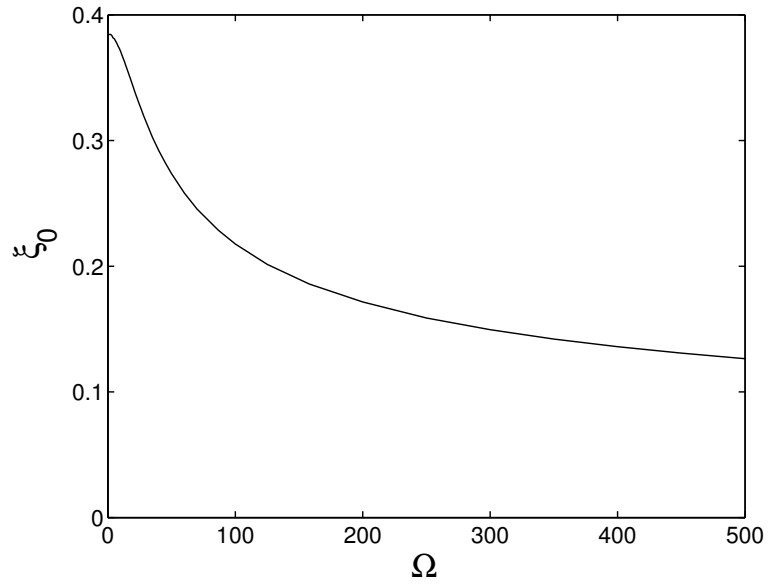

Figure 4.2: The computed coefficient ξ_0 versus Ω, which is independent of σ.

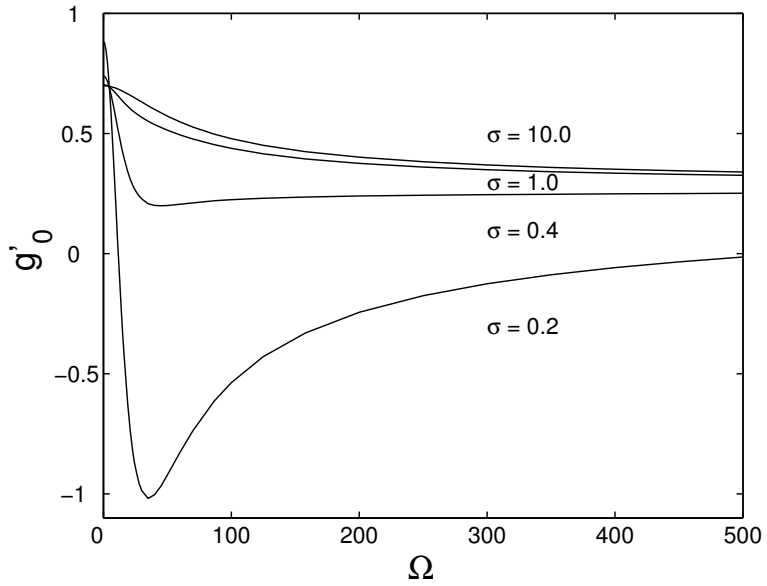

Figure 4.3: The computed coefficient g_0' versus Ω for $\sigma = 0.2$, 0.4, 1.0, 10.0.

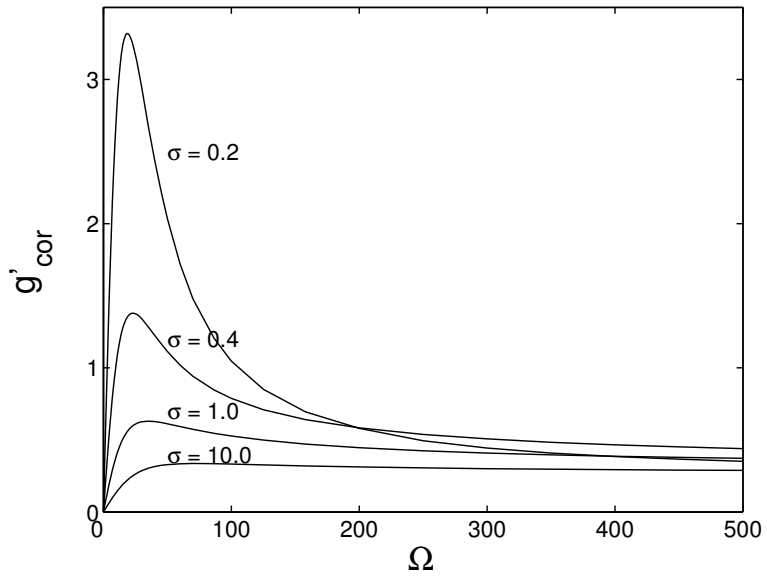

Figure 4.4: The computed coefficient $g_{\rm cor}'$ versus Ω for $\sigma = 0.2$, 0.4, 1.0, 10.0.

$$\partial_{\tilde{T}'} = (\tau_0)\,\partial_{T'}, \quad \text{and} \quad \tilde{g}_{\rm cor} = \left(\frac{k^{1/2}}{g'_0 \xi_0^{1/2}}\right) g'_{\rm cor}, \tag{4.12}$$

then (4.10) and (4.11) can be simplified. This gives

$$\partial_{\tilde{T}} \tilde{A}_0 \;=\; \tilde{A}_0 + (\partial_{\tilde{X}} - (i/2)\partial_{\tilde{Y}}^2)^2 \tilde{A}_0 - |\tilde{A}_0|^2 \tilde{A}_0 \tag{4.13}$$

and

$$-\partial_{\tilde{T}} \tilde{A}_1 + \tilde{A}_1 + (\partial_{\tilde{X}} - \tfrac{i}{2}\partial_{\tilde{Y}}^2)^2 \tilde{A}_1 - 2|\tilde{A}_0|^2 \tilde{A}_1 - \tilde{A}_0^2 \tilde{A}_1^* = \partial_{\tilde{T}'} \tilde{A}_0 + i\tilde{g}_{\rm cor} \tilde{A}_0 \partial_{\tilde{Y}} (|\tilde{A}_0|^2). \tag{4.14}$$

Note that the left-hand side of (4.14) can be thought of as a linearized perturbation solution to (4.13). If we rewrite (4.13) in operator notation:

$$\Lambda[\tilde{A}_0] = 0, \tag{4.15}$$

then (4.14) becomes

$$L\tilde{A}_1 = \partial_{\tilde{T}'} \tilde{A}_0 + i\tilde{g}_{\rm cor} (\tilde{A}_0 \partial_{\tilde{Y}} |\tilde{A}_0|^2), \tag{4.16}$$

where

$$L\delta\tilde{A}_0 \;=\; \Lambda[\tilde{A}_0 + \delta\tilde{A}_0] - \Lambda[\tilde{A}_0] + O(\delta\tilde{A}_0^2). \tag{4.17}$$

4.3.1 Specific Case—Partially rigid boundaries

To gain some insight into the effect of the new terms, let us assume the solutions to (4.13) and (4.14) are:

$$\begin{aligned} \tilde{A}_0 &= a(\tilde{X}, \tilde{Y}) e^{i\phi(\tilde{X}, \tilde{Y}, \tilde{T}')} \quad \text{and} \\ \tilde{A}_1 &= \delta a(\tilde{X}, \tilde{Y}, \tilde{T}, \tilde{T}') e^{i\phi(\tilde{X}, \tilde{Y}, \tilde{T}')}, \end{aligned} \tag{4.18}$$

where all the quantities are real. The solution $\tilde{A}_0(\tilde{X}, \tilde{Y}, \tilde{T}')$ is assumed to be a stationary solution to (4.13). The perturbation to this solution, $\tilde{A}_1(\tilde{X}, \tilde{Y}, \tilde{T}, \tilde{T}')$, is assumed to grow infinitesimally out of the stationary solution $\tilde{A}_0$. The time $\tilde{T}$ corresponds to the lowest order contribution to the time dynamics, and $\tilde{T}'$ is the next higher order (4.5). If we substitute (4.18) into (4.14) and equate reals and imaginaries, we obtain

$$\left[-\partial_{\tilde{T}} + 1 - 3a^2 + (\partial_{\tilde{X}} - \frac{i}{2}\partial_{\tilde{Y}}^2)^2\right] \delta a = 0 \quad \text{and} \tag{4.19}$$

$$-\partial_{\tilde{T}'}\phi = 2\tilde{g}_{\text{cor}} a \partial_{\tilde{Y}} a, \tag{4.20}$$

to first order in δa and ϕ.

To start with the simplest system possible, we will look at partially rigid boundaries: rigid in the y-direction (parallel to the rolls) but periodic in the x-direction (perpendicular to the rolls), and with an initial condition of straight parallel rolls. Then, the quantity a is independent of $\tilde{X}$. If we solve (4.19-4.20), we obtain

$$\delta a = Ce^{-(2+\frac{\kappa^4}{4})\tilde{T}} \cos(\kappa\tilde{Y} + \psi), \quad \text{and} \tag{4.21}$$

$$\phi = -\omega_p \tilde{T}', \tag{4.22}$$

where C, ψ, and κ are constants, we have assumed δa is also independent of $\tilde{X}$, and $\omega_p = 2\tilde{g}_{\text{cor}} a \partial_{\tilde{Y}} a$. Equation (4.21) tells us that the amplitude δa will decay in time. However, even near threshold, we see from equation (4.22) that the phase will grow in time as long as there is a gradient in the amplitude a in the y-direction. This linear increase in phase with time with opposite sign for $\tilde{Y}$ positive and negative indicates that the rolls will precess with time, and the sign indicates it will be in the same direction as the rotation (as viewed in the rotating frame). Hence, we will call ω_p the precession frequency. This simple case is pedagogically useful and can help us to understand more complex situations.

We can make a quantitative comparison using the above simplified model. We can solve (4.13) numerically[2] for a given ϵ. Remember for our simplified model,

[2]We used spectral methods [112, 15] to solve (4.13).

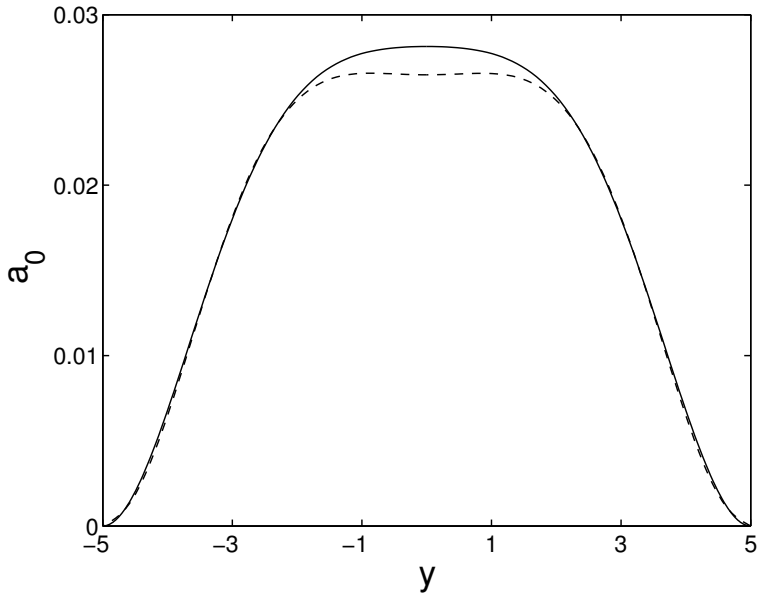

Figure 4.5: The amplitude a_0 versus y as computed from the amplitude equation (4.13) for $\partial_{\tilde{X}} a = 0$ as shown by the solid line and as computed from our numerical code Nek5000 [42] (taken at $t = 150$) as a dashed line. The following parameters were used: $\Gamma = 10, \sigma = 0.93, \Omega = 17.6, \epsilon = 0.0022$, periodic boundaries in the x-direction, and conducting boundaries in the y-direction.

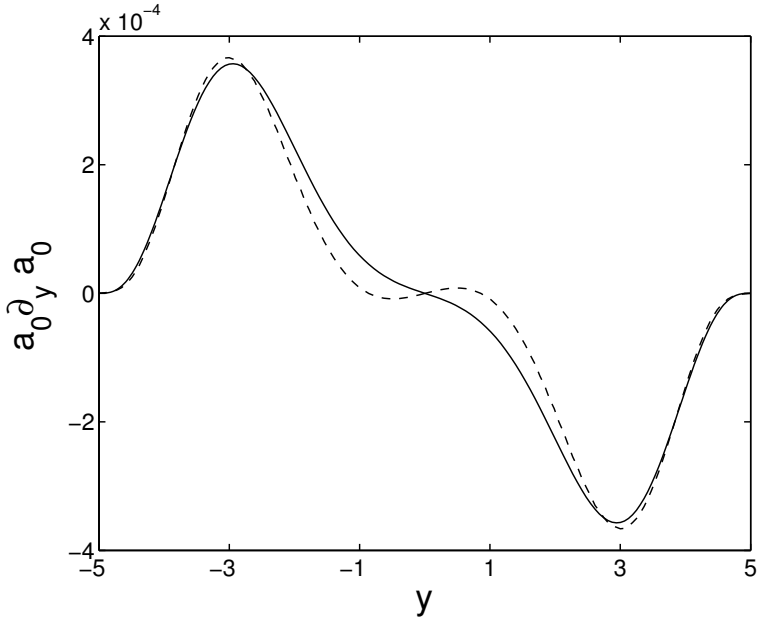

Figure 4.6: The quantity $a_0 \partial_y a_0$ versus y as computed from the amplitude equation (4.13) as shown by the solid line and as computed from our numerical code Nek5000 [42] as a dashed line. The parameters are the same as in Figure 4.5.

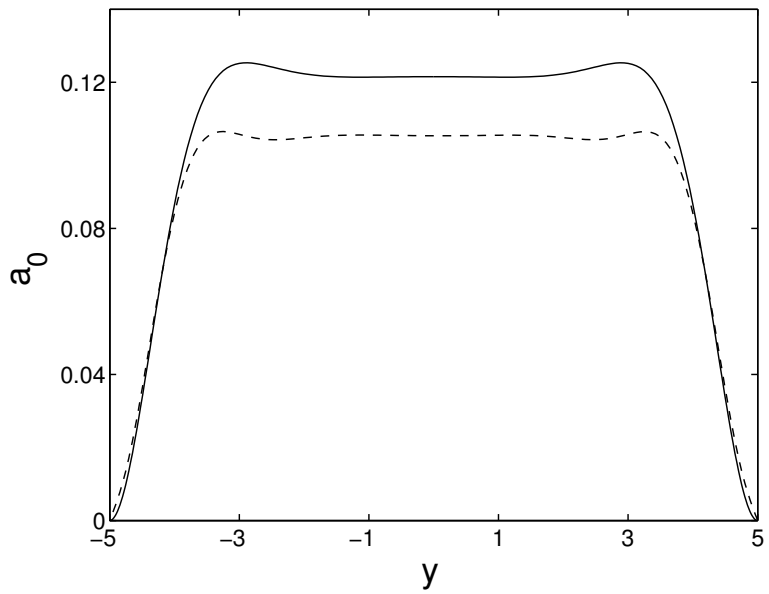

Figure 4.7: The amplitude a_0 versus y as computed from the amplitude equation (4.13) for $\partial_{\tilde{X}} a = 0$ as shown by the solid line and as computed from our numerical code Nek5000 [42] as a dashed line (taken at $t = 100$). The following parameters were used: $\Gamma = 10, \sigma = 0.93, \Omega = 17.6, \epsilon = 0.046$, periodic boundaries in the x-direction, and conducting boundaries in the y-direction.

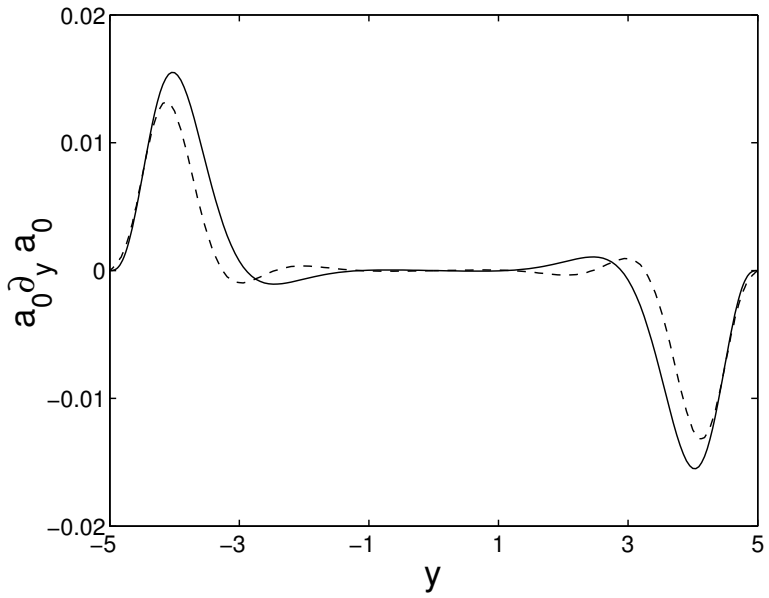

Figure 4.8: The quantity $a_0 \partial_y a_0$ versus y as computed from the amplitude equation (4.13) as shown by the solid line and as computed from our numerical code Nek5000 [42] as a dashed line. The parameters are the same as in Figure 4.7.

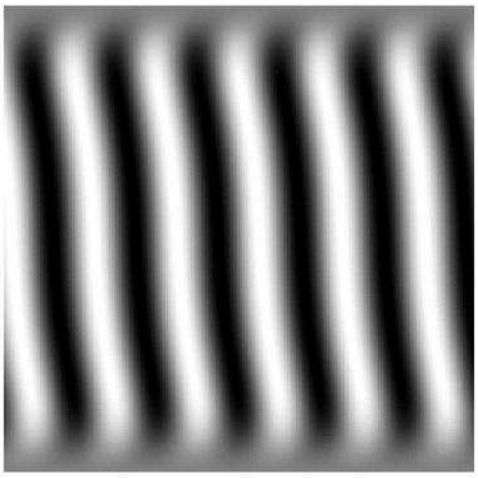

Figure 4.9: Snapshot of temperature deviation θ at the midplane from our numerical code [42]. The parameters are the same as in Figure 4.7. The gray denotes the conduction value ($\theta = 0$), and the lighter and darker shades give the values above and below this, which range from $\theta = 0.11$ to -0.11.

$\partial_{\tilde{X}} a = \partial_{\tilde{T}} a = 0$, so (4.13) becomes

$$a - \frac{1}{4}\partial_{\tilde{Y}}^4 a - a^3 = 0. \tag{4.23}$$

Our boundary conditions (2.24) become

$$a\left(\frac{M}{2}\right) = a\left(-\frac{M}{2}\right) = \partial_{\tilde{Y}} a\left(\frac{M}{2}\right) = \partial_{\tilde{Y}} a\left(-\frac{M}{2}\right) = 0, \tag{4.24}$$

where M is related to Γ by the appropriate scaling (4.28):

$$M = \sqrt{\frac{k\sqrt{\epsilon}}{\xi_0}}\Gamma. \tag{4.25}$$

Note that we have placed the center of the cell at $\tilde{Y} = 0$ in this case. Also note that the second set of boundary conditions placed on the $\tilde{Y}$ derivatives of a is derived in [18]. We can find M_c, the critical value of M, by inspection, or by solving the linear

problem (i.e., $a^3 \simeq 0$). We find $M_c = 3.348$; hence there is a slightly shifted onset ϵ:

$$\epsilon_c = \left(\frac{\xi_0}{k}\right)^2 \left(\frac{M_c}{\Gamma}\right)^4. \tag{4.26}$$

Hence, we used the following formula for M:

$$M = \sqrt{\frac{k\sqrt{(\epsilon + \epsilon_c)}}{\xi_0}}\Gamma. \tag{4.27}$$

A few notes on scaling are needed. We need to convert our solution to (4.23) back to unscaled variables. We do so by the scalings (the reverse of (4.12) and we include the ϵ dependence explicitly as well):

$$a_0 = \sqrt{\tfrac{\epsilon}{g_0}}a, \qquad \partial_y = \sqrt{\tfrac{k\sqrt{\epsilon}}{\xi_0}}\partial_{\tilde{Y}}, \qquad \partial_t = \tfrac{\epsilon^{\frac{5}{4}}}{\tau_0}\partial_{\tilde{T}'}, \quad \text{and} \quad \bar{g}_{\text{corr}} = \sqrt{\tfrac{\xi_0}{k}}g_0 g_{\text{cor}}. \tag{4.28}$$

Note here we are using the unnormalized g_0 and g_{cor} (4.225) with $\beta = 1/\sqrt{2}$. We obtain

$$\epsilon a_0 + \frac{\xi_0^2}{4k^2}\partial_y^4 a_0 - g_0 a_0^3 = 0 \quad \text{and} \tag{4.29}$$

$$\tau_0 \partial_t \phi = -2\bar{g}_{\text{cor}} a_0 \partial_y a_0. \tag{4.30}$$

From equation (4.30) we define our unscaled precession frequency ω as

$$\omega = \frac{2\bar{g}_{\text{cor}} a_0 \partial_y a_0}{\tau_0}. \tag{4.31}$$

Example solutions are shown in Figure 4.5 and Figure 4.7. Then, from our solution a_0 we can find $a_0\partial_y a_0$, as shown in Figure 4.6 and Figure 4.8. One sees that the rate of change of phase with time will be largest near the boundaries and in opposite directions on either end. By using our value of g'_{cor} from our amplitude equation analysis for a particular σ and Ω and our value of $a_0\partial_y a_0$ computed from (4.23), we

can compute an ω from (4.31).

We also ran a simulation of the Boussinesq equations with rotation (2.16, 2.17, 2.18) numerically to compare.[3] Section 2.3.2 provides more detail on this comparison between the amplitude equation and the numerical solutions. Figure 4.9 shows a snapshot of the simulation at one instant in time. One sees that the initially parallel rolls have started to bend and resemble the phase change seen from (4.30) and in Figure 4.6. Also, note that the rolls are bent to the left (negative x) for positive y (upper half plane) and to the right (positive x) for negative y (lower half plane), as is expected from (4.30). Eventually, higher order corrections will cause the rolls to either smooth out and remain in their tilted orientation or break up and reform at another orientation.

Mean flow is an important factor in computing our precession frequency ω. We find that the pattern textures and the Coriolis force both cause an overall large scale flow that must be included in our analysis to correctly model the system. We discuss the mean flow in Appendix 4.B.

We can compute the mean flow U_m from our theoretical analysis up to order $\epsilon^{5/4}$ using (4.191, 4.192) for u, v in (4.178), and compare with the mean flow computed from our numerical code. Since the mean flow has a y dependence, we compare the largest value achieved in either case. Also, note that our precession frequency ω (4.31) includes contributions from the mean flow (see (4.191, 4.192)).

The mean flow U_m is computed from the numerical simulations by taking (for each time slice) a vertical average of the horizontal velocity and then taking the x average of this quantity. The precession frequency is computed from the numerical simulations by following the x value of a temperature maximum at the y location where maximal bending occurs. This is plotted in Figure 4.10 for a representative case. The initial rate of change of x with respect to time t gives the velocity of the rolls c, and the phase drift ω can be found by multiplying this by k, i.e., $\omega = ck$.

The results given in Table 4.1 are in reasonably good agreement, except for the

[3] The details of this code are given in Section 2.2. For the systems in this section we used a spatial resolution of 0.1 and a time step of 0.005. The horizontal dimensions $x \times y$ were 10.5896×10, so rolls with a critical wavenumber of 3.56 for $\Omega = 17.6$ fit evenly in the x-direction.

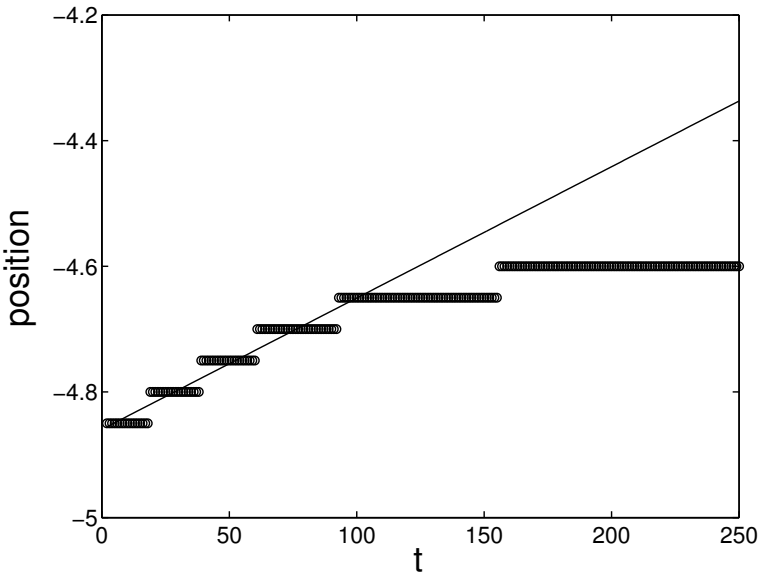

Figure 4.10: Finding ω by following the position of the rolls x as a function of time t in the place where the maximal bending occurs. The circles represent the x position corresponding to the first maximum in the temperature difference θ in the y row corresponding to the maximal mean flow value. There are discrete jumps due to the finite resolution ($dx = 0.05$ after interpolation) of our system. The slope of the line is found from a fit to the data between times $t = 1 - 100$. The parameters are the same as those in Table 4.1 for $\sigma = 0.93$. The slope of the line is 0.0021; hence the precession frequency is $0.0021 * 3.56 = 0.0074$.

Table 4.1: Comparison of values obtained from the amplitude equation (amp) as described in Section 4.3.1 to values obtained from numerical integration of the full Boussinesq equations (num) [42]. The parameters are the same as in Figure 4.5, except that a variety of Prandtl numbers σ are shown. First, the coefficients of the amplitude equation are listed, then the mean flow in the x-direction U_m, and the precession frequency ω are compared.

σ	0.78	0.93	6.8
τ_0	0.064	0.061	0.046
ξ_0	0.350	0.350	0.350
α	1.59	1.59	1.59
g_0'	0.590	0.613	0.668
g_{cor}'	0.670	0.577	0.226
U_m, amp	0.0043	0.0037	0.0011
U_m, num	0.0039 (10%)	0.0033 (11%)	0.00095 (15%)
ω, amp	0.0092	0.0083	0.0042
ω, num	0.0085 (8%)	0.0074 (11%)	0.0026 (47%)

value of ω for $\sigma = 6.8$. This discrepancy is not too surprising since as σ gets larger, the mean flow, and hence the precession effect, get smaller. The restoring forces due to roll curvature will come in more quickly in the simulations, so that it becomes harder to extract the initial precession rate. This is consistent with the direction of the error, since the amplitude equation predicts a larger precession rate.

We also investigated the behavior of the mean flow and precession frequency with ϵ for a fixed σ and Ω. These plots are shown in Figure 4.11 and Figure 4.12. One finds the agreement worsens with ϵ, as is expected from a small ϵ expansion. However, we find a slight disagreement in the scaling exponents, even for small ϵ. For the amplitude equation analysis discussed above, which we will now call method 1, we found a slope of 1.25, as expected for terms (such as U_m and ω) that enter at order $\epsilon^{\frac{5}{4}}$. However, the numerical results give a slope of 1.1, which is off by 14%. Hence, we explored this issue in more detail. One finds that the numerical amplitude does not scale as $\epsilon^{\frac{1}{2}}$ as expected. One can see this in Figure 2.6a and Figure 2.7a. One can also see this by comparing Figures 4.5 and 4.7. In Figure 4.7 the numerical amplitude is now significantly smaller than the value obtained from the amplitude

equation. One sees this in Figures 4.6 and 4.8 as well. As a result, we tried a second method of computing our mean flow and precession frequency from our amplitude equation formalism. Instead of computing the amplitude from (4.23) for a particular ϵ, we simply used the amplitude obtained from the numerical code (the dashed lines in Figures 4.5 and 4.7). Then we computed our $a_0\partial_y a_0$ from this solution (the dashed lines in Figures 4.6 and 4.8). To summarize:

- Method 1: Computed amplitude solution from (4.23). Used solid lines in Figures 4.6 and 4.8.
- Method 2: Computed amplitude solution from full solution to Boussinesq equations. Used dashed lines in Figures 4.6 and 4.8.

We compared both methods with the values obtained from the full Boussinesq equations in Figures 4.11 and 4.12. We do find the scaling to agree better between method 2 (exponent of 1.2) and the numerical results (exponent of 1.1), although the numerical results still give a slightly smaller exponent by 9%.

4.3.2 Specific Case—Gliding of defects

If we consider a stationary defect solution to (4.15) with periodic boundaries (2.26), then we will see that the new terms in (4.16) will cause the defect to glide in the rotating frame. Others have also found this result [77, 76]; however, their scaling laws differ from ours because they used a different form for the small ϵ expansion of V (4.6). We consider our form to be more appropriate for Rayleigh-Bénard systems. We will call the stationary defect solution $\tilde{A}_d(\tilde{X},\tilde{Y})$. This solution has been solved for by others [106, 93, 110, 109, 118] for non-rotating convection, and the resulting climbing motion of defects was studied [62, 61, 16]. We will follow an analogous derivation here.

By transforming into a frame moving with the glide velocity $v_{\text{glide}}\hat{\tilde{X}}$,

$$\tilde{A}_d(\tilde{X},\tilde{Y}) \to \tilde{A}_d(\tilde{X} - v_{\text{glide}}\tilde{T}',\tilde{Y}), \tag{4.32}$$

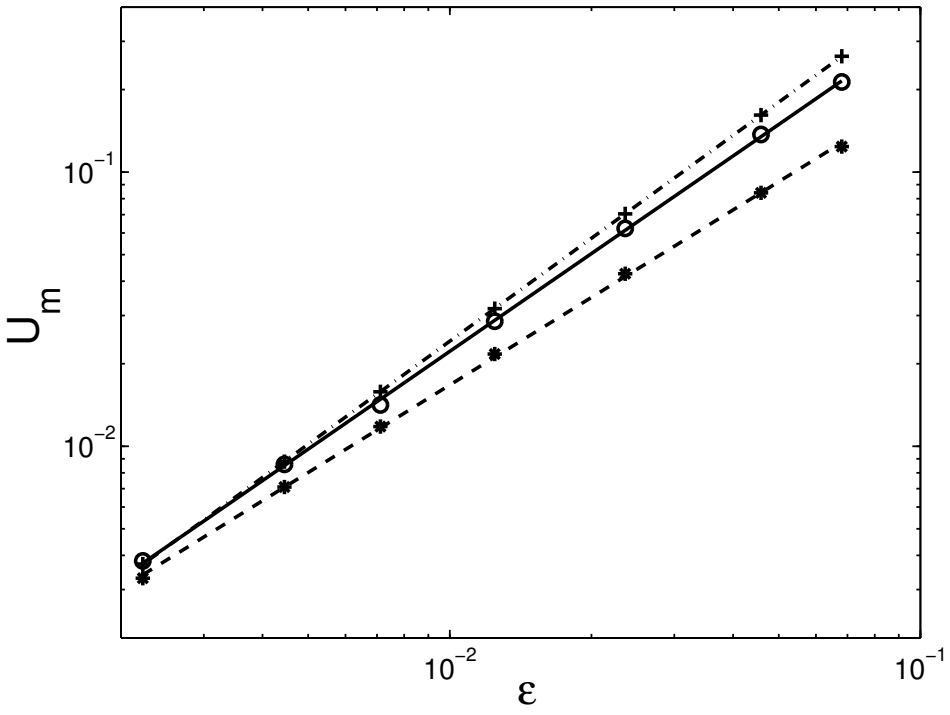

Figure 4.11: Mean flow U_{m} as a function of ϵ for $\Gamma = 10, \Omega = 17.6$, and $\sigma = 0.93$. Legend: "+" are amplitude equation results method 1, "o" are amplitude equation results method 2, and "$*$" are results from numerical integration of the full Boussinesq equations. The lines are least-squares fits to the respective data. The dashed-dotted line has a slope of 1.25, the solid line has a slope of 1.2, and the dashed line has a slope of 1.1. The data in Table 4.1 corresponds to the smallest ϵ.

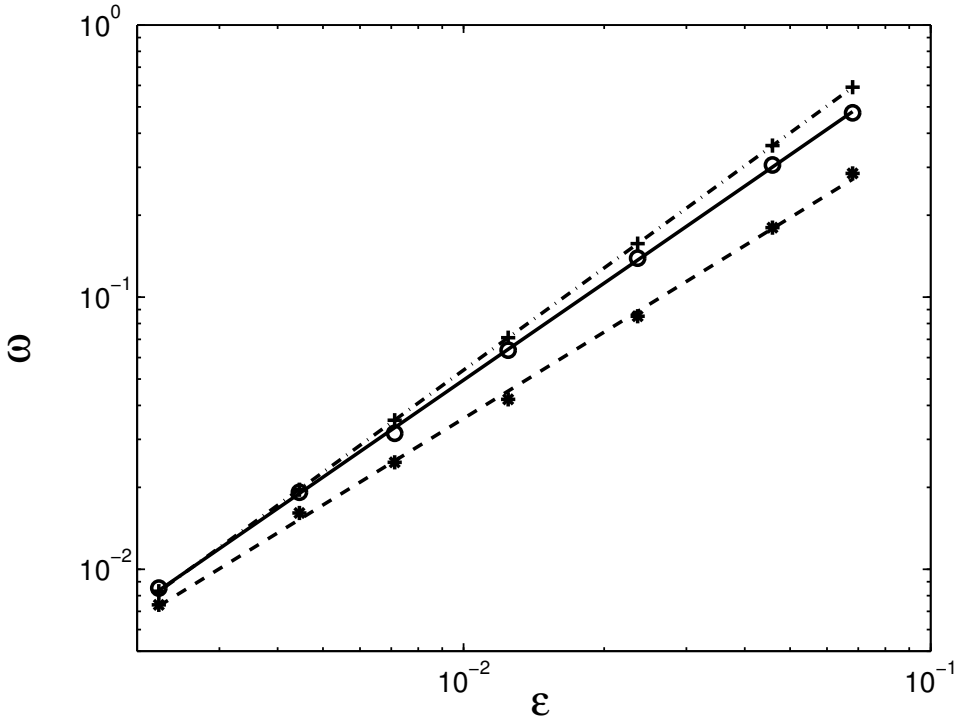

Figure 4.12: Precession frequency ω as a function of ϵ for $\Gamma = 10, \Omega = 17.6$, and $\sigma = 0.93$. Legend: "+" are amplitude equation results method 1, "o" are amplitude equation results method 2, and "$*$" are results from numerical integration of the full Boussinesq equations. The lines are least-squares fits to the respective data. The dashed-dotted line has a slope of 1.25, the solid line has a slope of 1.2, and the dashed line has a slope of 1.1. The data in Table 4.1 corresponds to the smallest ϵ.

then (4.16) becomes

$$L\tilde{A}_1 = i\tilde{g}_{\text{cor}}(\tilde{A}_d\partial_{\tilde{Y}}|\tilde{A}_d|^2) - v_{\text{glide}}\partial_{\tilde{X}}\tilde{A}_d. \tag{4.33}$$

In order to solve this equation, we need to find the zero eigenvalue mode of $L^\dagger$, the adjoint of L. Since L is self-adjoint, we can use the zero eigenvalue mode $\partial_{\tilde{X}}\tilde{A}_d$ of L, which corresponds to the translational symmetry of the dislocation perpendicular to the stripes. Hence, the right-hand side of (4.33) must be orthogonal to $\partial_{\tilde{X}}\tilde{A}_d$:

$$(\partial_{\tilde{X}}\tilde{A}_d, i\tilde{g}_{\text{cor}}(\tilde{A}_d\partial_{\tilde{Y}}|\tilde{A}_d|^2) - v_{\text{glide}}\partial_{\tilde{X}}\tilde{A}_d) = 0, \tag{4.34}$$

where

$$(u, v) = \int u^\dagger v d\tilde{X} d\tilde{Y}. \tag{4.35}$$

This yields the following relationship for the glide velocity:

$$v_{\text{glide}} = \frac{i\tilde{g}_{\text{cor}}(\partial_{\tilde{X}}\tilde{A}_d, \tilde{A}_d\partial_{\tilde{Y}}|\tilde{A}_d|^2)}{(\partial_{\tilde{X}}\tilde{A}_d, \partial_{\tilde{X}}\tilde{A}_d)}. \tag{4.36}$$

We can find a numerical value for v_{glide} for a given $\tilde{A}_d$ solution and value of $\tilde{g}_{\text{cor}}$ from (4.36) and compare with our numerical results from the Boussinesq simulations. The numerical simulations are described in Section 2.2. We used periodic boundary conditions and an aspect ratio Γ of 40. The method of determining velocities numerically is described in Section 5.4, and we use the same data as in Figure 5.15 (for periodic boundaries, of course). We have plotted this comparison in Figure 4.13. The agreement is remarkably good.

Just as with the precession frequency in Section 4.3.1, we computed a solution to (4.13), but this time we found the two-dimensional stationary defect solution $\tilde{A}_d$ (again via spectral methods) for periodic boundary conditions. Note that this stationary solution must be a pair of defects, as in Figure 1.1a, in order to satisfy the periodic boundary conditions. Then we used the values of the coefficients of the amplitude equation, as given in Table 4.1. One note about scaling: we want to again

convert to the unscaled amplitude equation by using (4.28). This amounts to finding

$$v_{\text{glide}} = \frac{i\bar{g}_{\text{cor}}(\partial_x a_d, a_d \partial_y |a_d|^2)}{\tau_o(\partial_x a_d, \partial_x a_d)}. \tag{4.37}$$

Note that for all ϵ cases we used the early time amplitude obtained from the Boussinesq numerical simulations for $\tilde{A}_d$ because the stationary defect solutions to (4.15) via spectral methods were too costly to obtain for such small ϵ values. This amounts to computing v_d by using the method 2 described in Section 4.3.1. We chose an intermediate time to compute our amplitude from the numerical simulations, allowing enough time for the solution to relax from its initial conditions (we used a pair of defects to start the simulations), but before the defects started to glide. It was difficult to determine the appropriate time, and the scatter in the amplitude equation data in Figure 4.13 is a result of this. For each amplitude equation data point, we performed an average over three vertical diffusion times, bracketing our selected appropriate time, to help reduce this scatter.

We can also determine the scaling of v_{glide} with ϵ. Reverting back to unscaled variables using (4.5) and (4.6) gives

$$v_{\text{glide}} \propto \epsilon^{3/4}. \tag{4.38}$$

This relationship is verified in Figure 4.13. We find a slope of 0.79 for the numerical results and a slope of 0.81 for the amplitude equation results, both of which agree with an exponent of 0.75 to within 7%. We also verified (4.38) for large aspect ratio numerical simulations of the full equations for rotating Rayleigh-Bénard convection with realistic boundary conditions in Section 5.4.

4.3.2.1 Glide-induced precession

As proved above, the new term due to the Coriolis force (4.33) will cause dislocation pairs which are stationary in a non-rotating frame to glide in a rotating frame, perpendicular to the rolls and in opposite directions. Their gliding path will cause an

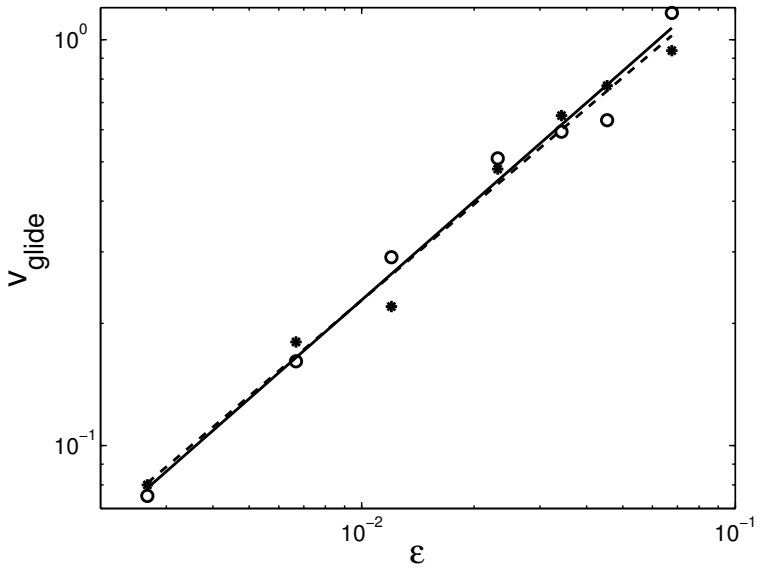

Figure 4.13: Glide velocity v_{glide} as a function of ϵ for $\Gamma = 40, \Omega = 17.6$, and $\sigma = 0.93$, and periodic boundaries. Legend: "o" are amplitude equation results, "$*$" are results from numerical integration of the full Boussinesq equations. The solid line is a fit to the amplitude equation results and gives a slope of 0.81. The dashed line is a fit to the numerical results and gives a slope of 0.79.

overall orientation change of the rolls due to the roll pinch-off that occurs as they glide. If one pair of dislocations is created in the center of a periodic cell, by the time they traverse the system, they will have caused the rolls to reorient by two roll diameters divided by the box length. This is known is glide-induced precession and is discussed in more detail in Chapters 5 and 6.

4.4 Conclusions

We have derived the amplitude equation to higher order for rotating Rayleigh-Bénard convection from the Boussinesq equations with rotation by using a multiple scales perturbation expansion. We have looked at the realistic case of no-slip velocity boundary conditions and consider both periodic and rigid lateral boundaries. We found that new terms enter at order $\epsilon^{7/4}$ due to the Coriolis force. These new terms indicate that the system will precess whenever there is a gradient in the amplitude in the direction

parallel to the rolls. This will cause rolls terminating at a rigid boundary to precess in the same direction as the rotation. This will also cause stationary defects to glide, which results in glide-induced precession.

Looking at a simplified case of rigid y boundaries (parallel to rolls) and periodic x boundaries (perpendicular to rolls), we computed the precession frequency and mean flow as predicted from the amplitude equation for a particular rotation rate Ω, Prandtl number σ, aspect ratio Γ, and control parameter ϵ. We find reasonably good agreement near threshhold between our amplitude equation and results obtained from the full simulation of the Boussinesq equations with rotation. For fully periodic boundary conditions, we find good agreement between glide velocities computed from the amplitude equation as compared to those found from our numerical simulations. This indicates that the amplitude equation formalism does correctly model this system for small ϵ.

Appendices

In these appendices we provide more details on our method of deriving the amplitude equation for rotating Rayleigh-Bénard convection with no-slip boundary conditions to higher order. In Appendix 4.A we provide the specific details of our ϵ expansion. This appendix is only suggested for those wishing to duplicate our calculations. The other appendices contain more general information about the derivation of the amplitude equation which can be applied to other situations and are suggested even for the general reader. In Appendix 4.B we discuss our method of treating mean flow, Appendix 4.C discusses solvability conditions, Appendices 4.D and 4.E apply useful invariances, and Appendix 4.F discusses our normalization condition.

Appendix 4.A Details of ϵ expansion

In this appendix we provide most of the details of our derivation of the amplitude equation for rotating Rayleigh-Bénard convection with no-slip boundary conditions to the next higher order. A few steps had to be done numerically and we performed those calculations in mathematica. A downloadable copy of those programs is at "http://www.its.caltech.edu/~jscheel/".

4.A.1 Operator notation

By inserting (4.5) and (4.6) into (4.1) and equating like powers of ϵ we obtain the following:

$$(\mathcal{O})\epsilon^{\frac{1}{2}}: \quad L_0V_0 = 0, \tag{4.39}$$

$$(\mathcal{O})\epsilon^{\frac{3}{4}}: \quad L_0V_1 + L_1V_0 = 0, \tag{4.40}$$

$$(\mathcal{O})\epsilon^{1}: \quad L_0V_2 + L_1V_1 + L_2V_0 = N_1(V_0), \tag{4.41}$$

$$(\mathcal{O})\epsilon^{\frac{5}{4}}: \quad L_0V_3 + L_1V_2 + L_2V_1 = N_2(V_0, V_1), \tag{4.42}$$

$$(\mathcal{O})\epsilon^{\frac{3}{2}}: \quad L_0V_4 + L_1V_3 + L_2V_2 + L_3V_0 = N_3(V_0, V_1, V_2), \quad \text{and} \tag{4.43}$$

$$(\mathcal{O})\epsilon^{\frac{7}{4}}: \quad L_0V_5 + L_1V_4 + L_2V_3 + L_3V_1 = N_4(V_0, V_1, V_2, V_3). \tag{4.44}$$

The operators are:

$$L_0 = \begin{bmatrix} \partial_x^2 + \partial_z^2 & 2\Omega & 0 & 0 & -\partial_x \\ -2\Omega & \partial_x^2 + \partial_z^2 & 0 & 0 & 0 \\ 0 & 0 & \partial_x^2 + \partial_z^2 & 1 & -\partial_z \\ 0 & 0 & R_c & \partial_x^2 + \partial_z^2 & 0 \\ \partial_x & 0 & \partial_z & 0 & 0 \end{bmatrix}, \tag{4.45}$$

$$L_1 = \begin{bmatrix} 0 & 0 & 0 & 0 & 0 \\ 0 & 0 & 0 & 0 & -\partial_Y \\ 0 & 0 & 0 & 0 & 0 \\ 0 & 0 & 0 & 0 & 0 \\ 0 & \partial_Y & 0 & 0 & 0 \end{bmatrix}, \tag{4.46}$$

$$L_2 = \begin{bmatrix} D & 0 & 0 & 0 & -\partial_X \\ 0 & D & 0 & 0 & 0 \\ 0 & 0 & D & 0 & 0 \\ 0 & 0 & 0 & D & 0 \\ \partial_X & 0 & 0 & 0 & 0 \end{bmatrix}, \tag{4.47}$$

$$L_3 = \begin{bmatrix} \partial_X^2 & 0 & 0 & 0 & 0 \\ 0 & \partial_X^2 & 0 & 0 & 0 \\ 0 & 0 & \partial_X^2 & 0 & 0 \\ 0 & 0 & R_c & \partial_X^2 & 0 \\ 0 & 0 & 0 & 0 & 0 \end{bmatrix}, \tag{4.48}$$

$$N_1(V_0) = \begin{bmatrix} \sigma^{-1}\left(u_0\partial_x u_0 + w_0\partial_z u_0\right) \\ \sigma^{-1}\left(u_0\partial_x v_0 + w_0\partial_z v_0\right) \\ \sigma^{-1}\left(u_0\partial_x w_0 + w_0\partial_z w_0\right) \\ u_0\partial_x\theta_0 + w_0\partial_z\theta_0 \\ 0 \end{bmatrix}, \tag{4.49}$$

and

$$N_2(V_0, V_1) = \begin{bmatrix} \sigma^{-1}\left(u_0\partial_x u_1 + u_1\partial_x u_0 + w_0\partial_z u_1 + w_1\partial_z u_0 + v_0\partial_Y u_0\right) \\ \sigma^{-1}\left(u_0\partial_x v_1 + u_1\partial_x v_0 + w_0\partial_z v_1 + w_1\partial_z v_0 + v_0\partial_Y v_0\right) \\ \sigma^{-1}\left(u_0\partial_x w_1 + u_1\partial_x w_0 + w_0\partial_z w_1 + w_1\partial_z w_0 + v_0\partial_Y w_0\right) \\ u_0\partial_x\theta_1 + u_1\partial_x\theta_0 + w_0\partial_z\theta_1 + w_1\partial_z\theta_0 + v_0\partial_Y\theta_0 \\ 0 \end{bmatrix}, \tag{4.50}$$

where $D = 2\partial_x\partial_X + \partial_Y^2$. The non-linear operator N_4 is too big to include here, and the dangerous terms of N_3 are given in (4.144). A downloadable copy of the program used to compute these solutions in mathematica is at "http://www.its.caltech.edu/~jscheel/".

4.A.2 Linear Stability Analysis via Potential Formulation

We want to solve the equation

$$L_0 V_0 = 0, \tag{4.51}$$

where L_0 is defined as in (4.45), and V_0 is defined as in (4.7). We will solve the linear stability solution by using a potential formulation.

First, the Boussinesq equations must be manipulated in order to simplify the potential formulation. We will start by taking the curl of (2.16) (with the centrifugal force set to zero) in order to eliminate the pressure term ($\nabla \times \nabla P = 0$), obtaining

$$\sigma^{-1}\left(\partial_t \nabla \times \mathbf{u} + \nabla \times (\mathbf{u}\cdot\nabla\mathbf{u})\right) = \nabla^2(\nabla\times\mathbf{u}) + \nabla\times(\theta\hat{z}) + 2\Omega\nabla\times(\mathbf{u}\times\hat{z}). \tag{4.52}$$

We can work out some of these terms:

$$\begin{aligned} \nabla \times (\theta)\hat{z} &= \partial_y \theta \hat{x} - \partial_x \theta \hat{y}, \\ 2\Omega \nabla \times (\mathbf{u} \times \hat{z}) &= 2\Omega \partial_z \mathbf{u}, \end{aligned} \tag{4.53}$$

and group together the $\nabla \mathbf{u}$ terms to obtain:

$$\left(-\sigma^{-1}(\partial_t) + \nabla^2\right) \nabla \times \mathbf{u} + \partial_y \theta \hat{x} - \partial_x \theta \hat{y} + 2\Omega \partial_z \mathbf{u} = \sigma^{-1} \left(\nabla \times (\mathbf{u} \cdot \nabla \mathbf{u})\right). \tag{4.54}$$

Next we will write a matrix equation which encompasses (4.54) and (2.17) by defining the column vector $\phi = (u, v, w, \theta)$ and the equation $L\phi = N\phi$, where the linear operator

$$L = \begin{bmatrix} 2\Omega\partial_z & -D\partial_z & D\partial_y & \partial_y \\ D\partial_z & 2\Omega\partial_z & -D\partial_x & -\partial_x \\ -D\partial_y & D\partial_x & 2\Omega\partial_z & 0 \\ 0 & 0 & R & \nabla^2 - \partial_t \end{bmatrix}, \tag{4.55}$$

and $D = \nabla^2 - \sigma^{-1}\partial_t$. The nonlinear operator is

$$N = \sigma^{-1} \begin{bmatrix} 0 & -\partial_z(\mathbf{u} \cdot \nabla) & \partial_y(\mathbf{u} \cdot \nabla) & 0 \\ \partial_z(\mathbf{u} \cdot \nabla) & 0 & -\partial_x(\mathbf{u} \cdot \nabla) & 0 \\ -\partial_y(\mathbf{u} \cdot \nabla) & \partial_x(\mathbf{u} \cdot \nabla) & 0 & 0 \\ 0 & 0 & 0 & \sigma(\mathbf{u} \cdot \nabla) \end{bmatrix}. \tag{4.56}$$

Things are not as simple as in the non-rotating case because the vertical vorticity ζ, defined as

$$\zeta = \partial_x v - \partial_y u, \tag{4.57}$$

no longer vanishes in the linearized equations. But these equations can be somewhat simplified into three equations containing only the variables w, ζ, and θ.

The third row of (4.55) gives us the evolution of the vorticity:

$$D\zeta + 2\Omega\partial_z w = \sigma^{-1}(-\partial_y(\mathbf{u}\cdot\nabla)u + \partial_x(\mathbf{u}\cdot\nabla)v). \tag{4.58}$$

Next we take ∂_y of the first row of (4.55) and subtract from it ∂_x of the second row. This gives the following equation:

$$\begin{aligned} &2\Omega\partial_z(\partial_y u - \partial_x v) - D\partial_z(\partial_y v + \partial_x u) + D(\partial_y^2 + \partial_x^2)w + (\partial_y^2 + \partial_x^2)\theta \\ &\quad = \sigma^{-1}\left[-\partial_z(\partial_y(\mathbf{u}\cdot\nabla)v + \partial_x(\mathbf{u}\cdot\nabla)u) + (\partial_y^2 + \partial_x^2)(\mathbf{u}\cdot\nabla)w\right]. \end{aligned} \tag{4.59}$$

Using (2.18), the second term becomes $D\partial_z^2 w$, which can be combined with the third term to obtain $D\nabla^2 w$. We then obtain

$$\begin{aligned} &2\Omega\partial_z(\partial_y u - \partial_x v) + D\nabla^2 w + \nabla_\perp^2\theta \\ &= \sigma^{-1}\left[-\partial_z(\partial_y(\mathbf{u}\cdot\nabla)v + \partial_x(\mathbf{u}\cdot\nabla)u) + \nabla_\perp^2(\mathbf{u}\cdot\nabla)w\right], \end{aligned} \tag{4.60}$$

which reduces to

$$\begin{aligned} &D\nabla^2 w - 2\Omega\partial_z\zeta + \nabla_\perp^2\theta \\ &= \sigma^{-1}\left[-\partial_z(\partial_y(\mathbf{u}\cdot\nabla)v + \partial_x(\mathbf{u}\cdot\nabla)u) + \nabla_\perp^2(\mathbf{u}\cdot\nabla)w\right]. \end{aligned} \tag{4.61}$$

Note that $\nabla_\perp^2 = \partial_x^2 + \partial_y^2$. Combining (4.61, 4.58) and the last line of (4.55), the linear operator for the three variables $\chi = (w, \zeta, \theta)$ is given as $L\chi = N$, where

$$L = \begin{bmatrix} D\nabla^2 & -2\Omega\partial_z & \nabla_\perp^2 \\ 2\Omega\partial_z & D & 0 \\ R & 0 & \nabla^2 - \partial_t \end{bmatrix}, \tag{4.62}$$

and the nonlinear operator $N =$

$$N = \sigma^{-1} \begin{bmatrix} -\partial_z(\partial_y(\mathbf{u}\cdot\nabla)v + \partial_x(\mathbf{u}\cdot\nabla)u) + \nabla_\perp^2(\mathbf{u}\cdot\nabla)w \\ -\partial_y(\mathbf{u}\cdot\nabla)u + \partial_x(\mathbf{u}\cdot\nabla)v \\ \sigma(\mathbf{u}\cdot\nabla) \end{bmatrix}. \tag{4.63}$$

The boundary conditions (2.23) translate to the eight boundary conditions

$$w = \theta = \zeta = \partial_z w = 0 \quad \text{at } z = \pm\tfrac{1}{2}. \tag{4.64}$$

Following Küppers and Lortz [70] and Schlüter [101], we can decompose the velocity into two arbitrary functions: ϕ, ψ:

$$\begin{aligned} u &= \partial_z\partial_x\phi - \partial_y\psi, \\ v &= \partial_z\partial_y\phi + \partial_x\psi, \quad \text{and} \\ w &= -(\partial_x^2 + \partial_y^2)\phi, \end{aligned} \tag{4.65}$$

which is analogous to a toroidal-poloidal decomposition but makes the L operator self-adjoint. The system of equations (4.65) is what is known as the potential formulation. Two nice relations that come from this formulation are that incompressibility is automatically satisfied, and $\zeta = (\partial_x^2 + \partial_y^2)\psi$. Now the linear operator becomes (using the column vector $\chi = (\phi, \psi, \theta)$)

$$L = \begin{bmatrix} -D\nabla^2\nabla_\perp^2 & -2\Omega\partial_z\nabla_\perp^2 & \nabla_\perp^2 \\ -2\Omega\partial_z\nabla_\perp^2 & D\nabla_\perp^2 & 0 \\ -R\nabla_\perp^2 & 0 & \nabla^2 - \partial_t \end{bmatrix}, \tag{4.66}$$

and the nonlinear operator becomes

$$N = \sigma^{-1} \begin{bmatrix} \alpha & \beta & 0 \\ \gamma & \delta & 0 \\ 0 & 0 & \xi \end{bmatrix}, \tag{4.67}$$

where $\alpha, \beta, \gamma, \delta, \xi$ come from converting equation (4.63) to ϕ and ψ.

The linear equations to be solved (for the zero growth rate solution, so $D = \nabla^2$, and for zero non-linear contribution so $L\chi = 0$) are:

$$\begin{aligned} \nabla_\perp^2[\nabla^4\phi + 2\Omega\partial_z\psi - \theta] &= 0, & (4.68)\\ \nabla_\perp^2[-2\Omega\partial_z\phi + \nabla^2\psi] &= 0, \quad \text{and} & (4.69)\\ -R\nabla_\perp^2\phi + \nabla^2\theta &= 0. & (4.70) \end{aligned}$$

We must also translate the boundary conditions (4.64) on (w, ζ, θ) to the new variables (ϕ, ψ, θ):

$$\phi = \theta = \psi = \partial_z\phi = 0 \text{ at } z = \pm\tfrac{1}{2}. \tag{4.71}$$

Note that the choice of the boundary conditions is arbitrary unless the mean flow terms are incorporated here [28]. However, it is unclear how to precisely incorporate the mean flow into this formulation for a specific set of parameters. Since this will have an effect on the higher order terms, we do not continue with this potential formulation to higher order.

The linear equations can be decoupled somewhat by taking ∇^2 of (4.68) to obtain

$$\nabla_\perp^2[\nabla^6\phi + 2\Omega\partial_z\nabla^2\psi - \nabla^2\theta] = 0. \tag{4.72}$$

Then using (4.69), one can eliminate ψ to obtain the new set of equations:

$$\begin{aligned} \nabla_\perp^2[\nabla^6\phi + 4\Omega^2\partial_z^2\phi - \nabla^2\theta] &= 0, & (4.73)\\ \nabla_\perp^2[-2\Omega\partial_z\phi + \nabla^2\psi] &= 0, \quad \text{and} & (4.74)\\ -R\nabla_\perp^2\phi + \nabla^2\theta &= 0. & (4.75) \end{aligned}$$

The $\nabla_\perp$ derivatives can be eliminated easily by assuming a stripe solution:

$$\theta = \Theta(z)\exp[i\mathbf{k}\cdot\mathbf{x}_\perp],$$

$$\begin{aligned} \phi &= \Phi(z)\exp[i\mathbf{k}\cdot\mathbf{x}_\perp], \quad \text{and} \\ \psi &= \Psi(z)\exp[i\mathbf{k}\cdot\mathbf{x}_\perp], \end{aligned} \tag{4.76}$$

where k is the orientation angle of the rolls and $\mathbf{x}_\perp = x\hat{x} + y\hat{y}$. Then (4.73, 4.74, 4.75) become

$$\nabla^6\Phi + 4\Omega^2\partial_z^2\Phi - \nabla^2\Theta = 0, \tag{4.77}$$

$$-2\Omega\partial_z\Phi + \nabla^2\Psi = 0, \quad \text{and} \tag{4.78}$$

$$Rk^2\Phi + \nabla^2\Theta = 0, \tag{4.79}$$

and $\nabla^2 = (\partial_z^2 - k^2)$.

We can use (4.79) to eliminate Θ from (4.77) to obtain

$$\nabla^6\Phi + 4\Omega^2\partial_z^2\Phi + Rk^2\Phi = 0. \tag{4.80}$$

We will use the following basis functions (inspired by Clune and Knobloch [28, 27], but slightly different):

$$\Theta = \sum_{j=0}^{3} C_j \frac{\cosh\lambda_j z}{\cosh\frac{\lambda_j}{2}}, \tag{4.81}$$

$$\Phi = \sum_{j=0}^{3} C_j \left[\frac{k^2-\lambda_j^2}{Rk^2}\right] \frac{\cosh\lambda_j z}{\cosh\frac{\lambda_j}{2}}, \quad \text{and} \tag{4.82}$$

$$\Psi = \sum_{j=0}^{3} C_j \left[\frac{Rk^2 + (\lambda_j^2-k^2)^3}{2\Omega Rk^2\lambda_j}\right] \frac{\sinh\lambda_j z}{\cosh\frac{\lambda_j}{2}}. \tag{4.83}$$

The constants C_j will be determined from (4.89). Substituting these basis functions into (4.77, 4.78, 4.79) leads to the following equation:

$$(k^2-\lambda_j^2)(4\Omega^2\lambda_j^2 + (\lambda_j^2-k^2)^3 + k^2R) = 0. \tag{4.84}$$

This can be solved for the eight cubic roots of λ_j (but we take only the positive ones since we have an even function), obtaining:

$$
\begin{aligned}
\lambda_0 &= k, \\
\lambda_1 &= \sqrt{k^2 + \frac{4(2^{\frac{1}{3}})\Omega^2}{\alpha} - \frac{\alpha}{3(2^{1/3})}}, \\
\lambda_2 &= \sqrt{\frac{24(2^{1/3})\left(-1+i\sqrt{3}\right)\Omega^2 + 12k^2\alpha + 2^{2/3}\left(1+i\sqrt{3}\right)\alpha^2}{12\alpha}}, \quad \text{and} \\
\lambda_3 &= \sqrt{\frac{24(2^{1/3})\left(-1-i\sqrt{3}\right)\Omega^2 + 12k^2\alpha + 2^{2/3}\left(1-i\sqrt{3}\right)\alpha^2}{12\alpha}},
\end{aligned} \tag{4.85}
$$

where $\alpha = \left(27k^2(4\Omega^2+R) + \sqrt{6912\Omega^6 + 729k^4(4\Omega^2+R)^2}\right)^{\frac{1}{3}}$. By imposing the boundary conditions (4.71), we obtain the following equation:

$$
M \begin{bmatrix} C_1 \\ C_2 \\ C_3 \\ C_4 \end{bmatrix} = 0, \tag{4.86}
$$

where

$$
M = \begin{bmatrix} 1 & 1 & 1 & 1 \\ \frac{\gamma_0}{\lambda_0} & \frac{\beta_1\gamma_1}{\lambda_1} & \frac{\beta_2\gamma_2}{\lambda_2} & \frac{\beta_3\gamma_3}{\lambda_3} \\ 0 & \alpha_1 & \alpha_2 & \alpha_3 \\ 0 & \gamma_1\alpha_1\lambda_1 & \gamma_2\alpha_2\lambda_2 & \gamma_3\alpha_3\lambda_3 \end{bmatrix}, \tag{4.87}
$$

and $\gamma_i = \tanh(\lambda_i/2)$, $\alpha_i = k^2 - \lambda_i^2$, and $\beta_i = 1 - \alpha_i^3/Rk^2$. We must first solve

$$
\det M = 0, \tag{4.88}
$$

which gives us an equation for $R(k)$, for a given Ω. By finding the k which minimizes R, we can solve for the marginally stable values R_c, k_c. (Note, however, that we will continue to use the variable k, but it is understood to be the critical wavenumber.) We show our results in Figure 4.14 and Figure 4.15. We are able to replicate the

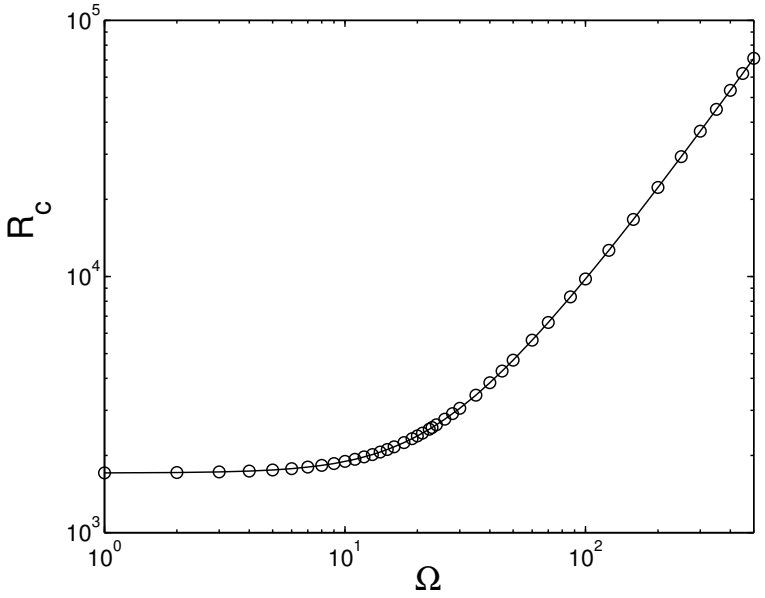

Figure 4.14: The critical Rayleigh number R_c versus Ω computed from equation (4.88).

R_c, k_c values from [20].

Solving for the coefficients yields:

$$\begin{aligned}
C_3 &= \frac{\alpha_2\lambda_2\lambda_3(\beta_1\gamma_1\lambda_0 - \gamma_0\lambda_1)(\gamma_1\lambda_1 - \gamma_2\lambda_2)}{D}, \\
C_2 &= -\frac{\alpha_3\lambda_2\lambda_3(\beta_1\gamma_1\lambda_0 - \gamma_0\lambda_1)(\gamma_1\lambda_1 - \gamma_3\lambda_3)}{D}, \\
C_1 &= \frac{\lambda_1\left(\alpha_3\lambda_3(\gamma_1\lambda_1 - \gamma_3\lambda_3)(\beta_2\gamma_2\lambda_0 - \gamma_0\lambda_2) - \alpha_2\lambda_2(\gamma_1\lambda_1 - \gamma_2\lambda_2)(\beta_3\gamma_3\lambda_0 - \gamma_0\lambda_3)\right)}{D}, \quad \text{and} \\
C_0 &= 1, \qquad (4.89)
\end{aligned}$$

where

$$D = (\lambda_0(\alpha_2\lambda_2(\gamma_1\lambda_1 - \gamma_2\lambda_2)(\beta_3\gamma_3\lambda_1 - \beta_1\gamma_1\lambda_3) - \alpha_3\lambda_3(\gamma_1\lambda_1 - \gamma_3\lambda_3)(\beta_2\gamma_2\lambda_1 - \beta_1\gamma_1\lambda_2))). \qquad (4.90)$$

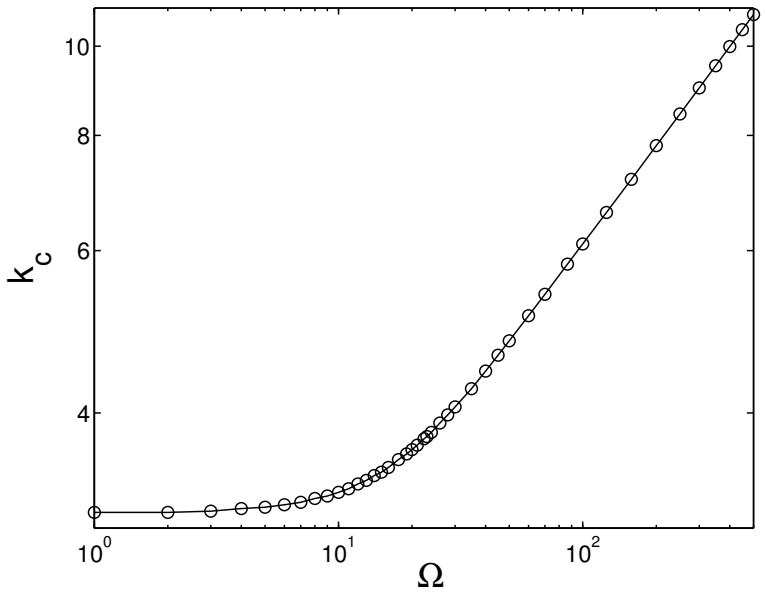

Figure 4.15: The critical wave number k_c versus Ω computed from equation (4.88).

4.A.3 Order $\epsilon^{1/2}$

From the formulation in Appendix 4.A.1 we obtain $\mathcal{V}$ (see (4.9)):

$$\bar{U}(z) = ik\sum_{j=0}^{3} A_j\lambda_j \sinh\lambda_j z, \tag{4.91}$$

$$\bar{V}(z) = ik\sum_{j=0}^{3} B_j \sinh\lambda_j z, \tag{4.92}$$

$$\bar{W}(z) = k^2\sum_{j=0}^{3} A_j \cosh\lambda_j z, \tag{4.93}$$

$$\bar{\Theta}(z) = \sum_{j=0}^{3} C'_j \cosh\lambda_j z, \quad \text{and} \tag{4.94}$$

$$\bar{P}(z) = \sum_{j=0}^{3} \mathcal{D}_j \sinh\lambda_j z, \tag{4.95}$$

where

$$A_j = \left[\frac{k^2-\lambda_j^2}{Rk^2}\right] C_j', \tag{4.96}$$

$$B_j = \left[\frac{Rk^2+(\lambda_j^2-k^2)^3}{2\Omega Rk^2\lambda_j}\right] C_j', \tag{4.97}$$

$$C_j' = \frac{C_j}{\cosh\frac{\lambda_j}{2}}, \quad \text{and} \tag{4.98}$$

$$\mathcal{D}_j = \left[\frac{1-\frac{(k^2-\lambda_j^2)^2}{R}}{\lambda_j}\right] C_j'. \tag{4.99}$$

The quantity λ_j is defined by (4.84). The variables C_j are constants to be determined from (4.89).

4.A.4 Order $\epsilon^{3/4}$

Now we need to solve

$$L_0 V_1 = -L_1 V_0. \tag{4.100}$$

This will have both a homogeneous solution ($L_0 V_{1h} = 0$) and a particular solution ($L_0 V_{1p} = -L_1 V_0$). The full solution is the sum of both:

$$V_1 = V_{1h} + V_{1p}, \tag{4.101}$$

where

$$\begin{aligned} V_{1h} &= A_1 e^{ikx}\bar{\mathcal{V}} + cc, \\ V_{1p} &= (\partial_Y A_0)\, e^{ikx}\left(\bar{\mathcal{V}}_{1p}\right) + cc, \end{aligned} \tag{4.102}$$

$\bar{\mathcal{V}}$ is given by (4.91)-(4.95), and $\bar{\mathcal{V}}_{1p}$ still needs to found. Let's look at the driving term:

$$L_1 V_0 = e^{ikx}\partial_Y A_0 \begin{bmatrix} 0 \\ \bar{P} \\ 0 \\ 0 \\ -\bar{V} \end{bmatrix}. \tag{4.103}$$

We can use the rotational invariance of our system to find the solution to this (see Appendix 4.E). Equation (4.217) provides us with the answer:

$$\bar{\mathcal{V}}_{1p} = \frac{i}{k} \begin{bmatrix} \bar{V} \\ -\bar{U} \\ 0 \\ 0 \\ 0 \end{bmatrix}. \tag{4.104}$$

4.A.5 Order ϵ

Now we need to solve

$$L_0 V_2 + L_1 V_1 + L_2 V_0 = N_1(V_0). \tag{4.105}$$

First we will work on the $L_2 V_0$ part, using the fact that we have minimized our V_0 solution about k to simplify this term. Using (4.210), we can rewrite $L_2 V_0 / e^{ikx} = L_{2k} A_0 \bar{\mathcal{V}}$ as

$$L_{2k} A_0 \bar{\mathcal{V}} = \frac{-DA_0}{2k}(\partial_k L_{0k})\bar{\mathcal{V}} + \frac{iDA_0}{2k} L_{2n}\bar{\mathcal{V}} + \partial_X A_0 L_{2n}\bar{\mathcal{V}}, \tag{4.106}$$

where

$$L_{2n} = \begin{bmatrix} 0 & 0 & 0 & 0 & -1 \\ 0 & 0 & 0 & 0 & 0 \\ 0 & 0 & 0 & 0 & 0 \\ 0 & 0 & 0 & 0 & 0 \\ 1 & 0 & 0 & 0 & 0 \end{bmatrix}. \tag{4.107}$$

Hence, using (4.212), we can write:

$$L_{2k}A_0\bar{\mathcal{V}} = \frac{DA_0}{2k}L_{0k}\partial_k\bar{\mathcal{V}} + \frac{iDA_0}{2k}L_{2n}\bar{\mathcal{V}} + \partial_X A_0 L_{2n}\bar{\mathcal{V}}. \tag{4.108}$$

Now since $D = (2ik\partial_X + \partial_Y^2)$, we find that $iD/2k = -\partial_X + i\partial_Y^2/2k$. When this is inserted into (4.108), we find

$$L_{2k}A_0\bar{\mathcal{V}} \;\; = \;\; \frac{DA_0}{2k}L_{0k}\partial_k\bar{\mathcal{V}} + i\frac{\partial_Y^2 A_0}{2k}L_{2n}\bar{\mathcal{V}}. \tag{4.109}$$

Refilling in the e^{ikx} dependence gives then

$$L_2V_0 \;\; = \;\; L_0\frac{DA_0}{2k}e^{ikx}\partial_k\bar{\mathcal{V}} + i\frac{\partial_Y^2 A_0}{2k}L_{2n}V_0. \tag{4.110}$$

Now, if we redefine V_2 to be

$$V_2 = \tilde{V}_2 - \frac{DA_0}{2k}e^{ikx}\partial_k\bar{\mathcal{V}}, \tag{4.111}$$

then (4.105) becomes

$$L_0\tilde{V}_2 + L_1V_1 + i\frac{\partial_Y^2 A_0}{2k}L_{2n}V_0 = N_1(V_0). \tag{4.112}$$

Next note that

$$L_1 V_1 = \partial_Y^2 A_0 e^{ikx} \begin{bmatrix} 0 \\ 0 \\ 0 \\ 0 \\ -i\bar{U}/k \end{bmatrix} + L_1 A_1 e^{ikx} \bar{\mathcal{V}}, \tag{4.113}$$

which, when inserted into (4.112), gives

$$L_0 \tilde{V}_2 = -\partial_Y A_1 e^{ikx} \begin{bmatrix} 0 \\ -\bar{P} \\ 0 \\ 0 \\ \bar{V} \end{bmatrix} + (i/2k)\partial_Y^2 A_0 e^{ikx} \begin{bmatrix} \bar{P} \\ 0 \\ 0 \\ 0 \\ \bar{U} \end{bmatrix} + N_1(V_0). \tag{4.114}$$

We can use our relationships derived in Appendix 4.E, (4.217), and (4.219) to solve for the linear parts:

$$V_{2\text{lin}} = -\frac{(DA_0)}{2k} e^{ikx} \partial_k \bar{\mathcal{V}} + A_2 e^{ikx} \bar{\mathcal{V}} + \partial_Y A_1 e^{ikx} \bar{\mathcal{V}}_{1p} + \frac{i}{2k} \partial_Y^2 A_0 e^{ikx} \bar{\mathcal{V}}_{2p} + cc, \tag{4.115}$$

where (see (4.219))

$$\bar{\mathcal{V}}_{2p} = \frac{i}{k} \begin{bmatrix} -\bar{U} \\ -\bar{V} \\ 0 \\ 0 \\ 0 \end{bmatrix}. \tag{4.116}$$

Now the nonlinear part $L_0 V_{2\mathrm{nl}} = N_1(V_0)$ can be worked out.

$$L_0 V_{2\mathrm{nl}} = A_0^2 e^{2ikx} \begin{bmatrix} \sigma^{-1}\left(ik\bar{U}^2 + \bar{W}\partial_z\bar{U}\right) \\ \sigma^{-1}\left(ik\bar{U}\bar{V} + \bar{W}\partial_z\bar{V}\right) \\ \sigma^{-1}\left(ik\bar{U}\bar{W} + \bar{W}\partial_z\bar{W}\right) \\ ik\bar{U}\bar{\Theta} + \bar{W}\partial_z\bar{\Theta} \\ 0 \end{bmatrix} + cc + |A_0|^2 \begin{bmatrix} 0 \\ 0 \\ \sigma^{-1}\left(-2ik(\bar{U}\bar{W}) + 2\bar{W}\partial_z\bar{W}\right) \\ -2ik(\bar{U}\bar{\Theta}) + 2\bar{W}\partial_z\bar{\Theta} \\ 0 \end{bmatrix}. \tag{4.117}$$

This gives us the form of our non-linear solutions, where the z-dependence is in the square brackets. The z-dependence can be solved algebraically after substituting in the solutions (4.91-4.95). A downloadable copy of the program used to compute these solutions in mathematica is at "http://www.its.caltech.edu/~jscheel/".

The full solution is

$$V_2 = -\frac{(DA_0)}{2k} e^{ikx}\partial_k\bar{\mathcal{V}} + A_2 e^{ikx}\bar{\mathcal{V}} + \partial_Y A_1 e^{ikx}\bar{\mathcal{V}}_{1p} + \frac{i}{2k}\partial_Y^2 A_0 e^{ikx}\bar{\mathcal{V}}_{2p} + A_0^2 e^{2ikx}\bar{F} + cc + |A_0|^2\bar{G}, \tag{4.118}$$

where $\bar{F}$ and $\bar{G}$ are the algebraic solutions to the non-linear terms and have the form:

$$\bar{F} = \begin{bmatrix} f_1 \\ f_2 \\ f_3 \\ f_3 \\ f_5 \end{bmatrix}, \qquad \bar{G} = \begin{bmatrix} 0 \\ 0 \\ 0 \\ g_4 \\ g_5 \end{bmatrix}, \tag{4.119}$$

and the f_i's and g_i's are only functions of z.

We would like to highlight that there is an ambiguity in our choice of g_5 in (4.119). Since there are no boundary conditions on the pressure term P, the operator L_0 permits an arbitrary z-constant term to be added to g_5. We will address this term when we discuss the mean flow in Appendix 4.B.

4.A.6 Order $\epsilon^{5/4}$

Now we need to solve

$$L_0 V_3 + L_1 V_2 + L_2 V_1 = N_2(V_0, V_1). \tag{4.120}$$

These actually start to get easier as we realize that analogous parts have already been solved for in lower orders. First let's look at the linear parts of our already-solved solutions, (4.101) and (4.115).

We will focus on the following terms:

$$\begin{aligned} V_{1\text{foc}} &= A_1 e^{ikx}\bar{\mathcal{V}} \quad \text{and} \\ V_{2\text{foc}} &= A_2 e^{ikx}\bar{\mathcal{V}} + \partial_Y A_1 e^{ikx}\bar{\mathcal{V}}_{1p}. \end{aligned} \tag{4.121}$$

Comparing (4.120) with (4.105), if we replace $1 \to 0$ and $2 \to 1$ in the V_i terms, then $L_1 V_{2\text{foc}} + L_2 V_{1\text{foc}} \to L_1 V_1 + L_2 V_0$. Hence, we have the same solutions as for order ϵ (4.115), but with $0 \to 1$, $1 \to 2$, and $2 \to 3$:

$$V_{3\text{foc}} = -\frac{(DA_1)}{2k} e^{ikx}\partial_k \bar{\mathcal{V}} + A_3 e^{ikx}\bar{\mathcal{V}} + \partial_Y A_2 e^{ikx}\bar{\mathcal{V}}_{1p} + \frac{i}{2k}\partial_Y^2 A_1 e^{ikx}\bar{\mathcal{V}}_{2p} + cc. \tag{4.122}$$

Now we still have to solve the extra part that we did not focus on in (4.121):

$$\begin{aligned} V_{1\text{ex}} &= \partial_Y A_0 e^{ikx}\left(\bar{\mathcal{V}}_{1p}\right) \quad \text{and} \\ V_{2\text{ex}} &= -\frac{(DA_0)}{2k} e^{ikx}\partial_k \bar{\mathcal{V}} + \frac{i}{2k}\partial_Y^2 A_0 e^{ikx}\bar{\mathcal{V}}_{2p}. \end{aligned} \tag{4.123}$$

This then gives us the following linear equation to solve (after plenty of algebra):

$$L_0 V_{3\text{ex}} = -L_1 V_{2\text{ex}} - L_2 V_{1\text{ex}} \quad \text{and}$$

$$= \frac{1}{2k}\partial_Y D A_0 e^{ikx} \begin{bmatrix} -2i\bar{V} \\ 2i\bar{U} - \partial_k \bar{P} \\ 0 \\ 0 \\ -\bar{V}/k + \partial_k \bar{V} \end{bmatrix}. \tag{4.124}$$

Again, rotational invariance will help us out. Equation (4.221) solves this order:

$$V_{3\text{ex}} = \frac{i}{2k^2}\partial_Y D A_0 e^{ikx} \bar{\mathcal{V}}_{3p}, \tag{4.125}$$

where

$$\bar{\mathcal{V}}_{3p} = \begin{bmatrix} -\partial_k \bar{V} + \bar{V}/k \\ \partial_k \bar{U} - \bar{U}/k \\ 0 \\ 0 \\ 0 \end{bmatrix}. \tag{4.126}$$

Finally, we can solve for the non-linear part, making sure to include the non-linear terms obtained from $L_1 V_2$: $L_0 V_{3\text{nl}} + L_1 V_{2\text{nl}} = N_2$, where N_2 is given in (4.50).

We get:

$$V_{3\text{nl}} = 2A_0 A_1 e^{2ikx}\bar{F}_0 + A_0 \partial_Y A_0 e^{2ikx}\bar{I} + (A_0 A_1^*)\,\bar{G} + cc + \partial_Y(|A_0|^2)\bar{J}, \tag{4.127}$$

where $\bar{F}$ and $\bar{G}$ are the same as in (4.119). We find also that

$$\bar{I} = \frac{i}{k} \begin{bmatrix} f_2 \\ -f_1 \\ 0 \\ 0 \\ 0 \end{bmatrix}, \tag{4.128}$$

where $f_1(z)$ and $f_2(z)$ are as found in (4.119). The equation for $\bar{J}$ needs to be found algebraically. We do find the following dependence for $\bar{J}$:

$$\bar{J} = \begin{bmatrix} j_1 \\ j_2 \\ 0 \\ 0 \\ 0 \end{bmatrix}, \tag{4.129}$$

where j_1 and j_2 are only functions of z. A downloadable copy of the program used to compute these solutions in mathematica is at "http://www.its.caltech.edu/~jscheel/". Putting it all together, the total solution for V_3 is

$$\begin{aligned} V_3 &= -\frac{(DA_1)}{2k} e^{ikx} \partial_k \bar{\mathcal{V}} + A_3 e^{ikx} \bar{\mathcal{V}} + \partial_Y A_2 e^{ikx} \bar{\mathcal{V}}_{1p} + \frac{i}{2k} \partial_Y^2 A_1 e^{ikx} \bar{\mathcal{V}}_{2p} + \frac{i}{2k^2} \partial_Y D A_0 e^{ikx} \bar{\mathcal{V}}_{3p} \\ &\quad + 2A_0 A_1 e^{2ikx} \bar{F}_0 + A_0 \partial_Y A_0 e^{2ikx} \bar{I} + (A_0 A_1^*) \bar{G} + cc + \partial_Y (|A_0|^2) \bar{J}. \end{aligned} \tag{4.130}$$

4.A.7 Order $\epsilon^{3/2}$

Next we need to solve

$$L_0 V_4 + L_1 V_3 + L_2 V_2 + L_3 V_0 = N_3(V_0, V_1, V_2). \tag{4.131}$$

Since we will impose our solvability condition here, this one is a bit easier than it first appears. We will not need to solve for the general form of V_4, but we only want the terms of the secular form e^{ikx}, which we will need to eliminate as our solvability condition. Note these terms did arise in the previous four orders, but they naturally vanished when the inner product (4.206) was formed.

By analogy to the $\epsilon^{5/4}$ case, V_4 will contain all the linear terms in V_3, but with the subscripts incremented by one:

$$V_{4\text{foc}} = -\frac{(DA_2)}{2k}e^{ikx}\partial_k\bar{\mathcal{V}} + A_4 e^{ikx}\bar{\mathcal{V}} + \partial_Y A_3 e^{ikx}\bar{\mathcal{V}}_{1p} + \frac{i}{2k}\partial_Y^2 A_2 e^{ikx}\bar{\mathcal{V}}_{2p} + \frac{i}{2k^2}\partial_Y DA_1 e^{ikx}\bar{\mathcal{V}}_{3p}. \tag{4.132}$$

Now our extra linear terms are

$$L_0\tilde{V}_{4\text{ex}} = -L_1\left[\frac{i}{2k^2}\partial_Y DA_0 e^{ikx}\bar{\mathcal{V}}_{3p}\right] - L_2\left[-\frac{(DA_0)}{2k}e^{ikx}\partial_k\bar{\mathcal{V}} + \frac{i}{2k}\partial_Y^2 A_0 e^{ikx}\bar{\mathcal{V}}_{2p}\right] - L_3V_0. \tag{4.133}$$

Now, lets work a bit on the L_3V_0 term, again using (4.212) and (4.107):

$$L_3V_0 = \frac{\partial_X^2 A_0}{2k}L_0 e^{ikx}\partial_k\bar{\mathcal{V}} + \frac{i\partial_X^2 A_0}{2k}L_{2n}e^{ikx}\bar{\mathcal{V}} - R_c A_0 e^{ikx}\begin{bmatrix}0\\0\\0\\\bar{W}\\0\end{bmatrix}. \tag{4.134}$$

So, by one redefinition

$$\tilde{V}_{4\text{ex}} = V'_{4\text{ex}} - \frac{(\partial_X^2 A_0)}{2k}e^{ikx}\partial_k\bar{\mathcal{V}}, \tag{4.135}$$

and by one more redefinition

$$V'_{4\text{ex}} = \tilde{V}'_{4\text{ex}} - \frac{1}{4k^3}\partial_Y^2 DA_0 e^{ikx}\bar{\mathcal{V}}_{4p} + \frac{i}{2k}\partial_X^2 A_0 e^{ikx}\bar{\mathcal{V}}_{2p}, \tag{4.136}$$

where

$$\bar{\mathcal{V}}_{4p} = \begin{bmatrix} \partial_k \bar{U} - \bar{U}/k \\ \partial_k \bar{V} - \bar{V}/k \\ 0 \\ 0 \\ 0 \end{bmatrix}, \tag{4.137}$$

as found in (4.223), and $\bar{\mathcal{V}}_{2p}$ is given by (4.116).

Putting this all together we get

$$L_0 \tilde{V}'_{4\text{ex}} = \frac{1}{2k} D^2 A_0 e^{ikx} \begin{bmatrix} \partial_k \bar{U} + \frac{i}{2k} \partial_k \bar{P} \\ \partial_k \bar{V} \\ \partial_k \bar{W} \\ \partial_k \bar{\Theta} \\ \frac{i}{2k}(-\partial_k \bar{U} + \bar{U}/k) \end{bmatrix} - R_c A_0 e^{ikx} \begin{bmatrix} 0 \\ 0 \\ 0 \\ \bar{W} \\ 0 \end{bmatrix}. \tag{4.138}$$

It turns out to simplify things at the next order if we eliminate the $\partial_k \bar{P}$ term, and we can do that using (4.223), we then get

$$L_0 \tilde{V}_{4\text{lin}} = \frac{1}{2k} D^2 A_0 e^{ikx} \begin{bmatrix} \partial_k \bar{U} - \bar{U}/k \\ \partial_k \bar{V} - \bar{V}/k \\ \partial_k \bar{W} \\ \partial_k \bar{\Theta} \\ \frac{i}{k}(-\partial_k \bar{U} + \bar{U}/k) \end{bmatrix} - R_c A_0 e^{ikx} \begin{bmatrix} 0 \\ 0 \\ 0 \\ \bar{W} \\ 0 \end{bmatrix}, \tag{4.139}$$

where

$$\tilde{V}'_{4\text{ex}} = \tilde{V}_{4\text{lin}} + \frac{D^2 A_0}{4k^3} e^{ikx} \bar{\mathcal{V}}_{4p}. \tag{4.140}$$

The equation (4.139) can be rewritten in the following simpler form:

$$L_0\tilde{V}_{4\text{lin}} = \frac{1}{2k}D^2 A_0 e^{ikx} S_1 - A_0 e^{ikx} S_2. \tag{4.141}$$

We define

$$S_1 = \begin{bmatrix} \partial_k \bar{U} - \bar{U}/k \\ \partial_k \bar{V} - \bar{V}/k \\ \partial_k \bar{W} \\ \partial_k \bar{\Theta} \\ \frac{i}{k}(-\partial_k \bar{U} + \bar{U}/k) \end{bmatrix} \tag{4.142}$$

and

$$S_2 = R_c \begin{bmatrix} 0 \\ 0 \\ 0 \\ \bar{W} \\ 0 \end{bmatrix}. \tag{4.143}$$

We will call $\tilde{V}_{4\text{lin}}$ the linear part of V_4 which contributes to the solvability condition. Note that $V_{4\text{foc}}$ (4.132) is not included since all of its terms (already solved for by solving for V_2, V_1, V_0) are zero when the solvability condition is imposed.

Let's now look at the dangerous non-linear terms, where we define the e^{ikx} terms of N_3 as

$$\tilde{N}_3(V_0, V_1, V_2) = \quad |A_0|^2 A_0 e^{ikx} S_3 + \partial_T A_0 e^{ikx} S_4, \tag{4.144}$$

where

$$S_3 = \begin{bmatrix} \sigma^{-1}(-ikf_1\bar{U} + \partial_z f_1 \bar{W} - f_3 \partial_z \bar{U}) \\ \sigma^{-1}(-2ikf_2\bar{U} + ikf_1\bar{V} + \partial_z f_2 \bar{W} - f_3 \partial_z \bar{V}) \\ \sigma^{-1}(\bar{W}(-ikf_1 + \partial_z f_3) + f_3(-2ik\bar{U} + \partial_z \bar{W})) \\ (-ikf_1\bar{\Theta} - 2ikf_4\bar{U} + f_3\partial_z\bar{\Theta} + \bar{W}(\partial_z f_4 + \partial_z g_4)) \\ 0 \end{bmatrix}, \quad (4.145)$$

and

$$S_4 = \begin{bmatrix} \sigma^{-1}\bar{U} \\ \sigma^{-1}\bar{V} \\ \sigma^{-1}\bar{W} \\ \bar{\Theta} \\ 0 \end{bmatrix}. \quad (4.146)$$

Working out the full solvability condition at this order, by combining the linear (4.141) and nonlinear (4.144) parts, gives

$$\begin{aligned} (V_0, L_0\tilde{V}_4) &= (V_0, S_4)\partial_T A_0 - (V_0, S_2)A_0 - 2k(V_0, S_1)(\partial_X - \frac{i}{2k}\partial_Y^2)^2 A_0 + (V_0, S_3)|A_0|^2 A_0 \\ &= 0. \end{aligned} \quad (4.147)$$

Substituting in (4.8) gives

$$\tau_0 \partial_T \bar{A}_0 - \bar{A}_0 - \xi_0^2(\partial_X - \frac{i}{2k}\partial_Y^2)^2 \bar{A}_0 + g_0|\bar{A}_0|^2\bar{A}_0 = 0, \quad (4.148)$$

where our coefficients are defined by

$$\begin{aligned} \tau_0 &= \frac{(V_0, S_4)}{(V_0, S_2)}, \\ \xi_0^2 &= \frac{2k(V_0, S_1)}{(V_0, S_2)}, \quad \text{and} \\ g_0 &= \frac{\beta^2(V_0, S_3)}{(V_0, S_2)}. \end{aligned} \quad (4.149)$$

For comparison with previous theoretical results [31], we will need to define our normalization α^2 as is described in Appendix 4.F. Note that A_0', g_0' are the appropriately normalized values (4.225):

$$\tau_0 \partial_T A_0' - A_0' - \xi_0^2 (\partial_X - \frac{i}{2k}\partial_Y^2)^2 A_0' + g_0' |A_0'|^2 A_0' = 0. \tag{4.150}$$

Equation (4.150) is the same as (4.10). A downloadable copy of the program used to compute the coefficients in mathematica is at "http://www.its.caltech.edu/~jscheel/".

Finally, for the next section we will need the full form of V_4:

$$\begin{aligned} V_4 &= -\frac{(DA_2)}{2k} e^{ikx} \partial_k \bar{\mathcal{V}} + A_4 e^{ikx} \bar{\mathcal{V}} + \partial_Y A_3 e^{ikx} \bar{\mathcal{V}}_{1p} + \frac{i}{2k} \partial_Y^2 A_2 e^{ikx} \bar{\mathcal{V}}_{2p} \\ &+ \frac{i}{2k^2} \partial_Y D A_1 e^{ikx} \bar{\mathcal{V}}_{3p} - \frac{(\partial_X^2 A_0)}{2k} e^{ikx} \partial_k \bar{\mathcal{V}} + \frac{1}{4k^3} (-\partial_Y^2 D + D^2) A_0 e^{ikx} \bar{\mathcal{V}}_{4p} \\ &+ \frac{i}{2k} \partial_X^2 A_0 e^{ikx} \bar{\mathcal{V}}_{2p} + L_0^{-1} (\tilde{N}_3 + \frac{1}{2k} D^2 A_0 e^{ikx} S_1 - A_0 e^{ikx} S_2) + cc. \end{aligned} \tag{4.151}$$

We have not formally inverted the L_0 operator in the last line because we only want to obtain the amplitude equation at the next order.

4.A.7.1 Comparisons to $\Omega = 0$ case

For the $\Omega = 0$ case, there is no vorticity, so $\zeta = 0$ (4.57) and hence $\psi = 0$ (4.65) in our potential formulation. This eliminates one of our equations in (4.66), the "vorticity-like" equation (always the middle one in each of our operators), and simplifies things enormously. With $\Omega = 0$, we find for our marginal stability analysis that $R_c = 1707.672$ and $k_c \equiv k = 3.117$.

Substituting these values into (4.84) gives the values:

$$\begin{aligned} q_1 &= 3.974i, \\ q_2 &= 5.195 - 2.126i, \quad \text{and} \\ q_3 &= 5.195 + 2.126i. \end{aligned} \tag{4.152}$$

Plugging (4.152) into (4.89,4.82,4.81) yields the following first order functions:

$$\begin{aligned}\Phi &= \cosh(q_1 z) + [-(0.03075 + 0.05193i)\cosh(q_2 z) + cc] \quad \text{and} \\ \Theta &= 650.53\cosh(q_1 z) + [(39.262 + 0.434i)\cosh(q_2 z) + cc]\,, \end{aligned} \tag{4.153}$$

where we have set the normalization so the coefficient of the $\cosh(q_1 z)$ term in Φ is one. This agrees with Cross [30] to the last two decimal places.

There is also an overall general normalization α that is described in Appendix 4.F. Results for the coefficients for $\Omega = 0$ and $\sigma = 0.93$ are in agreement to three decimal places:

From (4.149):

$$\begin{aligned}\tau_0 &= 0.079, \\ \xi_0^2 &= 0.148, \quad \text{and} \\ g_0' &= 0.704. \end{aligned} \tag{4.154}$$

Expected [31]:

$$\begin{aligned}\tau_0 &= \left(\frac{19.65\sigma}{\sigma + 0.5117}\right)^{-1} = 0.079, \\ \xi_0^2 &= 0.148, \quad \text{and} \\ g_0' &= 0.6995 - \frac{0.0047}{\sigma} + \frac{0.0083}{\sigma^2} = 0.704. \end{aligned} \tag{4.155}$$

4.A.8 Order $\epsilon^{7/4}$

Finally we need to solve

$$L_0 V_5 + L_1 V_4 + L_2 V_3 + L_3 V_1 = N_4(V_0, V_1, V_2, V_3). \tag{4.156}$$

Again, by defining away the terms identical to previous orders:

$$V_{5\text{foc}} = -\frac{(DA_3)}{2k}e^{ikx}\partial_k\bar{\mathcal{V}} + A_5e^{ikx}\bar{\mathcal{V}} + \partial_Y A_4 e^{ikx}\bar{\mathcal{V}}_{1p} + \frac{i}{2k}\partial_Y^2 A_3 e^{ikx}\bar{\mathcal{V}}_{2p} + \frac{i}{2k^2}\partial_Y DA_2 e^{ikx}\bar{\mathcal{V}}_{3p}. \tag{4.157}$$

We then get

$$\begin{aligned} &L_0\tilde{V}_5' + L_1\left[-\tfrac{(\partial_X^2 A_0)}{2k}e^{ikx}\partial_k\bar{\mathcal{V}} + \tfrac{1}{4k^3}(-\partial_Y^2 D + D^2)A_0e^{ikx}\bar{\mathcal{V}}_{4p} + \tfrac{i}{2k}\partial_X^2 A_0 e^{ikx}\bar{\mathcal{V}}_{2p}\right] \\ &+L_2\left[\tfrac{i}{2k^2}\partial_Y DA_0e^{ikx}\bar{\mathcal{V}}_{3p}\right] + L_3\left[\partial_Y A_0e^{ikx}\left(\bar{\mathcal{V}}_{1p}\right)\right] + L_1L_0^{-1}(N_3 + \tfrac{1}{2k}D^2A_0e^{ikx}S_1 - A_0e^{ikx}S_2) \\ &= N_4(V_0,V_1,V_2,V_3) + \tfrac{1}{2k}D^2A_1e^{ikx}S_1 - A_1e^{ikx}S_2, \end{aligned} \tag{4.158}$$

where $\tilde{V}_5' = V_{5\text{ex}} + V_{5\text{nl}}$. The last two terms above are included by analogy to the $\tilde{V}_4$ solution. With one more redefinition:

$$\tilde{V}_5' = \tilde{V}_5 + \frac{i}{2k^2}\partial_X^2\partial_Y A_0e^{ikx}\bar{\mathcal{V}}_{3p}, \tag{4.159}$$

and plenty of algebra, we obtain

$$\begin{aligned} &L_0\tilde{V}_5 + \tfrac{i}{2k^2}\partial_Y D^2A_0e^{ikx}\bar{\mathcal{V}}_{3p} + L_1L_0^{-1}(\tilde{N}_3 + \tfrac{1}{2k}D^2A_0e^{ikx}S_1 - A_0e^{ikx}S_2) \\ &= \tilde{N}_4(V_0,V_1,V_2,V_3) + \tfrac{1}{2k}D^2A_1e^{ikx}S_1 - A_1e^{ikx}S_2, \end{aligned} \tag{4.160}$$

where $\tilde{V}_5$ is the solution to the parts which will contribute to the solvability condition and hence amplitude equation at this order.

We will now focus on reducing the left-hand side (LHS). If we rename

$$G = \tilde{N}_3 + \frac{1}{2k}D^2A_0e^{ikx}S_1 - A_0e^{ikx}S_2 \tag{4.161}$$

and

$$F = \frac{i}{2k^2}\partial_Y D^2A_0e^{ikx}\bar{\mathcal{V}}_{3p} \tag{4.162}$$

we have

$$\text{LHS} = L_0\tilde{V}_5 + F + L_1L_0^{-1}(G). \tag{4.163}$$

We know from the solvability condition at order $\epsilon^{3/2}$ that

$$(V_0, G) = 0. \tag{4.164}$$

At order $\epsilon^{7/4}$, we will form the following inner products IP in imposing our solvability condition:

$$\text{IP} = (V_0, L_1L_0^{-1}G) + (V_0, F). \tag{4.165}$$

Let's focus on the first term and perform a little matrix algebra:

$$\begin{aligned}(V_0, L_1L_0^{-1}G) &= \int V_0^\dagger L_1 L_0^{-1} G, \\ &= -\int V_1^\dagger L_0 L_0^{-1} G, \\ &= -\int V_1^\dagger G, \quad \text{and} \\ &= -(V_1, G). \end{aligned} \tag{4.166}$$

We have used the following identity in the second line of (4.166): by taking the adjoint of (4.100) at order $\epsilon^{3/4}$, we get

$$\begin{aligned} V_1^\dagger L_0^\dagger = -V_0^\dagger L_1^\dagger \quad &\text{and} \\ V_1^\dagger L_0 = -V_0^\dagger L_1, \end{aligned} \tag{4.167}$$

and the second line in (4.167) holds true since L_0 and L_1 are self-adjoint for our inner product (4.206). By inserting (4.102) into (4.166), we get

$$(V_0, L_1L_0^{-1}G) = -(V_1, G) = -A_0 e^{-ikx}\partial_Y(\bar{\mathcal{V}}_{1p}, G), \tag{4.168}$$

where we have used (4.164) to remove the $A_1 e^{ikx}\bar{\mathcal{V}}$ term of V_1. So now,

$$\text{IP} = -A_0 e^{-ikx}\partial_Y(\bar{\mathcal{V}}_{1p}, G) + (V_0, F). \tag{4.169}$$

Next we will focus on the linear terms of (4.169):

$$\text{LI}: \quad -A_0 e^{-ikx}\partial_Y(\bar{\mathcal{V}}_{1p}, \frac{1}{2k}D^2 A_0 e^{ikx}S_1 - A_0 e^{ikx}S_2) + \frac{i}{2k^2}\partial_Y D^2 A_0 e^{ikx}(V_0, \bar{\mathcal{V}}_{3p}), \tag{4.170}$$

which equals zero as long as the correct inner product (4.206) is used. Now, let's focus on the rest of IP (i.e., $\tilde{N}_3$) using (4.144):

$$\begin{aligned} \text{IP} &= -A_0 e^{-ikx}\partial_Y(\bar{\mathcal{V}}_{1p}, |A_0|^2 A_0 e^{ikx}S_3 + \partial_T A_0 e^{ikx}S_4) \quad \text{and} \\ &= -A_0\partial_Y(|A_0|^2 A_0)(\bar{\mathcal{V}}_{1p}, S_3) - A_0\partial_Y\partial_T A_0(\bar{\mathcal{V}}_{1p}, S_4). \end{aligned} \tag{4.171}$$

Returning to the full solvability condition (4.160), we now obtain

$$(V_0, L_0\tilde{V}_5) = -\text{IP} + (V_0, \tilde{N}_4(V_0, V_1, V_2, V_3)) + \frac{1}{2k}D^2 A_1 e^{ikx}(V_0, S_1) - A_1 e^{ikx}(V_0, S_2). \tag{4.172}$$

If we work out the dangerous terms in $\tilde{N}_4$, we obtain

$$\begin{aligned} \tilde{N}_4 &= \partial_{T'} A_0 e^{ikx}S_4 + \partial_T A_1 e^{ikx}S_4 + \sigma^{-1}\partial_Y\partial_T A_0 e^{ikx}\bar{\mathcal{V}}_{1p} \\ &+ 2|A_0|^2 A_1 e^{ikx}S_3 + A_0^2 A_1^* e^{ikx}S_3 + |A_0|^2\partial_Y A_0 e^{ikx}T_1 + A_0^2\partial_Y A_0^* e^{ikx}T_2, \end{aligned} \tag{4.173}$$

where S_3-S_4 were defined at order $\epsilon^{3/2}$ (4.145-4.146), and T_1, T_2 are new at this order and are too big to include here.

When (4.173) is inserted into (4.172), note that the $\partial_Y\partial_T$ term in (4.173) will cancel with the second term in (4.171). The first term in (4.171) will combine with

the last two terms of (4.173). The final form for the amplitude equation at this order is then

$$\begin{aligned}(V_0, L_0\tilde{V}_5) &= (V_0,S_4)\partial_{T'}A_0 + (V_0,S_4)\partial_T A_1 - (V_0,S_2)A_1 - 2k(V_0,S_1)(\partial_X - \frac{i}{2k}\partial_Y^2)^2 A_1 \\ &+ 2(V_0,S_3)|A_0|^2 A_1 + (V_0,S_3)A_0^2 A_1^* + (V_0,X)A_0\partial_Y(|A_0|^2), \\ &= 0. \end{aligned} \tag{4.174}$$

The variable X is determined algebraically from the first term of (4.171) and the T_1 and T_2 terms of $\tilde{N}_4$. After simplification of these three terms (can be proven via symmetry too), one obtains the same coefficient, X, for the $|A_0|^2\partial_Y A_0$ term as for the $A_0^2\partial_Y A_0^*$ term. Substituting in (4.8) gives

$$\begin{aligned}&\tau_0\partial_{T'}\bar{A}_0 + \tau_0\partial_T\bar{A}_1 - \bar{A}_1 - \xi_0^2(\partial_X - \tfrac{i}{2k}\partial_Y^2)^2\bar{A}_1 \\ &+2g_0|\bar{A}_0|^2\bar{A}_1 + g_0\bar{A}_0^2\bar{A}_1^* + ig_{\rm cor}\bar{A}_0\partial_Y(|\bar{A}_0|^2) = 0,\end{aligned} \tag{4.175}$$

where τ_0, ξ_0, and g_0 are as defined in (4.149), and

$$g_{\rm cor} = \frac{\beta^2(V_0,X)}{i(V_0,S_2)}. \tag{4.176}$$

Finally, we add in our normalization from Appendix 4.F:

$$\begin{aligned}&\tau_0\partial_{T'}A_0' + \tau_0\partial_T A_1' - A_1' - \xi_0^2(\partial_X - \tfrac{i}{2k}\partial_Y^2)^2 A_1' \\ &+2g_0'|A_0'|^2 A_1' + g_0' A_0'^2 A_1'^* + ig_{\rm cor}' A_0'\partial_Y(|A_0'|^2) = 0,\end{aligned} \tag{4.177}$$

where $A_0', g_0', g_{\rm cor}'$ are the appropriately normalized values (4.225). Equation (4.177) is the same as (4.11). A downloadable copy of the program used to compute the coefficients in mathematica is at "http://www.its.caltech.edu/~jscheel/".

Appendix 4.B Mean Flow

Mean flow [34, 82, 28] corresponds to the following terms in the solution to the Boussinesq equations:

$$\begin{aligned} U_{\mathrm{m}}(X,Y,T,T') &= \frac{k}{2\pi}\int_0^{2\pi/k}\int_{-1/2}^{1/2} u(x,z,X,Y,T,T')dzdx \quad \text{and} \\ V_{\mathrm{m}}(X,Y,T,T') &= \frac{k}{2\pi}\int_0^{2\pi/k}\int_{-1/2}^{1/2} v(x,z,X,Y,T,T')dzdx. \end{aligned} \tag{4.178}$$

Hence, only $k = 0$ terms are left.

Mean flow is difficult to include in a potential formulation, since the boundary conditions are somewhat arbitrary and the pressure is no longer directly in our equations. However, mean flow becomes much more transparent in our formulation, where the pressure is always present, and the boundary conditions are quite clear.

The need to consider mean flow arose when we considered the simple case of rigid boundaries in the y-direction and periodic in the x-direction. When we solved (4.130) for u and v to order $\epsilon^{5/4}$ and then computed the mean flow using (4.178), we found a non-zero mean flow in the y-direction ($V_m \neq 0$). However, we expect the sidewalls to quench the mean flow and redirect it in the periodic x direction where it can flow uninterrupted. Hence, we needed to look more carefully at the ambiguity in the g_5 term of equation (4.119).

The place mean flow can enter is in the $k = 0$ pressure term. Since the pressure term is not constrained by any boundary conditions, the operator L_0 admits a z-constant $k = 0$ solution at each order. We expect the mean flow to enter at order $\epsilon^{\frac{5}{4}}$, since this is where we see the first non-zero contribution to the $k = 0$ solutions from the pattern textures. If we looked at the $k = 0$ solutions to the momentum part of the Boussinesq equations (2.16), this would correspond to a non-zero Reynolds-stress term entering at order $\epsilon^{\frac{5}{4}}$. Pressure gradients build up to counteract this. Hence, we expect an extra non-zero contribution to the pressure at order ϵ:

$$V_2^{\mathrm{P2}} = \begin{bmatrix} 0 \\ 0 \\ 0 \\ 0 \\ Q_2(X,Y,T,T') \end{bmatrix}. \tag{4.179}$$

This is a solution to $L_0 V_2^{\mathrm{P2}} = 0$ that satisfies the boundary conditions (2.24-2.26) for any Q_2 that is a function of X, Y, T, T' only.

Then, at the next higher order (4.42) we obtain $L_0 V_3^{\mathrm{P2}} = -L_1 V_2^{\mathrm{P2}}$, where

$$V_3^{\mathrm{P2}} = \begin{bmatrix} u_3^{\mathrm{P2}} \\ v_3^{\mathrm{P2}} \\ 0 \\ 0 \\ 0 \end{bmatrix}. \tag{4.180}$$

This becomes

$$\begin{aligned} \partial_z^2 u_3^{\mathrm{P2}} + 2\Omega v_3^{\mathrm{P2}} &= 0 \quad \text{and} \\ -2\Omega u_3^{\mathrm{P2}} + \partial_z^2 v_3^{\mathrm{P2}} &= \partial_Y Q_2. \end{aligned} \tag{4.181}$$

This has the solution

$$u_3^{\mathrm{P2}} = \frac{1}{2\Omega}\partial_Y Q_2 \left(\Re[\beta(z)] - 1\right) \quad \text{and} \tag{4.182}$$

$$v_3^{\mathrm{P2}} = \frac{1}{2\Omega}\partial_Y Q_2 \Im[\beta(z)], \tag{4.183}$$

where

$$\beta(z) = \frac{\cosh[\omega z]}{\cosh[\frac{\omega}{2}],} \tag{4.184}$$

and $\omega = \sqrt{\Omega}(1+i)$. We will stop here, since we are only interested in the lowest order contribution due to the mean flow. Note this will first show up in the amplitude equation at order $\epsilon^{\frac{7}{4}}$.

Now these $k = 0$ solutions will contribute to the mean flow incompressibility condition (2.18),

$$\partial_X U_{\mathrm{m}}(X, Y, T, T') + \partial_Y V_{\mathrm{m}}(X, Y, T, T') = 0, \tag{4.185}$$

at order $\epsilon^{6/4}$. Due to the pattern textures, we have other mean flow terms, $V_{3\mathrm{m}}^{\mathrm{rot}}$, coming in at order $\epsilon^{6/4}$, also contributing to the incompressibility condition. The non-zero Q_2 is set up to counteract this, which motivated the above discussion.

$$O(\epsilon^{6/4}): \qquad \partial_Y V_{3\mathrm{m}}^{\mathrm{P2}} + \partial_Y V_{3\mathrm{m}}^{\mathrm{rot}} = 0, \tag{4.186}$$

where

$$\begin{aligned} V_{3\mathrm{m}}^{\mathrm{P2}} &= \tfrac{1}{2\Omega}\partial_Y Q_2 \textstyle\int \Im[\beta(z)]dz, \\ V_{3\mathrm{m}}^{\mathrm{rot}} &= \partial_Y(|A_0|^2) \textstyle\int j_2(z)dz, \end{aligned} \tag{4.187}$$

and $j_2(z)$ is defined in (4.129). This provides us with a relation between Q_2 and A_0:

$$\partial_Y^2 Q_2 = -\gamma \partial_Y^2(|A_0|^2), \tag{4.188}$$

where

$$\gamma = 2\Omega \frac{\int j_2(z)dz}{\int \Im[\beta(z)]dz}. \tag{4.189}$$

Solving (4.188) gives

$$Q_2 = -\gamma(|A_0|^2) + c. \tag{4.190}$$

The integration term proportional to Y is zero in order to satisfy the boundary conditions (2.24-2.26). We also find that the integration constant term c will drop out of our analysis.

One can think of j_2, and hence the j_2 part of v_3 (i.e., the $k = 0$ part), as being modified by (4.183):

$$v_3^{\mathrm{k=0}} = \partial_Y(|A_0|^2)\left[j_2[z] - \frac{\gamma}{2\Omega}\Im[\beta(z)]\right]. \tag{4.191}$$

Likewise, the u_3 term is modified by (4.182)

$$u_3^{\mathrm{k=0}} = \partial_Y(|A_0|^2)\left[j_1[z] - \frac{\gamma}{2\Omega}\left[\Re[\beta(z)] - 1\right]\right]. \tag{4.192}$$

When we insert (4.191) and (4.192) into (4.178), we find $V_{\mathrm{m}} = 0$ and $U_{\mathrm{m}} \neq 0$ up to order $\epsilon^{5/4}$.

Finally, note that the g_5 term in (4.119) is no longer ambiguous (up to the constant c, which drops out of the analysis):

$$g_5^{k=0} = g_5 + Q_2. \tag{4.193}$$

If there is no rotation, i.e., $\Omega \to 0$, then the j_1 term is zero. If we take the limit as $\Omega \to 0$ in (4.182) and (4.183), we obtain

$$u_3^{\mathrm{P2}} = 0 \quad \text{and} \tag{4.194}$$

$$v_3^{\mathrm{P2}} = \partial_Y Q_2\left(\frac{z^2 - 1/4}{2}\right). \tag{4.195}$$

This is the usual form for the Poiseuille profile. In either case of rotation or no

rotation, the pattern textures cause a non-zero y-component to the mean flow at order $\epsilon^{5/4}$. In order to satisfy incompressibility at order $\epsilon^{6/4}$, a y-dependent pressure must build up. Hence, one finds a non-zero Q_2 contribution to the pressure at order ϵ. However, for the case of no rotation, everything occurs in the y-direction, so the pressure cancels the non-zero mean flow from the pattern and the total mean flow is zero at order $\epsilon^{5/4}$. However, in the case of rotation, the new terms due to the Coriolis force cause the y-dependent pressure to drive a non-zero x mean flow at order $\epsilon^{5/4}$.

Note that our above formulation works best with periodic (where there is no quenching of mean flow) or partially rigid boundaries, since the mean flow is only quenched in the y-direction and allowed to flow freely in the x-direction. For fully rigid boundaries, we expect the mean flow to be zero at all the boundaries. Since the mean flow is proportional to the amplitude A_0, as long as the amplitude goes to zero at the boundaries, so will the mean flow. Since the amplitude falls of as $\sqrt{\epsilon}$ in the x-direction instead of $\epsilon^{1/4}$ as in the y-direction, our formulation to order $\epsilon^{5/4}$ is still valid. However, we do need to go to the next higher order to get corrections to this which will cause quenching in the x-direction and a flow in the y-direction, resulting in a net circulation, as should be the case with fully rigid boundaries.

Appendix 4.C Solvability Condition

When performing a perturbation analysis, such that the first-order problem is homogeneous but the higher orders are inhomogeneous, one needs to be careful to eliminate secular terms (those resonant with the first order solution) by imposing certain solvability conditions [81]. This is discussed in Section 2.3. The simplest is to make sure none of the inhomogeneous terms drive any eigenvector with zero eigenvalue (i.e., are resonant with the first order homogeneous solution). Let's start by writing our perturbation solution to first (4.39) and second order (4.40) as

$$L_0 V_0 = 0 \quad \text{and} \tag{4.196}$$

$$L_0 V_1 = G, \tag{4.197}$$

where $G = -L_1 V_0$ is the driving term. The form for V_0 is given in (4.7) and for V_1 in (4.101). We define the following inner product (the star denotes complex conjugation),

$$\begin{aligned}(V_i, V_j) &= \frac{k}{2\pi}\int\int V_i^\dagger V_j dx dz \quad \text{and} \\ &= \frac{k}{2\pi}\int_0^{2\pi/k} dx \int_{-1/2}^{1/2} dz A_i^* A_j e^{i(k_j - k_i)x}\left[\bar{U}_i^*\bar{U}_j + \bar{V}_i^*\bar{V}_j + \bar{W}_i^*\bar{W}_j + \bar{P}_i^*\bar{P}_j + \frac{\bar{\Theta}_i^*\bar{\Theta}_j}{R_c}\right],\end{aligned} \tag{4.198}$$

where we have added the R_c to help make the operator L_0 more self-adjoint [30]. We define the adjoint of L_0 as follows: If

$$L_0 V_i = \lambda_i V_i \tag{4.199}$$

is an eigenvalue equation for L_0, then

$$L_0^\dagger V_i^\dagger = \lambda_i^* V_i^\dagger \tag{4.200}$$

is the adjoint equation, where the adjoint operator is defined to have the property

$$(V_i, L_0^\dagger V_j) = (V_j, L_0 V_i)^*. \tag{4.201}$$

Then, for an arbitrary vector W_0 operating on $L_0 V_1$,

$$(W_0, L_0 V_1) = (L_0^\dagger W_0, V_1). \tag{4.202}$$

If W_0 is $V_0^\dagger$, the eigenvector of $L_0^\dagger$, the adjoint to L_0 with an eigenvalue of zero, then the second term is zero. This implies

$$(W_0, L_0 V_1) = (V_0, G) = 0. \tag{4.203}$$

So, unless V_1 is orthogonal to L_0 (and hence is a trivial solution), then G must be orthogonal to $V_0^\dagger$.

Note, as long as L_0 is self-adjoint, $V_0^\dagger$ is trivial to find: we simply take the complex

conjugate of the transpose of V_0. In our case, the adjoint is still rather easy to find, since the only reason it is not self-adjoint is because of the asymmetric $\bar{V}$ term in (4.45). Our V_0 is defined as in (4.7), and we find if we define

$$V_0^\dagger = A_0^* e^{-ikx} \left[\bar{U}^*, -\bar{V}^*, \bar{W}^*, \bar{\Theta}^*, \bar{P}^*\right], \tag{4.204}$$

then the product

$$(\bar{V}_0, L_0 \bar{V}_0)^\dagger = (\bar{V}_0, L_0 \bar{V}_0) \tag{4.205}$$

gives us a self-adjoint relation. Hence, all scalar products with the adjoint eigenvector will have the form

$$(V_0, V_j) = \tfrac{k}{2\pi} \int_0^{2\pi/k} dx \int_{-1/2}^{1/2} dz A_0^* A_j e^{i(k_j - k)x} \left[\bar{U}_0^* \bar{U}_j - \bar{V}_0^* \bar{V}_j + \bar{W}_0^* \bar{W}_j + \bar{P}_0^* \bar{P}_j + \tfrac{\bar{\Theta}_0^* \bar{\Theta}_j}{R_c}\right]. \tag{4.206}$$

Appendix 4.D Minimization in k

We evaluate the linear operator in the following way:

$$L_0 \left[e^{ikx} A_0 \bar{\mathcal{V}}\right] = e^{ikx} A_0 L_{0k} \bar{\mathcal{V}} = 0 \rightarrow L_{0k} \bar{\mathcal{V}} = 0, \tag{4.207}$$

where

$$L_{0k} = \begin{bmatrix} \partial_z^2 - k^2 & 2\Omega & 0 & 0 & -ik \\ -2\Omega & \partial_z^2 - k^2 & 0 & 0 & 0 \\ 0 & 0 & \partial_z^2 - k^2 & 1 & -\partial_z \\ 0 & 0 & R_c & \partial_z^2 - k^2 & 0 \\ ik & 0 & \partial_z & 0 & 0 \end{bmatrix}. \tag{4.208}$$

Then we can differentiate $L_{0k}\bar{\mathcal{V}} = 0$ with respect to k. We obtain

$$\partial_k(L_{0k}\bar{\mathcal{V}}) = L_{0k}\partial_k\bar{\mathcal{V}} + (\partial_k L_{0k})\bar{\mathcal{V}} = 0, \tag{4.209}$$

where

$$\partial_k L_{0k} = \begin{bmatrix} -2k & 0 & 0 & 0 & -i \\ 0 & -2k & 0 & 0 & 0 \\ 0 & 0 & -2k & 0 & 0 \\ 0 & 0 & 0 & -2k & 0 \\ i & 0 & 0 & 0 & 0 \end{bmatrix}. \tag{4.210}$$

As a consequence of expanding about the minimum R_c, we have taken advantage of the fact that

$$\partial_k R_c(k) = 0. \tag{4.211}$$

We then get the following identity:

$$L_{0k}\partial_k\bar{\mathcal{V}} = -(\partial_k L_{0k})\bar{\mathcal{V}}. \tag{4.212}$$

Appendix 4.E Rotational Invariance

If the linear solution at wavevector $k\hat{x}$ is $V_0 = A_0\bar{\mathcal{V}}e^{ikx}$ with $\bar{\mathcal{V}}$ given in (4.9), then the form given by rotating through an angle θ is

$$V_0 = A_0\bar{\mathcal{V}}(\theta)e^{ik(x\cos\theta + y\sin\theta)}, \tag{4.213}$$

where

$$\bar{\mathcal{V}}(\theta) = [\bar{U}\cos\theta - \bar{V}\sin\theta, \bar{U}\sin\theta + \bar{V}\cos\theta, \bar{W}, \bar{\Theta}, \bar{P}] \tag{4.214}$$

is also a solution if the system is rotationally invariant. Just as in (4.207), the linear equation for this solution is $L_0 V_0 = 0 \rightarrow L_k(\theta)\bar{\mathcal{V}}(\theta) = 0$, where

$$L_k(\theta) = \begin{bmatrix} -k^2 + \partial_z^2 & 2\Omega & 0 & 0 & -ik\cos\theta \\ -2\Omega & -k^2 + \partial_z^2 & 0 & 0 & -ik\sin\theta \\ 0 & 0 & -k^2 + \partial_z^2 & 1 & -\partial_z \\ 0 & 0 & R_c & -k^2 + \partial_z^2 & 0 \\ ik\cos\theta & ik\sin\theta & \partial_z & 0 & 0 \end{bmatrix}. \tag{4.215}$$

We can get the relationships implied by the rotational invariance by differentiating $L_k(\theta)\bar{\mathcal{V}}(\theta) = 0$ with respect to θ and then evaluating at $\theta = 0$. Note that $L_k(\theta = 0) = L_{0k}$ is given by (4.208). Also, we will make use of (4.211).

Differentiating once with respect to θ gives

$$(\partial_\theta L_k(\theta))\bar{\mathcal{V}}(\theta) + L_k(\theta)(\partial_\theta \bar{\mathcal{V}}(\theta)) = 0. \tag{4.216}$$

Evaluating this at $\theta = 0$ gives the identity

$$L_{0k} \begin{bmatrix} -\bar{V} \\ \bar{U} \\ 0 \\ 0 \\ 0 \end{bmatrix} = \begin{bmatrix} 0 \\ ik\bar{P} \\ 0 \\ 0 \\ -ik\bar{V} \end{bmatrix}. \tag{4.217}$$

Similarly, differentiating twice with respect to θ gives

$$(\partial_\theta^2 L_k(\theta))\bar{\mathcal{V}}(\theta) + 2(\partial_\theta L_k(\theta))(\partial_\theta \bar{\mathcal{V}}(\theta)) + L_k(\theta)(\partial_\theta^2 \bar{\mathcal{V}}(\theta)) = 0, \tag{4.218}$$

and leads to the identity

$$L_{0k}\begin{bmatrix}\bar{U}\\ \bar{V}\\ 0\\ 0\\ 0\end{bmatrix} = \begin{bmatrix}ik\bar{P}\\ 0\\ 0\\ 0\\ ik\bar{U}\end{bmatrix}. \tag{4.219}$$

Next we can differentiate (4.216) with respect to k and use (4.210), giving

$$L_{0k}\begin{bmatrix}-\partial_k\bar{V}\\ \partial_k\bar{U}\\ 0\\ 0\\ 0\end{bmatrix} = \begin{bmatrix}-2k\bar{V}\\ ik\partial_k\bar{P}+2k\bar{U}\\ 0\\ 0\\ i\bar{V}-ik\partial_k\bar{V}\end{bmatrix} + \begin{bmatrix}0\\ i\bar{P}\\ 0\\ 0\\ -i\bar{V}\end{bmatrix}. \tag{4.220}$$

If we then substitute (4.217), then this reduces to

$$L_{0k}\begin{bmatrix}-\partial_k\bar{V}+\bar{V}/k\\ \partial_k\bar{U}-\bar{U}/k\\ 0\\ 0\\ 0\end{bmatrix} = \begin{bmatrix}-2k\bar{V}\\ ik\partial_k\bar{P}+2k\bar{U}\\ 0\\ 0\\ i\bar{V}-ik\partial_k\bar{V}\end{bmatrix}. \tag{4.221}$$

Likewise we can differentiate (4.218) with respect to k and obtain

$$L_{0k}\begin{bmatrix}\partial_k\bar{U}\\ \partial_k\bar{V}\\ 0\\ 0\\ 0\end{bmatrix} = \begin{bmatrix}ik\partial_k\bar{P}+2k\bar{U}\\ 2k\bar{V}\\ 0\\ 0\\ -i\bar{U}+ik\partial_k\bar{U}\end{bmatrix} + \begin{bmatrix}i\bar{P}\\ 0\\ 0\\ 0\\ i\bar{U}\end{bmatrix}. \tag{4.222}$$

If we substitute (4.219), we obtain

$$L_{0k}\begin{bmatrix} \partial_k\bar{U}-\bar{U}/k \\ \partial_k\bar{V}-\bar{V}/k \\ 0 \\ 0 \\ 0 \end{bmatrix} = \begin{bmatrix} ik\partial_k\bar{P}+2k\bar{U} \\ 2k\bar{V} \\ 0 \\ 0 \\ -i\bar{U}+ik\partial_k\bar{U} \end{bmatrix}. \tag{4.223}$$

Appendix 4.F Normalization Condition

There is an overall general normalization. The convention is to scale the amplitude such that $(\mathcal{N}-1)R/R_c = |A_0'|^2$, where A_0' is the appropriately normalized amplitude and $\mathcal{N}$ is the reduced Nusselt number (2.27).

The reduced Nusselt number can be found by taking the following average: $(\mathcal{N}-1)R/R_c = \langle w_0^*\theta_0\rangle/R_c$, where w_0 and θ_0 are defined in (4.2) and (4.7). Note that the average $\langle\ \rangle$ is over x and z, and we divide by R_c to be consistent with our inner product (4.206). We can adjust for this normalization by defining the quantity α: $|A_0'|^2 = (\mathcal{N}-1)R/R_c = \langle w_0^*\theta_0\rangle/R_c = \alpha^2|\bar{A}_0|^2$, where $\alpha \equiv \sqrt{\langle w_0^*\theta_0\rangle/(R_c|\bar{A}_0|^2)}$. Next note that the x integration of the $\langle w_0^*\theta_0\rangle$ term is trivial and gives us a factor of $2\beta^2$. Hence we are left with an average over z:

$$\alpha = \sqrt{2\beta^2\langle\bar{W}(z)\bar{\Theta}(z)\rangle/R_c}, \tag{4.224}$$

where $\bar{W}$ and $\bar{\Theta}$ are given by (4.93) and (4.94), respectively, and β is $1/\sqrt{2}$ as defined in (4.8).

We therefore define our normalized variables as

$$\begin{aligned} g_0' &= g_0/\alpha^2, \\ g_{\rm cor}' &= g_{\rm cor}/\alpha^2, \quad \text{and} \\ A_0' &= \alpha A_0. \end{aligned} \tag{4.225}$$

Chapter 5

Scaling Laws for Rotating Rayleigh-Bénard Convection

5.1 Introduction

In this section we study the scaling laws for the transition to the domain chaos state [99]. As mentioned in Section 1.3, rotating a Rayleigh-Bénard convection cell breaks the reflection symmetry. As a result, the system undergoes a supercritical bifurcation to a chaotic state, directly from the uniform state. A supercritical bifurcation is particularly useful to study since the new state evolves continuously out of the old state. If the bifurcation to chaos is smooth, then we can study the scaling laws near such a transition.

Küppers and Lortz [70, 69] predicted this supercritical bifurcation from a conducting state to an unstable convection state. The unstable convection state consists of straight parallel rolls which are unstable to rolls at a different, distinct orientation. For large Prandtl number (> 10), this orientational angle is about 60° with respect to the original. The Küppers-Lortz instability can be seen in Figure 5.2, where the dominant roll orientation is plotted as a function of time for simulations in a periodic geometry. After about 400 vertical diffusion times (enough to allow the transients to relax), the orientation of the rolls switches discretely. However, one can see that the time between switches gets longer and longer.[1] This is completely consistent with the

[1] This slowing down is seen for the duration of our simulation. It is possible that if the simulation is run out for longer, the switching time will become constant.

Figure 5.1: Snapshot of temperature deviation θ at the midplane for a domain chaos state with the following parameters: $\Gamma = 40$, $\sigma = 0.93$, $\Omega = 17.6$, $\epsilon = 0.068$, and $t = 430\,\tau_\nu$. Lateral temperature boundary conditions are conducting. The gray denotes the conduction value ($\theta = 0$), and the lighter and darker shades give the values above and below this, which range from θ = -0.15 to 0.15.

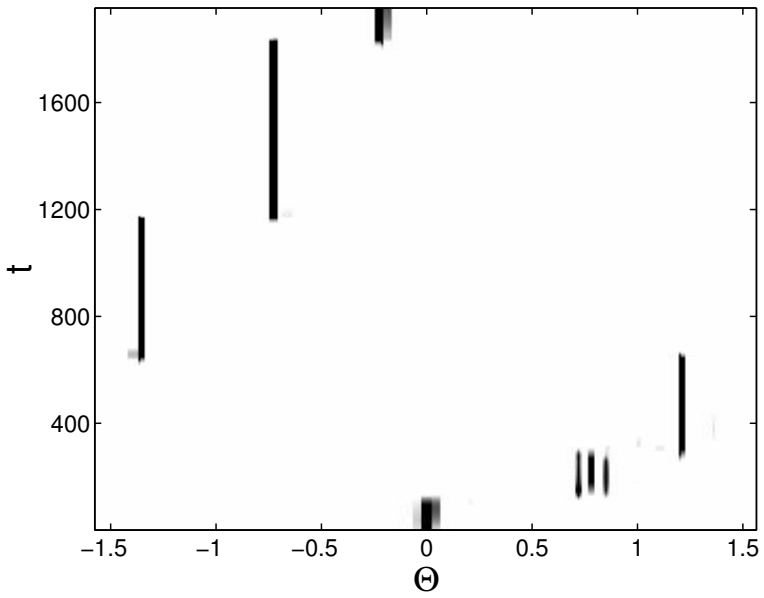

Figure 5.2: A density plot of the radially averaged Fourier power, $F(\Theta, t)$, as a function of orientation angle Θ and time t. Black corresponds to the largest value, and white to the smallest. Because the angle of the rolls is a director field, only angles from $-\pi/2$ to $\pi/2$ are shown. Note that $-\pi/2$ maps on to $\pi/2$. The following parameters were used: $\Gamma = 40$, $\sigma = 0.93$, $\Omega = 17.6$, $\epsilon = 0.007$, and periodic boundaries. We cannot measure an $f_{\rm pre}$ for this ϵ because the slope of the line through successive maxima increases with time.

predictions of Busse and Heikes [19], who noted that the time between roll switches should increase as the perturbation which causes the instability decays.

However, in experimental systems, one typically sees a more constant switching frequency such as that seen in Figure 5.3, which is for the same system as Figure 5.2, but for larger ϵ. As discussed in Section 1.3, it was eventually determined that chaotic fluctuations from a complex spatial structure are important, leading to roll switches occurring at a relatively constant rate.

This led to theoretical modeling of rotating Rayleigh-Bénard convection via three coupled Ginzburg-Landau equations [113, 33, 64]. The patterns switched at a constant rate and looked similar to those seen in experiments. The theory uses periodic boundary conditions and assumes that the dynamics is dominated by domain wall motion. When one set of rolls is replaced by another, the region containing the new, growing set of rolls spreads by the motion of a front, i.e., the boundary between the

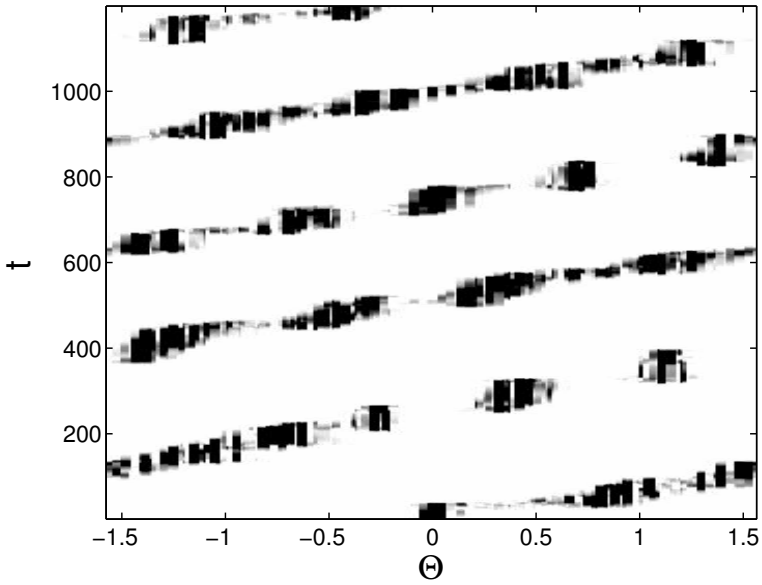

Figure 5.3: The same type of plot as in Figure 5.2, except $\epsilon = 0.045$. The inverse of the slope of the dark line made from the dominant Θ as a function of time gives the precession frequency, which is 0.0126 radians/vertical diffusion time in this case.

two different regions of roll orientation. Except for the special case of a front perpendicular to the rolls, the velocity of propagation of the front scales as $\epsilon^{1/2}$ [12], and the pertinent length scale varies as $\epsilon^{-1/2}$. This leads to the time scale for perturbations to grow, which scales as ϵ^{-1}. These scaling predictions are some of the first quantitative, theoretical predictions for a spatiotemporally chaotic state.

As discussed in Section 1.3, extensive experiments were done on cylindrical rotating Rayleigh-Bénard cells for aspect ratios 20 and 40 [121, 57, 58, 59]. The scaling laws for characteristic lengths and times were found to differ from the theoretical predictions. Experimenters measured the scaling exponent for lengths to be -0.2 and times to be -0.6, if they assumed that the length and time quantities diverged at onset [57]. (However, the data could also be fit by assuming no divergence at onset.) This is in contradiction to the theoretical values of -0.5 for lengths and -1.0 for times.

Our numerical code enables us to simulate periodic boundary conditions, as shown in Figure 5.4, which more closely resemble the theoretical model. We can also simulate conducting lateral boundaries, as shown in Figure 5.1, which closely resemble the

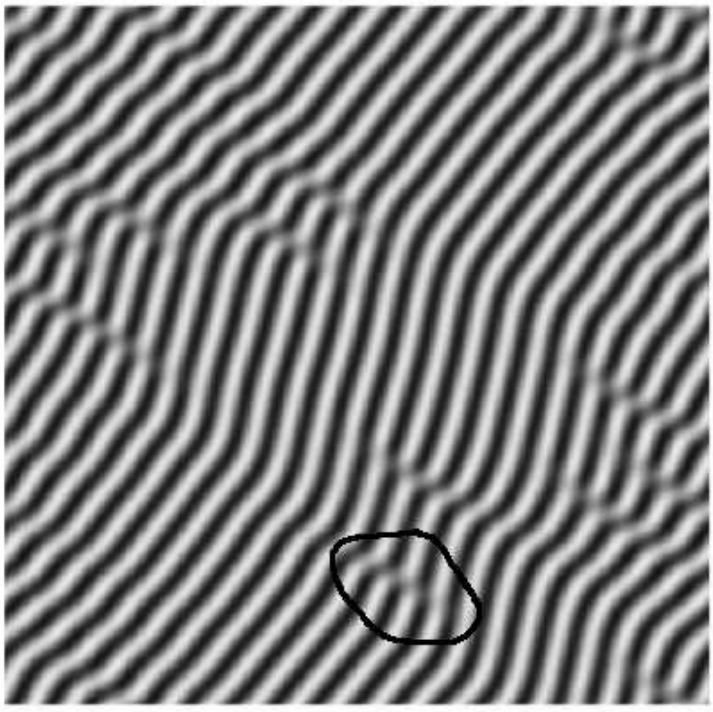

Figure 5.4: Snapshot of temperature deviation θ at the midplane for a domain chaos state with the following parameters: $\Gamma = 40$, $\sigma = 0.93$, $\Omega = 17.6$, $\epsilon = 0.045$, and $t = 214\,\tau_\nu$. Lateral temperature boundary conditions are periodic. The gray denotes the conduction value ($\theta = 0$), and the lighter and darker shades give the values above and below this, which range from θ = -0.12 to 0.12. A representative dislocation is circled.

experiment (as discussed in Appendix 5.A). By analyzing both types of geometries, we can determine the effect, if any, of realistic boundaries. Numerical analysis of a model equation had already indicated that realistic boundaries may play a role in the discrepancy between theory and experiment [32, 73]. These boundaries should give rise to more complex spatial structure than periodic boundaries. This may have a stronger effect on the dynamics near onset.

We will also study the gliding motion of defects which gives rise to glide-induced precession, another mechanism for precession in addition to the roll switching as described in Section 4.3.2.1. It was this mechanism which motivated us to derive the higher order terms in the amplitude equation in Chapter 4. In this Chapter we will present the results from our simulations, which we have also used for comparison to the theory in Section 4.3.2.

We ran our simulations out to 800 vertical diffusion times or longer for each ϵ in order to obtain good accuracy. As a result, our data for the precession frequencies and correlation lengths are accurate to 1% or better. We used a spatial resolution of 0.1 and a time step of 0.005. We used straight, parallel rolls as initial conditions for our simulations with conducting boundary conditions, and straight parallel rolls with a dislocation pair (as in Figure 1.1a) for our simulations with periodic boundary conditions. We used the dislocation pair to study the motion of defects in the periodic systems in more detail.

In order to determine scaling laws, the critical point, i.e., the point where $\epsilon \to 0$, must be determined precisely. In the spirit of experiments, we used the reduced Nusselt number (2.27) to determine the critical Rayleigh number, R_c. We determined the average reduced Nusselt number versus R for our simulations of both periodic and conducting boundaries. From the quadratic fits shown we find R_c (i.e., the x-intercept) to be 2246 for the periodic case and 2247 for the conducting case (See Figure 5.5). If we instead perform a linear extrapolation through the first two data points, we find R_c is 2248 for both cases. Our own results from linear stability analysis (Figure 4.14), along with Chandrasehkar's results [20], give a critical Rayleigh number of 2248. Since we would expect the effect of finite size to increase the critical Rayleigh

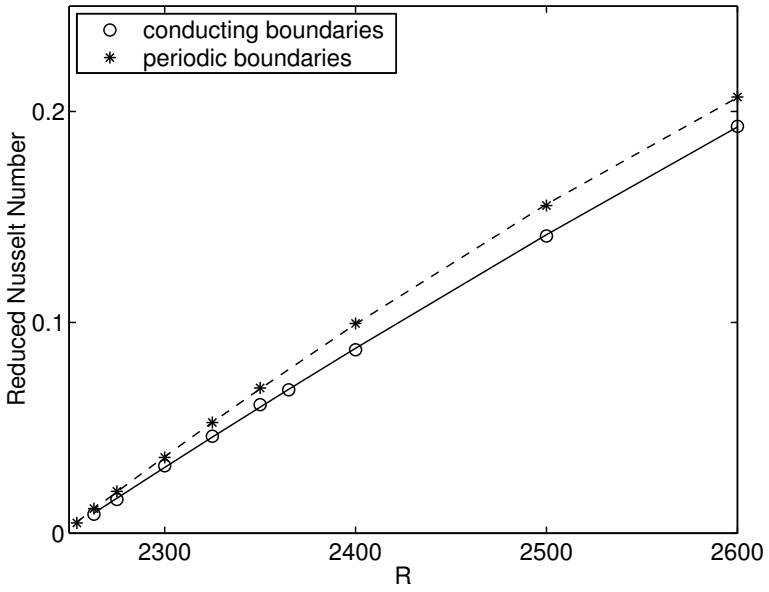

Figure 5.5: Reduced Nusselt number versus Rayleigh number (R) for both conducting and periodic boundaries. The following parameters were used in both cases: $\Gamma = 40$, $\sigma = 0.93$, and $\Omega = 17.6$. The solid line is a quadratic fit to the conducting boundary data, and the dashed line is a quadratic fit to the periodic boundary data.

number, we choose to use our linear extrapolation results of $R_c = 2248$. We find if we use the values from our quadratic fits instead, our scaling exponents change by at most 5%. Our Nusselt number results agree reasonably well with the experimental results of Hu et al. [58]. We are unable to make a side-by-side comparison since they published their Nusselt number versus R results for $\Omega = 15.4$, not $\Omega = 17.6$, but the numbers do agree to within 25%, with our Nusselt numbers being a bit larger as is expected for a larger rotation rate.

5.2 Precession Frequency

One finds that the orientation of the rolls precesses (not necessarily smoothly) with time in a counter-clockwise direction for positive Ω, as observed in the rotating frame. The precession frequency provides us with a good diagnostic quantity for time scaling. The precession frequency, f_{pre}, is measured by first determining the dominant orientation angle, Θ, as a function of time. To obtain this quantity we first find the

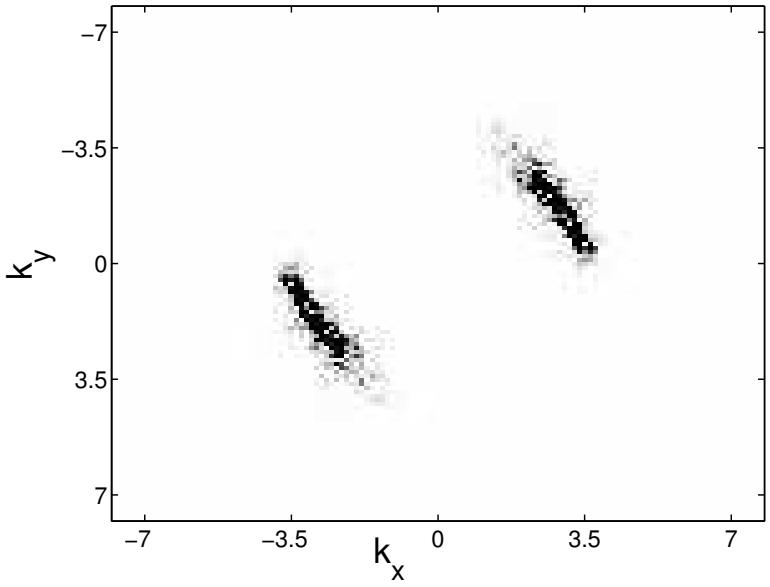

Figure 5.6: The Fourier power, $F(\mathbf{k})$, for the state shown in Figure 5.4.

square of the modulus of the Fourier transform of the midplane temperature field, $F(\mathbf{k})$, as a function of wavenumber $\mathbf{k}$ at one instant in time t. A representative plot of $F(\mathbf{k})$ is shown in Figure 5.6. A radial average of this quantity gives us $F(\Theta)$, i.e., the Fourier power as a function of orientation angle. Then we can find this quantity for each time slice to give us $F(\Theta, t)$. Angle-time plots from representative cases are shown in Figure 5.2 and Figure 5.3. The rate of change of the orientation angle of the maximum in $F(\Theta, t)$ with respect to time gives the precession frequency.

Another quantity that can be measured is the domain switching frequency, τ_{dsw}^{-1}. According to the theory for rotating Rayleigh-Bénard convection [113], domains of straight parallel rolls become unstable to rolls at a different orientation. At threshold ($\Omega = \Omega_c$) there is one distinct orientation, and for $\Omega > \Omega_c$ there exists a band of orientation angles. This instability will cause the rolls to precess in a discrete manner. We can see this switching in Figure 5.2 and Figure 5.3 by noticing that the upward sloping trend of the maximal value of $F(\Theta, t)$ often has discrete jumps. One can measure how long it takes for one set of rolls to become unstable to another set of rolls. The inverse of this transition time is known as the domain switching frequency. We find τ_{dsw}^{-1} by first taking the autocorrelation function of the angle-time plot (see

Figure 5.7). Then, the inverse of the time difference between the first peak (on either side) and the central peak gives the domain switching frequency. We can also find the domain switching angle θ_{sw} by finding the difference in angle between the first peak and the central peak. We can then convert to the same units as f_{pre} by multiplying τ_{dsw}^{-1} by θ_{sw}:

$$f_{\text{dsw}} = \tau_{\text{dsw}}^{-1}\theta_{\text{sw}}. \tag{5.1}$$

The two precession frequencies f_{pre} and f_{dsw} should agree if the dominant method of precession is due to domain switching.

The domain switching angle θ_{sw} is plotted as a function of ϵ for both periodic and realistic boundary conditions in Figure 5.8. The theoretical value for the maximum growth rate for this Prandtl number ($\sigma \approx 1$) is about 0.7 radians [28]. Our results are in good agreement with this value. Note, however, that this is in disagreement with the experiments [57], which measured a switching angle of about 1.0 radians and found a slight decrease in angle with ϵ. We will revisit this discrepancy in Section 6.3.

The quantities f_{pre} and f_{dsw} are plotted versus ϵ in Figure 5.9 on a log-log scale for periodic and conducting boundaries. The slope of these lines gives the scaling of these frequency quantities with ϵ. The scaling for both periodic and conducting boundary conditions does agree reasonably well with the theoretical results of time-like quantities scaling as ϵ^{-1}. The average of all the slopes is 1.12. We find that we can obtain a closer agreement with theory by noting that θ_{sw} also has a slight ϵ dependence, as can be seen in Figure 5.8. Hence, if we instead look at inverse transition times by dividing each of our f_{pre} by its corresponding θ_{sw}, we can remove this slight bias:

$$\tau_{\text{pre}}^{-1} = \frac{f_{\text{pre}}}{\theta_{\text{sw}}}. \tag{5.2}$$

This is done in Figure 5.10. Now we find that the average of all the slopes is 1.06. The theory [113] predicts that the dominant method for precession is due to domain switching events. We see that our τ_{pre}^{-1} and τ_{dsw}^{-1} very nearly coincide and that our scaling is consistent with theory. Hence, one can conclude that predictions of the theoretical model for domain switching are consistent with the numerics, which are

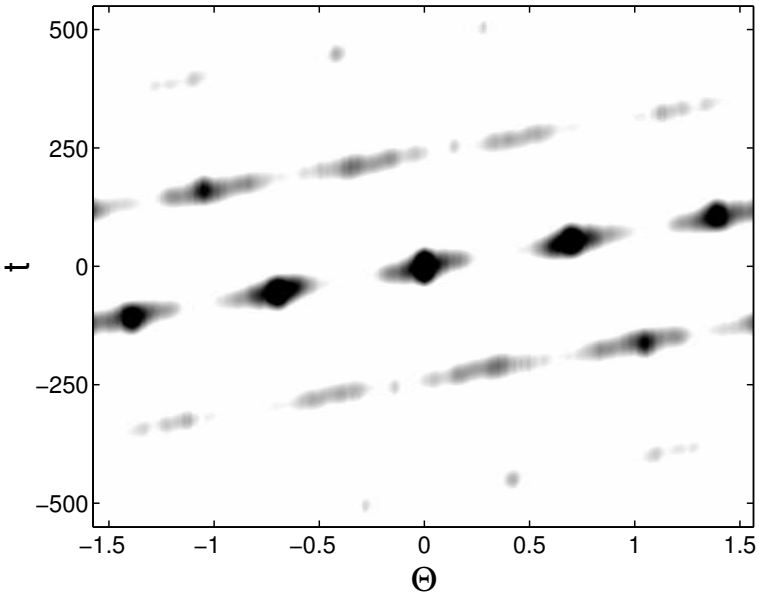

Figure 5.7: The two-dimensional autocorrelation function of the angle-time plot shown in Figure 5.3 (where the first 100 τ_ν were removed before taking the autocorrelation, to allow the transients to die out). The time between successive peaks is 55.5 τ_ν, hence $f_{\rm dsw}$ is 0.018. The switching angle $\theta_{\rm sw}$ is the difference in angle between successive peaks, and is 0.7 $\pm$ 0.05 for this case.

simulations of a realistic ideal Rayleigh-Bénard convection experiment.

However, the experimental results do not agree, as seen in Figure 5.11. We only plot $f_{\rm pre}$ (in units of radians/vertical diffusion time) to compare with the experimental results [57]. Note that the experimental results are for exactly the same parameters as the numerics for conducting boundaries, so it is somewhat surprising to find that the precession frequencies differ significantly in magnitude. One also sees that scaling laws differ: the experiments find a slope of 0.58, whereas the theoretical slopes average to 1.1. However, if one looks only at the latter data points for the numerical conducting boundary case, one finds a slope of 0.68, which is in better agreement with the experiment. This leads us to surmise that the experiments may not be measuring the theoretically predicted precession via domain switching, which should dominate for small enough ϵ.

In addition, we have verified that there is another mechanism for precession, namely that of the gliding motion of defects (see Section 5.4). This phenomenon can

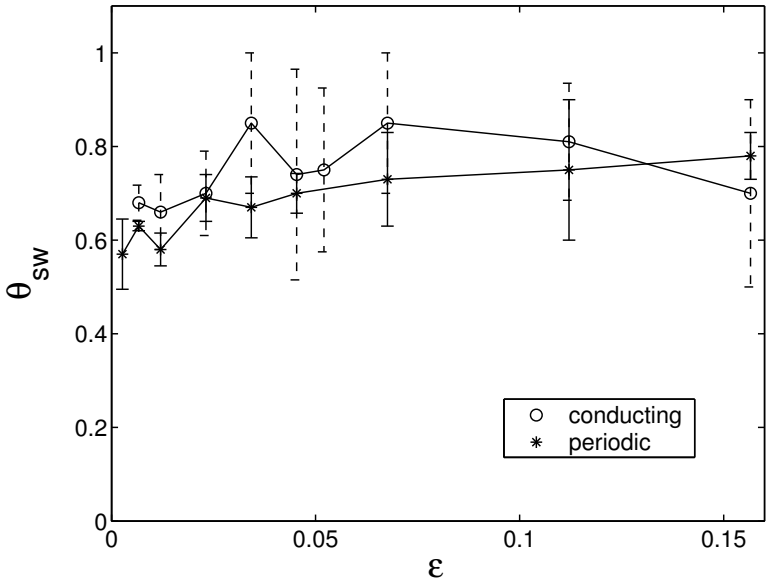

Figure 5.8: Domain switching angle $\theta_{\rm sw}$ versus ϵ for both periodic and conducting boundaries for the same parameters as in Figure 5.9. Note the slight ϵ dependence of $\theta_{\rm sw}$. The error bars (dashed for conducting and solid for periodic) are included to indicate the spread in angle on the autocorrelation plot (see Figure 5.7 for an example).

be explained by studying the amplitude equation with rotation (see Section 4.3.2). The new terms due to the Coriolis force (4.16) will cause dislocation pairs, which are stationary in a non-rotating system, to glide in a rotating system perpendicular to the rolls and in opposite directions. As mentioned in Section 4.3.2.1, their gliding path will cause an overall orientation change of the rolls.

Even more generally, precession will occur whenever there is a gradient in the amplitude in the direction parallel to the rolls, as we noted in Section 4.3.1. The precession will cause straight parallel rolls (whose amplitude goes to zero at a lateral boundary, for example) to bend and curve, ultimately creating dislocation pairs to release the stress. Dislocations will also appear if a domain switching event does not cleanly switch between one set of parallel rolls and another. This happens more often for higher ϵ, where domains are smaller. This always happens for conducting boundaries, where the rolls can never fit perfectly. Dislocations can also be injected from sidewalls and created in regions of high curvature resulting from mean flows.

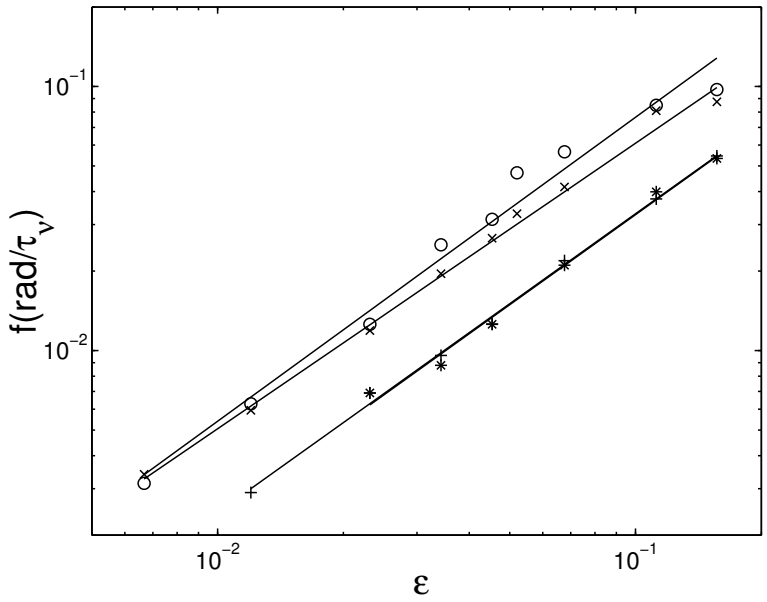

Figure 5.9: Frequencies $f_{\rm pre}$ and $f_{\rm dsw}$ (in units of radians/vertical diffusion time) versus control parameter ϵ. Legend: Conducting boundaries: "o" = $f_{\rm pre}$, slope = 1.15, "x" = $f_{\rm dsw}$, and slope = 1.08. Periodic boundaries: "$*$" = $f_{\rm pre}$, slope = 1.13, "+" = $f_{\rm dsw}$, and slope = 1.13. The following parameters were used: $\Gamma = 40$, $\sigma = 0.93$, and $\Omega = 17.6$.

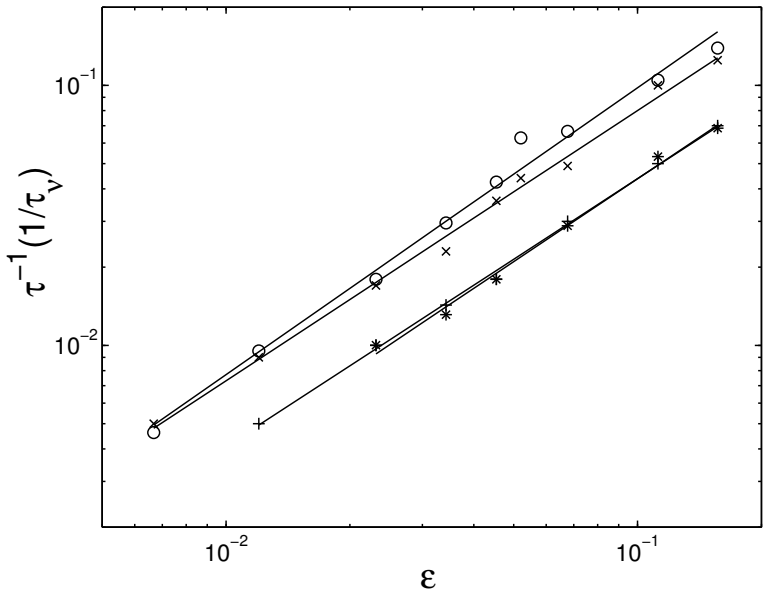

Figure 5.10: Frequencies $\tau_{\rm pre}^{-1}$ and $\tau_{\rm dsw}^{-1}$ (in units of inverse vertical diffusion times) versus control parameter ϵ for the same parameters as in Figure 5.9. Legend: Conducting boundaries: "o" = $\tau_{\rm pre}^{-1}$, slope = 1.10, "x" = $\tau_{\rm dsw}^{-1}$, and slope = 1.04. Periodic boundaries: "$*$" = $\tau_{\rm pre}^{-1}$, slope = 1.06, "+" = $\tau_{\rm dsw}^{-1}$, and slope = 1.03.

We expect the glide-induced precession frequency to scale differently with ϵ than precession via domain switching. We predict the glide-induced precession frequency f_{glide} will scale as

$$f_{\text{glide}} \propto \rho_d v_{\text{glide}}, \tag{5.3}$$

where ρ_d is the linear density of defects and v_{glide} is the glide velocity. We have found (see Section 5.4 again) the glide velocity to scale as $\epsilon^{3/4}$. If the density of defects remains relatively constant, then the glide-induced precession frequency should also scale with an exponent of 0.75. This agrees better with the experimental slope of 0.58 and our own conducting boundary slope at larger ϵ of 0.68.

As support for our reasoning, note that Busse and Heikes also performed measurements on rotating Rayleigh-Bénard convection [19, 54]. They used water as the fluid and measured the transition time, i.e., the time between domain switches. They found this transition time scaled with an exponent of -0.75. They were further from threshold than the experiments of Hu et al. [57], but this scaling law supports our hypothesis of glide-induced precession being the dominant mode of precession at larger ϵ.

5.3 Correlation length

For completeness, we have measured correlation lengths in the usual manner [78], even though recent work by Becker and Ahlers [8] have shown that this method is somewhat problematic. The basic idea is to measure the decay length of the azimuthally averaged autocorrelation function of the temperature field. This decay length gives the size over which domains are correlated: hence it is known as the correlation length. We accomplish this measurement by taking the Fourier transform of the midplane temperature field, finding the square of the modulus of this data, $F(\mathbf{k})$ as in Section 5.2, but this time performing an azimuthal average. This is known as the structure function, $S(k)$, which is a measure of the wavenumber distribution. We then average this structure factor over all of our time slices from 100 vertical

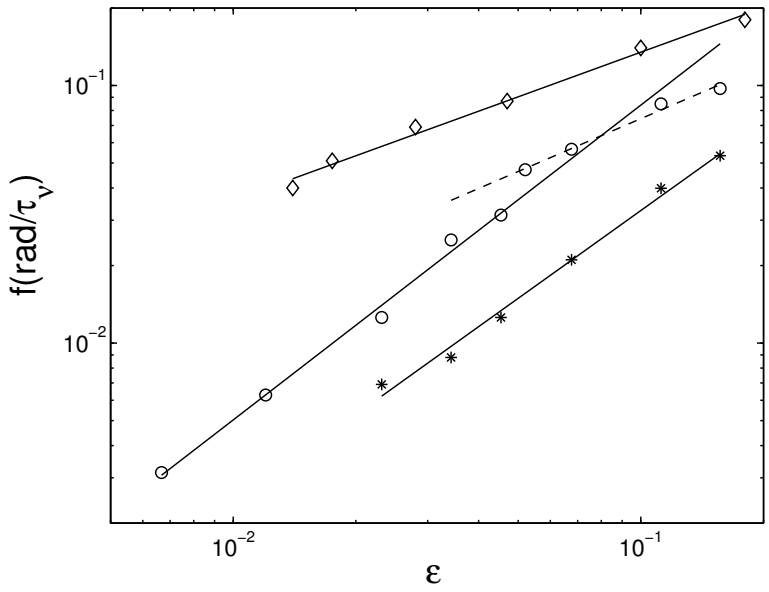

Figure 5.11: Frequencies $f_{\rm pre}$ (in units of radians/vertical diffusion time) versus control parameter ϵ for the same parameters as in Figure 5.9. Legend: "o" = Conducting boundaries, slope for early data points = 1.22, slope for latter data points = 0.68 (dashed line), "$*$" = Periodic boundaries, slope = 1.13, "$\diamond$" = experimental results, and slope= 0.58 [57].

diffusion times and up. Next, we fit the peak in this averaged structure function to a squared Lorentzian function. The inverse of the half-width is the correlation length ξ. It turns out that this procedure is rather sensitive to the fitting function: a Gaussian can yield different values, as does a simpler calculation of the second moment of the structure function. However, we find that a square Lorentzian fit best models the data.

The results are shown in Figure 5.12. Due to the finite size of the conducting cell, one is unable to measure a diverging correlation length for very small ϵ. Eventually the rolls fill almost the entire cell, and the correlation length is determined by the aspect ratio; hence it levels off. As a result, our fit is only to the region where the correlation length begins to drop, which is the last six data points. For the periodic case, the correlation length is too large to measure accurately at any of our control parameters, so we do not show these results. The exponent in the conducting case of -0.39 is a bit smaller than the theoretical prediction of lengths scaling as $\epsilon^{-1/2}$, but

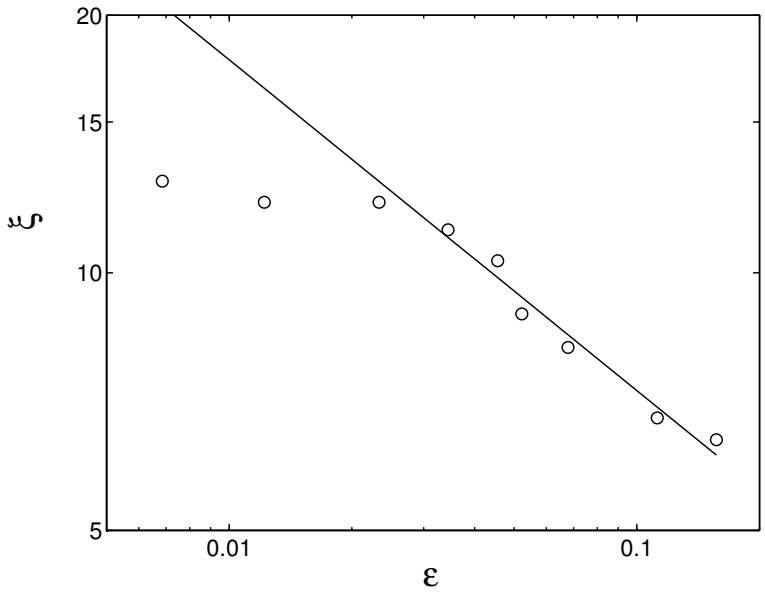

Figure 5.12: Correlation length ξ versus control parameter ϵ for conducting boundaries for the same parameters as in Figure 5.9. The fit is to the last six data points, whose slope is -0.39.

is still in better agreement with the theory than the experiment. The experimental results find an exponent of -0.2.

5.4 Dislocations

Dislocations are present in our simulations. An example is circled in Figure 5.4. Dislocations that are stationary in a non-rotating system will glide in a direction perpendicular to the rolls (parallel to the roll wavevector) in the rotating system. An extensive analysis of defect velocities indicates that the dominant defect motion is perpendicular to the rolls for both our periodic and our realistic systems. The results can be seen for the periodic case in Figure 5.13 and for the conducting case in Figure 5.14. The dominant orientation angle of the rolls, Θ, is plotted versus the angle of the velocity of the defects, θ_v. We determined the dominant Θ by finding the Θ value corresponding to the maximum value of $F(\Theta)$ (such as in Figure 5.3) at the instant in time when a defect is moving at its measured velocity. In both figures,

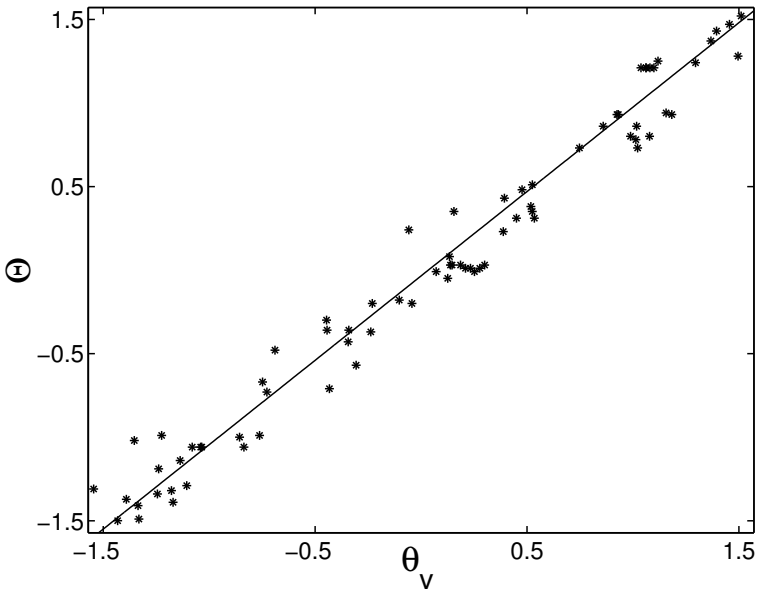

Figure 5.13: Angle of the rolls, Θ, versus angle of the velocity of defects, θ_v, for periodic boundaries and the same parameters as in Figure 5.9. The slope of the line is 1.01, indicating that the defects mainly glide in a direction perpendicular to the rolls.

the data is scattered about, but close to a line with unit slope passing through the origin. This does indeed prove that the dominant motion of our defects is glide, i.e., motion perpendicular to the rolls.

Our recently developed theoretical analysis has led to an understanding of the scaling of glide velocities with ϵ. A derivation is given in Section 4.3.2. One finds that

$$v_{\text{glide}} \propto \epsilon^{3/4}. \tag{5.4}$$

This is in excellent agreement with the numerical results in Figure 5.15 for both the conducting and the periodic boundaries.

In the periodic case, one can separate out two different types of defect motion. One is the motion of isolated defect pairs and the other is the motion of defects during a domain switching event. As mentioned earlier, in a domain switching event, one set of rolls is replaced by another through the motion of a front. On the boundary between the two sets of rolls there is a superposition of both sets. This superposition

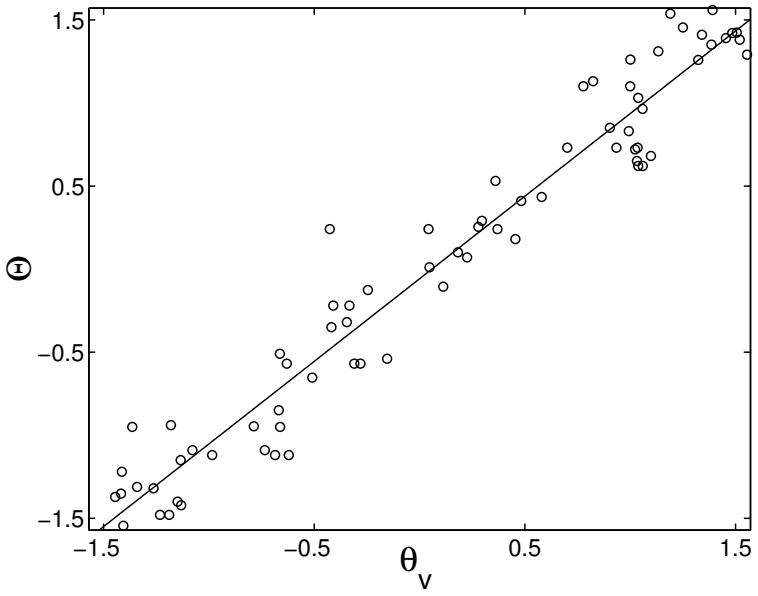

Figure 5.14: The same type of plot as Figure 5.13, but for conducting boundaries. The slope of the line is 0.98, indicating that the defects mainly glide in a direction perpendicular to the rolls in the conducting case, too. There is, however, more scatter than for the periodic case.

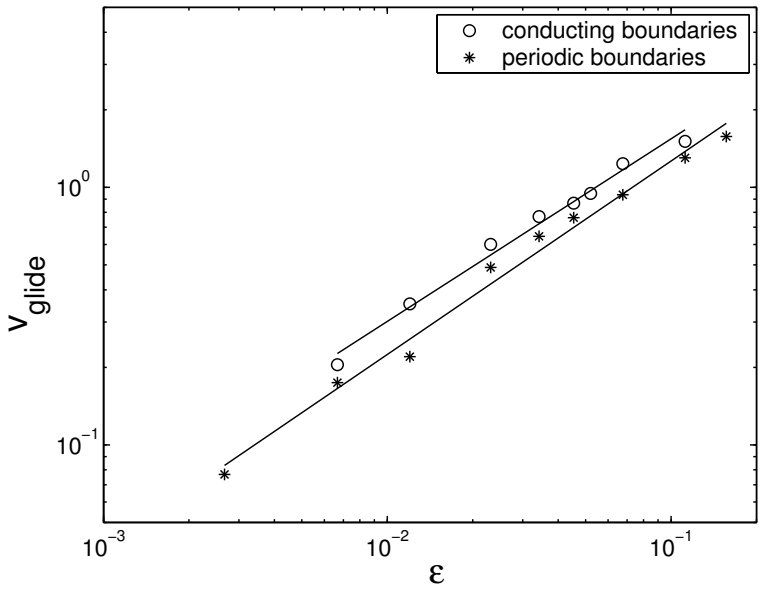

Figure 5.15: Glide velocity of defects versus ϵ for the same parameters as in Figure 5.9. Legend: "o" = Conducting boundaries, slope = 0.71, "$*$" = Periodic boundaries, and slope = 0.75. Approximately 150 defects were tracked, half for the conducting case, and half for the periodic case.

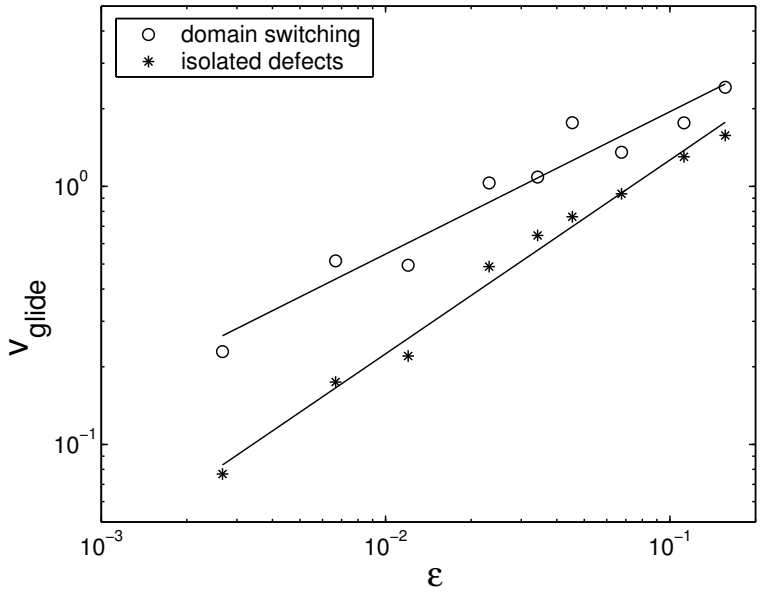

Figure 5.16: Comparison of glide velocities from isolated defects and domain switching defects for the same parameters as in Figure 5.9, but for periodic boundaries only. Legend: "o" = domain switching defects, slope = 0.55, "$*$" = isolated defects, and slope = 0.75.

creates a line of minima/maxima along the front. It is the motion of these minima that we track and call "domain switching defects."

We have plotted both types of defect motion in Figure 5.16. (Note that the glide velocities shown in Figure 5.15 for periodic boundaries are the isolated defects). We find that the domain switching defects lead to larger glide velocities, but they have an ϵ scaling exponent that is smaller (0.55) than the exponent for the isolated defects (0.75). We expect the velocity of the front to scale as $\epsilon^{0.5}$, which is in agreement with the results in Figure 5.16. We could not clearly differentiate between these two types of defects in the conducting case, so the conducting data in Figure 5.15 most likely contain both types of defects. This may explain the slightly smaller slope.

One can also measure the diameters of the axes of the defects, as shown in Figure 5.17. Defects have a long and a short axis, and both were measured as a function of ϵ for periodic as well as conducting boundaries. The method of finding defect lengths is as follows: First, we demodulated the midplane temperature field data, removing the underlying roll structure and only revealing the amplitude, as shown in

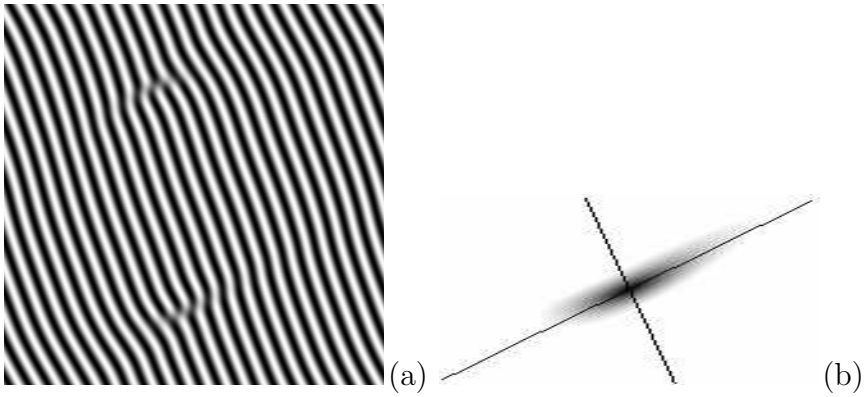

Figure 5.17: (a) Plot for the same parameters as in Figure 5.4, but for $t = 285$, where the state is cleaner. (b) We have demodulated and zoomed in on the defect at the top of (a). The two lines are the long and short axes for this defect. The colormap for (b) is defined so that black is zero and white is the maximal value of the amplitude (0.1 in this case).

Figure 5.17b, for a representative defect. Then, we found the full width at half the height in the depression of the amplitude at the defect for both the long axis and the short axis of the defect. The multiple scales expansion (4.5) predicts the long axis, perpendicular to the rolls, to scale as $\epsilon^{-1/2}$, and the short axis, parallel to the rolls, to scale as $\epsilon^{-1/4}$. We plot our scaling results in Figure 5.18. In both the periodic and conducting cases, we find the long and short axes to scale with somewhat smaller exponents: the long axis scales with an average exponent of -0.36, and the short axis with an average exponent of -0.15. It is possible that we are unable to determine the correct scaling for the short axis, since we are measuring lengths smaller than a roll size. However, the long axis data should be correct. The long axis scaling does agree quite well with our correlation length scaling for conducting boundaries (see Figure 5.12).

Next, we turn to the scaling of defect areas. The theory predicts defect areas to scale as $\epsilon^{-3/4}$. If we compute defect areas by using the formula area $= \pi$(long axis)(short axis)/4, our areas will scale as $\epsilon^{-0.51}$. We mention this since our numerical results do agree slightly better with preliminary experimental results [7]. It is unclear how to explain the discrepancy with theory.

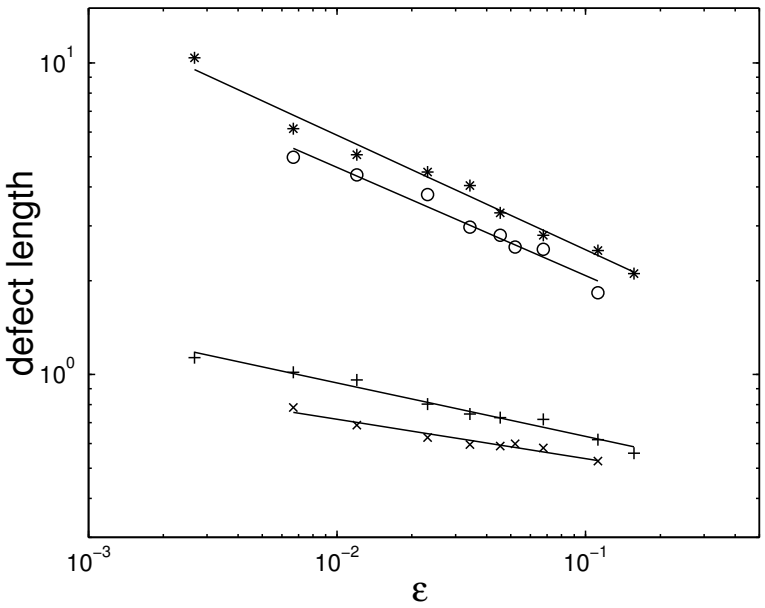

Figure 5.18: Lengths of defects versus ϵ for the same parameters as in Figure 5.9. Legend: Conducting boundaries: "o" = length of long axis, slope = -0.35, "x" = length of short axis, and slope = -0.13. Periodic boundaries: "$*$" = long axis, slope = -0.37, "+" = short axis, and slope = -0.17.

5.5 Conclusions

Our numerical results (Coriolis force only) for both periodic and conducting lateral temperature boundary conditions are in excellent agreement with the theoretical scaling laws for time as ϵ^{-1}. We measured the precession frequency to scale with ϵ with an average exponent of 1.1 for periodic and conducting boundaries[2]. Hence, we find that time scales as $\epsilon^{-1.1}$. This is in disagreement with the experiments using the same parameters: they find that time scales as $\epsilon^{-0.6}$. It is possible that glide-induced precession may account for this discrepancy, since the theory assumes the precession of the roll orientation is entirely due to domain-switching events. The hypothesis of glide-induced precession with a constant dislocation density predicts precession frequencies to scale as $\epsilon^{0.75}$, which does agree better with the experiments.

We were unable to use correlation lengths to conclusively determine the length

[2]The accuracy in our exponents is about 5%, with the largest source of error being the determination of R_c.

scaling for our numerical simulations with periodic boundary conditions, since the domains were simply too large. For our conducting boundary conditions we found correlation lengths to scale as $\epsilon^{-.39}$, which is smaller than the theoretical prediction of $\epsilon^{-0.5}$, but is in worse disagreement with the experimental results of $\epsilon^{-0.2}$.

We will revisit this discrepancy of scaling exponents in Chapter 6, where we include the centrifugal force in our simulations.

We did not choose to study the dependence of the scaling exponents on aspect ratio, since significantly larger aspect ratios are prohibitively expensive, and one does not expect good scaling for the smaller ones. Earlier simulations on model equations [32, 73] found little effect on correlation times for aspect ratios comparable to the ones we use, although the correlation length was significantly affected.

Our theoretical calculations for the motion of defects in Chapter 4 predicts that glide velocities will scale as $\epsilon^{0.75}$. Our numerical results confirm this. It is also interesting to note that for the conducting case, our length and time scales give a consistent velocity scaling: lengths (as $\epsilon^{-.39}$) divided by times (as $\epsilon^{-1.1}$) gives velocities to scale as $\epsilon^{0.71}$. It would be very interesting for experimenters to also look at the scaling of velocities.

From our numerical results, we determined that defect areas scale on average as $\epsilon^{-0.51}$ for conducting boundaries and for periodic boundaries. This is in disagreement with the theory, which predicts defect areas should scale as $\epsilon^{-0.75}$. In addition we looked at how the different axes in the defects scaled, and found the axis perpendicular to the rolls scaled as $\epsilon^{-0.36}$ and the axis parallel to the rolls scaled as $\epsilon^{-0.15}$, which clearly indicates there is a separation of scales in rotating Rayleigh-Bénard convection. However, the separation of scales is smaller than the predicted scaling of $\epsilon^{-0.5}$ and $\epsilon^{-0.25}$, respectively.

Appendix 5.A Motivation for using Conducting Sidewalls

In this section we make an estimation of the thermal properties of the sidewalls for the experimental systems [57]. The fluid was compressed carbon dioxide, and the sidewalls were paper. We will use the equation for the continuity of heat

$$\frac{\partial \theta}{\partial r} - \mu\theta = 0 \text{ at } r = \Gamma. \tag{5.5}$$

This equation reduces to insulating boundary conditions (2.25) when $\mu \to 0$ and to conducting boundary conditions (2.24) when $\mu \to \infty$.

From Kuo and Cross [67], we know that

$$\mu = K_\omega k_\omega \tanh(k_\omega l_\omega), \tag{5.6}$$

where K_ω is the ratio of the thermal conductivities of the sidewall to the fluid, l_ω is the thickness of the sidewall, and

$$k_\omega^2 = \left(q_x^2 + \pi^2 + \frac{\Gamma}{\kappa_\omega}\right), \tag{5.7}$$

where κ_ω is the ratio of the thermal diffusivities of the sidewall to the fluid, Γ is the growth rate, and q_x is the wavenumber. Equation (5.6) was derived under the assumptions that we have stress-free velocity boundary conditions and a system of straight parallel rolls with some amplitude modulation.

We use the following experimental parameters [6]:

$$\begin{aligned} l_\omega = 0.34, \qquad K_\omega = 10, \qquad \kappa_\omega = 1, \\ q_x \simeq \pi, \qquad \Gamma \simeq 1, \quad \text{and} \qquad k_\omega \simeq 4.55, \end{aligned} \tag{5.8}$$

where the last equation follows from (5.7). We make the approximation that $\Gamma = 1$, on the order of a vertical diffusion time (compare with Figure 3.2). Plugging these

parameters into (5.6) yields a value of $\mu = 42$. Since μ is rather large, we are certainly closer to conducting than insulating boundary conditions. Since our aspect ratios are all rather large, we expect a minimal effect from solving the conjugate problem for the boundary conditions (i.e., solving (5.5) concurrently with (2.13)).

Chapter 6

Effect of the Centrifugal Force in Rotating Rayleigh-Bénard Convection

6.1 Introduction

Recent experiments by Becker et al. [9] clearly show that the centrifugal force cannot be neglected in the theoretical formulation of rotating Rayleigh-Bénard convection for large aspect ratio. Becker and Ahlers performed experiments on aspect ratios $\Gamma = 36, 60$, and 80. For the largest aspect ratio, a novel hybrid state is evident, as shown in Figure 6.1. This state exhibits domain chaos in the interior, but radial rolls in the annular region along the perimeter. The entire state contains defects, which glide azimuthally. The outer radial roll state, not seen for smaller aspect ratio, strongly indicates that the centrifugal force cannot be neglected, at least for the largest aspect ratios. In this chapter we will show that it cannot be neglected even for moderate aspect ratios, such as $\Gamma = 20$ and 40.

6.2 Rotational Corrections to the Boussinesq Equations

If we look at equation (2.13) we see that although most of the centrifugal force term can be absorbed into a redefinition of the pressure gradient (2.4), there is a

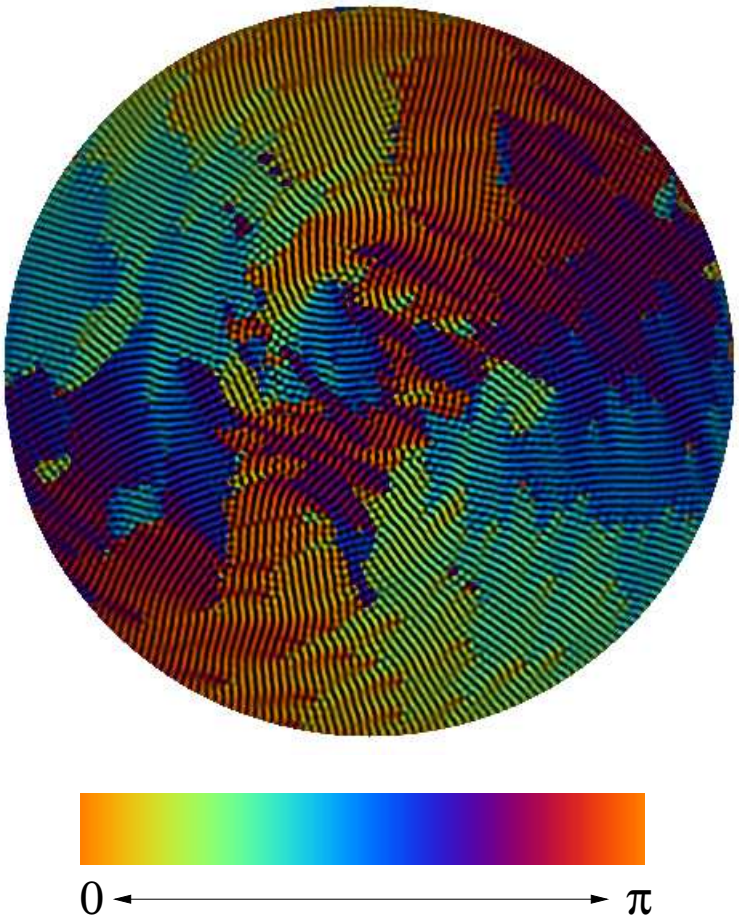

Figure 6.1: Hybrid state of domain chaos with radial rolls and defects along the outer annulus. System parameters are $\Gamma = 80$, $\sigma = 0.821$, $\epsilon = 0.05$, and $\Omega = 16.25$. The gray-scale (false color in the electronic version) overlay is $\theta(\mathbf{r})$, the angular component of the local wave-director field. These are experimental results. Reprinted with permission from Nathan Becker.

temperature-dependent part (2.15), due to the temperature dependence of the density (2.3). This term has the form

$$|F_{\text{cent}}| \;=\; \beta\sigma\Omega^2\frac{R}{R_c}(T-\bar{T})\mathbf{r} = \frac{\sigma^2 Rd}{g\tau_\nu^2}\Omega^2(T-\bar{T})\mathbf{r}. \tag{6.1}$$

Physically speaking, a radial density gradient resulting from the imposed temperature difference gives rise to a temperature-dependent centrifugal force. The influence of this centrifugal force is to induce a large scale radial circulation (LSC). The wave director of the convection rolls tends to align orthogonally to the LSC [26].

The presence of the centrifugal force results in an imperfect bifurcation for the transition to domain chaos, as can be seen in Figure 6.2 for $\Gamma = 20$. In a perfect bifurcation, the system switches sharply from the uniform state to the new state exactly at the bifurcation point. In an imperfect bifurcation, the transition point is more rounded, and a partial pattern is seen as soon as the system is in nonequilibrium. The various states corresponding to the different Rayleigh numbers can be seen in Figure 6.3. Even below the threshold-critical Rayleigh number for the transition, the centrifugal force induces an LSC. However, this state is uniform in the bulk and has radial symmetry, as can be seen in Figures 6.3a and b. At the critical Rayleigh number, one still sees the transition to a roll state exhibiting domain chaos, as in Figures 6.3c-f. However, the region over which this domain chaos exists in the bulk depends on the relative strengths of the centrifugal and Coriolis force. For the systems shown in Figure 6.3, the centrifugal force is too small to cause a hybrid state except for very low ϵ (as in Figure 6.2c). This can be contrasted with Figure 6.1, where the hybrid state is persistent for much larger ϵ.

Previous work on domain chaos [70, 19, 28, 113, 33, 32] neglected the centrifugal force because the Froude number, $\omega^2 r/g$, is small for typical systems. Hart [51] has suggested that the Froude number is not the only relevant parameter. He provides numerical estimations of the regions where the centrifugal force is relevant; however, he assumes that the rotation rate ω is greater than 500, so we cannot apply his

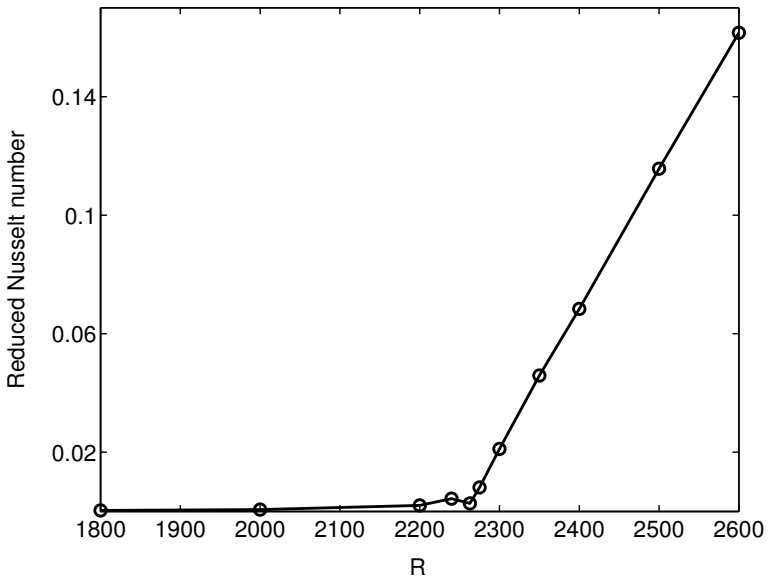

Figure 6.2: Reduced Nusselt number versus Rayleigh number R. The parameters used were $\Gamma = 20, \Omega = 17.6, \sigma = 0.93$, conducting boundary conditions and the centrifugal force twice as large. The critical Rayleigh number R_c is determined to be 2257 by performing a fit to the data for $R > 2263$.

estimates. Instead, we consider the ratio of the centrifugal term to the Coriolis term.

The ratio of the magnitude of the centrifugal term to the magnitude of the Coriolis term is evaluated at the position where the Coriolis force reaches its maximum value, which is where the magnitude of horizontal velocity $u_\perp$ is a maximum. To first order in $\epsilon^{1/2}$ we can define this magnitude $|u_\perp| = u_0\epsilon^{1/2}$, which occurs at $z = z_0$. At this point, $|T - \bar{T}| = z_0$, since the temperature due to the conduction profile is equal to $-z$ in our scaled variable scheme. (Note we have neglected convective corrections to the conduction profile, since these are of order $\epsilon^{1/2}$). We also want to evaluate the centrifugal force at the horizontal location where it reaches its maximum value, which is at $r = \Gamma$, which then yields

$$\mathcal{A} = \frac{\beta\sigma\Omega\Gamma z_0}{2u_0\epsilon^{1/2}}. \tag{6.2}$$

This parameter $\mathcal{A}$ is the small-ϵ approximation to the ratio of the magnitude of the maximum of the centrifugal term, evaluated near the outer edge of the sample, to the magnitude of the Coriolis term evaluated where it reaches a maximum in the vertical direction, $z = z_0$. The quantity $\mathcal{A}$ is an indicator of the transition from domain

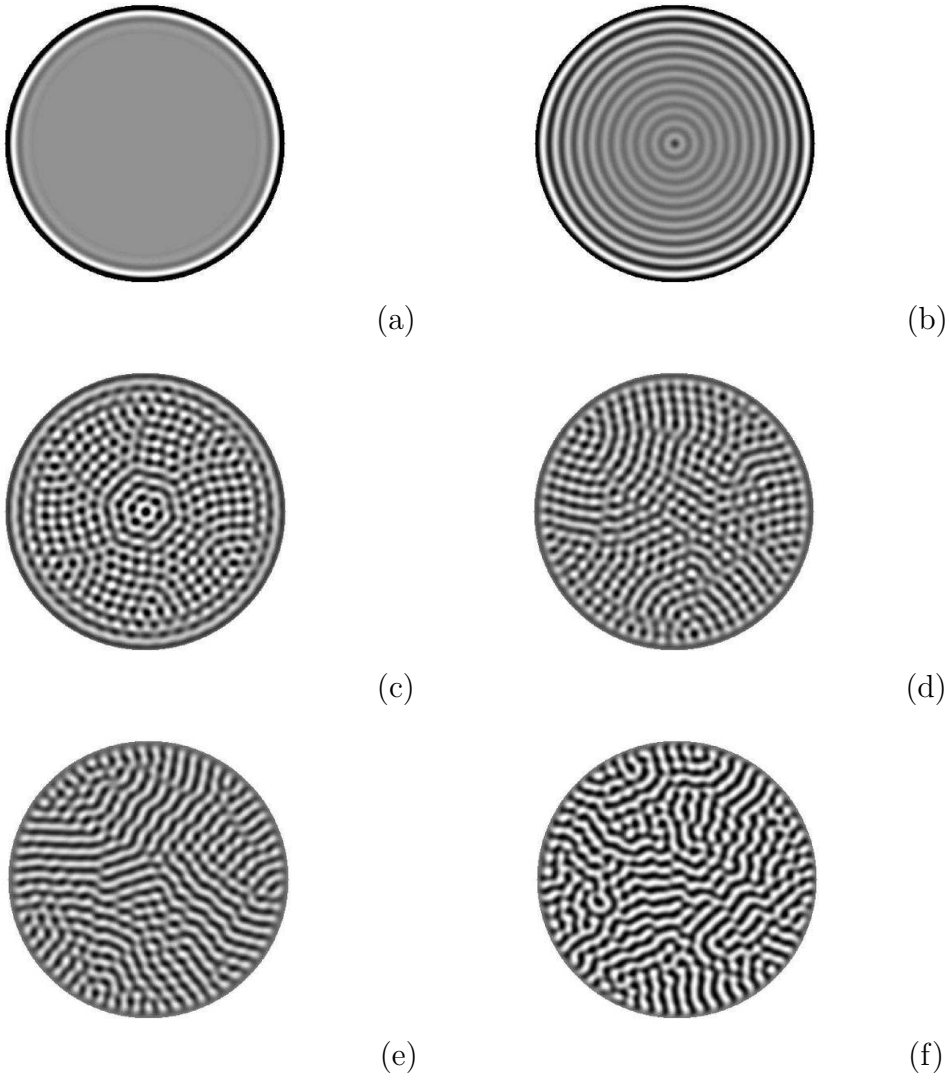

Figure 6.3: Snapshot of temperature deviation θ at the midplane, for the same parameters as Figure 6.2, and (a) $R = 1800, t = 500$, (b) $R = 2240, t = 466$, (c) $R = 2263, t = 807$, (d) $R = 2275, t = 810$, (e) $R = 2350, t = 748$, (f) $R = 2600, t = 715$. Lateral temperature boundary conditions are conducting. The gray denotes the conduction value ($\theta = 0$), and the lighter and darker shades give the values above and below this.

chaos to a hybrid state. One sees from equation (6.2) that the size of $\mathcal{A}$ depends on some of the parameters of the system, such as the Prandtl number σ and the thermal expansion coefficient α. This suggests that altering these parameters can affect of the influence of the centrifugal force and the resulting hybrid state. However, the LSC induced by the centrifugal force will always play some sort of role, even if the hybrid state is not obvious. We will discuss this in Section 6.3.

We can obtain an approximate numerical value for u_0. From our linear stability analysis in Section 4.A.3 we get the functional form of the horizontal velocity. We then use the simulation to find the Nusselt number versus ϵ dependence so that the normalization (see Section 4.F) is correct. For the case of $\Gamma = 40$, $\sigma = 0.93$, and $\Omega = 17.6$, we find $u_0 = 12.3$ at $z_0 = 0.3$. These values should also approximately apply for our experimental parameters, which do not vary significantly from the parameters used to obtain the numerical values; the exception is Γ, whose dependence is explicit. For the $\Gamma = 80$ sample, $\mathcal{A} = 0.61$ for $\epsilon = 0.05$, indicating that the centrifugal force is almost as influential as the Coriolis force, but for the $\Gamma = 36$ sample and $\epsilon = 0.05$, $\mathcal{A} = 0.12$, indicating that the Coriolis force dominates. Both samples have similar values of Ω and σ, so it is not surprising that we observe a Γ-dependent transition to a hybrid state induced by competition between the centrifugal force and the Coriolis force.

6.3 Results

We provide supporting evidence for the hybrid state by running numerical simulations with the centrifugal force included (6.1) for experimentally realistic parameters. To allow for a side-by-side comparison of the systems of Hu et al. [57] we used $\Gamma = 40$, $\sigma = 0.93$, $\Omega = 17.6$, $d = 1.06$mm, $\tau_\nu = 4.8$s, $g = 9.8\text{m/s}^2$, and conducting boundaries. We also used a Γ of 20 for some of our other simulations (see Figure 6.4). To compare with the recent experiments, as in Figure 6.5, we used a $\Gamma = 36$, $\sigma = 0.821$, $\Omega = 16.25$, $d = 1.23$mm, and $\tau_\nu = 6.1$s. For all of our simulations (expect where noted) we used a spatial resolution of 0.1 and a time resolution of 0.005.

Figure 6.4: Simulation of the Boussinesq equations with $\Gamma = 20$, $\sigma = 0.93$, $\Omega = 17.6$, $\epsilon = 0.055$, and an artificially large centrifugal force in order to model the effect of an inaccessibly large Γ. Left: zero centrifugal force. Center: centrifugal force is 4 times the physical value. Right: centrifugal force is 10 times the physical value. We used a time resolution of 0.001 for these simulations.

However, we were unable to run our simulations at very large aspect ratios due to time constraints, so we artificially increased the centrifugal force to simulate the larger aspect ratios. An example is shown in Figure 6.4. We see that as the centrifugal force increases, the domain size decreases. We do eventually observe the hybrid state in the third panel of our figure. This is convincing proof that the hybrid state is indeed the result of the centrifugal force.

We also performed a side-by-side comparison with experimental results as shown in Figure 6.5. The agreement of the experimental results with the simulations using the centrifugal force is again quite convincing. By comparing the figures, one sees that the domain size is considerably smaller in the centrifugal simulations and the experimental results than in the simulations with only the Coriolis force. This was verified quantitatively by comparing correlation lengths in [9].

When we ran simulations with only the Coriolis force, we found precession frequencies which disagree quantitatively with the experiments for the exact same parameters, as can be seen in Figure 5.11. Hence, we repeated our simulations with the centrifugal force included using the exact physical values for $\Gamma = 40$ [57]. These results are shown in Figure 6.6. We see that the simulations which neglected the centrifugal force give a scaling exponent of 1.15, in good agreement with the theoretical prediction of 1.0 from the amplitude equations which also neglected the centrifugal force. There is also good agreement between the experimental data and the results,

Figure 6.5: Images of domain chaos in Rayleigh-Bénard convection with $\Gamma = 36$, $\sigma = 0.821$, $\epsilon = 0.05$, and $\Omega = 16.25$. Left: the temperature profile at the mid-plane from simulation of the Boussinesq equations with no centrifugal force. Center: shadowgraph image from experiment. Right: the temperature profile at the mid-plane from simulation of the Boussinesq equations including centrifugal force.

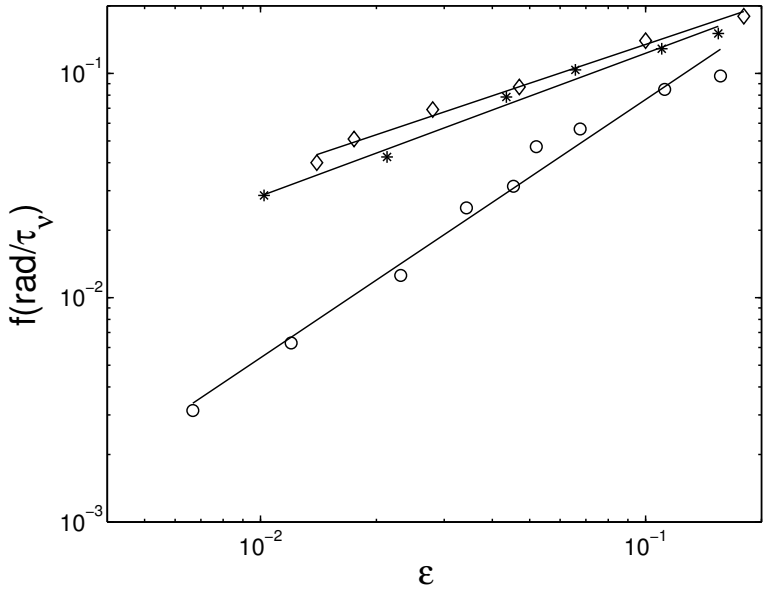

Figure 6.6: Frequencies $f_{\rm pre}$ (in units of radians/vertical diffusion time) versus control parameter ϵ for the same parameters as in Figure 5.9, but conducting boundaries were used for all simulations. Legend: "$*$" = simulations with centrifugal and Coriolis force, slope = 0.63, "o" = simulations with Coriolis force only, slope = 1.15, "$\diamond$" = experimental results, and slope = 0.58 [57].

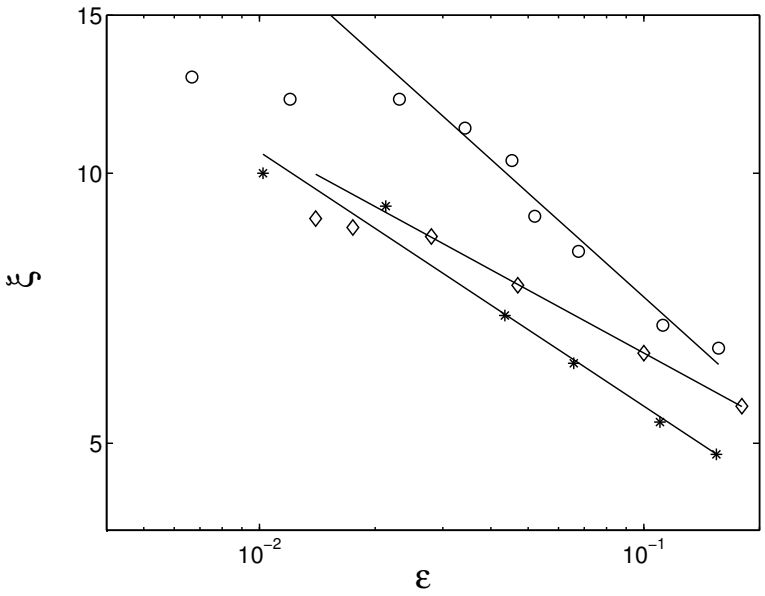

Figure 6.7: Correlation lengths ξ versus control parameter ϵ for the same parameters as in Figure 5.12, but conducting boundaries were used for all simulations. Legend: "$*$" = simulations with centrifugal and Coriolis force, slope = -0.28, "o" = simulations with Coriolis force only, slope = -0.39, "$\diamond$" = experimental results, and slope= -0.23 [57].

which included both the centrifugal and the Coriolis force. Not only did the numerical simulation yield a scaling exponent of 0.63, very close to the exponent of 0.58 obtained from the experiment, but it also reproduced the actual values of f_{pre} in the experiment remarkably well.

Although it is clear that the scaling is affected by the centrifugal force, we surmise that this change in scaling is not due to the fact that we have an imperfect bifurcation, since we have been careful to remain above R_c. Instead, the LSC introduced by the centrifugal force promotes defect formation. As a result, glide-induced precession, as discussed in Section 4.3.2.1 and Section 5.2, is more prevalent at lower ϵ when this LSC is present. We have shown that glide-induced precession does have a smaller scaling exponent, namely $\epsilon^{3/4}$. This also explains why we see smaller domains when we include the centrifugal force: the presence of more defects breaks the domains up into smaller regions.

We have included our correlation length results, although recent evidence has sug-

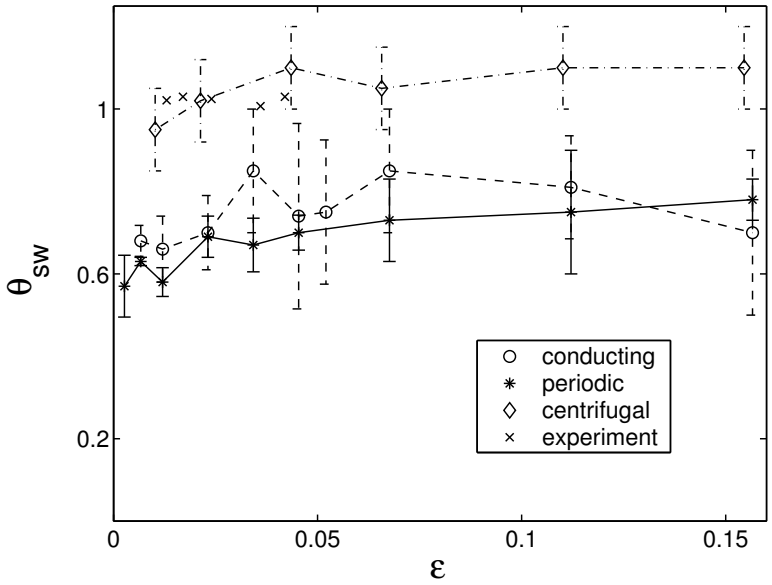

Figure 6.8: Domain switching angle $\theta_{\rm sw}$ versus ϵ. The simulations with only the Coriolis force (both periodic and conducting boundaries) are the same as in Figure 5.8. We have also included the results from simulations with both the centrifugal and Coriolis force, "$\diamond$", and from experiment, "$\times$" [59].

gested that our methods of determining correlation length are somewhat problematic [8]. We describe these methods of computing correlation length in Section 5.3. The experimental results [59] use the second moment of $S(k)$ to determine the correlation length, as discussed in [78], rather than performing a square Lorentzian fit to the data, as we did for our numerical results. We find less quantitative agreement between either simulation and experiment; however the values of the correlation lengths do all fall within the same order of magnitude. Generally, the experimental data still agrees better with the results from the simulations, which include both the centrifugal as well as Coriolis force. However, the agreement is not as good as for the precession frequency. We do find better agreement with the scaling laws. The scaling exponent for the simulations with both the centrifugal as well as the Coriolis force was found to be -0.28, in reasonably good agreement with the experimental results of -0.23. Again, the exponent found from the simulations with only the Coriolis force yielded an exponent of -0.39, in better agreement with the theoretical prediction of an exponent of -0.5.

Finally, we have included our results for domain switching angle θ_{sw} versus ϵ in order to clear up the discrepancy described in Section 5.2. In Figure 5.8 we had found that the switching angle for the simulations with only the Coriolis force agree well with the theoretical value for the maximum growth rate for this Prandtl number ($\sigma \approx 1$) of about 0.7 radians [28]. However, experiments [59] measured a switching angle of about 1.0 radians, in disagreement with this. We find that our simulations with the centrifugal as well as Coriolis force agree well with the experimental results as shown in Figure 6.8. Hu et al. did note that a switching angle, of about 1.0 radians corresponded to the largest switching angle which still gave a positive growth rate. Hence, it appears that the presence of the centrifugal force drives the switching angle to be as large as possible for a given set of parameters.

6.4 Conclusions

Although the Froude number may remain small for rotating Rayleigh-Bénard systems, we have shown here that the relevant parameter for evaluating the significance of the centrifugal force is $\mathcal{A}$, the ratio of the centrifugal to the Coriolis force. Hence, we cannot always neglect the centrifugal force, even for relatively small Γ. We find the presence of the centrifugal force results in an overall LSC which affects domain size and precession frequency. If the aspect ratio is large enough, we observe (both experimentally and via simulations) a transition to a hybrid state consisting of domain chaos in the interior surrounded by radial rolls.

We find we obtain much better agreement with experimental results when we include the centrifugal as well as the Coriolis force to model rotating Rayleigh-Bénard convection. This has resolved a long-standing discrepancy between experiment and theory (which has previously neglected the centrifugal force) about the scaling laws for the domain chaos state of rotating Rayleigh-Bénard convection. Although it is much more difficult to model the centrifugal force theoretically, this is something we would like to investigate in the future.

Chapter 7

Lyapunov Exponents for Rotating Rayleigh-Bénard Convection

7.1 Introduction

Leading order Lyapunov exponents and their corresponding eigenvectors have been computed numerically for Rayleigh-Bénard convection cells. For the first time, we show that for certain parameters, these systems are indeed chaotic in the sense of having a positive Lyapunov exponent. A discussion of our computational methods is given in Section 2.4.

As discussed in Section 1.2, by developing a Lyapunov solver which computes the leading Lyapunov exponent and eigenvector for realistic boundary conditions (2.23, 2.24, 2.25), we have made the first step in computing the full spectrum of positive Lyapunov exponents and hence the Lyapunov spectral density for our systems. If we can show that the Lyapunov spectral density scales extensively with the system size, this would provide us with a rigorous definition of spatiotemporal chaos.

We will focus first [98] on the experiments by Ahlers and Behringer [2, 1, 10, 11] for small aspect ratio cylindrical cells ($\Gamma = 2.08$ and 4.72) in addition to the experiments performed by Gollub and Benson [46] for small rectangular cells (dimension 3.50×2.08). These systems are non-rotating; however, we study them for their historical significance and because their dynamics is simpler. We then study larger aspect ratio ($10 < \Gamma < 40$) [60] simulations of rotating Rayleigh-Bénard convection.

We will also test if the claims in the Egolf et al. [39] study on the SDC state for periodic cells can be generalized. The Egolf paper studied visualizations of the perturbation field corresponding to the largest Lyapunov exponent (this perturbation field is also known as the Lyapunov eigenvector) and demonstrated that the regions where the perturbation grows are relatively localized and are correlated with dynamical events such as roll breaking/reconnection. They also found that these dynamical events were correlated with large spikes in the short-time dynamics of the leading order Lyapunov exponent. The Egolf paper makes the conclusion that the mechanism for generating chaotic dynamics in SDC is roll breaking/reconnection.

We show the results of our detailed investigation of the contribution of dislocation creation/annihilation events to the leading order Lyapunov exponent λ_1 for non-rotating small aspect ratio cells. While we do find that dislocation events are highly correlated with the short time dynamics of λ_1, we find that not all dislocation events are associated with contributions to the long time average of λ_1. We will also discuss the quantity S_λ (2.62), which we find is more useful for understanding the chaotic dynamics than either the short-time Lyapunov exponent λ_1^{inst} (2.58) or the long-time average Lyapunov exponent λ_1 (2.56). We find the short-time Lyapunov exponent can be somewhat misleading, since it can fluctuate wildly, even when the overall average Lyapunov exponent is either zero or negative. Blindly computing the long-time average Lyapunov exponent can also be problematic, since transient dynamics can make a significant contribution to the exponent or require much longer evolution times for convergence.

We will also explore the relation of the short-time Lyapunov exponent λ_1^{inst} to defect dynamics in our larger aspect ratio rotating Rayleigh-Bénard cells. We find here that not all defects are even associated with spikes in the leading Lyapunov eigenvector. In addition, we investigate the correlations between λ_1^{inst} and the reduced Nusselt number $\mathcal{N}$. We also investigate correlations between λ_1^{inst} and the defect density ρ_d. We will also study how the leading Lyapunov exponent λ_1 varies with aspect ratio Γ and with the control parameter ϵ.

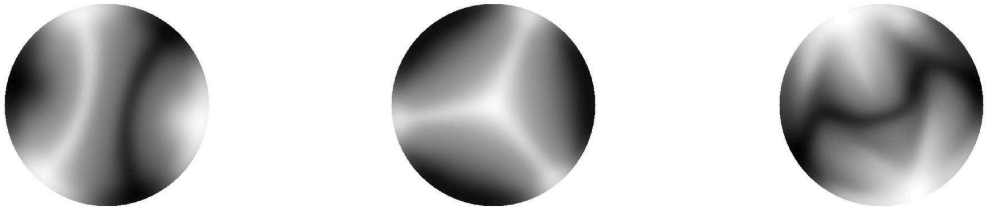

(a) (b) (c)

Figure 7.1: Snapshot of temperature deviation θ at the midplane, for $\Gamma = 2.08, \sigma = 0.78, \Omega = 0$ and (a) $R = 10000, t = 20$, (b) $R = 10000, t = 66.2$, (c) $R = 18800, t = 29.3$. Lateral temperature boundary conditions are insulating. The gray denotes the conduction value ($\theta = 0$), and the lighter and darker shades give the values above and below this.

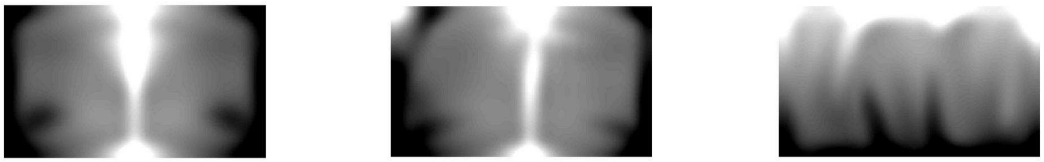

(a) (b) (c)

Figure 7.2: Same as Figure 7.1 but for a rectangular cell of dimensions $3.50 \times 2.08, \sigma = 2.5, \Omega = 0$ and (a) $R = 42500, t = 25.78$, (b) $R = 52110, t = 54.2$, (c) $R = 56000, t = 24.1$. Lateral temperature boundary conditions are insulating. The power spectral density of these states is shown in Figure 7.3.

7.2 Results for Small Aspect Ratio Cells: Nonrotating case

The results shown here use the same parameters as the experiments by Ahlers and Behringer [2] and Gollub and Benson [46]. For the experiments by Ahlers and Behringer, we use a Prandtl number σ of 0.78 and investigate aspect ratios $\Gamma = 2.08$ and 4.72. We use a time resolution dt of 0.001 and a spatial resolution dx of 0.1 for $\Gamma = 4.72$, and a dt of 0.0001 and dx of 0.05 for $\Gamma = 2.08$. For the experiments by Gollub and Benson we use a rectangular cell of dimensions 3.50×2.08, a σ of 2.5, a dt of 0.0001, and a dx of 0.08. Note that there is no rotation for these cells. We explore rotating cells for larger aspect ratio in Section 7.3.

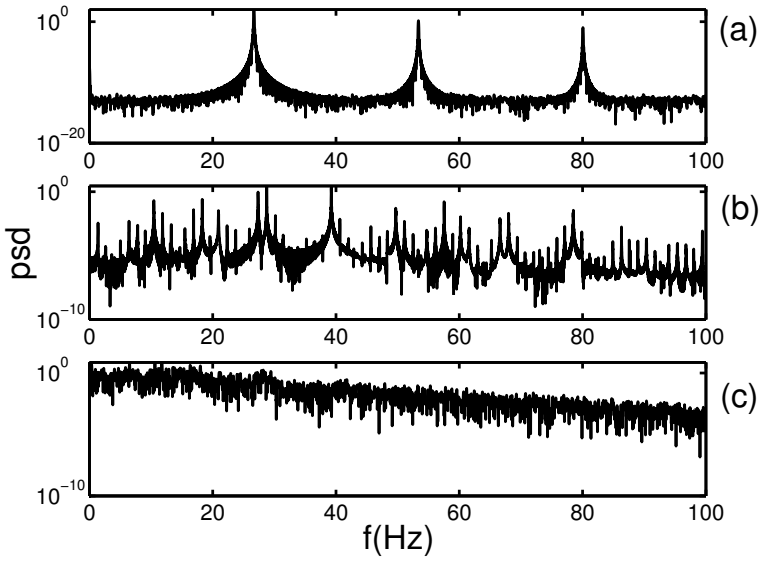

Figure 7.3: The power spectral density of the Nusselt number as a function of frequency for the states shown in Figure 7.2.

We verified convergence both with respect to spatial and temporal resolutions in Appendix 7.A. We also verified that our results were independent of the initial perturbation field in Appendix 7.B. We chose our resolution to give us an accuracy of 1×10^{-3} for the evolution of our fluid elements (this achieved the best balance between accuracy and integration time). Note that the error in the Lyapunov exponent will be somewhat larger since it requires an average over long evolution times and the convergence can be rather noisy. We needed a finer resolution for smaller aspect ratios, since the Rayleigh numbers required for chaos were much larger, as shown in Figure 7.9.

We will explore a variety of Rayleigh numbers R both before and after the transition to aperiodic time dynamics. We use insulating thermal sidewall boundary conditions for the $\Gamma = 2.08$ and rectangular cases, which most closely resemble the experiment [11]. We use conducting boundary conditions for the $\Gamma = 4.72$ case to be consistent with [90], but the boundaries should matter less in the larger aspect ratio system (the experiments used insulating boundary conditions for all aspect ratios).

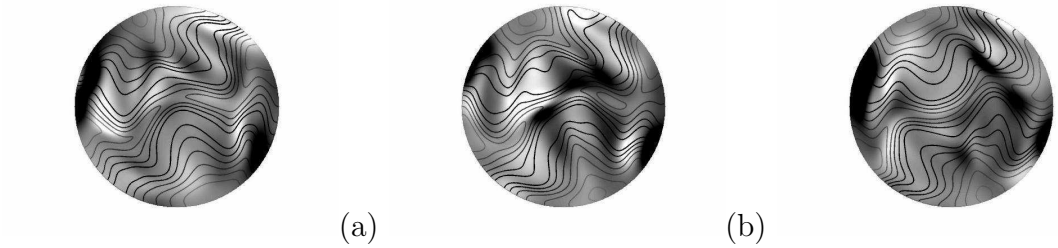

(a) (b) (c)

Figure 7.4: Overlay of a grayscale density plot of the midplane temperature perturbation field $\delta\theta$ (same color scheme as in Figure 7.1) and a contour plot of the midplane full temperature field θ. The parameters are $\Gamma = 2.08, \sigma = 0.78, R = 18800, \Omega = 0$, and (a) $t = 29.36$, (b) 29.39, (c) 29.43. Lateral temperature boundary conditions are insulating. A visualization of the temperature field is given in Figure 7.1c.

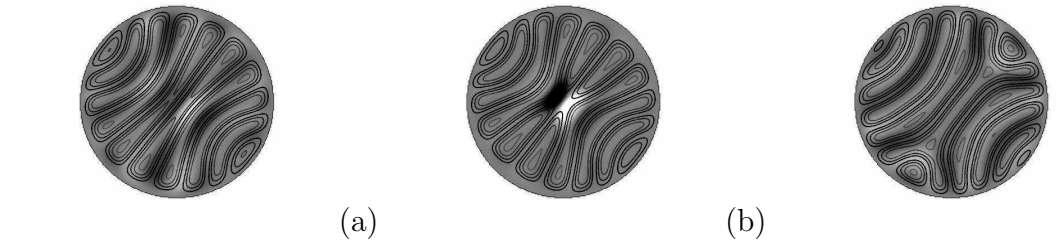

(a) (b) (c)

Figure 7.5: Same type of plot as in Figure 7.4 but for the following parameters: $\Gamma = 4.72, \sigma = 0.78, R = 2800, \Omega = 0$, and (a) $t = 427.8$, (b) 438, (c) 448.2. Lateral temperature boundary conditions are conducting.

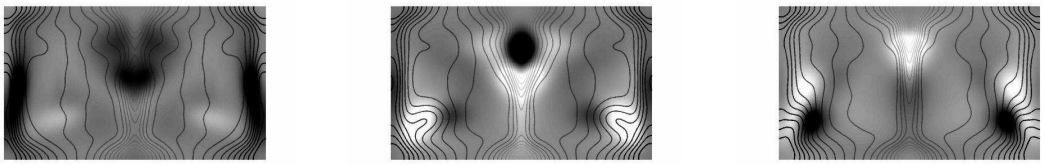

(a) (b) (c)

Figure 7.6: Same type of plot as in Figure 7.4 but for a rectangular cell of dimensions $3.50 \times 2.08, \sigma = 2.5, R = 42500, \Omega = 0$, and (a) $t = 25.77$, (b) 25.78, (c) 25.79. Lateral temperature boundary conditions are insulating. A visualization of the temperature field is given in Figure 7.2a.

7.2.1 Visualizations

Ahlers and Behringer did not perform any visualizations of their cells, so we have provided a few pictures of the smallest aspect ratio cells. A plethora of different states exist in these tiny cells, as shown in Figure 7.1. Note that Figure 7.1a and Figure 7.1b correspond to the same R, but occur at different times. The three states have also been seen in recent experimental visualizations by Hof et al. [56] and computed by Borońska and Tuckerman [14], along with a variety of other planforms.

In Figure 7.2 we show visualizations of the rectangular cells. The two-roll system shown in Figure 7.2a and Figure 7.2b are similar to those observed by Gollub and Benson. The noisy dynamics in Figure 7.2c was not visualized by Gollub and Benson. It is interesting to note that the roll orientation has switched from Figure 7.2b to Figure 7.2c. The power spectral density of the Nusselt number is reported in Figure 7.3 for the corresponding Rayleigh numbers in Figure 7.2. We find a periodic state for $R = 42500$, as evidenced by the single frequency in Figure 7.3a (and its harmonics). We find a quasiperiodic state at $R = 52110$, since two incommensurate frequencies are present in Figure 7.3b. Finally, we see a very broad power spectrum for the chaotic state at $R = 56000$, as shown in Figure 7.3c. Similar power spectra were observed by Gollub and Benson.

We have also found it productive to visualize the temperature perturbation field $\delta\theta$ as defined in (2.59). Note that the perturbation field $\delta\mathbf{y} = [\delta\mathbf{u}, \delta\theta]$ is also known as the Lyapunov eigenvector. The quantity $\delta\theta$ is the temperature part of $\delta\mathbf{y}$ after being normalized by $\|\delta\mathbf{y}(\Delta t)\|$. We make the point to plot this field after being scaled to have unit norm so we can investigate the structure of the eigenvector field and not its absolute size. When we looked at stationary systems we found the perturbation field to be extended, asymmetric, and stationary. In contrast, we found that the perturbation field for systems with time dependence in the Nusselt number (either periodic or aperiodic) is characterized by localized bursts associated with some type of dynamical event such as defect creation or roll compression. This has also been seen by Egolf et al. [39] for larger aspect ratio (but using periodic boundary conditions)

and for the parameter regime where SDC exists. We do expect the eigenvector to be proportional to the time derivative of the full field for periodic states (i.e., when $\lambda_1 = 0$).

In Figure 7.4 we have plotted an overlay of a grayscale density plot of the temperature perturbation field $\delta\theta$ and a contour plot of the full temperature field θ. We plot an overlay to determine if localized activity in the perturbation field corresponds to certain features in the full field. For the parameters in Figure 7.4, the system is undergoing oscillatory dynamics [25]. It oscillates between the state in Figure 7.4a to its reflection in Figure 7.4c and then back to a state which is similar to Figure 7.4a The associated perturbation field shows a small, localized region of activity near the center whenever the system switches from one orientation to its inverted orientation. This can be seen in Figure 7.4b. This behavior is somewhat dwarfed by the extremely large activity near the edge of the cell. We do not have an explanation for the source of this activity.

In Figure 7.5 we show a similar overlay plot for a $\Gamma = 4.72$ cell. This time sequence shows that the creation of a dislocation pair is accompanied by a rather large spike in the perturbation field exactly where and when the defects are created.

Finally, in Figure 7.6 we show an overlay plot for the periodic state of the rectangular cell shown in Figure 7.2a. This periodic sequence starts with the two-roll state shown in Figure 7.6a. Then a "bubble" forms in the middle of the cell, as shown in Figure 7.6b. This bubble climbs until it dissipates, as shown in Figure 7.6c. Then the sequence repeats. Notice that there is a large region of activity in the perturbation field when the bubble is formed in Figure 7.6b. We also see activity along the sidewalls which is associated with the roll distortion that occurs there. In all cases (Figure 7.4, Figure 7.5, and Figure 7.6) the increase in the perturbation field activity is associated with a spike in λ_1^{inst}.

7.2.2 Positive Leading Order Lyapunov Exponents

We computed the quantity λ_1 (2.56) for a variety of parameters and found it to be positive in the regimes where Ahlers and Behringer and Gollub and Benson detected an aperiodic time dependence in the Nusselt number (2.27). For example, in Figure 7.7 we have plotted S_λ (2.62) versus time for $\Gamma = 2.08, \sigma = 0.78, R = 18800$, and insulating boundary conditions (solid line). We see a general upward trend to S_λ as a function of time, and the long time average slope is $\lambda_1 = 0.71 \pm 0.09$. This system shows chaotic behavior to at least 54 vertical diffusion times, which is quite long considering a horizontal diffusion time (2.22) is equal to $\Gamma^2 \approx 4$ for this case. We determined our error in λ_1 by dividing the time series S_λ into approximately 6-8 equal parts, finding the slope, and hence λ_1, associated with each smaller time series. The mean of these values is close to the λ_1 found from the slope of the entire time series, and the error is determined by finding the standard deviation of these values (divided by the square root of the number of values). This works as long as the separation of the sample series is longer than the correlation time, which is true for our cases.

We also computed λ_1 for the larger aspect ratio case $\Gamma = 4.72, \sigma = 0.78, R = 6950$, and with conducting boundary conditions as shown in the dashed line of Figure 7.7. Again we see a long time upward trend, and the slope is $\lambda_1 = 0.62 \pm 0.06$. Finally, we computed λ_1 for the chaotic state of the rectangular cell of dimensions $3.50 \times 2.08, \sigma = 2.5, R = 56000$, and insulating boundary conditions. We find a very steady, very large long time upward trend, as shown in Figure 7.8. The slope gives a λ_1 equal to 7.3 ± 0.3, indicating the chaos is much stronger in this system. These positive exponents prove that these aperiodic systems are truly chaotic in the sense of exponential divergence of nearby trajectories.

We have plotted the λ_1 values for a variety of ϵ values in Figure 7.9 and Figure 7.10. We see similar behavior for all three of our convection cells. We find that λ_1 is zero when the cells exhibit periodic or quasiperiodic behavior (or at least zero within our limit of accuracy), as is expected. We find that λ_1 is positive and increases with ϵ when the cells exhibit nonperiodic behavior. Note that the first data point in

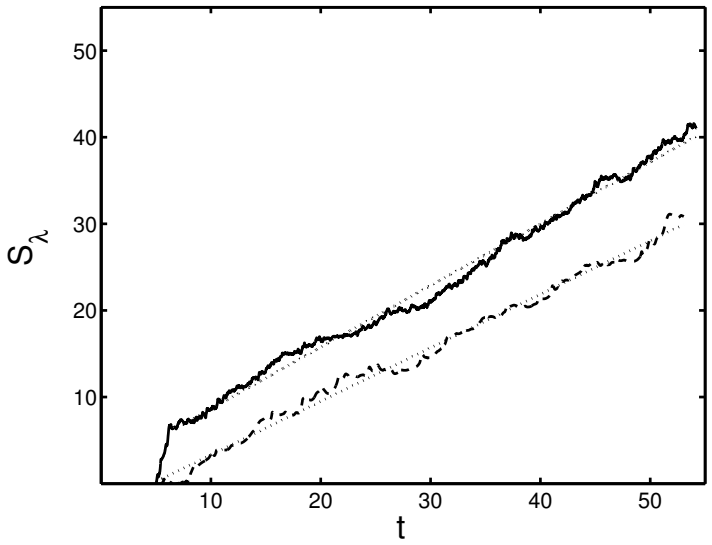

Figure 7.7: The quantity S_λ versus time. The slope of each graph converges to its respective λ_1, which is positive, indicating these systems are chaotic. We used the following parameters, Solid line: $\Gamma = 2.08, \sigma = 0.78, R = 18800, \Omega = 0$, and insulating boundaries. The associated dotted line is the slope taken from 7 vertical diffusion times and up and gives $\lambda_1 = 0.71 \pm 0.09$ (A visualization of this state is shown in Figure 7.1c. and Figure 7.4), Dashed line: $\Gamma = 4.72, \sigma = 0.78, R = 6950, \Omega = 0$, and conducting boundaries. The slope (associated dotted line) is taken from 10 vertical diffusion times and up and gives $\lambda_1 = 0.62 \pm 0.06$.

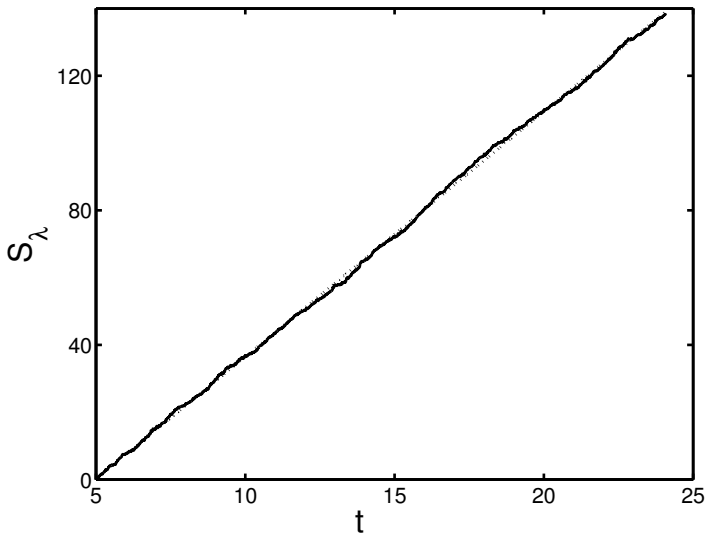

Figure 7.8: The same as Figure 7.7 but for a rectangular cell of dimensions $3.50 \times 2.08, \sigma = 2.5, R = 56000, \Omega = 0$, and insulating boundaries. The slope (associated dotted line) is taken from 7 vertical diffusion times and up and gives $\lambda_1 = 7.3 \pm 0.3$. A visualization of this state is shown in Figure 7.2c.

Figure 7.9a does correspond to the steady state shown in Figure 7.15 for $t > 50$. However, all of the other data points in that figure correspond to either periodic or aperiodic dynamics. For the $\Gamma = 2.08$ cell (Figure 7.9a), we find periodic behavior for $4.8 < \epsilon \leq 8.8$ and a transition to chaos somewhere between $8.8 < \epsilon < 9.4$. Likewise for $\Gamma = 4.72$ (Figure 7.9b), we find periodic behavior for $0.6 < \epsilon \leq 1.56$ and a transition to chaotic behavior for $1.56 < \epsilon < 1.64$. These results are consistent[1] with the results of Ahlers and Behringer, who found a transition to chaos for $\epsilon \simeq 10$ for the $\Gamma = 2.08$ cell and $\epsilon \simeq 1$ for the $\Gamma = 4.72$ cell. Finally, for our rectangular system (Figure 7.9c) we find periodic behavior for $21 < \epsilon \leq 26$ and a transition to chaos for $26 < \epsilon < 27$. Likewise, these results are consistent[2] with Gollub and Benson, who found a transition to chaos for $\epsilon = 27$.

Although we have computed a λ_1 value equal to zero for all periodic states, we find negative λ_1 values associated with steady states near threshhold, as is plotted in Figure 7.10 for our rectangular cells. One also sees the value λ_1 rise up to a value of zero (as opposed to negative values elsewhere) as we go through threshhold, as is expected for a bifurcation [50].

We have not explored the scaling of λ_1 with ϵ or Γ in any detail for our smaller aspect ratios, since the dynamics is much more variable for smaller aspect ratios. For example, Hof [56] has shown that eight different states coexist for $\Gamma \simeq 2$. It would be very difficult to distinguish between trends as a result of a transition to a different state versus trends due to an increase in R and Γ for the same state. In addition, these systems often undergo transitions to different states after a long evolution time (see Figure 7.15), making such a comparison doubly difficult. We have explored the scaling of λ_1 with ϵ and Γ for our larger aspect ratio rotating systems in Section 7.3.2.

[1]The agreement is reasonable since we assumed our $R_c = 1708$ for these systems and did not accurately measure R_c.

[2]In this case we did accurately measure an $R_c = 1930$.

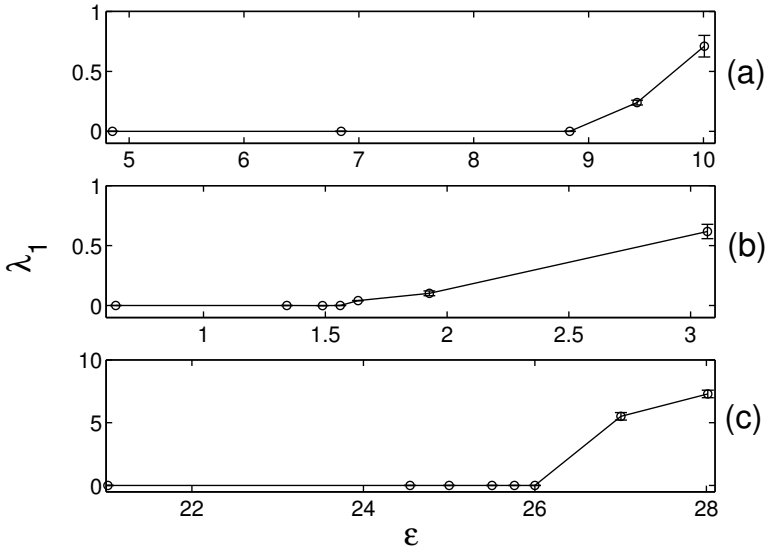

Figure 7.9: The quantity λ_1 versus ϵ for the following: (a) $\Gamma = 2.08, \sigma = 0.78, \Omega = 0$, $R_c = 1708$ (R_c is assumed, not measured), and insulating boundaries, (b) $\Gamma = 4.72, \sigma = 0.78, \Omega = 0$, $R_c = 1708$ (R_c is assumed, not measured), and conducting boundaries, (c) Rectangle of dimensions $3.50 \times 2.08, \sigma = 2.5, \Omega = 0$, $R_c = 1930$ (R_c is measured), and insulating boundaries. In all cases the computed λ_1 is the value corresponding to the state the system converges to after a long period of time. Initial transient states and the contribution they make to λ_1 were neglected.

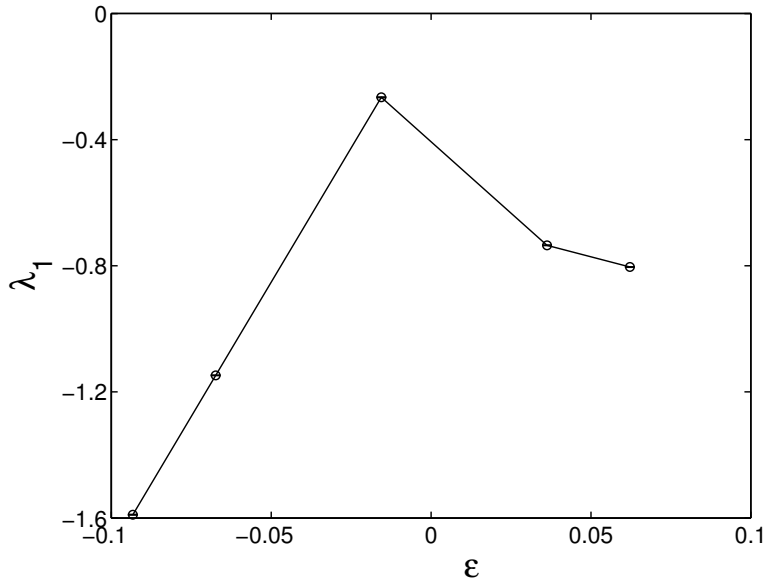

Figure 7.10: The same as Figure 7.9c, but very near threshhold.

7.2.3 Short time Dynamics of Leading Lyapunov Exponents

We would like to use the short time dynamics of λ_1 to identify sources of chaos. It was suggested by Egolf [39], who studied the SDC state of Rayleigh-Bénard convection, that roll breaking/reconnection events caused spikes in the short time Lyapunov exponent λ_1^{inst}, which in turn provided the most significant contributions to the long time Lyapunov exponent λ_1. By looking at small aspect ratio cells, we have determined that this claim is not true in general.

We will analyze a rather simple, periodic state for $\Gamma = 4.72$, $\sigma = 0.78$, and $R = 2800$ (corresponding to $\epsilon = 0.64$). These states have already been investigated by Paul et al. [90], and the dynamics is shown in Figure 7.11 for a long time series. The first panel shows the reduced Nusselt number $\mathcal{N}$ as a function of time. One sees the pattern is almost periodic after $t = 150$ vertical diffusion times and becomes periodic after $t = 1700$ vertical diffusion times. There is a characteristic pattern to the dislocation creation/annihilation events. For example, the large dip in the first panel at $t = 438.36$ corresponds to the dislocation pair creation, as shown in Figure 7.5b, and is immediately followed by dislocation climb to the opposite sides of the container shown in Figure 7.5c. Then, the dislocations slowly glide along the rim until they are annihilated successively. The annihilation of the first dislocation occurs at $t = 526$, and the second dislocation is annihilated at $t = 662$, just before the next creation event at $t = 675.76$. Note that each dislocation event is associated with a spike in S_λ (second panel). However, after the sequence occurs,[3] there is little net rise in S_λ. This can be seen in the relatively flat regions of S_λ in the second panel, such as $400 < t < 700$, $1100 < t < 1400$, and $t > 1700$. This indicates that while a dislocation creation/annihilation event is associated with a localized stretching of phase space, it is not necessarily associated with the long time Lyapunov exponent.

We have also plotted λ_1^{inst} as a function of time in the third panel of Figure 7.11. While each dislocation event does cause a burst of activity in λ_1^{inst}, it is very difficult to tell from looking at λ_1^{inst} which dislocation events contribute to the long-time exponent

[3] We have found that the behavior of S_λ is relatively insensitive to the choice of initial conditions $\delta\mathbf{y}(0)$, as is illustrated in Figure 7.31.

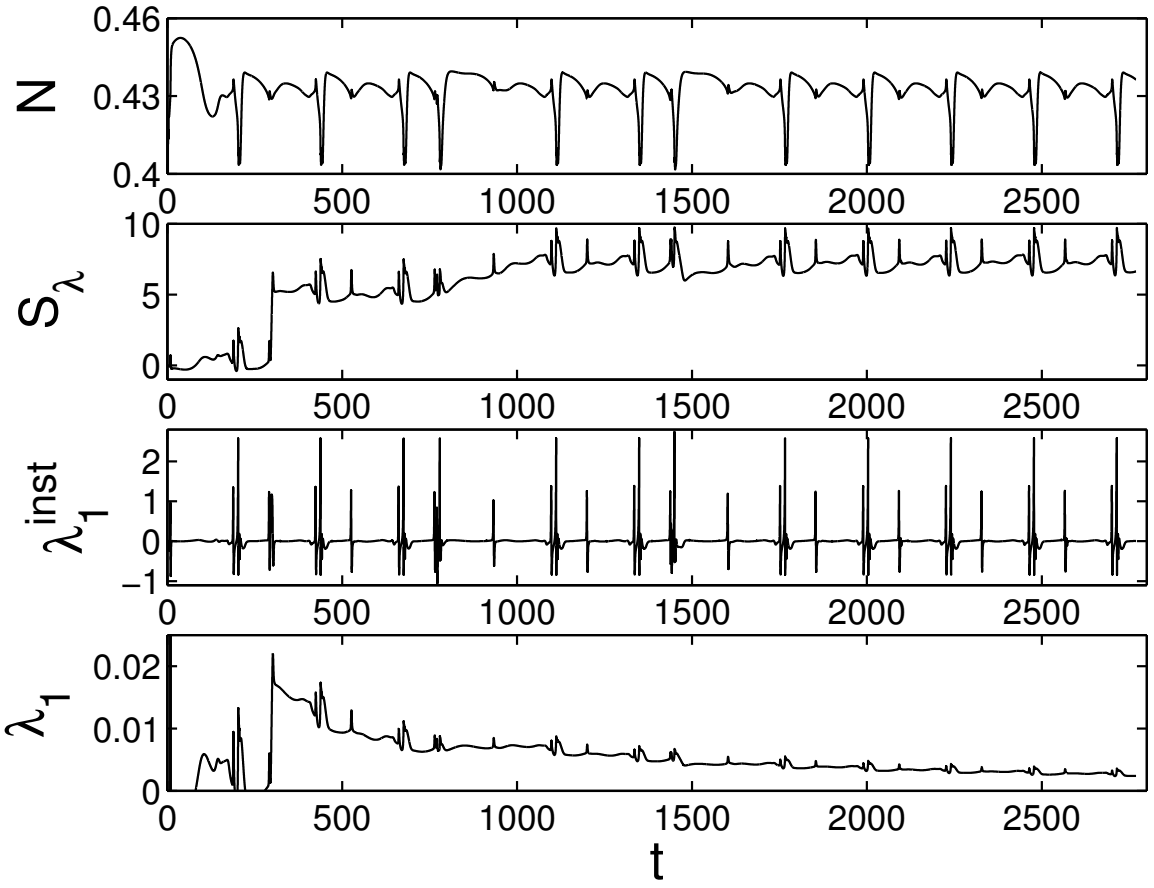

Figure 7.11: First panel: Reduced nusselt number $\mathcal{N}$ as a function of time t for $\Gamma = 4.72, \sigma = 0.78, \Omega = 0$, $R = 2800$, and conducting boundaries. Second panel: Corresponding S_λ as a function of time t. Third panel: Corresponding λ_1^{inst} as a function of time t. Fourth panel: Corresponding λ_1 as a function of time t. A visualization of this state is shown in Figure 7.5.

λ_1; hence we prefer to look at S_λ versus time. This is reinforced in the fourth panel where we show λ_1 versus time. The quantity $\lambda_1(t)$ is found by evaluating (2.56) from some initial time t_{init} to the time t. Note that the value of λ_1 remains positive because of the large initial transients, including the one at $t = 300$. It is much more accurate to find λ_1 from evaluating the slope of S_λ, selecting the region where the transients have died out. When we do this (for $t > 2000$), we obtain $\lambda_1 = 0.000 \pm 0.001$ for the state shown in Figure 7.11.

We focus in more detail on the dislocation/creation events in Figure 7.12, where successive time intervals of about 250 vertical diffusion times have been shifted

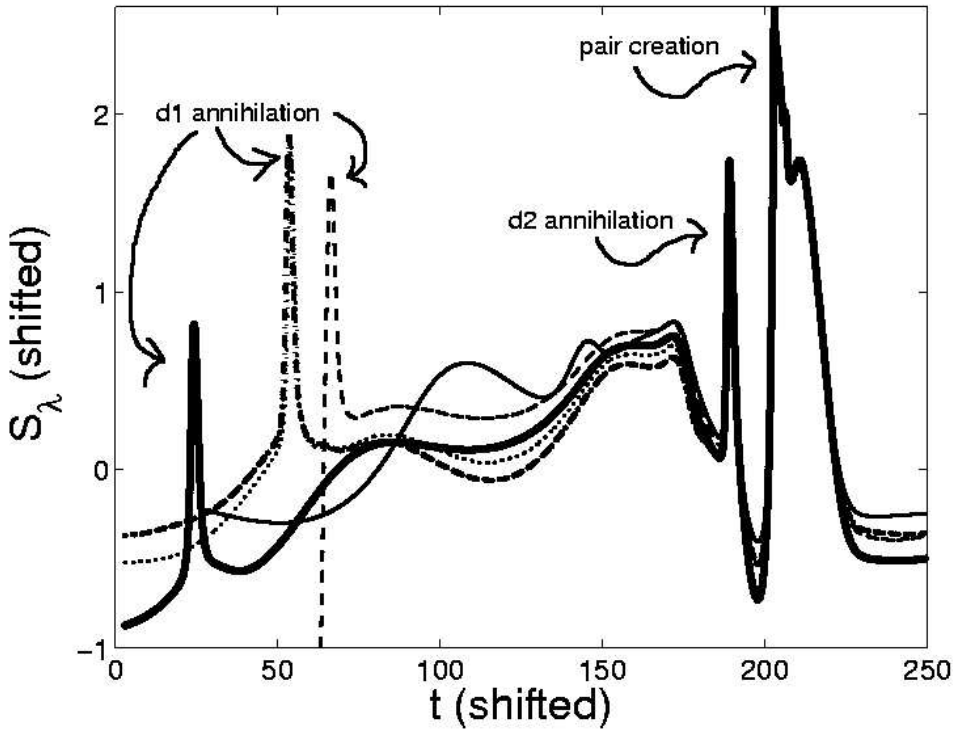

Figure 7.12: Shifted S_λ versus shifted t to compare the events. Approximately 250 vertical diffusion time sections of the S_λ versus t plot in Figure 7.11 have been shifted horizontally and vertically to coincide with the peak at $t = 202.92$, corresponding to a dislocation pair creation. The defect annihilation peaks are also highlighted as "d1", corresponding to the preceding first defect annihilation and "d2" corresponding to the second. Legend: thin solid line, peak at $t = 202.92$, dashed line, peak at $t = 438.36$, dashed-dotted line, peak at $t = 675.76$, thick solid line, peak at $t = 1120$, dotted line, peak at $t = 1349.2$.

horizontally and vertically to correspond to the dislocation pair creation peak at $t = 202.92$. One sees that the dislocation pair creation events neatly overlap. One also sees a return to almost the exact same S_λ value after the event. Hence, one can conclude that these repeated dislocation events are not associated with a positive λ_1. If we compare the most regular cases, $t = 675.76$ (dashed-dotted line) and $t = 1329.2$ (dotted line), we see that even the preceding first dislocation annihilation events located near t(shifted) = 50 overlap. However, note that the other preceding first dislocation annihilation events do not overlap (look at the thick solid line, corresponding to $t = 1120$, and the dashed line corresponding to $t = 438.36$). Visualization of these regions show a different pattern to the events at those times. It is precisely these regions where one sees the largest rise in S_λ. The rise at $t = 300$ does correspond to an unusual roll pinch-off event; however, the rise between $900 < t < 1100$ only corresponds to a slower than average first dislocation annihilation. Likewise, at $t = 800$, the first dislocation annihilation event is almost immediately followed by the second dislocation annihilation and pair creation events.

One sees further support for this by looking at other Rayleigh numbers. The results for $R = 4000$ are plotted in Figure 7.13. Here the defect creation/annihilation events arrive at a much higher frequency. We also see that after $t = 100$ there is an almost perfect periodicity to the pattern; hence one finds no rise in S_λ, and possibly a very slight decline. Conversely, for systems exhibiting non-repeated events in the Nusselt number, one sees S_λ exhibiting an overall positive slope (such as in Figure 7.7). We plot even further results for $\Gamma = 4.72$ in Figure 7.14 and for $\Gamma = 2.08$ in Figure 7.16.

Finally, we show the results for the periodic state of the rectangular cell in Figure 7.17. This state does not involve a defect creation/annihilation event, but instead the roll compression event described in Figure 7.6. We have only shown the last vertical diffusion time, since the oscillation frequency is so large in this system. However, the system was run out from zero to 23 vertical diffusion times. We again see that a periodic system gives us a zero λ_1, even though the short time dynamics of λ_1 are very strong. We plot even further results for the rectangular cell in Figure 7.18.

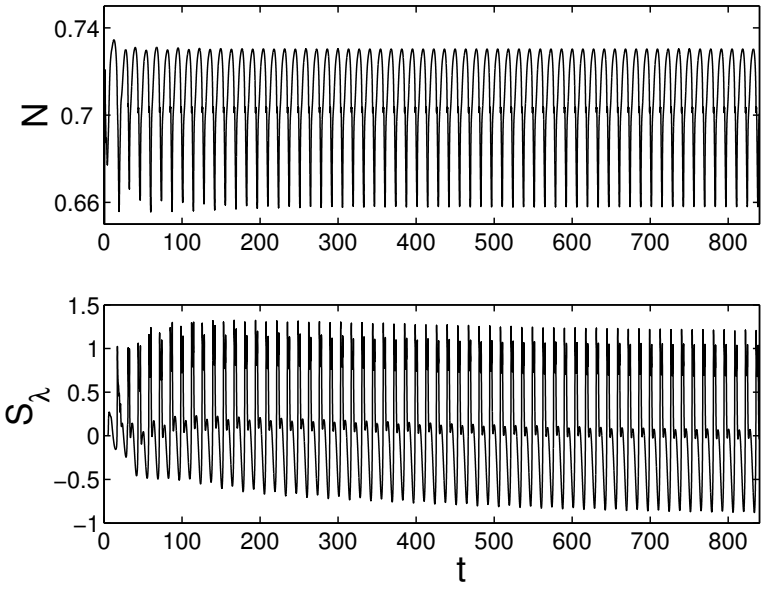

Figure 7.13: Top panel: Reduced nusselt number $\mathcal{N}$ as a function of time t for $\Gamma = 4.72, \sigma = 0.78, \Omega = 0$, $R = 4000$, and conducting boundaries. Bottom panel: Corresponding S_λ as a function of time t.

Hence, we conclude that dynamical events such as dislocation creation/annihilation and roll compression events are not always associated with an overall net rise in S_λ and, hence, λ_1. For all the cases we have studied, we find that if the dynamical events are repeated, they are not associated with a positive λ_1, and if they are not repeated, they are associated with a positive λ_1.

7.2.4 Lyapunov Exponents and Stationary States

We wanted to verify that our Lyapunov solver was working by studying λ_1 in the regime where a time-independent state was observed by Ahlers and Behringer. We choose an R value of 10000, well within the region of stationary, convecting states specified by Ahlers and Behringer. We first evolved the system out to about 20 vertical diffusion times and did observe $\mathcal{N}$ converging to a constant value, as shown in the top panel of Figure 7.15 for $t < 20$. The system settles down to the roll state shown in Figure 7.1a. However, we were surprised to find that the quantity S_λ had a positive slope, as shown in the bottom panel of Figure 7.15 for $t < 20$. This indicated

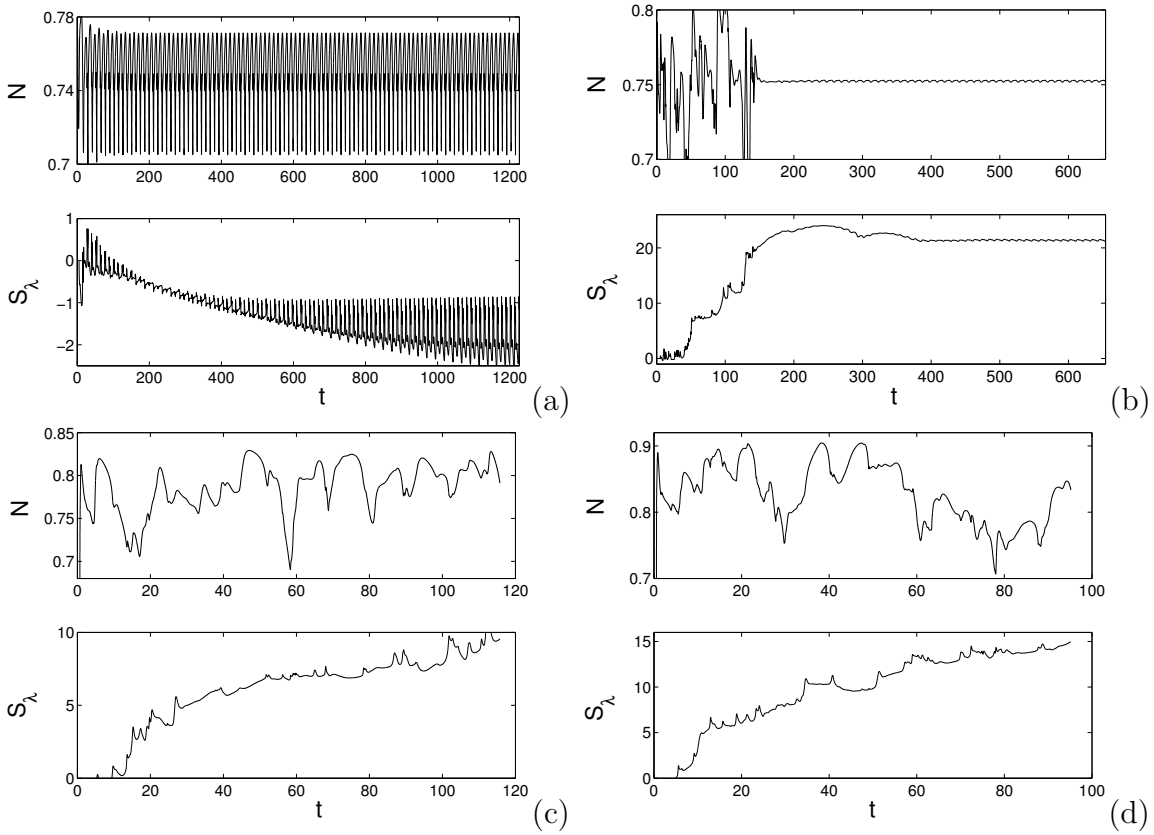

Figure 7.14: Same as Figure 7.13 but for (a) $R = 4250$, (b) $R = 4350$, (c) $R = 4500$, and (d) $R = 5000$.

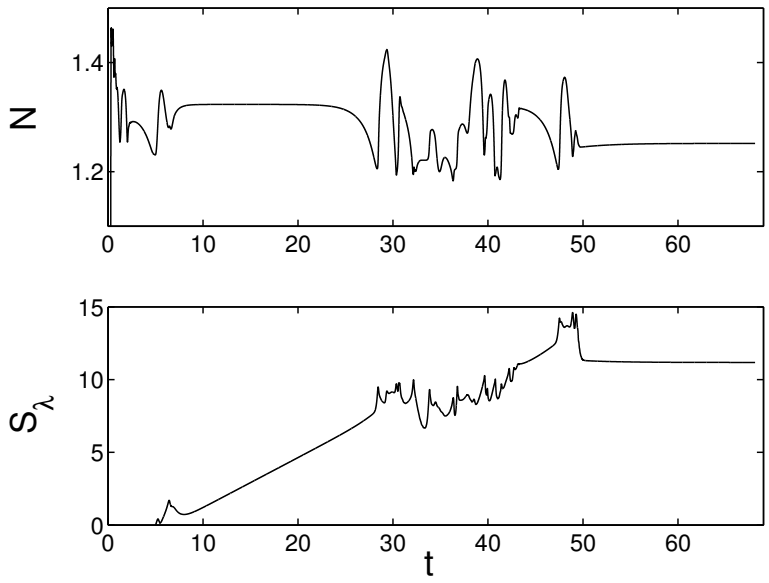

Figure 7.15: Top panel: Reduced Nusselt number $\mathcal{N}$ as a function of time for $\Gamma = 2.08, \sigma = 0.78, \Omega = 0, R = 10000$, and insulating boundaries. Bottom Panel: Corresponding S_λ versus time. Visualizations of this state are given in Figure 7.1a and b.

that the system was in a transient state. When we evolved the system even longer, we found that this parallel roll state eventually evolved into a state with noisy dynamics, which lasted for another 20 vertical diffusion times. Then, the system settled into another stationary state, this time the Mercedes-like pattern shown in Figure 7.1b. This state has a λ_1 that is very slightly negative. Since λ_1 is no longer positive, we can be assured that the system is now in its stationary state. Without the knowledge of λ_1, however, we would not be assured that this state is transient without running the system out for a much longer time.

7.3 Results for Large Aspect Ratio Cells: Rotating Case

In this section we present our results from simulations on a rotating cylinder with aspect ratios in the range $10 < \Gamma < 40$, Prandtl number $\sigma = 0.93$, and angular speed $\Omega = 17.6$, while varying the Rayleigh number over the range $2275 < R < 3000$

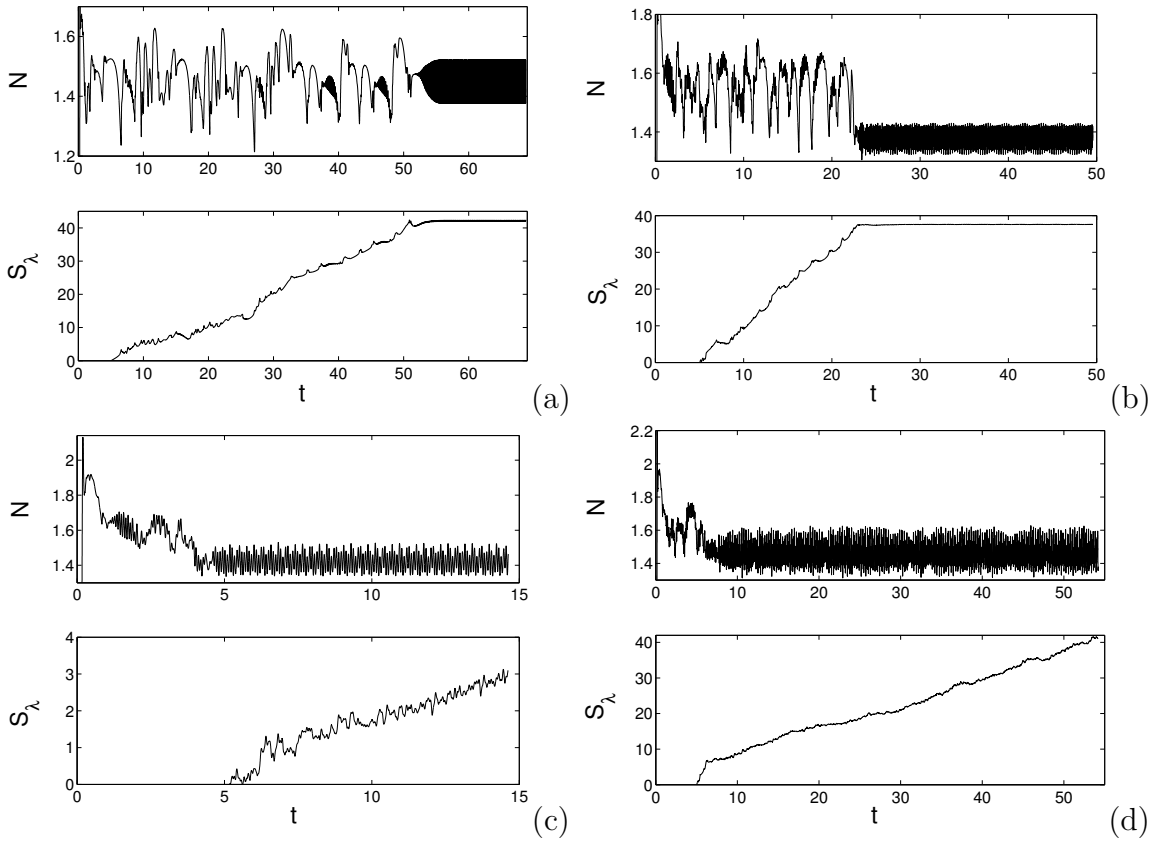

Figure 7.16: Same as Figure 7.15 but for (a) $R = 13400$, (b) $R = 16800$, (c) $R = 17800$, and (d) $R = 18800$. Visualizations of the state in (d) are given in Figure 7.1c and Figure 7.4.

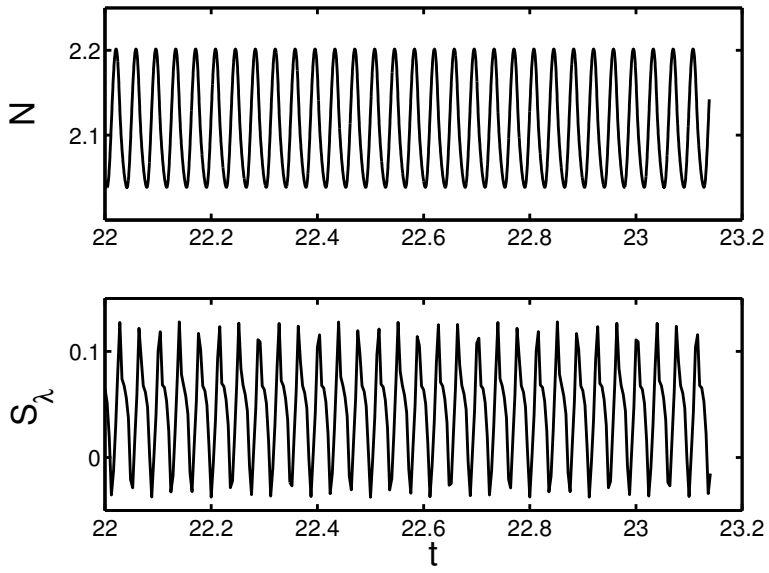

Figure 7.17: Top panel: Reduced nusselt number $\mathcal{N}$ as a function of time t for a rectangular cell of dimensions $3.50 \times 2.08, \sigma = 2.5, \Omega = 0, R = 42500$, and insulating boundaries. Bottom panel: Corresponding S_λ as a function of time t. Visualizations of this state are given in Figure 7.2a and Figure 7.6.

[60]. We used conducting lateral thermal boundary conditions.

7.3.1 Relation of the Exponent $\lambda_1^{\text{inst}}(t)$ to Defect Dynamics

In Figure 7.19 we plot S_λ versus time for $\Gamma = 40$, $\sigma = 0.93$, $\Omega = 17.6$, $\epsilon = 0.012$, and conducting boundaries. The system is in the domain chaos state for these parameters. The largest Lyapunov exponent λ_1 is positive, indicating that domain chaos state is truly chaotic in the sense of having a positive Lyapunov exponent. Figure 7.19a shows that λ_1 converges slowly with large fluctuations toward its limit of $\lambda_1 = 0.011 \pm 0.003$. We also plot the instantaneous Lyapunov exponent $\lambda_1^{\text{inst}}(t)$ versus time in Figure 7.19b. There are large, positive fluctuations so that the overall dynamics is chaotic. There are also brief intervals when the quantity λ_1^{inst} becomes negative, corresponding to temporarily increased stability of the dynamics.

Just as in Section 7.2.3, we find that the spatial structure in the Lyapunov eigenvector that occurs close in time to the peaks of λ_1^{inst} can be related to dynamical events in the full field. We find that the situation is less clear than what was ob-

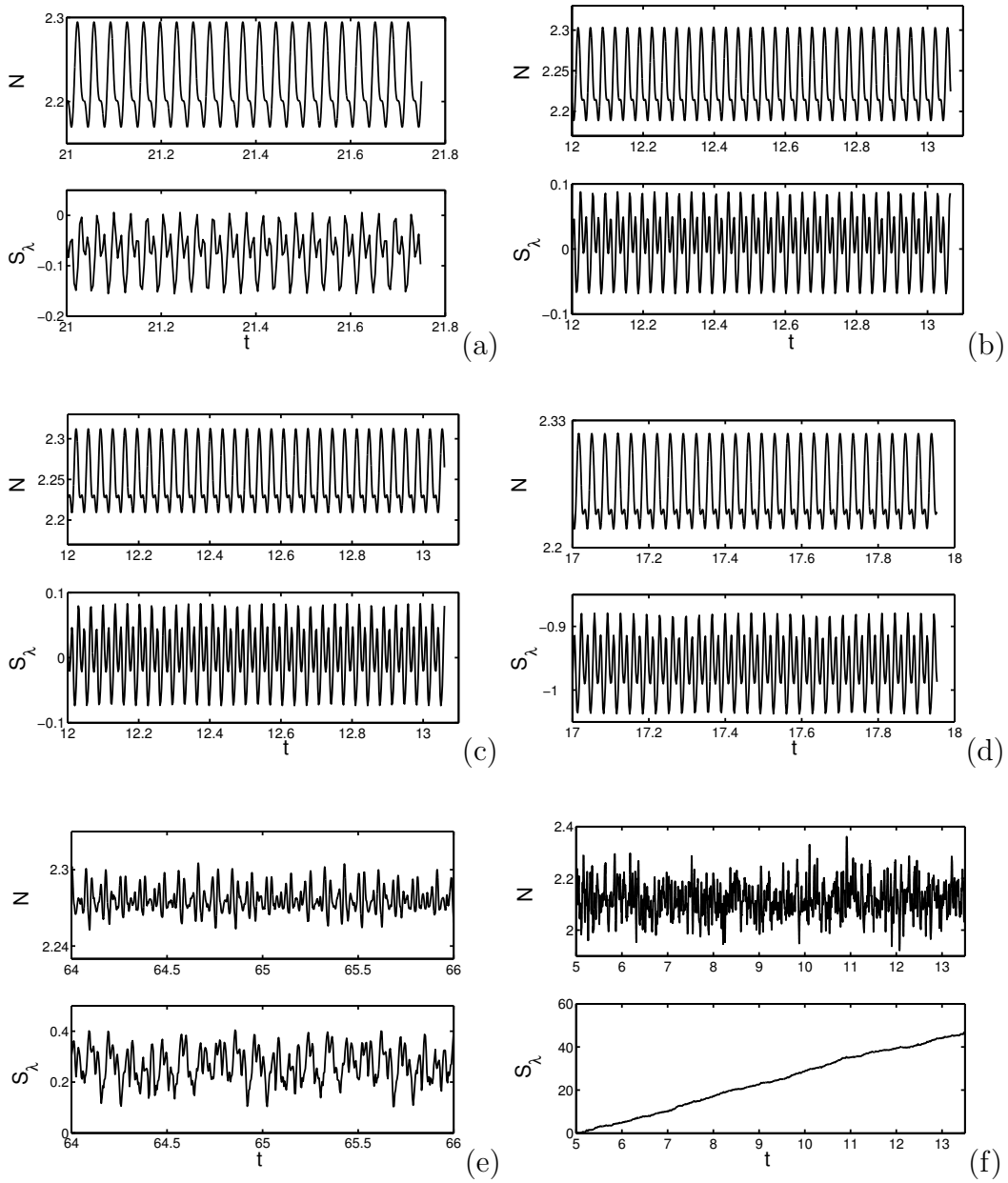

Figure 7.18: Same as Figure 7.17 but for (a) $R = 49300$, (b) $R = 50180$, (c) $R = 51145$, (d) $R = 51628$, (e) $R = 52110$, and (f) $R = 54046$.

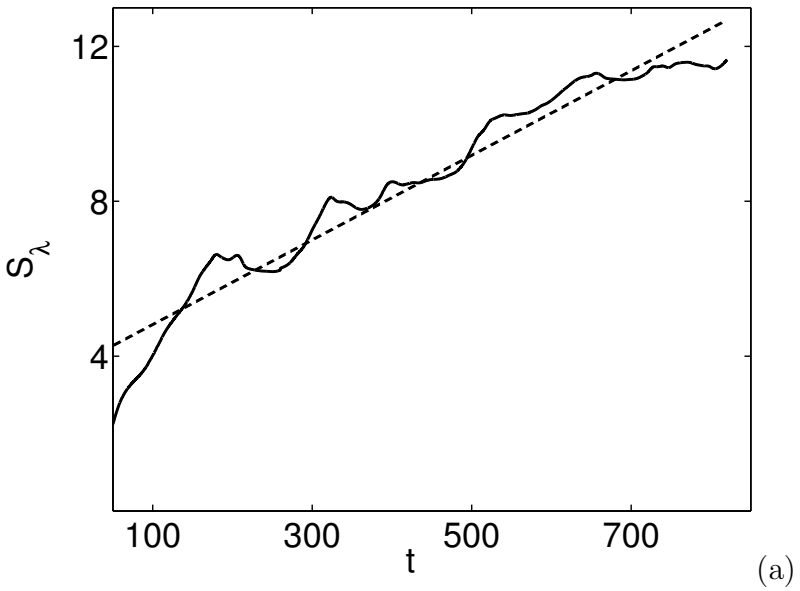

(a)

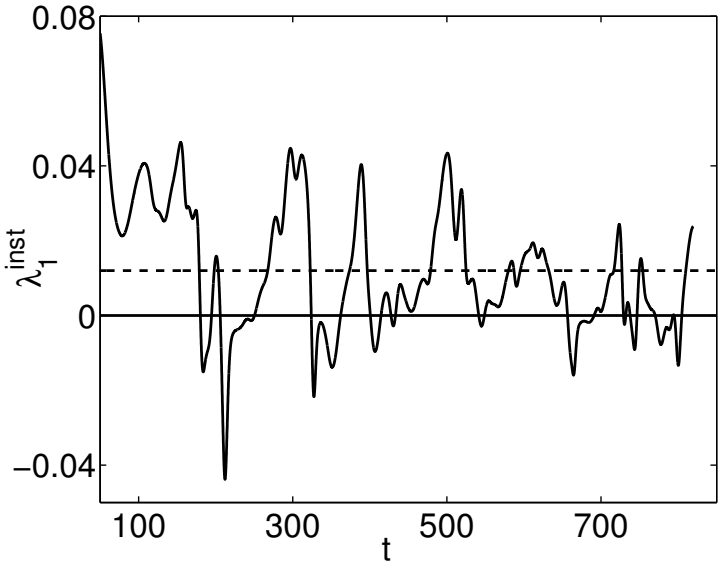

(b)

Figure 7.19: (a) Evolution of S_λ (2.62) as a function of time t, for a domain chaos state for the parameters $\Gamma = 40$, $R = 2275$ ($\epsilon = 0.012$), $\sigma = 0.93$, and $\Omega = 17.6$. The convergence to the infinite time limit is slow and noisy. The slope of the dotted line gives a Lyapunov exponent of 0.011 ± 0.003. (b) Corresponding instantaneous largest Lyapunov exponent $\lambda_1^{\rm inst}(t)$ at time t during the same time period as panel (a). The dashed line is the average value of $\lambda_1^{\rm inst}(t) = 0.012$, which is almost the same as λ_1.

served for the smaller aspect ratio systems. For these large aspect ratio systems we find that some defects have no effect at all on the leading λ_1^{inst}, as can be seen by looking at the evolution of the perturbation field as in Figures 7.20 and 7.21. In both figures, which correspond to the same parameters as in Figure 7.19, we have plotted the temperature deviation field θ on the left and the temperature perturbation field $\delta\theta$ on the right. Just as in Figures 7.4 and 7.5, large spikes in the temperature perturbation field correspond to times where there is a spike in λ_1^{inst}. We investigate in detail the spatial dynamics for the large spikes in λ_1^{inst}, from Figure 7.19 at $t = 297$ and $t = 389$ in Figures 7.20 and 7.21, respectively.

In Figure 7.20d, we see asymmetric activity in the perturbation field, which is largely localized on the right side. This activity is just arising in Figure 7.20b and subsiding in Figure 7.20f. We find, however, that there is very little activity associated with the domain wall motion seen in Figures 7.20a and 7.20c. The activity is instead associated with a few isolated defects located near the right edge, and the activity glides along with the defects. However, the same defects are located along the left edge (this very low ϵ case is almost reflection symmetric), but the activity in the associated perturbation field is much smaller. The activity in Figure 7.20b located near the left edge corresponds to another defect event, which is subsiding.

To avoid any generalizations about the evolution in the perturbation field from Figure 7.20, we show the activity associated with the next large spike in λ_1^{inst} at $t = 398$. In Figure 7.21d we see a much more symmetric distribution of activity on the upper right and lower left sides. This time the activity does appear to be associated with the domain wall motion seen in Figure 7.21c. Just as in Figure 7.20, we see the activity just beginning to arise in Figure 7.21b and subsiding in Figure 7.21f. If one looks at all of the figures, one sees that there is always some sort of defect or domain wall motion associated with each large spike in the perturbation field.

After studying numerous such spatial fields, we generally find that not all defect structures contribute equally to the eigenvector associated with the instantaneous Lyapunov exponent. Possible reasons include the following: (1) the largest Lyapunov eigenvector is not along the instantaneous fastest stretching direction but has some

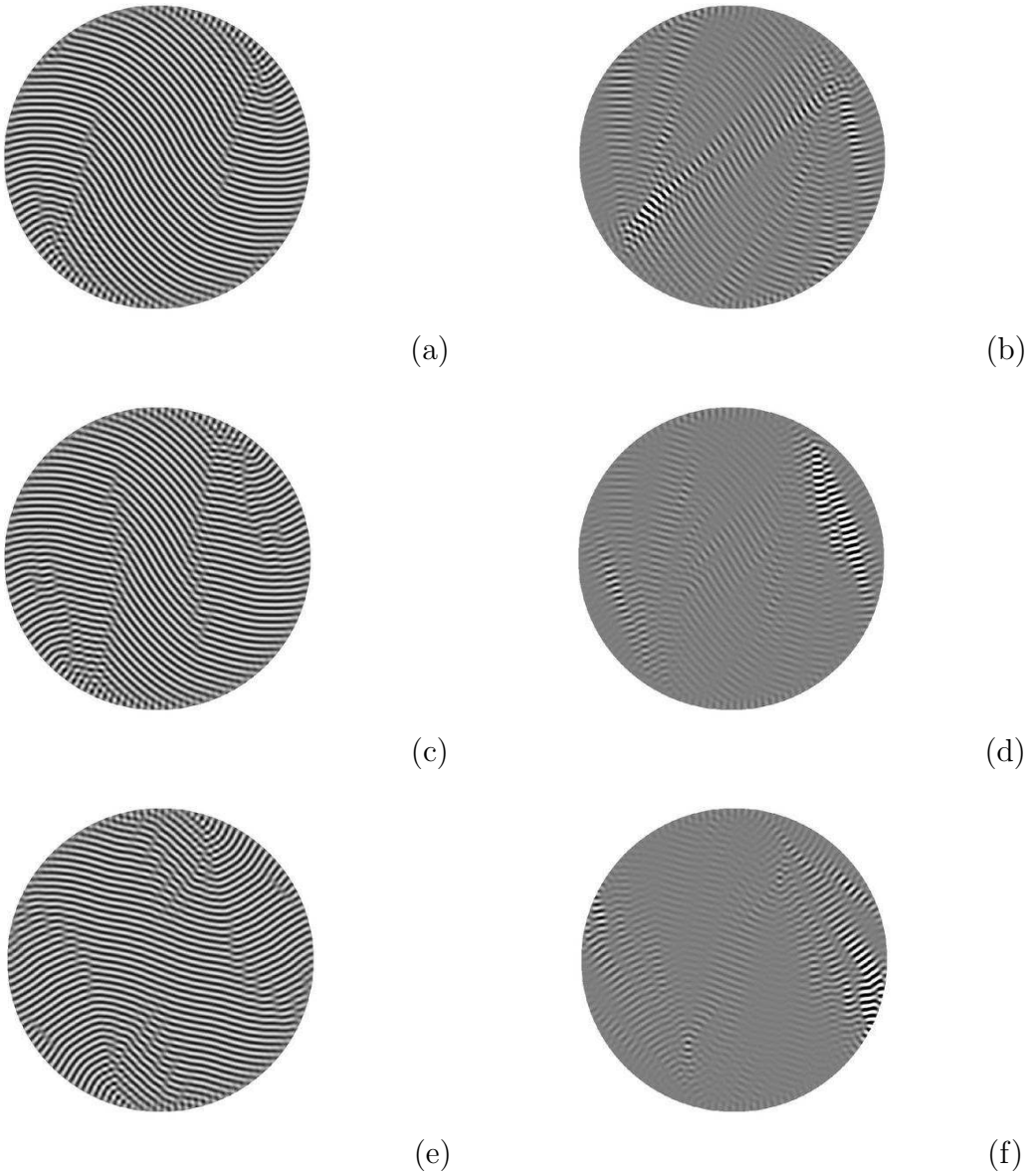

Figure 7.20: Snapshot of temperature deviation θ (a, c, e) and temperature perturbation field $\delta\theta$ (b, d, f) at the midplane, for $\Gamma = 40, \sigma = 0.93, \Omega = 17.6, R = 2275$ and (a, b) $t = 250$, (c, d) $t = 297$, (e, f) $t = 350$. Lateral temperature boundary conditions are conducting. The gray denotes the conduction value ($\theta = \delta\theta = 0$), and the lighter and darker shades give the values above and below this.

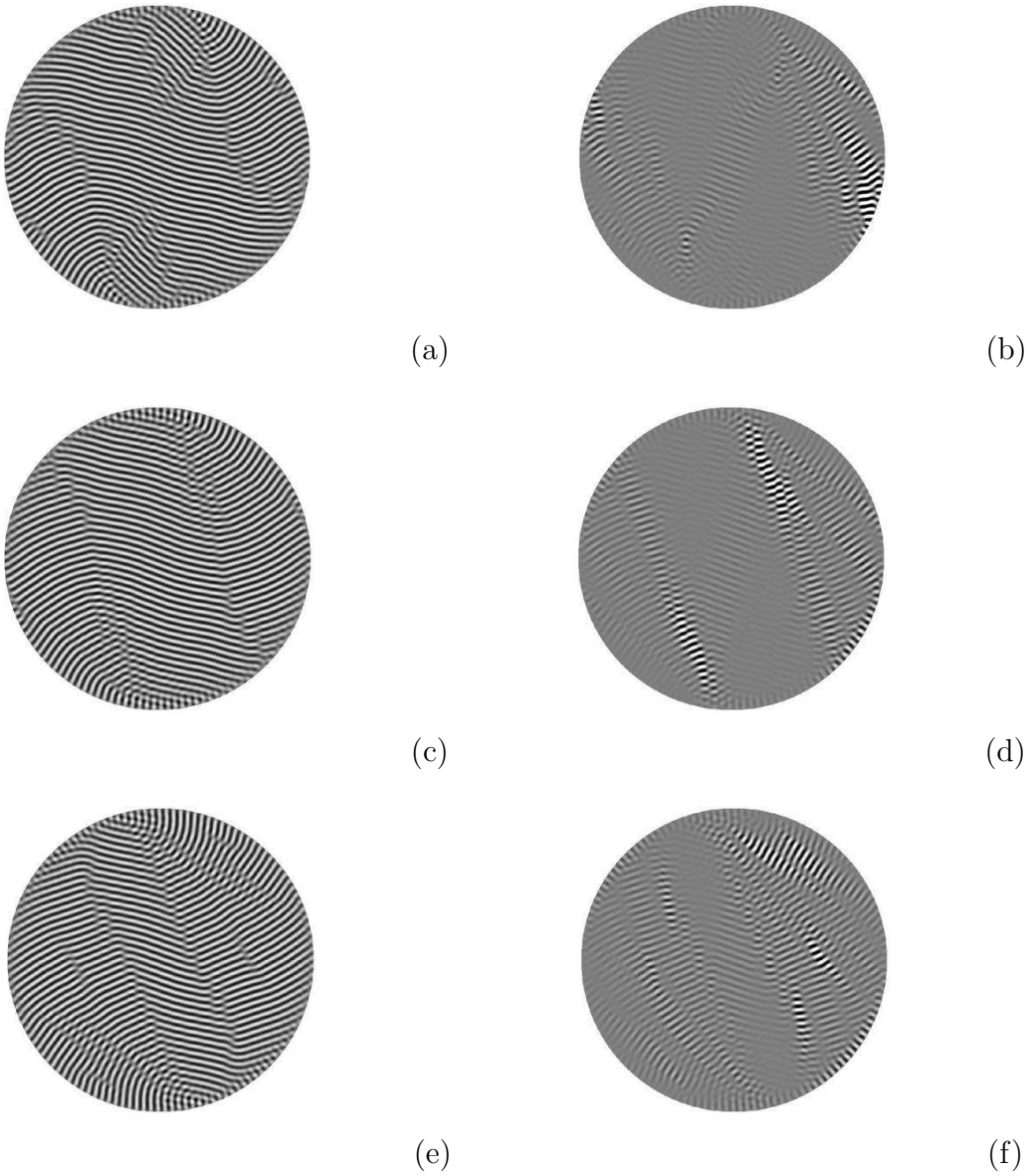

Figure 7.21: Snapshot of temperature deviation θ (a, c, e) and temperature perturbation field $\delta\theta$ (b, d, f) at the midplane, for $\Gamma = 40, \sigma = 0.93, \Omega = 17.6, R = 2275$ and (a, b) $t = 350$, (c, d) $t = 389$, (e, f) $t = 440$. Lateral temperature boundary conditions are conducting. The gray denotes the conduction value ($\theta = \delta\theta = 0$), and the lighter and darker shades give the values above and below this.

memory of previous stretching; (2) in a large system, successive largest Lyapunov eigenvalues are close, and the defects that don't appear in the eigenvector spatial field associated with the largest exponent might be picked up by the other eigenvectors; and (3) although at large enough times the tangent space vector is expected to converge to the eigenvector for the largest Lyapunov exponent, the time for this to happen is not known and may well be long in a large system. Hence, for a different set of perturbation initial conditions, we may find the defect on the left side of Figure 7.20c contributing more substantially (although we did not actually do this).

We also studied the correlations between λ_1^{inst} and another diagnostic quantity, the reduced Nusselt number $\mathcal{N}$ (2.27). The reduced Nusselt number is a positive constant for a system of purely straight parallel rolls in its steady state, and it changes when the dynamics changes [90]. For example, when a dislocation is created, the quantity $\mathcal{N}$ dips below its straight parallel roll value, since a system with a dislocation is a less efficient transporter of heat across the cell in the vertical direction. Conversely, if a dislocation is annihilated, $\mathcal{N}$ will rise. Other changes, such as a local change in wavenumber or domain wall formation, will also cause changes in $\mathcal{N}$. We are currently unable to use the Nusselt number to distinguish between dislocation creation/annihilation and other changes to the pattern. However, changes in $\mathcal{N}$ do correspond to dynamical events, and larger values of $\mathcal{N}$ indicate regions of more order and vice versa.

We computed the correlation function between $\mathcal{N}$ and λ_1^{inst} as shown in Figure 7.22 for $\Gamma = 40, \sigma = 0.93, \Omega = 17.6$, and $R = 2275$. We see that $\mathcal{N}$ is partially anticorrelated with λ_1^{inst}: The largest negative value in the correlation function occurs for close to zero time delay. We found this for other R values as well.

It makes sense that $\mathcal{N}$ is anticorrelated with λ_1^{inst}, because λ_1^{inst} peaks when the system becomes more disordered, whereas an increase in disorder is associated with a dip in $\mathcal{N}$. This anticorrelation indicates that dynamical events contribute to λ_1^{inst}, including (but not exclusively) dislocation creation/annihilation events. We note that while the value of the anticorrelation near zero lag in Figure 7.22 is significant, it is not perfect, indicating that other factors may contribute to changes in λ_1^{inst} that cannot

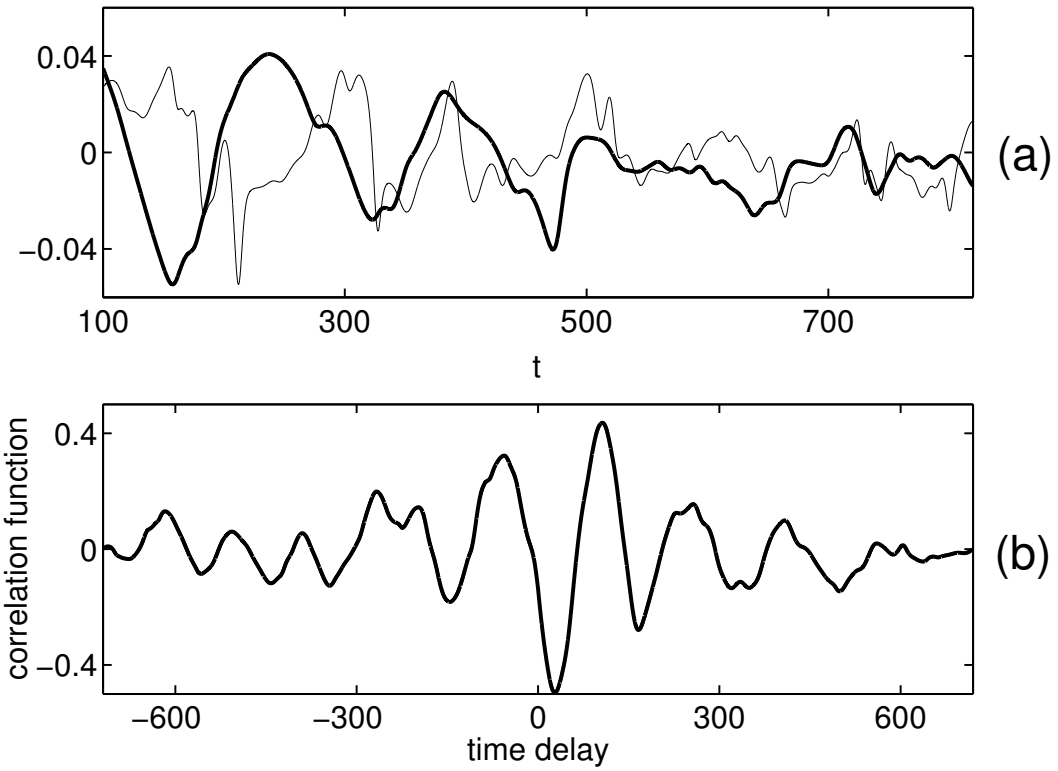

Figure 7.22: (a) Reduced Nusselt number $\mathcal{N}$ (thick curve) and instantaneous Lyapunov exponent λ_1^{inst} (thin curve) as a function of time for the following parameters: $\Gamma = 40, \sigma = 0.93, \Omega = 17.6$, and $R = 2275$ ($\epsilon = 0.012$). Note that the mean was subtracted from each of the dependent quantities, and their amplitudes have been rescaled for ease of comparison. (b) Correlation function between the reduced Nusselt number $\mathcal{N}$ and the instantaneous Lyapunov exponent λ_1^{inst}.

be detected by looking at $\mathcal{N}$.

Because the Nusselt number $\mathcal{N}$ is anticorrelated with λ_1^{inst} and $\mathcal{N}$ is itself related to the pattern of defects, we also studied directly the correlation between λ_1^{inst} and the defect density ρ_d for the parameter values $\Gamma = 40$, $\sigma = 0.93$, $\Omega = 17.6$ and $R = 2275$. We computed an area of the flow associated with defects as described in [88] by identifying regions of large local curvature in the computed local unit wave vector. The defect density ρ_d was then calculated as the ratio of the total area of defects to the total area of the cell. We then computed the correlation function between ρ_d and λ_1^{inst}, as shown in Figure 7.23. We see that ρ_d is partially correlated with λ_1^{inst} since there is a relatively large peak near zero time delay. However, the correlation is not perfect.

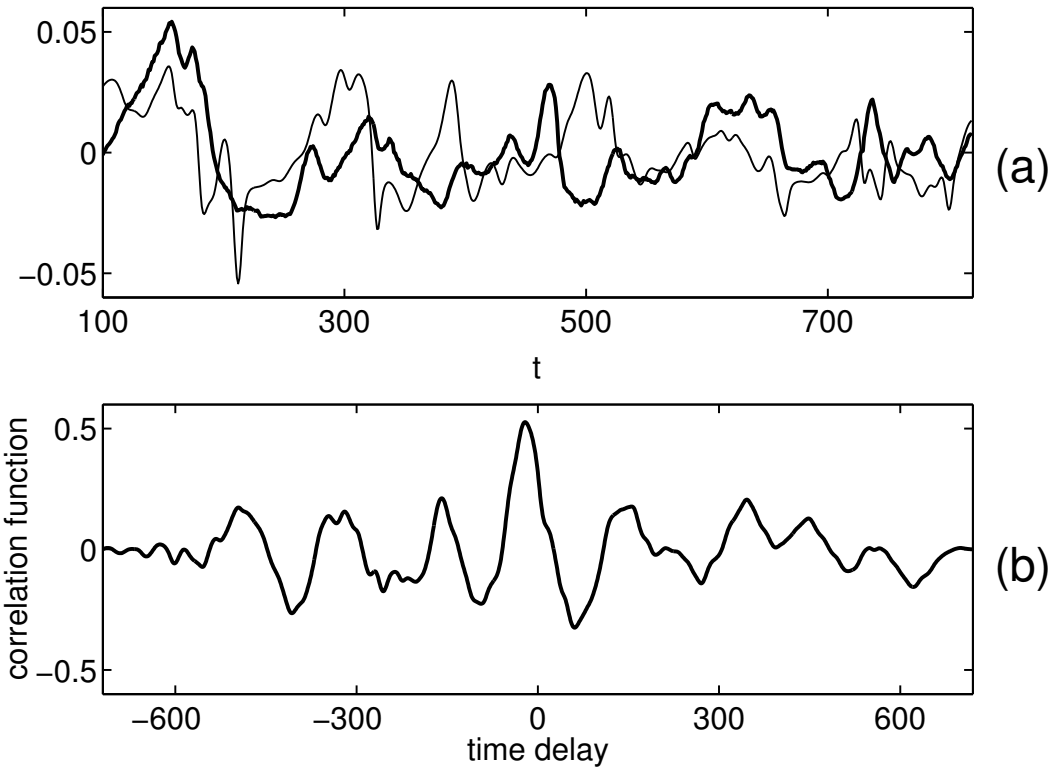

Figure 7.23: (a) Defect density ρ_d (thick curve) and instantaneous Lyapunov exponent λ_1^{inst} (thin curve) as a function of time for the following parameters: $\Gamma = 40, \sigma = 0.93, \Omega = 17.6$, and $R = 2275$ ($\epsilon = 0.012$). Note that the mean was subtracted from each of the dependent quantities, and their amplitudes were independently rescaled for ease of comparison. (b) Correlation function between the defect density ρ_d and the instantaneous Lyapunov exponent λ_1^{inst}.

Figure 7.23b provides quantitative evidence of our previously qualitative observation that some, but not all, defects contribute to λ_1^{inst}. Just as with the Nusselt number $\mathcal{N}$, our method of counting defects is unable to distinguish between dislocations and domain walls, so we were unable to compare and contrast the correlations between λ_1^{inst} and specific types of defects.

7.3.2 Scaling of the Largest Lyapunov Exponent λ_1 near Onset

Just as in Chapter 5, we have investigated how λ_1 scales with ϵ. We expect, since λ_1 is a frequency-like quantity, that it should scale linearly with ϵ.

A serious problem when computing Lyapunov exponents, especially for systems with many degrees of freedom, is that the convergence is slow. Hence, we ran each simulation out to at least 800 vertical diffusion times, about one-half a horizontal diffusion time for the largest aspect ratio, $\Gamma = 40$.

Figure 7.24 shows that the behavior of λ_1 is consistent with the expected linear approach to zero as we approach onset. The x-intercept is 0.007 for $\Gamma = 40$. We performed a fit to the data from Figure 7.24 on a log-log plot, as shown in Figure 7.25. The slope of this line also gives us the scaling with ϵ. We found the slope to be 1.1, in good agreement with a linear dependence of λ_1 on ϵ.

We also investigated this relationship for smaller aspect ratios ($\Gamma = 10, 20$) in [60]. We found that λ_1 reaches zero at a nonzero value of ϵ, which decreases with aspect ratio. This indicates that the linear scaling is not valid close to onset for smaller aspect ratios.

7.3.3 The Dependence of the Lyapunov Exponent λ_1 on Aspect Ratio

The rigid lateral walls of the convection cell impose strong restrictions on the dynamics inside the cell since the fluid velocity is forced to be zero at the cell wall. Another related effect of the rigid boundary is that the rolls are forced to intersect the wall

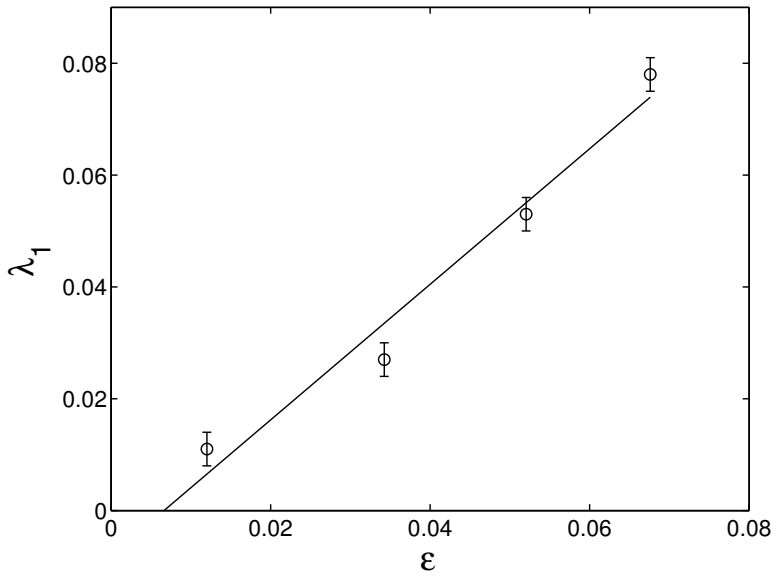

Figure 7.24: Largest Lyapunov exponent λ_1 vs the reduced Rayleigh number ϵ for aspect ratio $\Gamma = 40$. The solid line is a linear-least-squares fit to the data and intercepts the ϵ-axis at $\epsilon = 0.007$. The slope of the fitted line is 1.21 for $\Gamma = 40$. The method of determining error bars is discussed in Section 7.2.2.

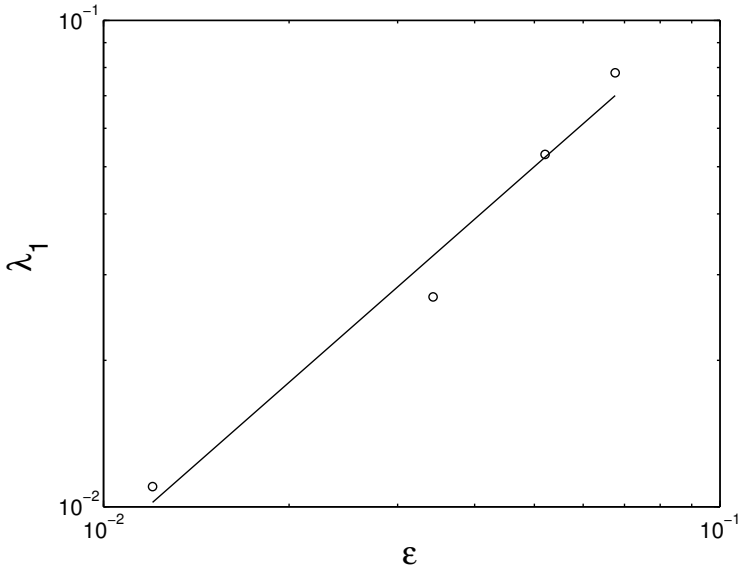

Figure 7.25: Determining the scaling for the data in Figure 7.24, by plotting the data on a log-log plot. The slope of the line is 1.1, which is consistent with a linear scaling with ϵ.

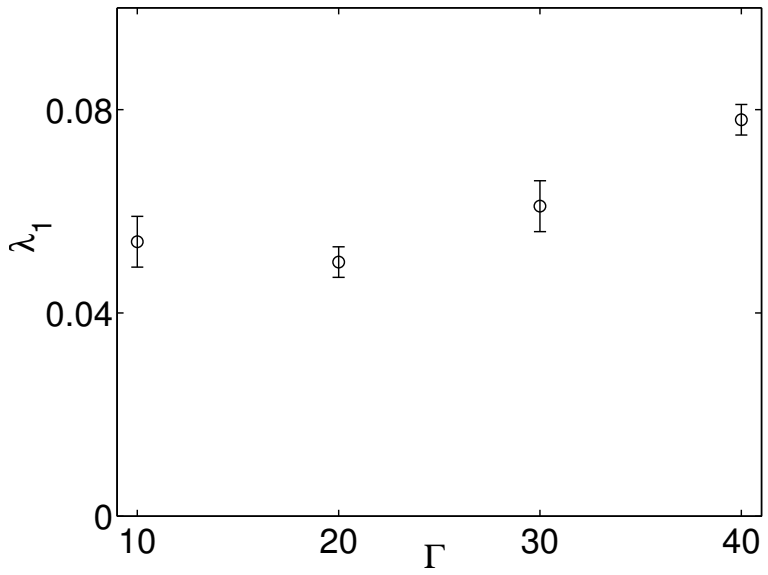

Figure 7.26: The largest Lyapunov exponent λ_1 versus the aspect ratio Γ for the domain chaos state of a convecting fluid in a rotating cylindrical cell with conducting lateral walls. The approximately linear dependence (for $20 < \Gamma < 40$) shows that the exponent λ_1 does not act as an intensive quantity, which would be expected for localized sources of chaos. For these runs, the Rayleigh number, rotation rate, and Prandtl number had the values $R = 2400(\epsilon = 0.064)$, $\Omega = 17.6$, and $\sigma = 0.93$.

transversely. This restriction implies that the strength of chaos in the cell depends on the surface to volume ratio for moderate values of Γ. Figure 7.26 confirms this dependence. For a given ϵ, the dynamics in the larger aspect ratio cell has a higher value of λ_1. One would expect that for very large aspect ratio cells the boundary effects would be minimal, and hence λ_1 would not show an aspect ratio dependence. We do not see any flattening of the curve for $20 < \Gamma < 40$. We note that this aspect ratio dependence does appear to flatten out as Γ becomes smaller (compare $\Gamma = 20$ to $\Gamma = 10$). For small aspect ratio systems, the boundary more completely dominates the dynamics.

Given that the dependence of λ_1 in Figure 7.26 is contrary to that expected of an intensive quantity in a large-aspect-ratio cell, we also examined how the standard deviation σ (root-mean-square time average) of λ_1^{inst} depended on Γ. As shown in Figure 7.27, σ decreases with increasing aspect ratio. This indicates that the fluctuations in λ_1^{inst} get smaller with aspect ratio. This is somewhat expected since the

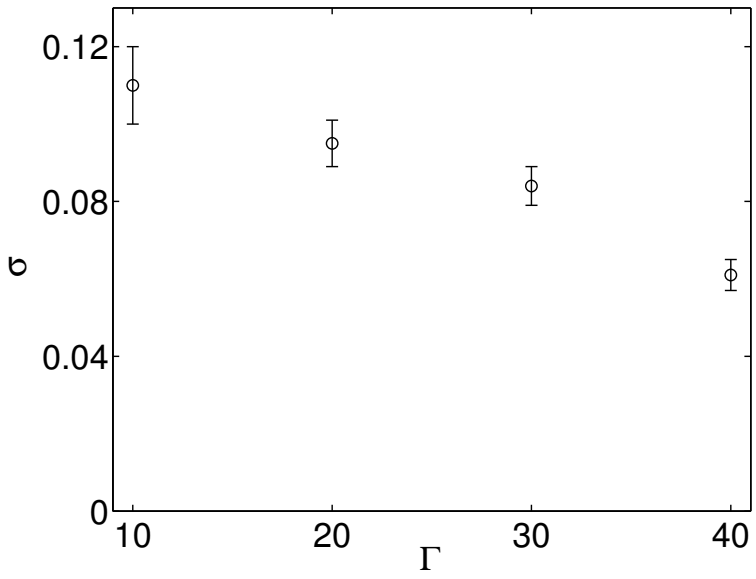

Figure 7.27: Plot of the root-mean-square time average σ of the instantaneous Lyapunov exponent λ_1^{inst} versus the aspect ratio Γ for the same parameters as in Figure 7.26. The fluctuations about λ_1 decrease with Γ.

fluctuations from different spatial regions will overlap in time.

7.4 Conclusions

We have shown for the first time that the systems with an aperiodic time dependence as observed by Ahlers and Behringer and Gollub and Benson have positive leading order Lyapunov exponents; hence they are indeed chaotic as defined by the exponential divergence of nearby trajectories. We have also computed a positive λ_1 for the domain chaos state of a rotating convecting fluid with experimentally realistic boundary conditions. For rotating Rayleigh-Bénard convection we have also shown that λ_1 scales linearly with respect to ϵ, in agreement with the predictions of amplitude equation theory that time scales near onset should diverge as ϵ^{-1}.

We have also visualized the evolution of the perturbation field. For cases associated with a time-dependent Nusselt number, the perturbation field consists of localized regions of disturbances which coincide with some dynamical event. Conversely, perturbation fields corresponding to stationary systems are extended, asymmetric and

stationary.

In addition, we have compared the correlations between S_λ, and hence λ_1, with defect creation/annihilation and roll compression events for small aspect ratio non-rotating cells. While repeated defect creation/annihilation events are associated with a temporary change in the stretching rate of phase space, we do not find there to be an overall net increase in S_λ, and hence a positive λ_1. We find instead that non-repeated events are associated with a positive λ_1. Hence, the suggestion by Egolf that roll breaking/reconnection events contribute significantly to the largest Lyapunov exponent is incorrect, at least in a general sense. Merely looking at λ_1^{inst} is insufficient to determine chaotic dynamics. It is more productive to instead look at the long time evolution of S_λ.

In the future we would like investigate the contributions to S_λ in more detail. We wish to determine what precisely causes S_λ to rise, such as a slow drift due to mean flow or the timing between events or something else entirely.

For larger aspect ratio rotating cells, we have shown that although there is a correlation between defect generation and contributions to λ_1^{inst}, not all defects contribute to the instantaneous leading-order Lyapunov exponent. It is, however, possible that some of the defects that do not contribute to the instantaneous leading exponent could contribute to the higher-order Lyapunov exponents. We also have seen that the reduced Nusselt number $\mathcal{N}$ is somewhat anticorrelated with λ_1^{inst}, indicating that both quantities are a good measure of the occurrence of dynamical events in the system.

Egolf's calculation for the SDC state (with periodic boundary conditions) shows that system size does not change λ_1. Our computations of the SDC state confirm Egolf's results [60]. For the domain chaos state, however, we find an unexpected nonintensive behavior of λ_1 for $20 \leq \Gamma \leq 40$. The expectation of intensive behavior of λ_1 comes from the arguments originally given by Ruelle [95] that for large systems distant regions will be dynamically independent. The observed nonintensive behavior is possibly a consequence of the extended fronts, which can grow in size with increasing Γ. This nonintensive behavior of λ_1 might therefore imply that for the do-

main chaos state, long-range correlations affect the dynamics in distant regions [33]. Computational experiments in larger domains (which are currently too expensive) are required to understand this phenomenon. Since SDC has a λ_1 independent of aspect ratio and since domain chaos shows an aspect ratio dependence, it would also be interesting to study the transition as a function of rotation rate from SDC to domain chaos (see the bent line in Figure 1.3).

Appendix 7.A Convergence tests for Lyapunov exponents

We did perform additional convergence tests on our Lyapunov exponent solver to make sure the code was performing optimally after our modifications. These are similar to what was done in Chapter 2. In all the cases presented in this section, the code was run for a square box of aspect ratio $\Gamma = 4$, periodic boundary conditions, $\Omega = 0$, $\sigma = 0.78$, and $R = 3000$.

In Figure 7.28 we plot the error in the Nusselt number Δ Nusselt as defined in (2.28); however our reference spatial resolution is $N = 15$ in this case. We see again that the convergence is exponential; however, the slope is a bit less than that in Figure 2.3 (-0.9 versus -1.6). We have not plotted the corresponding plot of Δ Nusselt versus dt, because the Nusselt numbers agree to within 9 digit accuracy for $dt < 0.002$ and for $N = 11$. We have used a third order accurate time scheme for all of our Lyapunov computations, as compared to the second order time scheme in Figure 2.4.

We have also plotted the error in the normalization:

$$\text{norm} = \|\delta\mathbf{y}(\Delta t)\|, \tag{7.1}$$

which is then used to compute S_λ (2.62), λ_1 (2.56), and λ_1^{inst} (2.58). We define the error Δnorm for the spatial resolution as

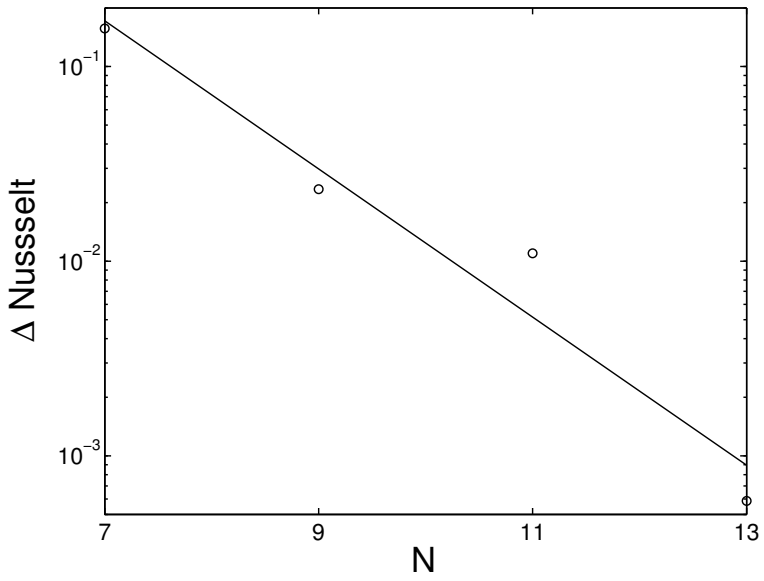

Figure 7.28: Δ Nusselt number versus spatial resolution N for the Lyapunov code. The following parameters were used: $\Gamma = 4$, $\Omega = 0$, $\sigma = 0.78$, $R = 3000$, and periodic boundary conditions. We used a time resolution $dt = 0.001$. This plot shows convergence is somewhat exponential in N. The slope of the line is -0.9.

$$\Delta\text{norm} = \left(\frac{\text{norm}_N - \text{norm}_{15}}{\text{norm}_{15}} \right), \tag{7.2}$$

analogous to (2.28). We have plotted this quantity in Figure 7.29 and find again that convergence is exponential with a slope of -2.0.

We also investigate the error for our time step, which we define as

$$\Delta\text{norm} = \left(\frac{\text{norm}_{dt} - \text{norm}_{0.0001}}{\text{norm}_{0.0001}} \right), \tag{7.3}$$

analogous to (2.29). We have plotted this quantity in Figure 7.30. We find the convergence is not third-order accurate, even though we are using a third-order Adams-Bashforth time stepping routine. Instead we get something closer to second order accurate. We are not sure why this is the case.

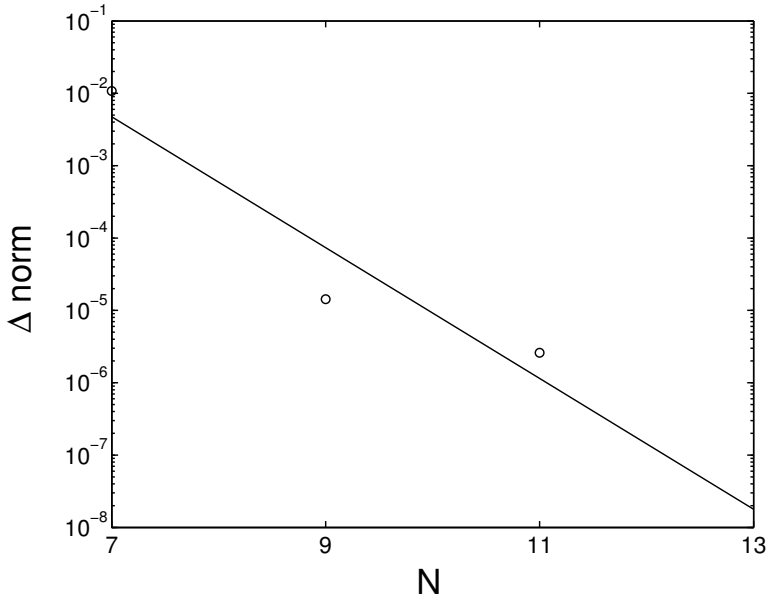

Figure 7.29: Δnorm versus versus spatial resolution N for the Lyapunov code and the same parameters as in Figure 7.28. Note that the error Δnorm for $N = 13$ is zero to 9 digit accuracy. The slope of the line is -2.0.

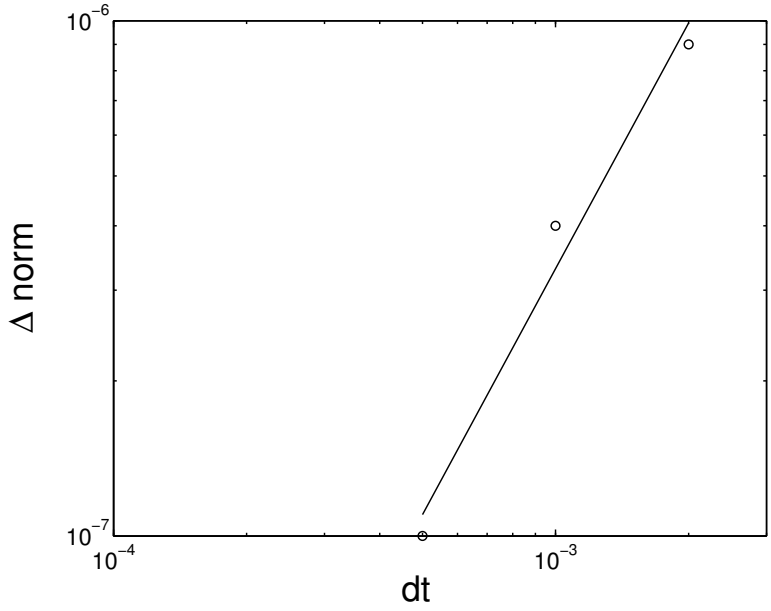

Figure 7.30: Δnorm versus versus temporal resolution dt for the Lyapunov code and the same parameters as in Figure 7.28 and a spatial resolution $N = 11$. The slope of the line is 1.6.

Appendix 7.B Different initial conditions

To make sure our computation of the leading order Lyapunov exponent is robust, we ran two different simulations with the same full field $\mathbf{y}(t)$ but for two different random initial conditions for the perturbation field $\delta\mathbf{y}(0)$. We plot the quantity S_λ versus t in Figure 7.31. The parameters used were $\Gamma = 4.72, \sigma = 0.78, \Omega = 0, R = 2800$, and conducting boundaries. Other details for this simulation are given in Figure 7.11 and Figure 7.12. Although the initial trajectories for the two runs are quite different, after about $t = 150$ the two trajectories do tend to track one another. Note we have shifted the dashed-dotted line in Figure 7.31 down by a constant value to compare the overlap at later times. Even though the magnitude of S_λ differs (as one would expect for different initial separations), the main features occur at the same time, such as the large jump at $t = 300$ and the characteristic dislocation events at $t = 202.92$, etc. This indicates that the computation of values from S_λ, such as λ_1 and λ_1^{inst}, are due to the stretching induced from the full field and are not dependent on the details of the initial perturbation $\delta\mathbf{y}(0)$.

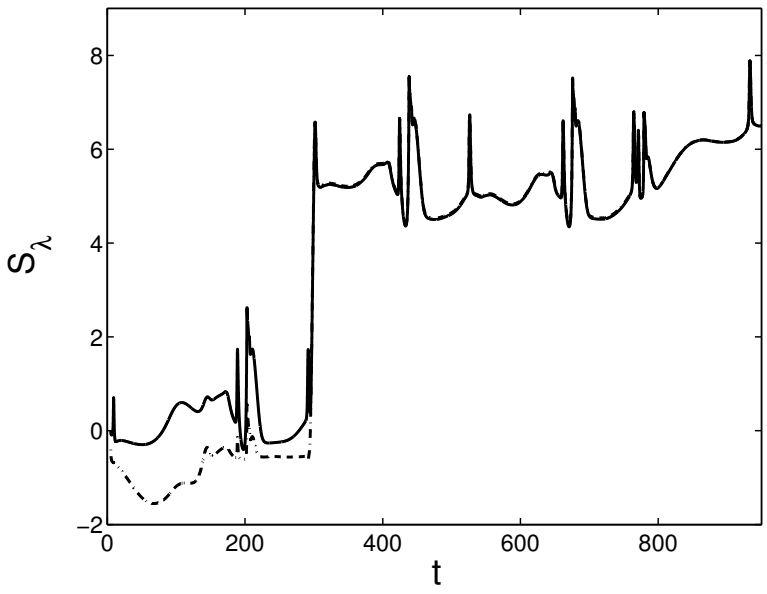

Figure 7.31: The quantity S_λ versus t for two different initial conditions for $\delta\mathbf{y}(0)$. The parameters used were $\Gamma = 4.72, \sigma = 0.78, \Omega = 0, R = 2800$, and conducting boundaries. Other details for this simulation are given in Figure 7.11 and Figure 7.12. Note that we shifted down the curve for the second set of initial conditions (the dashed-dotted line) by a constant value = 0.0394, so we could compare the overlap of the results at later times.

Chapter 8

Lagrangian Particle Tracking

In this section we present our preliminary results on particle tracking. As mentioned in Section 2.5, we are interested in extending Aref's equivalence between real space and phase space for a two-dimensional fluid to large aspect ratio Rayleigh-Bénard systems. We also want to investigate rotating Rayleigh-Bénard convection as a physical application of the blinking roll model of chaotic advection presented by Mullowney et al. [79]. In the blinking roll model of chaotic advection, a three-dimensional model state consisting of parallel rolls is replaced aperiodically by a set of rolls at an orthogonal orientation. Particles have been shown to mix well (i.e., explore the entire available real space) in such a blinking roll state.

Chaotic advection is important for studying understanding the mixing properties of convective flows. This has application to many areas of science and engineering whenever heat and mass transport are important, such as in atmospheric and oceanic flows and also in combustion.

We described our Lagrangian method of particle tracking in Section 2.5. We want to highlight the fact that we are following individual fluid elements. We follow the idealized fluid elements since we want to study the phase space explored by such trajectories. We would need to add in a diffusion term if we wished to follow real tracer particles [23]. One can do this by adding a noise term to (2.64):

$$\frac{d\mathbf{x}}{dt} = \mathbf{v}(x, y, z, t) + \eta(t), \tag{8.1}$$

where $\eta(t)$ is a Langevin noise term introduced to represent molecular diffusion. We have not explored this option in this thesis, however. This was explored in the thesis of Keng-Hwee Chiam [22], but for an Eulerian approach to scalar transport. He studied the transport of tracer particles in SDC and found the tracer diffusivity was enhanced by SDC. Our Lagrangian method of tracking particles could also be used to study diffusion, and it is possible to make the diffusivity arbitrarily small (by letting $\eta \to 0$), which is difficult to do in an Eulerian approach.

8.1 Finding a Clean Domain Chaos State

When we turn on the rotation for a periodic domain chaos state, we want the cleanest possible roll switching state, so that defects (such as those in Figure 5.4) do not interfere with the particle transport purely due to roll switching. Hence we chose a periodic domain of size $11 \times \left(11 * 2/\sqrt{3}\right) = 11 \times 12.7$, which should generate roll switches of multiples of 60°. Our parameters are $R = 2500$, $\Omega = 17.6$, $\sigma = 0.93$, periodic boundary conditions, 64 elements, a dx of 0.07, and a dt of 0.003.

As shown in Figure 8.1, the size of our cell is motivated by the intersection of the selected wavenumber and the lattice of available wavenumbers. We computed the lattice of available wavenumbers by defining our fundamental k_x and k_y as

$$k_x = \frac{2\pi}{11}, \quad k_y = \frac{2\pi}{12.7}. \tag{8.2}$$

Then, we determined the average wave number k to be 3.44 for this set of parameters by using the results from our periodic simulations in Chapter 5 for the same parameters (but for a Γ of 40). This is the inner circle of Figure 8.1. The outer circle corresponds to the critical wave vector magnitude $k_c = 3.56$, which occurs just at threshold. However, we are a bit above threshold here for $R = 2500$, so the wave number is shifted downward toward the zig-zag boundary. The straight lines in Figure 8.1 correspond to angles of multiples of 60°. We see that the lines intersect the inner circle at lattice points. This implies that rolls at angles of 60° should be pre-

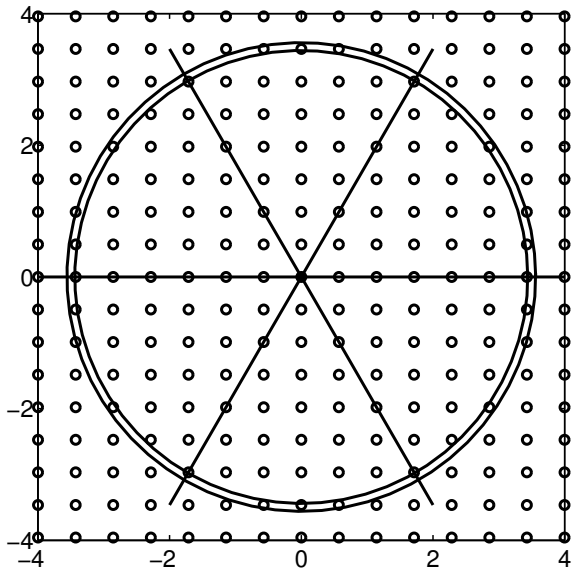

Figure 8.1: Expected wave number space for $\Gamma = 11 \times 12.7, \sigma = 0.93, \Omega = 17.6$, and $R = 2500$. The lattice of points are multiples of k_x, k_y given in (8.2). The radial lines are separated by multiples of 60°. The inner circle is at $k = 3.44$ and the outer circle is at $k = 3.56$.

ferred for these parameters. We started our initial conditions as straight parallel rolls at an angle of 0°.

We have plotted the orientational angle versus time results from our simulation in Figure 8.2. We see that instead of multiples of 60°, the system prefers switching between the angles $0°, 47.3°, 90°$, and $-47.3°$. We can understand this by looking at Figure 8.3. Through an analysis of wave number using a local method [40], we find the wave number changes from $k \simeq 3.5$ to $k \simeq 3.4$ back to $k \simeq 3.5$, simultaneously with the rolls switching from 0° to 47.3° to 90°. When we plot the wave number circles corresponding to $k = 3.4, 3.5$, we see the preferred angles (i.e., intersection of a circle with a lattice point) occur at $0°, 47.3°$, and 90°, respectively as is shown in Figure 8.3. We surmise that the system prefers slightly smaller jumps in angle, closer to the theoretical value for the maximal growth rate for this Prandtl number of about 40°, as discussed in Section 5.2. This is also close to the selected angle for the larger aspect ratio simulations $\Gamma = 40$, as shown in Figure 5.8. Hence, the system changes its wavenumber slightly to accommodate this. However, the roll switching is

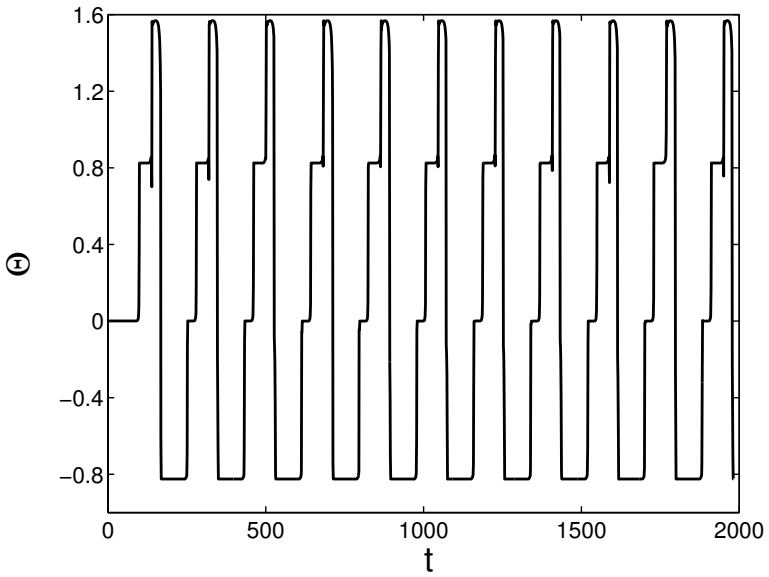

Figure 8.2: Orientational angle Θ as a function of time t for a clean domain chaos state with the following parameters: $\Gamma = 11 \times 12.7, R = 2500, \sigma = 0.93$, and $\Omega = 17.6$.

extremely regular and clean (i.e., defect free), as can be seen in Figure 8.2; hence we will use this state for our tracking of particles.

8.2 Results

We tracked particles by the method described in Section 2.5. We first looked at a stationary state of straight parallel rolls with no rotation. As long as there are no transients present, the particles will follow the rolls in a two-dimensional elliptical path with complete regularity as shown in Figure 8.4 for a representative case.

Since the particles follow the rolls perfectly when in a stripe state, we decided to "reduce" the number of degrees of freedom by looking at a type of Poincaré section [50]. We will only plot the particles when they intersect the midplane. The Poincaré section corresponding to the real space plot in Figure 8.4 would be two points, one during upflow and the other during downflow, very similar to the plot show in Figure 8.5a.

We show the results of tracking 900 individual particle trajectories for the clean

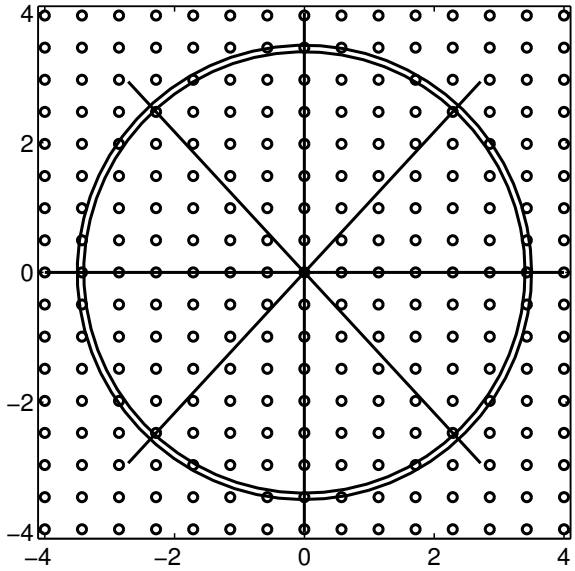

Figure 8.3: Actual wave number space for $\Gamma = 11 \times 12.7, \sigma = 0.93, \Omega = 17.6$, and $R = 2500$. The lattice of points are multiples of k_x, k_y given in (8.2). The radial lines are at the angles $0°, 47.3°, 90°$, and $-47.3°$. The inner circle is at $k = 3.4$, and the outer circle is at $k = 3.5$.

domain switching system with $\Gamma = 11 \times 12.7, \sigma = 0.93, \Omega = 17.6, R = 2500$, and periodic boundaries (see Figure 8.2). We start the 900 particles in an area near the center of the cell of size 0.05×0.05. We plot the Poincaré sections in Figures 8.5 and 8.6.

In Figure 8.5 we see the spreading of the initially very localized distribution of particles. In Figure 8.5a, the 900 particles are confined to one roll, since the system has not switched yet. In Figure 8.5b, the first roll switch has occurred, and one sees that the roll switching causes the particles to spread out, although they still remain confined to rolls after the switch. If there were no switching, the particles would remain in the path shown in Figure 8.5a. By Figure 8.5c, after 10 roll switches, the particles have almost completely filled the entire cell.

In Figure 8.6 the particles are evenly distributed, and they remain so for the duration of the simulation. We have plotted four successive roll switches in Figures 8.6a-d. Between the roll switches, the particles follow the rolls. This is why we see stripes in the Poincaré section. However, when the rolls switch, the particles move as well. This

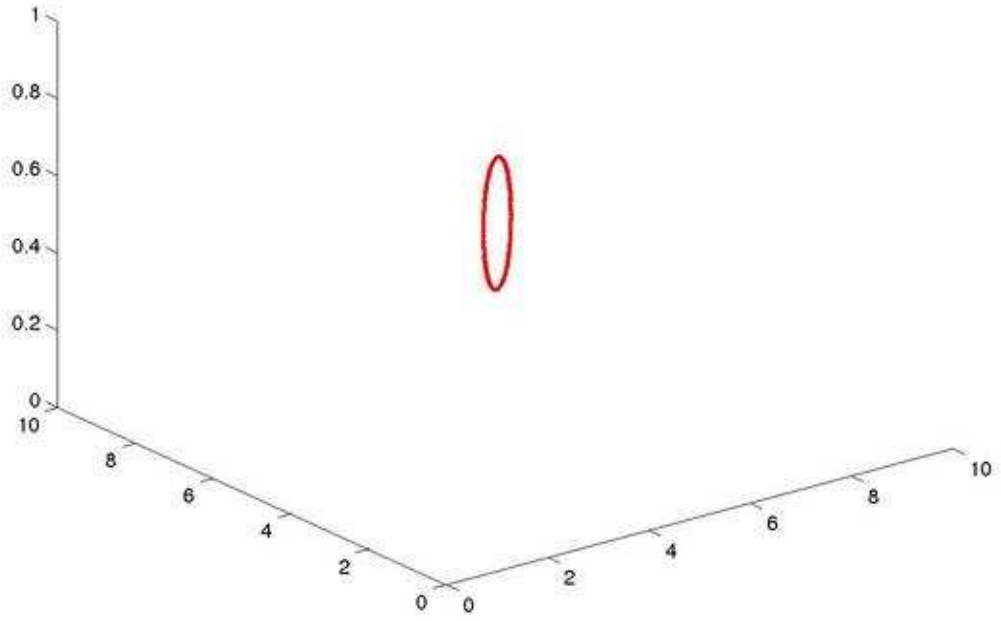

Figure 8.4: Particle trajectory for $\Gamma = 10, \sigma = 0.93, \Omega = 0, R = 2500, 0 < t < 67.5$, and periodic boundaries.

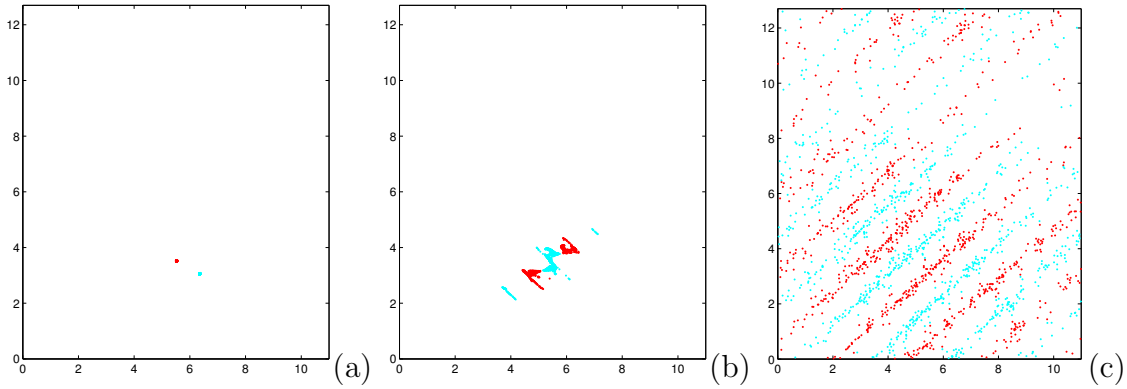

Figure 8.5: Poincaré sections for $\Gamma = 11 \times 12.7, \sigma = 0.93, \Omega = 17.6, R = 2500$ and (a) $t = 3$, (b) $t = 120$, (c) $t = 540$. The dark gray (red in electronic version) dots are those that intersect the midplane during upflow and the light gray (blue in electronic version) dots are those that intersect the midplane during downflow. Exactly 900 particles were used, originally confined to an area of size 0.05×0.05 at the location of the dark gray (red) dots in (a).

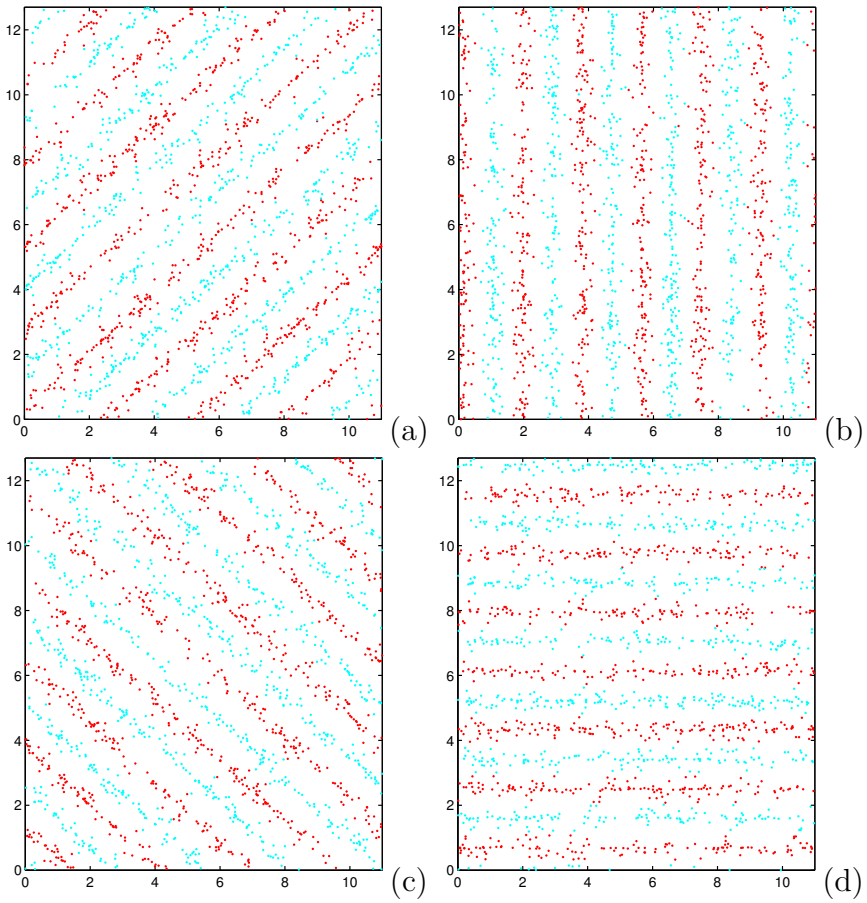

Figure 8.6: Same as Figure 8.5 but for (a) $t = 1500$, (b) $t = 1530$, (c) $t = 1575$, and (d) $t = 1605$.

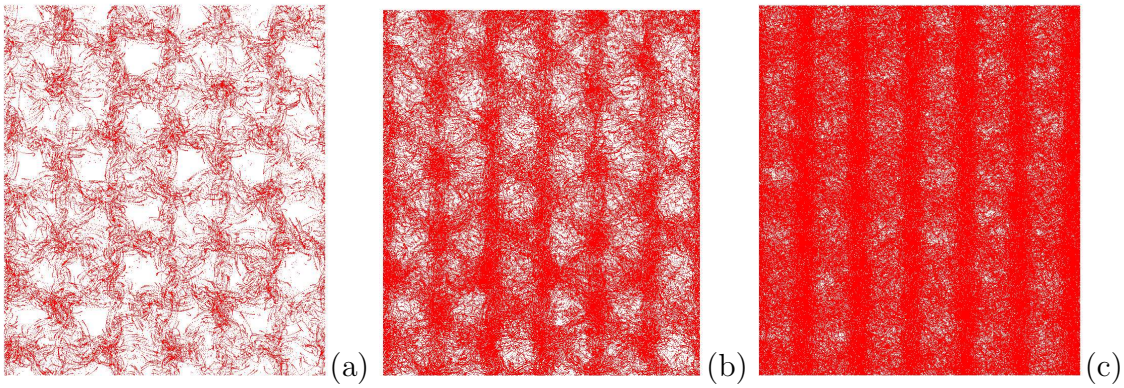

Figure 8.7: Long-time Poincare section for the same parameters as in Figure 8.5 but only upflow particles are plotted. The time ranges are (a) $1500 < t < 1860$, (b) $600 < t < 1983$, and (c) $800 < t < 4788$. Note that in (c) only 576 particles are tracked which were started evenly distributed throughout the midplane of the cell.

occurs very quickly, on the order of a vertical diffusion time for the given parameters. One can slow this down by going to smaller ϵ, but then the time between roll switches becomes longer too.

We then plotted long-time Poincaré sections to see if there was any structure to the particle trajectories. In Figure 8.7a we superimpose the Poincaré sections (upflow only) for time slices between 1500 and 1860 vertical diffusion times (each successive time slice is separated by 0.3 vertical diffusion times). This comprises two full rotations of the rolls, i.e., eight roll switches. We notice a somewhat hexagonal pattern, indicating that the particles are not exploring all of the available phase space during the upflow. Note that the corresponding downflow pattern fills in the white areas shown in Figure 8.7a. When we look at a longer time range, as in Figure 8.7b and c, we find more and more of the available phase space becomes filled up.

We also investigated if there were any fixed points in the Poincaré section, as was found by Mullowney et al. [79] for their blinking roll model. However, we were unable to find any particles which remained localized for our systems. We checked various ϵ and initial particle distributions and found that all of our particles explored a wide range of phase space. Representative particle trajectories are shown superimposed on the long-time Poincaré section in Figure 8.8. The most localized particle is the one

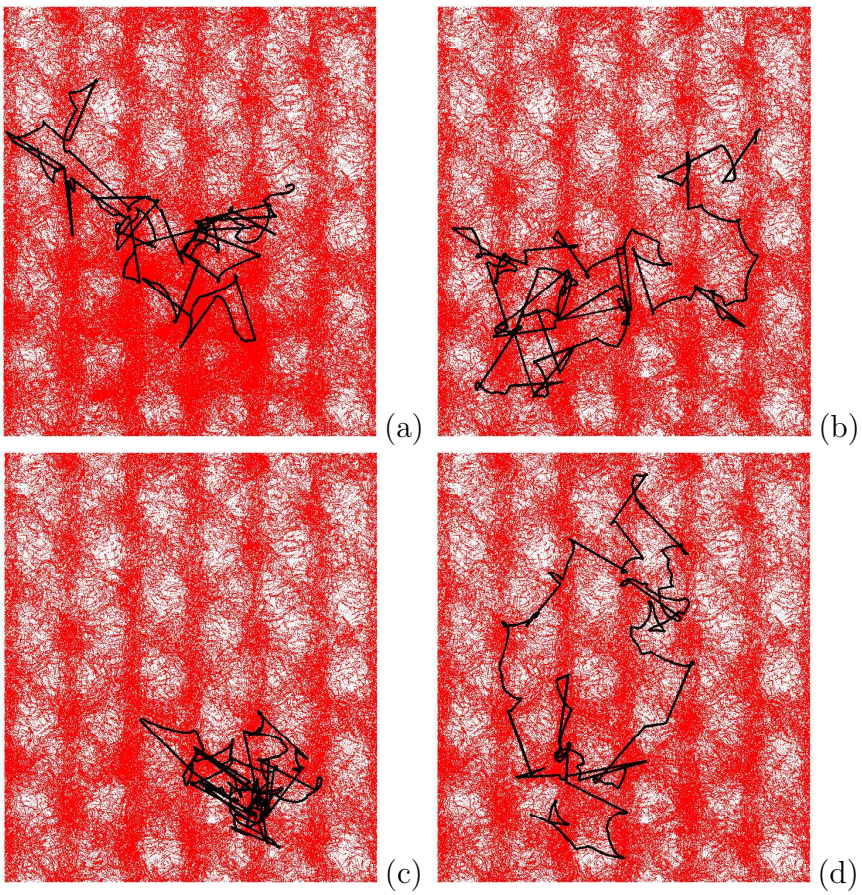

Figure 8.8: Superposition of four different individual particle trajectories (a-d) on the Poincaré section given in Figure 8.7b.

shown in Figure 8.8c. The most widely traveled particle is the one in Figure 8.8d. Hence, we can conclude that domain chaos is a very efficient mixer of fluid particles. However, there still may be fixed points for these systems, but we were unable to find any with our analysis techniques.

Figure 8.2 looks extremely regular. However, the particle trajectories are chaotic in the fact that the trajectories (started initially very close to one another) explore most of their available phase space. This is similar to what was observed by Aref [4] for a blinking vortex and by Mullowney et al. [79] for a blinking roll system.

8.3 Conclusions

By tracking individual fluid particles, we have determined that the domain chaos state of a rotating Rayleigh-Bénard system is very efficient mixer of fluid particles. We start the trajectories very close to one another and run a simulation of a system which switches very clean between four different roll orientations. We find the particles explore the available phase space.

We would like to investigate these systems in a more systematic manner by computing Lagrangian coherent structures (LCS) [105], which unite the ideas of Lyapunov exponents and particle trajectories. LCS were originally proposed by Haller [48, 49] as a method of understanding the Lagrangian behavior of time-dependent, two-dimensional fluid systems. LCS have been rigorously defined by Shadden, Lekien, and Marsden [105], as ridges in the leading-order finite-time Lyapunov exponent field of particle trajectories. This Lyapunov exponent field is the finite-time average of the maximum expansion or contraction rate of a field of particle trajectories. One can find LCS by first evolving particle trajectories and then forming the deformation gradient F by taking the derivatives of the particle trajectories with respect to their initial conditions. From this one can form the finite-time Cauchy-Green deformation tensor by taking $F^T F$. The maximal eigenvalue λ of this tensor is found for each trajectory, and the largest Lyapunov exponent can then be formed from the time average of the logarithm of the square root of the λ associated with that trajectory.

The curvature ridges of the scalar field formed from these Lyapunov exponents are then found, and these ridges are the LCS. Each ridge is locally the highest point in the field transverse to the ridge. Also, at each point on the ridge the direction the topography decreases most rapidly is transverse to the ridge. In two dimensions these ridges are curves and in three dimensions these ridges are surfaces.

LCS have many interesting properties. For example, the ridges form boundaries in the sense that very little flux traverses such boundaries. Hence, LCS are barriers to mixing. More generally, LCS are the nearly invariant manifolds of fixed points and periodic orbits. Most of the applications have been two-dimensional. There is much interest in applying LCS techniques to study three-dimensional systems.

By computing LCS, we hope to gain information about the invariant manifolds of chaotic Rayleigh-Bénard convection systems, something which has never been computed before. Just like Poincaré sections are invaluable for describing chaos in systems with a few degrees of freedom, computing LCS shows promise as a powerful tool for analyzing large-dimensional chaotic systems, by computing invariant manifolds and describing transport and mixing in such systems. Due to the intimate relationship between phase space and real space for fluids in two dimensions and the possible extension of this into three dimensions, the stretching of particle trajectories should be studied in addition to the evolution of the velocity field.

Chapter 9

Conclusion

We have investigated rotating Rayleigh-Bénard convection both numerically and theoretically in order to gain insight into a system which undergoes a supercritical bifurcation to a spatiotemporal chaotic state.

We first explored traveling waves in Chapter 3 in order investigate the claims of chaos in these systems for a certain parameter range as well as to gain experience with amplitude equations and our numerical simulations. The numerical simulations of the Boussinesq equations with the Coriolis force for realistic no-slip boundary conditions and a finite annular domain reproduce the traveling waves observed experimentally. These traveling waves are studied near-threshhold by using the complex Ginzburg-Landau equation (CGLE): a mode analysis enables the CGLE coefficients to be determined. The CGLE coefficients agree well with previous experimental and theoretical results. Mean flows are also computed and found to be more significant as the Prandtl number decreases. In addition, the mean flow around the outer radius of the annulus appears to be correlated with the mean flow around the inner radius. The CGLE is chaotic for certain values of the coefficients. However, for the experimentally realistic parameters in the numerical simulations those chaotic regimes were not realized.

In Chapter 4 the higher order amplitude equation for rotating Rayleigh-Bénard convection is derived from the Boussinesq equations for realistic boundary conditions and with the Coriolis force included. In order to keep track of the mean flow, we look at the full system of equations instead of a potential formulation. This leads to the

usual amplitude equation at order $\epsilon^{3/2}$, but new rotation terms enter at order $\epsilon^{7/4}$. These rotation terms will cause a change of phase with respect to time, whenever there is a gradient in the amplitude in the direction parallel to the rolls. As a result, rolls terminating perpendicularly to a wall will precess in the direction of rotation. The new rotation terms will also cause stationary dislocations to glide perpendicular to the rolls. We compare our amplitude equation results for a specific set of parameters to numerical results from simulations of the full equations. We find good agreement for mean flow, wall induced precession and dislocation glide.

In Chapter 5 numerical simulations of large aspect ratio, 3-D rotating Rayleigh-Bénard convection for no-slip boundary conditions have been performed in both cylinders and periodic boxes. We have focused near the threshold for the supercritical bifurcation from the conducting state to a convecting state exhibiting domain chaos and have used the same parameters as experiments. We find that the time scaling law agrees with the theoretical prediction, which is in contradiction to experimental results. Our correlation length results also agree better with the theory. We also have looked at the scaling of defect lengths and defect glide velocities. We find a separation of scales in defect diameters perpendicular and parallel to the rolls, as expected, but the scaling laws for the two different lengths are in contradiction to theory. The defect velocity scaling law agrees with our new theoretical prediction from our amplitude equation analysis in Chapter 4.

In Chapter 6 we include the centrifugal force in our numerical simulations to investigate a hybrid state observed by experimenters for larger aspect ratio and to improve the agreement between experiment and theory for the scaling laws. We also observe this hybrid state for large enough centrifugal force. When we model exactly the same parameters as the experiments studied in Chapter 5, we find we get excellent agreement with the experimental results for precession frequencies and orientational angle, both in terms of the magnitude and the scaling. Our correlation length scaling results agree with the experiments, however the numerical values do not agree as well.

In Chapter 7 leading order Lyapunov exponents and their corresponding eigenvectors have been computed numerically for small aspect ratio nonrotating Rayleigh-

Bénard convection cells in addition to large aspect ratio rotating cells. Our work confirms that the dynamics in these cells truly are chaotic as defined by a positive Lyapunov exponent. We also find the leading order Lyapunov eigenvector to be characterized by localized bursts whenever the system is time-dependent. In addition, we study the contributions to the leading order Lyapunov exponent for both periodic and aperiodic systems and find that while repeated dynamical events such as dislocation creation/annihilation and roll compression do contribute to the short time Lyapunov exponent dynamics, they do not contribute to the long time Lyapunov exponent. We find instead that non-repeated events provide the most significant contribution to the long time leading order Lyapunov exponent.

For the larger aspect ratio systems we find that although there is a correlation between dynamical events and the short-time dynamics of the leading order Lyapunov exponent, not all dynamical events contribute. It is, however, possible that some of the defects that do not contribute to the leading exponent could contribute to the higher-order Lyapunov exponents. We also have seen that the reduced Nusselt number is somewhat anticorrelated with the short-time Lyapunov exponent, indicating that both quantities are a good measure of the occurrence of dynamical events in the system. We also show that the leading order Lyapunov exponent is not intensive for aspect ratios Γ over the range $20 < \Gamma < 40$ and that the scaling exponent of the leading order Lyapunov exponent near onset is consistent with the value predicted by the amplitude equation formalism.

In Chapter 8, Lagrangian particle tracking methods are employed to study particle trajectories in rotating Rayleigh-Bénard convection. We find that these systems exhibit chaotic advection in that initially localized particle trajectories explore most of the available phase space.

The results in this thesis provide us with new areas of study. Now that we realize the centrifugal force cannot be neglected, we would like to incorporate it in our amplitude equation formalism. We would also like to combine our results for traveling waves with those of domain chaos to gain insight into the square patterns observed by Sánchez-Álvarez et al. [96].

Now that we can compute leading order Lyapunov exponents, we would like to extend this to computing the entire spectrum of positive Lyapunov exponents and hence the Lyapunov spectral density. If we can establish the extensiveness of the Lyapunov spectral density for Rayleigh-Bénard convection systems, this would provide us with a rigorous definition of spatiotemporal chaos. We would also like to explore our analysis of the time evolution of S_λ in more detail to determine what causes it to rise, and hence identify the sources of chaos in Rayleigh-Bénard convection. Finally, based on our work on Lagrangian particle tracking, we would like to compute Lagrangian Coherent structures for Rayleigh-Bénard systems, which should provide us with more insight into the chaos in these systems.

Bibliography

[1] G. Ahlers. Low-temperature studies of the Rayleigh-Bénard instability and turbulence. *Phys. Rev. Lett.*, 33:1185–1188, 1974.

[2] G. Ahlers and R. P. Behringer. Evolution of turbulence from the Rayleigh-Bénard instability. *Phys. Rev. Lett.*, 40:712–716, 1978.

[3] I. S. Aranson and L. Kramer. The world of the complex Ginzburg-Landau equation. *Rev. Mod. Phys.*, 74:99–143, 2002.

[4] Hassan Aref. Stirring by chaotic advection. *J. Fluid Mech.*, 143:1–21, 1984.

[5] K. M. S. Bajaj and G. Ahlers. Rayleigh-Bénard convection with rotation at small Prandtl numbers. *Phys. Rev. E*, 65:056309, 2002.

[6] N. Becker. private communication, 2004.

[7] N. Becker and G. Ahlers. private communication, 2004.

[8] Nathan Becker and Guenter Ahlers. The domain chaos puzzle and the calculation of the structure factor and its half-width. *Phys. Rev. E*, 73(046209), 2006.

[9] Nathan Becker, J. D. Scheel, M. C. Cross, and Guenter Ahlers. Effect of the centrifugal force on domain chaos in Rayleigh-Bénard convection. *Phys. Rev. E*, 73(066309), 2006.

[10] B. P. Behringer and G. Ahlers. Heat transport and critical slowing down near the Rayleigh-Bénard instability in cylindrical containers. *Phys. Lett.*, 62A:329–331, 1977.

[11] R. P. Behringer and G. Ahlers. Heat transport and temporal evolution of fluid flow near the Rayleigh-Bénard instability in cylindrical containers. *J. Fluid Mech.*, 125:219–258, 1982.

[12] E. Ben-Jacob, H. R. Brand, G. Dee, L. Kramer, and J. S. Langer. Pattern propagation in nonlinear dissipative systems. *Physica*, 14D:348, 1985.

[13] E. Bodenschatz, W. Pesch, and G. Ahlers. Recent developments in Rayleigh-Bénard convection. *Ann. Rev. Fluid Mech.*, 32:709, 2000.

[14] K. Borońska and L. S. Tuckerman. presented at the 58th annual DFD conference, 2005.

[15] John P. Boyd. *Chebyshev and Fourier Spectral Methods*. Dover, 2000.

[16] H. Brand and K. Kawasaki. Macroscopic dynamics of systems with a small number of topological defects in equilibrium and non-equilibrium systems. *J. Phys. A*, 17:L095–L910, 1984.

[17] Oliver Brausch. *Rayleigh-Bénard konvection in verschiedenen isotropen und anisotropen systemen*. PhD thesis, Universität Bayreuth, 2001.

[18] S. N. Brown and K. Stewartson. On thermal convection in a large box. *Stud. in Appl. Math.*, 57:187, 1977.

[19] F. H. Busse and K. E. Heikes. Convection in a rotating layer: A simple case of turbulence. *Science*, 208:173–175, 1980.

[20] S. Chandrasekhar. *Hydrodynamic and Hydromagnetic Stability*. Oxford University Press, 1961.

[21] W. Chang and J. Vinials. Pattern formation in weakly damped parametric surface waves. *J. Fluid Mech.*, 336:301, 1997.

[22] K.-H. Chiam. *Spatiotemporal Chaos in Rayleigh-Bénard Convection*. PhD thesis, California Institute of Technology, 2003.

[23] K.-H. Chiam, M. C. Cross, H. S. Greenside, and P. F. Fischer. Enhanced tracer transport by the spiral defect chaos state of a convecting fluid. *Phys. Rev. E*, 71(036205), 2005.

[24] K.-H. Chiam, M. R. Paul, M. C. Cross, and H. S. Greenside. Mean flow and spiral defect chaos in Rayleigh-Bénard convection. *Phys. Rev. E*, 67(056206), 2003.

[25] R. M. Clever and F. H. Busse. Nonlinear oscillatory convection. *J. Fluid Mech.*, 176:403–417, 1987.

[26] R. M. Clever and F. H. Busse. Instabilities of longitudinal rolls in the presence of Poiseuille flow. *J. Fluid Mech.*, 229:517, 1991.

[27] T. Clune. *Pattern selection in convecting systems.* PhD thesis, University of California at Berkeley, 1993.

[28] T. Clune and E. Knobloch. Pattern selection in rotating convection with experimental boundary conditions. *Phys. Rev. E*, 47:2536–2550, 1993.

[29] S. M. Cox and P. C. Matthews. Instability of rotating convection. *J. Fluid Mech.*, 403:153, 2000.

[30] M. C. Cross. Derivation of the amplitude equation at the Rayleigh-Bénard instability. *Phys. Fluids*, 23:1727–1731, 1980.

[31] M. C. Cross and P. C. Hohenberg. Pattern formation outside of equilibrium. *Rev. Mod. Phys.*, 65:851–1112, 1993.

[32] M. C. Cross, M. Louie, and D. Meiron. Finite size scaling of domain chaos. *Phys. Rev. E*, 63(045201), 2001.

[33] M. C. Cross, D. Meiron, and Y. Tu. Chaotic domains: A numerical investigation. *Chaos*, 4:607–619, 1994.

[34] M. C. Cross and A. C. Newell. Convection patterns in large aspect ratio systems. *Physica*, 10D:299–328, 1984.

[35] M. O. Deville, P. F. Fischer, and E. H. Mund. *High-Order Methods for Incompressible Flow*. Cambridge University Press, 2002.

[36] R. C. DiPrima and H. L. Swinney. Instabilites and transition in flow between concentric rotating cylinders. In H. L. Swinney and J. P. Gollub, editors, *Hydrodynamic Instabilities and the transition to turbulence*. Springer-Verlag, 1981.

[37] J. P. Eckmann and D. Ruelle. Ergodic theory of chaos and strange attractors. *Rev. Mod. Phys.*, 57:617–656, 1985.

[38] J. P. Eckmann, D. Ruelle, and S. Ciliberto. Liapunov exponents from time series. *Phys. Rev. A*, 34:4971–4979, 1986.

[39] D. A. Egolf, I. M. Melnikov, W. Pesch, and R. E. Ecke. Mechanisms of extensive spatiotemporal chaos in Rayleigh-Bénard convection. *Nature*, 404:733–736, 2000.

[40] D. A. Egolf, I. V. Melnikov, and E. Bodenschatz. Importance of local pattern properties in spiral defect chaos. *Phys. Rev. Lett*, 80:3228–3231, 1998.

[41] el Hamdi, M. Gorman, and K. A. Robbins. Deterministic chaos in laminar premized flames: Experimental classification of chaotic dynamics. *Comb. Sci. and Technol.*, 94:87, 1993.

[42] P. F. Fischer. An overlapping Schwartz method for spectral element solutions of the incompressible Navier-Stokes equations. *J. Comp. Phys.*, 133:84–101, 1997.

[43] P. F. Fischer, N. I. Miller, and H. M. Tufo. *Parallel Solution of Partial Differential Equations*, pages 158–180. Springer-Verlag, 2000.

[44] K. Geist, U. Parlitz, and W. Lauterborn. Comparison of different methods for computing Lyapunov exponents. *Prog. Theo. Phys.*, 83:875–893, 1990.

[45] H. F. Goldstein, E. Knobloch, I. Mercader, and M. Net. Convection in a rotating cylinder. part 1: linear theory for moderate Prandtl numbers. *J. Fluid Mech.*, 248:583–603, 1993.

[46] J. P. Gollub and S. V. Benson. Many routes to turbulent convection. *J. Fluid Mech.*, 100:449–471, 1980.

[47] P. S. Hagen and M. S. Cohen. Diffusion-induced morphogenesis in the development of Dictyosteluim. *J. Theor. Bio.*, 92:881, 1981.

[48] G. Haller. Distinguished material surfaces and coherent structures in three-dimensional fluid flows. *Physica D*, 149:248–277, 2001.

[49] G. Haller. Lagrangian coherent structures from approximate velocity data. *Phys. Fluids*, 14:1851–1861, 2002.

[50] L. N. Hand and J. D. Finch. *Analytical Mechanics*. Cambridge University Press, 1998.

[51] J. E. Hart. On the influence of centrifugal buoyancy on rotating convection. *J. Fluid Mech*, 403:133, 2000.

[52] M. Van Hecke. *The amplitude description of nonequilibrium patterns*. PhD thesis, Universiteit Leiden, 1996.

[53] M. Van Hecke and W. van Saarloos. Convection in rotating annuli: Ginzburg-Landau equations with tunable coefficients. *Phys. Rev. E*, 55:R1259–R1262, 1997.

[54] K. E. Heikes. *An Experimental Study of Convection in a Rotating Layer*. PhD thesis, University of California, Los Angeles, 1979.

[55] J. Herrmann and F. H. Busse. Asymptotic theory of wall-attached convection in a rotating fluid layer. *J. Fluid Mech.*, 255:183–194, 1993.

[56] B. Hof, G. J. Lucas, and T. Mullin. Flow state multiplicity in convection. *Physics of Fluids*, 11:2815–2817, 1999.

[57] Y. Hu, R. E. Ecke, and G. Ahlers. Time and length scales in rotating Rayleigh-Bénard convection. *Phys. Rev. Let.*, 74:5040–5043, 1995.

[58] Y. Hu, R. E. Ecke, and G. Ahlers. Convection under rotation for Prandtl numbers near 1: Linear stability, wave-number selection and pattern dynamics. *Phys. Rev. E*, 55:6928–6949, 1997.

[59] Y. Hu, W. Pesch, G. Ahlers, and R. E Ecke. Convection under rotation for Prandel numbers near 1: Küppers-Lortz instability. *Phys. Rev. E*, 58:5821–5833, 1998.

[60] A. Jayaraman, J. D. Scheel, H. S. Greenside, and P. F. Fischer. Characterization of the domain chaos convection state by the largest Lyapunov exponent. *Phys. Rev. E.*, 74:016209, 2006.

[61] K. Kawasaki. Defect-phase dynamics for dissipative media with potential. *Prog. Th. Phys. Supp.*, 80:123–138, 1984.

[62] K. Kawasaki. Topological defects and non-equilibrium. *Prog. Th. Phys. Supp.*, 79:161–190, 1984.

[63] D. A. Kessler, J. Koplik, and H. Levine. Pattern selection in fingered growth phenomenon. *Adv. Phys.*, 37:255, 1988.

[64] E. Knobloch. Rotating convection: Recent developments. *International Journal of Engineering Science*, 36:1421–1450, 1998.

[65] P. Kolodner. Collisions between pulses of traveling-wave convection. *Phys. Rev. A*, 44:6466, 1991.

[66] L. Kramer and W. Pesch. Convection instabilities in nematic liquid crystals. *Annu. Rev. Fluid Mech.*, 27:515, 1995.

[67] E. Y. Kuo. *Dynamic states in rotating Rayliegh-Bénard convection systems.* PhD thesis, California Institute of Technology, 1994.

[68] E. Y. Kuo and M. C. Cross. Traveling-wave wall states in rotating Rayleigh-Bénard convection. *Phys. Rev. E*, 47:R2245–R2248, 1993.

[69] G. Küppers. The stability of steady finite amplitude convection in a rotating fluid layer. *Phys. Lett.*, 32A:7–8, 1970.

[70] G. Küppers and D. Lortz. Transition from laminar convection to thermal turbulence in a rotating fluid layer. *J. Fluid Mech.*, 35:609–620, 1969.

[71] D. Laveder, T. Passot, Y. Ponty, and P. L. Sulem. Effect of a random noise on scaling laws of finite Prandtl number rotating convection near threshold. *Phys. Rev. E*, 59(R4745), 1999.

[72] Y. Liu and R. E. Ecke. Nonlinear traveling waves in rotating Rayleigh-Bénard convection. *Phys. Rev. Let.*, 59:4091–4105, 1999.

[73] M. Louie. *Numerical study of pattern forming proceses in models of rotating Rayleigh-Bénard conevction.* PhD thesis, California Institute of Technology, 2001.

[74] P. Manneville. *Dissipative Structures and Weak Turbulence.* Academic Press, 1990.

[75] J. Maurer and A. Libchaber. Rayleigh-Bénard experiment in liquid helium; frequency locking and the onset of turbulence. *J. Phys. Lett.*, 40:L419, 1979.

[76] J. Millán-Rodríguez, M. Bestehorn, C. Pérez-García, R. Friedrich, and M. Neufeld. Defect motion in rotating fluids. *Phys. Rev. Let.*, 74:530–533, 1995.

[77] J. Millán-Rodríguez, C. Pérez-García, M. Bestehorn, M. Neufeld, and R. Friedrich. Motion of defects in rotating fluids. *Chaos*, 4:369–376, 1994.

[78] S. W. Morris, E. Bodenschatz, D. S. Cannel, and G. Ahlers. Spiral defect chaos in large aspect ratio Rayleigh-Bénard convection. *Phys. Rev. Let.*, 71:2026–2029, 1993.

[79] P. Mullowney, K. Julien, and J. D. Meiss. Blinking rolls: Chaotic advection in a three-dimensional flow with an invariant. *SIAM Applied Dynamical Systems*, 4:159–185, 2005.

[80] A.H. Nayfeh. *Perturbation Methods*. John Wiley and Sons, 1973.

[81] A.H. Nayfeh. *Introduction to Perturbation Techniques*. John Wiley and Sons, 1993.

[82] A. C. Newell, T. Passot, and M. Souli. The phase diffusion and mean drift equations for convection at finite Rayleigh numbers in large containers. *J. Fluid Mech.*, 220:187–252, 1990.

[83] L. Ning and R. E. Ecke. Rotating Rayleigh-Bénard convection: Aspect-ratio dependence of the initial bifurcations. *Phys. Rev. E*, 47:3326–3333, 1993.

[84] J. Oh and G. Ahlers. Thermal-noise effect on the transition to Rayleigh-Bénard convection. *Phys. Rev. Lett.*, 91(094501), 2003.

[85] T. S. Parker and L. O. Chua. *Practical Numerical Algorithms for chaotic numerical systems*. Springer-Verlag, 1989.

[86] D. J. Patil, B. R. Hunt, E. Kalnay, J. Yorke, and E. Ott. Local low dimensionality of atmospheric dynamics. *Phys. Rev. Lett.*, 86:5878, 2001.

[87] M. R. Paul, K.-H. Chiam, and M. C. Cross. Pattern formation and dyanmics in Rayleigh-Bénard convection: Numerical simulations of experimentally realistic geometries. *Physica D*, 184:114–126, 2003.

[88] M. R. Paul, K.-H. Chiam, M. C. Cross, and P. F. Fischer. Rayleigh-Bénard convection in large-aspect-ratio domains. *Phys. Rev. Lett.*, 93(064503), 2004.

[89] M. R. Paul, M. C Cross, and P. F. Fischer. Rayleigh-Bénard convection with a radial ramp in plate separation. *Phys. Rev. E*, 66(046210), 2002.

[90] M. R. Paul, M. C. Cross, P. F. Fischer, and H. S. Greenside. Power-law behavior of power spectra in low Prandtl number Rayleigh-Bénard convection. *Phys. Rev. Lett.*, 87(154501), 2001.

[91] E. Plaut. Nonlinear dynamics of traveling waves in rotating Rayleigh-Bénard convection: effects of the boundary conditions and of the topology. *Phys. Rev. E*, 67(046303), 2003.

[92] E. Plaut and F. H. Busse. Low Prandtl number convection in a rotating cylindrical annulus. *J. Fluid Mech.*, 464:345–363, 2002.

[93] Y. Pomeau, S. Zaleski, and P. Manneville. Dislocation motion in cellular structures. *Phys. Rev. A*, 27:2710–2726, 1983.

[94] W. H. Press, S. A. Teukolsky, W. T. Vetterling, and B. P. Flannery. *Numerical recipes in C*. Cambridge University Press, 1988.

[95] David Ruelle. Large volume limit of the distribution of characteristic exponents in turbulence. *Commun. Math. Phys.*, 87:287–302, 1982.

[96] J. J. Sánchez-Álvarez, E. Serre, E. Crespo del Arco, and F. H. Busse. Square patterns in rotating Rayleigh-Bénard convection. *Phys. Rev. E*, 72(036307), 2005.

[97] J. D. Scheel and M. C. Cross. The amplitude equation for rotating Rayleigh-Bénard convection. in preparation.

[98] J. D. Scheel and M. C. Cross. Lyapunov exponents for small aspect ratio Rayleigh-Bénard convection. submitted to *Phys. Rev. E*, 2006.

[99] J. D. Scheel and M. C. Cross. Scaling laws for rotating Rayleigh-Bénard convection. *Phys. Rev. E*, 72(056315), 2005.

[100] J. D. Scheel, M. R. Paul, M. C. Cross, and P. F. Fischer. Traveling waves in rotating Rayleigh-Bénard convection: Analysis of modes and mean flow. *Phys. Rev. E*, 68(066216), 2003.

[101] A. Schlüter, D. Lortz, and F. Busse. On the stability of steady finite amplitude convection. *J. Fluid Mech.*, 23:129–144, 1965.

[102] W. Schöpf and W. Zimmermann. Convection in binary fluids: Amplitude equations, codimension-2 bifurcation, and thermal fluctuations. *Phys. Rev. E*, 47:1739, 1993.

[103] S. K. Scott. *Chemical Chaos*. Oxford University Press, 1991.

[104] B. Sensoy and H. Greenside. Pattern formation near onset of a convection fluid in an annulus. *Phys. Rev. E*, 64:046204, 2001.

[105] S. C. Shadden, F. Lekien, and J. E. Marsden. Definition and properties of Lagrangian coherent structures from finite-time Lyapunov exponents in two-dimensional aperiodic flows. *Physica D*, 212:271–304, 2005.

[106] E. Siggia and A. Zippelius. Dynamics of defects in Rayleigh-Bénard convection. *Phys. Rev. A*, 24:1036–1049, 1981.

[107] J. T. Stuart. On the nonlinear mechanics of hydrodynamic stability. *J. Fluid Mech.*, 4:1–12, 1958.

[108] S. Tajima and H. Greenside. Microextensive chaos of a spatially extended system. *Phys. Rev. E*, 66(017205), 2002.

[109] G. Tesauro. *Steady-state dynamics and selection principles in nonequilibrium pattern-forming systems*. PhD thesis, Princeton University, 1985.

[110] G. Tesauro and M. C. Cross. Climbing of dislocations in nonequilibrium patterns. *Phys. Rev. A*, 34:1363–1379, 1986.

[111] W. A. Tokaruk, T. C. A. Molteno, and S. W. Morris. Bénard-Marangoni convection in two-layered liquids. *Phys. Rev. Lett.*, 84:3590, 2000.

[112] Lloyd N. Trefethen. *Spectrial Methods in Matlab*. SIAM, 2000.

[113] Y. Tu and M C. Cross. Chaotic domain structure in rotating convection. *Phys. Rev. Let.*, 69:2515–2518, 1992.

[114] H. M. Tufo and P. F. Fischer. Fast parallel direct solvers for coarse grid problems. *J. Parallel Distrib. Comput.*, 61:151–177, 1999.

[115] A. M. Turing. The chemical basis of morphogenesis. *Phil. Trans. R. Soc. London B*, 237:37, 1952.

[116] W. van Saarloos. Complex Ginzburg-Landau equation for beginners. In P. E. Claudius and P. Palffy-Muhoray, editors, *Spatio-Temporal Patterns*, pages 19–31. Addison-Wesley, 1995.

[117] W. van Saarloos and P. C. Hohenberg. Fronts, pulses, sources and sinks in generalized complex Ginzburg-Landau equations. *Physica D*, 56:303–367, 1992.

[118] Thomas Walter. *Zur dynamik von dislokationen in der Rayleigh-Bénard konvektion*. PhD thesis, Universität Bayreuth, 2000.

[119] F. Witknowski, L. Leon, P. Penkoske, W. Files, M. Spano, W. Ditto, and A. Winfree. Spatiotemporal evolution of ventricular fibrillation. *Nature*, 392:78, 1998.

[120] A. Wolf, J. B. Swift, H. L. Swinney, and J. A. Vastano. Determining Lyapunov exponents from a time series. *Physica D*, 16:285–317, 1985.

[121] F. Zhong and R. E. Ecke. Pattern dynamics and heat transport in rotating Rayleigh-Bénard convection. *Chaos*, 2:163–171, 1992.